Modélisation hygro-mécanique non locale de l'endommagement dans les structures thermoplastiques renforcées en relation avec la microstructure

Soheil Satouri

HESAM UNIVERSITÉ

Arts et Métiers Sciences et Technologies

ÉCOLE DOCTORALE SCIENCES ET MÉTIERS DE L'INGÉNIEUR
[LEM3 - Campus de Metz]

THÈSE

présentée par : **Soheil SATOURI**
soutenue le : **5 janvier en 2023**

pour obtenir le grade de : **Docteur d'HESAM Université**

préparée à : **École Nationale Supérieure d'Arts et Métiers**

Spécialité : **Mécanique des matériaux**

Modélisation hygro-mécanique non locale de l'endommagement dans les structures thermoplastiques renforcées en relation avec la microstructure.

THÈSE dirigée par :
[Dr. CHATZIGEORGIOU George, Prof. MERAGHNI Fodil]

et co-encadrée par :
[Dr. BENAARBIA Adil]

Jury

M. Samuel FOREST, DR CNRS, Mines Paris	Président
Mme. Elhem GHORBEL, Professeure, Université de Cergy-Pontoise	Rapportrice
M. Jean-Luc BOUVARD, Professeur, Mines Paris	Rapporteur
M. Thomas BOHLKE, Professeur, Institut de technologie de Karlsruhe	Examinateur
M. Francisco CHINESTA, Professeur, Arts et Métiers Institute of Technology-Paris	Examinateur
M. George CHATZIGEORGIOU,CR-HDR CNRS, LEM3	Examinateur
M. Fodil MERAGHNI, Professeur, Arts et Métiers Institute of Technology-Metz	Examinateur
M. Adil BENAARBIA, MCF-HDR, Arts et Métiers Institute of Technology-Metz	Examinateur
M. Giles ROBERT, Docteur, Domo Chemicals	invité
M. Francis PRAUD, MCF, Arts et Métiers Institute of Technology-Metz	invité

THÈSE

To my parents, thank you for the unconditional love and support.

Acknowledgements

I would like to sincerely thank my thesis supervisors, Dr. George Chatzigeorgiou, Prof. Fodil Meraghni, and Dr. Adil Benaarbia, for their encouragement, guidance, and support over these three years. Their expertise and knowledge in the field have been invaluable in helping me develop my skills, expand my knowledge, and complete this work.

I would also like to express my appreciation to the committee members, Dr. Samuel Forest, Prof. Elhem Gorbel, Prof. Jean-Luc Bouvard, Prof. Thomas Böhlke, Prof. Francisco Chinesta, Dr. Giles Robert, and Dr. Francis Praud, for dedicating time to read my thesis and attending the defense. I deeply appreciate their productive comments that improved the quality of my thesis.

I would like to acknowledge the great support that I have received from the SMART team and LEM3 laboratory. Their scientific contribution to my work and the facilities provided to me have been of great importance for the successful completion of my thesis. In this regard, I would also like to thank Dr. Laurent Peltier and Dr. Rabii Chekkour for their valuable contribution throughout the experimental phase of my project. Furthermore, I would like to acknowledge the productive scientific and technical discussions with Dr. Boris Pitrowski.

Finally, I would also like to thank my family and friends who have provided me with unconditional support and encouragement over these years.

Résumé

Les thermoplastiques et les composites thermoplastiques renforcés de verre ont de nombreuses applications grâce à leurs solides propriétés physiques et à leur facilité de production. Aujourd'hui, ils sont utilisés dans les équipements médicaux, les composants mécaniques des automobiles, les emballages et de nombreuses autres industries. Compte tenu de leur large applicabilité dans plusieurs domaines, ils sont soumis à une variété de conditions environnementales telles que l'humidité et la température, affectant le comportement des thermoplastiques et principalement les mécanismes inélastiques non linéaires, qui seront traités dans cette étude.

Pour prédire les réponses mécaniques, on considère la viscoélasticité, la viscoplasticité et l'endommagement ductile, qui ont déjà été intégrées dans un modèle phénoménologique basé sur le critère de plasticité de von Mises. Cependant, en vue de la sensibilité des thermoplastiques à la pression hydrostatique, en plus de présenter une asymétrie tension-compression, le critère de plasticité de von Mises n'est pas satisfait dans aucun de ces deux cas. Cette étude présente un critère de plasticité I_1-J_2 qui capture à la fois l'effet de la pression hydrostatique et le comportement asymétrique, sur la base duquel une étude paramétrique est réalisée permettant d'étudier le comportement du modèle sous chargement cyclique et multiaxial.

L'absorption d'eau influence le comportement du matériau en affectant la température de transition vitreuse, ce qui change les réponses mécaniques de l'état vitreux à caoutchoutique. À cette fin, une campagne expérimentale est menée pour calibrer les modèles basés sur les critères de plasticité de von Mises et I_1-J_2, en tenant compte de différents niveaux d'humidité relative (HR). La base de données expérimentale est ensuite utilisée pour étudier l'effet de l'absorption d'eau et son influence sur les paramètres du modèle.

Le phénomène d'adoucissement est aussi observé dans les thermoplastiques quand les niveaux

d'endommagement sont élevés, ce qui mène à un problème mal posé dans le modèle local et, par conséquent, à des instabilités et à la non-objectivité des modèles éléments finis. Pour résoudre ce problème, une approche non locale est adoptée pour introduire l'échelle de longueur interne non locale dans le modèle de continuum local. La variable non locale est alors traitée sous deux possibilités ; dans le premier cas, elle est représentée par l'endommagement non local, dans le deuxième cas, on considère la variable d'état d'écrouissage non local. Une étude paramétrique est mise en œuvre pour évaluer l'efficacité des deux options dans le traitement des réponses non-objectives dans un matériau fortement endommagé.

Une autre tâche de cette thèse est d'adopter un modèle non local pour les composites à matrice polymère. A cette fin, la séparation d'échelle et l'application du champ non local aux échelles macro et micro sont étudiées en étendant le modèle non local dans un cadre multi-échelles, sur lequel un cadre d'homogénéisation Mori-Tanaka/TFA approprié est défini. Des études paramétriques révèlent que lorsque l'échelle de longueur interne non locale est déterminée à l'échelle microscopique, les hypothèses théoriques de base de l'homogénéisation ne sont pas satisfaites, et la localisation non-objective des variables d'état à l'échelle macroscopique ne peut pas être prise en compte.

La conclusion principale de la présente étude est que l'application de la variable d'état d'écrouissage non locale est plus pertinent et efficace pour traiter la localisation des variables d'état internes, et que le cadre multi-échelles non local présenté conduit à des réponses plus stables par rapport au modèle local lorsque le matériau est fortement endommagé.

Mots-clés : thermoplastiques renforcés de verre, approche non locale, humidité relative, analyse multi-échelles, asymétrie tension-compression.

Abstract

Thermoplastics and glass reinforced thermoplastic composites have a wide range of applications thanks to their strong physical properties and ease of production. Today, they are used in medical equipment, mechanical components in automobiles, packaging, and many other industries. Considering their broad applicability, they are employed in a variety of environmental and loading conditions. Thermoplastics often exhibit several nonlinear inelastic mechanisms, such as rate dependency, hygro-thermal sensitivity, and ductile damage, to name but few. With this in mind, modeling and predicting this complex behavior requires addressing certain challenges, some of which are presented in this research as follows.

To predict the mechanical responses of thermoplastics, viscoelasticity, viscoplasticity, and ductile damage are considered, which has already been developed as a phenomenological model based on the von Mises yield function. However, thermoplastics are also pressure-sensitive materials that exhibit tension-compression asymmetry in yield behavior, and the von Mises yield function satisfies none of them. This study presents an I_1-J_2 yield function that captures both hydrostatic pressure effect and asymmetric yield behavior, based on which a parametric study is performed and the behavior of the model under cyclic and multi-axial loading is studied.

The water uptake influences the behavior of the material by affecting the glass transition temperature, which changes the mechanical responses from rubbery to glassy. To this end, an experimental campaign is designed to calibrate the models based on von Mises and I_1-J_2 yield functions, taking into account different Relative Humidity (RH) levels. The data extracted from the mechanical tests are used to first study experimentally the effect of water uptake and then to observe its influence on the model parameters.

Thermoplastics exhibit softening behavior at high levels of damage leading to an ill-posed problem

in the local continuum framework and consequent instabilities and non-objectivity in the finite element models. To address this problem, a gradient enhanced nonlocal approach is adopted to introduce the nonlocal length scale into the local continuum model. Two different options are introduced as nonlocal variable: first nonlocal damage and then nonlocal hardening state variable. A parametric study is implemented to evaluate the effectiveness of both options in treating non-objective and non-physical responses in a severely damaged material.

Another task of this thesis is to adopt a nonlocal-type model for polymer-based composites. To this end, the scale separation and application of the nonlocal field at macro and micro scales are investigated by extending the nonlocal model into a multi-scale framework, upon which an appropriate Mori-Tanaka/TFA homogenization framework is defined. Parametric studies reveal that when the nonlocal length scale is set at the microscale, the basic theoretical assumptions of homogenization are not satisfied, and the non-objective localization of state variables at the macroscale is not addressed. As a key conclusion from the present study, the application of the nonlocal hardening state variable shows good efficiency in addressing the localization of internal state variables, specially plasticity and damage, and the presented nonlocal multi-scale framework leads to more stable responses compared to the conventional model when the material is heavily damaged.

Keywords: glass reinforced thermoplastics, nonlocal approach, relative humidity, multi-scale analysis, tension-compression asymmetry.

Contents

List of Tables

List of Figures

Chapter 1

Introduction

1.1 Preface

Polymers can be reinforced using a variety of inclusions to form polymer composites with superior thermomechanical and chemical performances. In this respect, polyamide-based composites are among the most widely used materials in a variety of engineering industries such as aerospace, automotive, and energy because of their durability, multi-functionality, and strength. Polyamides are considered as semicrystalline polymers with an ordered molecular structure. One important characteristic of polyamides is that they are quite sensitive to environmental conditions. They have a high moisture absorption rate and their behavior can change from glassy or brittle to rubbery due to the change in glass transition temperature. Consequently, several inelastic deformation mechanisms can occur and interact depending on the environmental and loading conditions, based on which the numerical model is developed to predict the mechanical responses. To this end, a nonlinear rheology must be designed taking into account the dominant mechanisms, and then the phenomenological model and the corresponding constitutive laws are derived. However, at high levels of damage, polymers show material softening, resulting ill-posed problem and subsequently non-physical and non-unique responses in the computational models. To address this, it is required to apply a nonlocal approach and define a proper multi-scale homogenization framework to model polymer composites behaviors. In the following sections, an overview about the mechanical responses in polymers, the available models and approaches, and the proposed methodology in this study is presented briefly.

1.2 Nonlinear rheology in polyamides

When it comes to active mechanisms in polyamides, environmental effects, such as temperature and humidity, are of key importance. Polyamides tend to absorb water, which strongly affects their mechanical response through interaction with hydrogen bonds in their molecular structure changing thereby the material behavior from glassy to rubbery state [3]. The degree or intensity of the active mechanisms in polyamides always depends on the temperature and their water content. Thus, depending on the environmental conditions, different mechanical responses are expected, on the basis of which many physical and phenomenological models have been proposed [4–13].

There are two main theories for modeling deformation: small and large deformation theories. In the small or infinitesimal deformation theory, the material displacement is assumed to be much smaller

than the corresponding body, and the associated geometry remains unchanged. Under this assumption, the corresponding equations of continuum mechanics become much simpler. On the contrary, in the theory of large deformations or finite deformation theory, the deformation and rotation are large enough to violate the small deformation assumptions, which requires more complicated formulations.In this study, the framework is developed for polyamide materials, but the goal is to adopt the model in multi-scale analyses. For fiber-reinforced composites, the deformation levels are usually small, thus it is reasonable to develop the present nonlocal framework using small deformations/rotations hypothesis.

Under the supposed yield strength, polyamides at room temperature exhibit viscoelastic effects, which can be observed using creep-recovery tests [14, 15]. There are a variety of rheological models to describe the viscoelastic mechanisms [16–18]. Viscoelastic models are often obtained through two major approaches: integral and differential forms representations [19, 20]. The integral representation requires the integration of the entire time history to describe the stress-strain relation. Green, Rivlin, and Spencer [21], Pipkin and Rogers [22], etc., are some examples of these models using integral formulations. On the other hand, differential representation proposes linear viscoelastic models, such as Maxwell, Kelvin-Voigt, Burgers, and their extensions, which are modeled using rheological elements as linear springs and dashpots. This approach allows simulating the viscoelastic mechanisms using state variables and their corresponding conjugate variables.

Exceeding the polymers yield limit and changes in the polymer macromolecular structure result in rate-dependent irreversible viscoplastic mechanisms leading to ductile damage. Plastic deformation and eventually necking are examples of these irreversible mechanisms that can be observed and emphasized using creep-recovery tests [14, 15]. It is accompanied by creep and rate dependent mechanical effects, upon which the irreversible nonlinear mechanisms, occurring after the yield point, can be modeled by unified or non-unified viscoplasticity theories [23, 24]. In the unified theory, the plasticity and viscosity are considered as a single rate dependent inelastic variable in the constitutive model [25, 26]. However, the non-unified theory proposes two separate variables for plasticity and creep which are rate independent and rate dependent, respectively [27, 28]. The non-unified theory is efficient when the creep is dominant, which normally occurs at high temperatures [29]. In the contrary, difficulties in finite element implementation are reported in the room temperature for material models using non-unified theories [30].

In viscoplasticity framework, it is necessary to identify the elastic region by defining an appropriate

yield surface considering the material type. Tresca, Mohr-Coulomb, von Mises, Drucker-Prager, and their extensions are the most frequently used yield criteria for polymers [31–34]. The yield surfaces are defined in terms of principal stresses or stress tensor and its deviatoric part invariants. The first invariant of the stress tensor, I_1, introduces the hydrostatic pressure effect, and the second and third invariants of the stress deviatoric part (J_2 and J_3) correspond to pure shear and rotation, respectively. Many studies have used von Mises criterion to investigate the inelastic behavior of polymers [1, 14, 35, 36]. However, the classical von Mises yield surface is not accurate enough to describe the material behavior under multi-axial loading. Indeed, in polymers, the yield behavior is not only dependent on the stress deviatoric part but also on the hydrostatic pressure effect, and the yield stress is slightly higher in compression [37–41]. From this perspective, although Drucker-Prager has more parameters to be experimentally identified, it is more accurate for pressure-dependent materials such as polymers and captures the tension-compression asymmetry and hydrostatic pressure effect. In this connection, some research works have tried to extend Drucker-Prager model or combine it with other ones to account for more mechanisms [42–44].

As mentioned above, in polymers, plastic deformation depends on environmental conditions leading to ductile damage. Modeling of damage can be conducted under different assumptions. One may consider damage resulting from coalescing and widening of voids based on the micromechanics framework, such as Gurson model [45], and the other one considers it based on continuum damage mechanics (CDM) and derives damage based on Thermodynamics of Irreversible Processes (TIP) [46]. There is a great deal of studies in the open literature, in which the classical Gurson model is modified to a semi-phenomenological model accounting for ductile damage [47–49]. In CDM models, damage is defined as an internal state variable, and the model parameters can be simply extracted by macroscopic mechanical tests.

1.3 Nonlocal modeling

At high levels of damage, polymers exhibit material softening, resulting in ill-posed problems in typical continuum frameworks and, consequently, non-unique and non-physical responses in computational models. This results in the localization of internal variables in the narrowest possible area by any mesh refinement in the thermodynamical-based models [50,51]. To address this issue, "localization limiters" are proposed in the literature, among which nonlocal approaches are the most popular [52,53].

Nonlocal models are introduced in the local continuum framework in different forms. The integral type model is the basic form of nonlocal approaches, in which the local variable is replaced by the weighted average over the corresponding neighborhood determined by the internal length scale [54–58]. The Taylor expansion of the nonlocal integral form equation leads to the explicit gradient-enhanced model, from which the implicit gradient form can be derived [58–62]. There are also some other nonlocal approaches applied to address the computational model instability in the open literature, such as micromorphic [63], phase field [64–68], and peridynamics [69, 70]. Nonlocal micromorphic models are also employed to implement the nonlocal analysis that is defined based on generalized continuum theories and thermodynamically based micromorphic constitutive equations. [61, 71, 72]. In phase-field approach, the discontinuous sharp crack is approximated as a smeared zone, which is originated from the thermodynamic framework presented by Griffith and Taylor [73]. The underlying mathematical logic of the theory relies on the energy balance between the mass energy (away from the crack) and the energy dissipated from the crack [66]. In peridynamics approach, the internal body forces are considered as interactions within a network of springs. The behavior of the springs is described through their length and direction. The original model is called link-based peridynamics. Some disadvantages and limitations, such as constraining Poisson's ratio, have led to develop another type of this theory called state-based, on which, the forces are no longer described independently and depend on the collective deformation of all the bonds [74].

In thermodynamically based constitutive models, implementation of the nonlocal approach requires introducing a nonlocal field derived from the internal state variables. The corresponding nonlocal variable is defined in terms of the material type and its corresponding mechanical response (i.e. from rubber-like to glassy state). This directly influences the non-physical responses or spurious localization of internal variables. The nonlocal variable for glassy polymers is often derived from the damage [55, 75]. However, plasticity-related variable is used to introduce the nonlocal field when materials exhibit softer mechanical responses accompanied by ductile damage. In those cases, localization of plasticity is also expected as well as the damage non-unique responses [55, 76, 77].

1.4 Multi-scale analysis

All of the previous sections discuss the nonlinear inelastic mechanical responses of polymers and the thermodynamically based models available to predict their behavior. However, this part of the present

work aims to address the modeling limitations in the glass-reinforced polymers when undergoing high levels of plasticity-induced damage. Generally speaking, composites display material heterogeneity and variation in their internal structure at the microscale due to the presence of inclusions in the matrix. Depending on the inclusions geometries and their configurations in the micro structure, the overall material response is affected in the macroscale. To model the overall behavior of composites, the heterogeneous medium must be replaced by its equivalent homogeneous medium using a homogenization approach. To this end, the Representative Volume Element (RVE) and its corresponding characteristic size are introduced to capture the local material behavior in the microscale and estimate the overall response using homogenization mathematical framework. In this respect, there have been many studies conducted as innovative works [45, 78–82]. Finite element based (full-field) approaches and mean-field methods are applied to compute the effective responses of the RVE. However, mean-field methods are less computationally expensive and more popular in multi-scale analyses notably for composites with random or quasi-random microstructures. Eshelby solution based micromechanical methods, such as Mori-Tanaka and self consistent, are some of the most popular mean-field approaches [2].

Generally speaking, each RVE consists of different sub-phases, some of which may exhibit locally nonlinear behaviors. The multi-scale framework requires linking the nonlinear behaviors of the sub-phases to the macroscale constitutive equations. To this end, three main categories of methods are proposed in the literature: analytical, integrated, and sequential approaches. In analytical approaches, the nonlinear behavior of sub-phases is modeled by linearizing the Eshelby problem for inclusions [83–86]. The integrated approaches try to model the microstructure as close as possible to its real properties and configuration without constitutive equations at the macroscale, as multi-level finite element (FE^n) and FFT-based models [87–89]. In the sequential approach, the macroscale constitutive equations rely on a multi-scale framework derived from the unit cell decomposition into sub-phases accounting for inelastic and nonlinear behaviors. In this respect, Dvorak presented Transformation Field Analysis (TFA), based on which the RVE is decomposed to sub-phases, and an inelastic part of deformation is introduced to the multi-scale model [90]. Using the TFA framework, Kruch and Chaboche presented a multi-scale elasto-viscoplastic model with damage to analyze the nonlinear behavior of heterogeneous materials [91]. Moreover, some more advanced models are recently presented for composites accounting for viscoelastic viscoplastic mechanisms with damage using Mori-Tanaka/TFA approach [36, 92, 93].

Similar to pure polyamides, reinforced polyamide composites also undergo material softening lead-

ing to a consequent non-physical responses in the computational models. To address this issue, as mentioned earlier, a nonlocal approach must be implemented through a proper homogenization framework. Developing the nonlocal model requires to introduce a new degree of freedom in the problem's formulation. An additional related equation is then required into the multi-scale model. It depends on the nonlocal length scale and can be defined at macro or micro scale. In this regard, Bharali et al. [94] developed a phase field model in a multi-scale framework, in which the corresponding nonlocal variable appears only in the RVE size. In another study, Fantoni et al. [95] implemented nonlocal phase field approach at macroscale and presented a nonlocal homogenization framework to study composites. The challenge of the nonlocal implementation in multi-scale models and the equations solved in different scales were also discussed in [96, 97].

1.5 Aims and objectives

This study aims at developing a nonlocal multi-scale model to describe the mechanical response of glass-reinforced polyamides by considering nonlinear inelastic mechanisms with plasticity-induced ductile damage and accounting for the tension-compression asymmetry. To this end, a pressure-sensitive I_1-J_2 yield function is introduced to consider the hydrostatic pressure effect and the asymmetric yielding behavior of polyamides. However, the model parameters vary in different RH and require calibration with different water contents. To address this, an experimental campaign is designed and carried out using macroscopic mechanical tests. They allowed to identify the parameters models based on von Mises and I_1-J_2 yield functions. Since material softening in polymers at high damage levels leads to non-unique and non-physical responses and spurious localization of the internal state variables, the nonlocal gradient enhanced approach is adopted to control state variables localization. In this respect, two different nonlocal variables derived from the damage and the hardening state variable are considered and the corresponding model responses are evaluated to find the most effective option. The nonlocal Viscoelastic Viscoplastic framework accounting for ductile damage (VEVPD) is then extended to a multi-scale model, and an appropriate homogenization framework is adopted to study glass-reinforced polyamide composites at a high damage level. The novelties of the present research can be summarized as follows:

- The model parameters are identified considering nonlinear inelastic mechanisms and ductile

damage. The water uptake effect on each parameter for two different yield functions (i.e. von Mises and I_1-J_2) is studied.

- A parametric study is performed to investigate the capability of the gradient enhanced model in yielding mesh objective and physically meaningful solutions within the highly damaged zones under softening, which considers all inelastic mechanisms (i.e. viscoelasticity at different time scales, VE, viscoplasticity, VP, ductile damage, D, etc.).

- The nonlocal hardening state variable is introduced to address the damage localization in a VEVPD model, where its efficiency is justified compared to the nonlocal damage.

- A multi-scale nonlocal framework is developed to capture mechanisms such as viscoelasticity, viscoplasticity and ductile damage for the matrix phase and provides more stable results compared to the local framework.

Considering the contributions mentioned above, the chapters of the thesis and their corresponding objectives are elaborated upon hereunder.

In the second chapter, the initial limitations of the VEVPD model, including the effect of hydrostatic pressure and the tensile-compressive yield strength asymmetry, are discussed. The conventional von Mises yield function, based on the second invariant of the deviatoric stress tensor, J_2, is extended to the I_1-J_2 model. In addition, the asymmetry between tensile and compressive elastic limits is accounted for by an asymmetry ratio, m, in the yield function. Parametric studies show how the model behaves under different types of loading. Self-heating caused by dissipative mechanisms is also discussed.

In the third chapter, the water uptake effect on polyamide 66 is studied in an experimental-numerical framework. First, an experimental campaign is designed using the dog bone samples, which are conditioned at different RH, namely RH 0%, RH 25%, RH 50%, RH 65%, and RH 80%. Then, the samples are subjected to monotonic, creep, and cyclic loading at different loading rates to calibrate and validate the conventional VEVPD model with von Mises yield function. The obtained experimental observation from dog bone samples along with tensile-torsion tests on diabolo samples are used to calibrate the I_1-J_2 model. The parameters identified from von Mises and I_1-J_2 are studied where the effect of RH is evaluated.

In the fourth chapter, an extended thermodynamical framework based on the gradient enhanced nonlocal model is adopted to develop nonlocal constitutive laws. To this end, the thermodynamic potential is enhanced with nonlocal terms which subsequently appear in constitutive laws depending on the nonlocal variable choice. In this study, nonlocal hardening state variable and nonlocal damage, as nonlocal variable options, are considered in two different cases, and parametric investigation is performed and their efficiency is assessed.

In the fifth chapter, the nonlocal model presented in chapter 4, is extended to a multi-scale framework. To this end, the relation between the nonlocal length scale and the corresponding RVE size is studied, and two different cases are considered: first, when the length scale is less than or comparable with the RVE size; second, when the nonlocal length scale is much larger than the RVE size. The active mechanisms and the equations used in the macro and micro scales are explored through asymptotic expansion. Based on the above studies, a proper homogenization framework is presented, and Mori-Tanaka/TFA is adopted to homogenize the presented nonlocal multi-scale model. Finally, the solutions are validated with a full structure multi-layered composite and the model is evaluated in different numerical examples.

Chapter 2

Viscoelastic-viscoplastic-damageable response of thermoplastic polymers accounting for pressure sensitivity and tension-compression asymmetry

Contenu

2.1 Introduction

As discussed in the chapter 1, to study the mechanical responses of glass-reinforced thermoplastics, it is first necessary to properly model the nonlinear inelastic behavior of the matrix phase. Many reports in the literature have investigated the active mechanisms through macroscopic mechanical tests [14, 15, 51, 98]. In this respect, viscoelastic viscoplastic models accounting for ductile damage have been developed and presented in the literature [14, 99–103].

Thermoplastics are pressure-sensitive materials exhibiting asymmetric yield behavior, in which the yield strength is slightly higher under compression. However, conventional phenomenological models for thermoplastics are usually based on von Mises yield function [14,103,104], in which the polymers are assumed pressure-insensitive materials with symmetric behavior. In this regard, Ghorbel has developed a general yield function accounting for tension-compression asymmetry and hydrostatic pressure effect for a viscoplastic material [44]. However, the latter model does not capture viscoelasticity and damage. In this chapter, a I_1-J_2 yield criterion, inspired from [44], is integrated in the VEVPD model. The thermodynamic framework, developed in [14], is modified based on the new yield function. Then, the corresponding constitutive laws are derived and implemented on the computational model. Using this, a User-defined Material (UMAT) subroutine is developed to implement the model on the FE software (ABAQUS). Using a homemade 0D solver, the model is subjected to different loading conditions, and a basic parametric study is conducted. Then, the self-heating caused by the dissipative mechanisms and the effect of the asymmetry parameter are studied using 3D numerical examples. The parametric study indicates the importance of the asymmetry parameter on the model mechanical responses, particularly under compression and multi-axial loading. Furthermore, it is found that the probable temperature change due to self-heating under quasi-static loading conditions is quite small for a single loading cycle. This implies that for considerable coupled thermo-mechanical effects, the number of cycles must be high enough to affect the mechanical responses. Since no fatigue or material behavior studies under high loading rates are planned in this study, this observation allows thermo-mechanical coupling to be ignored for the rest of this study with good accuracy.

This chapter is structured as follows: in section 2.2, the nonlinear inelastic mechanisms of thermoplastics and their pressure-sensitive mechanical response are first discussed, and an appropriate I_1-J_2 yield function is presented, based on which the thermodynamical framework is developed and the con-

stitutive laws are derived; in section 2.3, the model is implemented numerically using "convex cutting plane" return mapping algorithm, and the corresponding tangent operators are derived; in section 2.4, a parametric study is presented using a homemade 0D solver and the commercial FE program (ABAQUS), and the effect of the asymmetry parameter and the influence of the thermo-mechanical coupling on the mechanical responses are studied.

2.2 Theoretical background and thermodynamical framework

2.2.1 Nonlinear inelastic mechanisms and constitutive model

Many constitutive laws have been proposed to capture the nonlinear behavior of thermoplastics using macromolecular network-based [5,11] and phenomenological approaches [10,14,20,105]. Most of these models have been formulated within the framework of thermodynamics of irreversible processes [106, 107]. For the polyamide 66, cyclic creep-recovery tests have been conducted in [51, 98] and have shown that capturing the material behavior requires to assume decomposition of the total strain into elastic, viscoelastic and viscoplastic components [108]. In the present study, a viscoelastic viscoplastic rheological model accounting for ductile damage (VEVPD) is adopted to describe the dissipative mechanisms involved during the deformation process of the material.

A Kelvin-Voight model is capable of capturing the viscous effects observed during the deformation process of thermoplastics. Defining more than one Kelvin-Voigt branch allows to describe viscoelasticity at several characteristic times [14] (see Figure 2.1-a,b). Each viscoelastic branch is modeled as a combination of a linear spring and a dashpot.

Moreover, viscoplastic mechanisms can be captured based on either unified or non-unified viscoplasticity theories [23]. Hereafter, the unified theory is adopted with an isotropic hardening function, R, defined such as:

$$R(r) = H_m \, r^{H_p}, \tag{2.1}$$

where r is the hardening state variable, and H_m and H_p are the model parameters. The viscoplastic mechanism is modeled by a parallel assembly of a nonlinear spring and a nonlinear dashpot in the rheological model (see Figure 2.1-c). In this study, reduction of the material stiffness is expressed through ductile damage. Here, damage is defined as a scalar internal state variable, D, and introduced

to the model through the effective stress concept, $\tilde{\boldsymbol{\sigma}}$ [109–111]:

$$\tilde{\boldsymbol{\sigma}} = \frac{\boldsymbol{\sigma}}{1-D}. \tag{2.2}$$

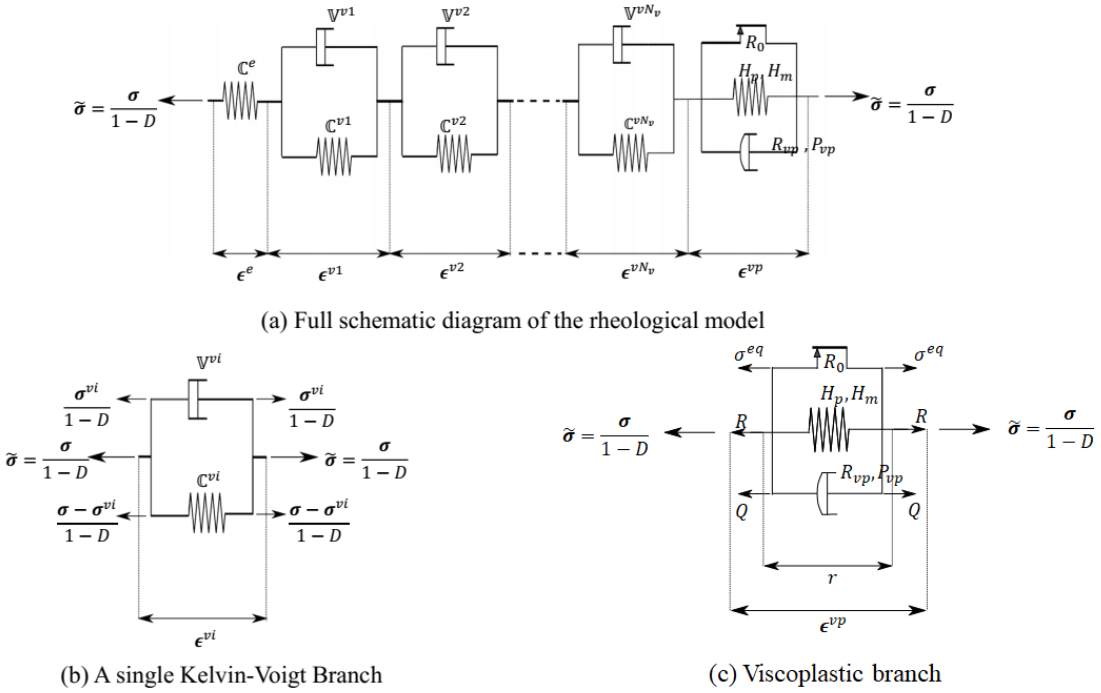

Figure 2.1: Schematics of the VEVPD rheological model.

Implementing the present rheological model requires defining a proper yield surface, based on which the plastic flow and subsequently the viscoplastic mechanism is expressed. In the following sections, the pressure sensitivity and asymmetry in tension-compression yield strength is discussed, and a proper yield function is introduced.

2.2.2 Hydrostatic pressure effect and tension-compression asymmetry

The hydrostatic pressure effect has an undeniable role in describing the mechanical behavior of thermoplastics [38, 40, 41, 112, 113]. Thus, their behavior can be described using pressure-dependent models. Since the yield stress is expected to be higher in compression compared to the tension, the typical von Mises yield function based on J_2 (stress invariant) is not accurate enough to capture the plastic flow in thermoplastics. In this respect, there are some criteria, such as the Mohr-Coloumb and Drucker-Prager models [42–44]. However, it is often preferred using Drucker-Prager and its extensions

to describe the plastic surface in thermoplastics [37].

2.2.3 I_1-J_2 yield function

Considering an isotropic hardening function, an I_1-J_2 yield surface coupled with damage inspired from [44], is considered as:

$$f = f^* - R_0 - R, \qquad \text{with} \quad R = H_m r^{H_p}, \tag{2.3}$$

and:

$$f^* = C_2\sqrt{\tilde{J}_2} + C_1\tilde{I}_1, \qquad C_1 = \frac{m-1}{m(m+1)}, \qquad C_2 = \frac{\sqrt{3}}{m}, \qquad m = \sigma_y^c/\sigma_y^t, \tag{2.4}$$

where m is the asymmetry parameter introduced to the model as the ratio between compression and tensile yields, and $\tilde{I}_1$ and $\tilde{J}_2$ are respectively first invariant of the effective stress and second invariant of the effective deviatoric stress tensor, defined as:

$$\tilde{I}_1 = \frac{I_1}{1-D}, \qquad \tilde{J}_2 = \frac{J_2}{(1-D)^2}, \tag{2.5}$$

with I_1 and J_2 given by:

$$I_1 = \text{trace}(\boldsymbol{\sigma}), \qquad J_2 = \frac{1}{2}\boldsymbol{\sigma}' : \boldsymbol{\sigma}', \tag{2.6}$$

where $\boldsymbol{\sigma}'$ denotes the deviatoric stress tensor. Figure 2.2-a shows the yield surface in the 2D field of principle stresses. As observed, an increase in m leads to more pronounced asymmetry in the compression zone. Also, the yield surface is plotted based on the different plastic deformations by giving $m = 1.3$, which is depicted in Figure 2.2-b. To model the material plastic flow properly and satisfy the positive dissipation, the yield criterion should be convex. The convexity of the presented function, f, can be easily proved as:

$$\frac{\partial f}{\partial \boldsymbol{\sigma}}(\boldsymbol{\sigma} - \boldsymbol{\sigma}_0) \leq f(\xi) - f(\boldsymbol{\sigma}_0). \tag{2.7}$$

The present yield function and the rheological model introduced in the previous sections allow developing the constitutive laws through a thermodynamical framework, which is given in the next section.

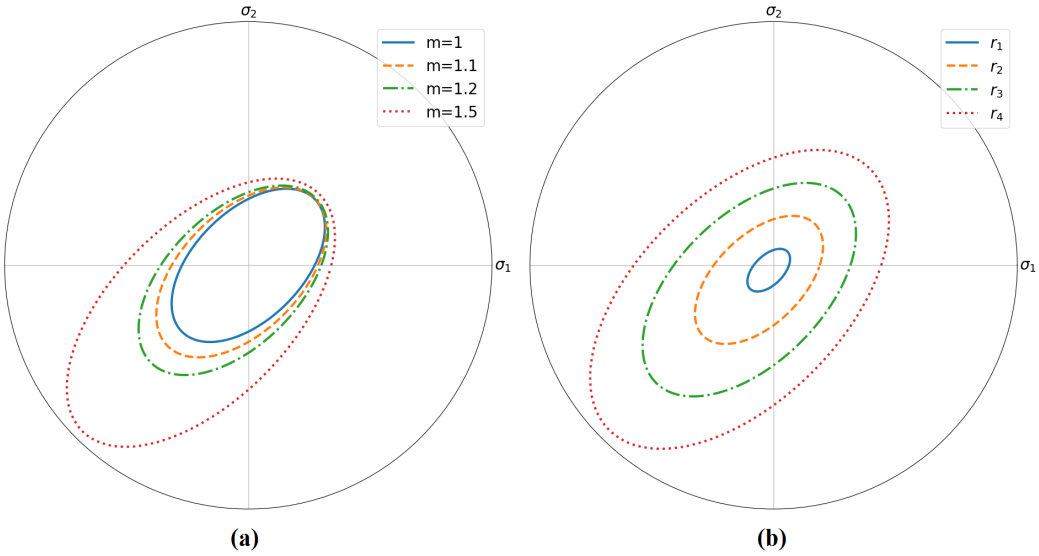

Figure 2.2: a) Schematics of the yield surface in the principle stresses field and its change by increasing the asymmetry parameter, m; b) Schematics of the yield surface in the principle stresses field and its change by increasing the plastic deformation.

2.2.4 Constitutive laws

2.2.4.1 State laws

In the thermodynamical framework, the total strain, $\boldsymbol{\epsilon}$ is the observable state variable, and viscoelastic strains, $\{\boldsymbol{\epsilon}^{vi}\}_{i=1,N_v}$, hardening state variable, r, Damage, D, and viscoplastic strain, $\boldsymbol{\epsilon}^{vp}$, are the internal state variables. Ignoring thermal effects, the Helmholtz free energy function is divided into elastic part, Ψ^e, set of viscoelastic potentials, $\{\Psi_i\}_{i=1,N_v}$, and the viscoplastic free energy, Ψ^{vp} [14]:

$$\Psi(\boldsymbol{\epsilon}, \boldsymbol{\epsilon}^{vi}, \boldsymbol{\epsilon}^{vp}, r, D) = \Psi^e(\boldsymbol{\epsilon}, \boldsymbol{\epsilon}^{vi}, \boldsymbol{\epsilon}^{vp}, D) + \sum_{i=1}^{N_v} \Psi^{vi}(\boldsymbol{\epsilon}^{vi}, D) + \Psi^{vp}(r), \tag{2.8}$$

with

$$\begin{aligned} \Psi^e &= \frac{1}{2}\left(\boldsymbol{\epsilon} - \sum_{i=1}^{N_v} \boldsymbol{\epsilon}^{vi} - \boldsymbol{\epsilon}^{vp}\right) : (1-D)\mathbb{C}^e : \left(\boldsymbol{\epsilon} - \sum_{i=1}^{N_v} \boldsymbol{\epsilon}^{vi} - \boldsymbol{\epsilon}^{vp}\right), \\ \Psi^{vi} &= \frac{1}{2}\boldsymbol{\epsilon}^{vi} : (1-D)\mathbb{C}^{vi} : \boldsymbol{\epsilon}^{vi}, \qquad \Psi^{vp} = \int_0^r R(\alpha)\mathrm{d}\alpha, \end{aligned} \tag{2.9}$$

where $\mathbb{C}^e$ and $\mathbb{C}^{vi}$ are the elastic and viscoelastic stiffness tensors, respectively. The conjugate variables are derived by partial derivatives of the thermodynamic potential with respect to $\boldsymbol{\epsilon}$, $\boldsymbol{\epsilon}^{vi}$, $\boldsymbol{\epsilon}^{vp}$, r, and D:

$$\begin{aligned}
&\boldsymbol{\sigma} = \frac{\partial \Psi}{\partial \boldsymbol{\epsilon}} = (1-D)\mathbb{C}_e : \left(\boldsymbol{\epsilon} - \sum_{i=1}^{N_v} \boldsymbol{\epsilon}^{vi} - \boldsymbol{\epsilon}^{vp}\right), \\
&\boldsymbol{\sigma}^{vi} = -\frac{\partial \Psi}{\partial \boldsymbol{\epsilon}^{vi}} = \boldsymbol{\sigma} - (1-D)\mathbb{C}^{vi} : \boldsymbol{\epsilon}^{vi}, \qquad \boldsymbol{\sigma} = -\frac{\partial \Psi}{\partial \boldsymbol{\epsilon}^{vp}}, \\
&R(r) = \frac{\partial \Psi}{\partial r}, \qquad Y = -\frac{\partial \Psi}{\partial D} = \frac{\boldsymbol{\epsilon}^e : \boldsymbol{\sigma}}{2(1-D)} + \frac{1}{2}\sum_{i=1}^{N_v} \boldsymbol{\epsilon}^{vi} : \mathbb{C}^{vi} : \boldsymbol{\epsilon}^{vi}.
\end{aligned} \tag{2.10}$$

2.2.4.2 Evolution laws

Based on the second principle of thermodynamics, in the form of Clausius-Duhem inequality, the dissipated energy rate is always positive or equal to zero. It is expressed as the difference between the deformation energy, P_m, and the stored energy, $\dot{\Psi}$:

$$\begin{aligned}
\mathcal{D} &= P_m - \dot{\Psi} \geq 0 \\
&= \boldsymbol{\sigma} : \dot{\boldsymbol{\epsilon}} - \left(\frac{\partial \Psi}{\partial \boldsymbol{\epsilon}} : \dot{\boldsymbol{\epsilon}} + \sum_{i=1}^{N_v} \frac{\partial \Psi}{\partial \boldsymbol{\epsilon}^{vi}} : \dot{\boldsymbol{\epsilon}}^{vi} + \frac{\partial \Psi}{\partial \boldsymbol{\epsilon}^{vp}} : \dot{\boldsymbol{\epsilon}}^{vp} + \frac{\partial \Psi}{\partial r} : \dot{r} + \frac{\partial \Psi}{\partial D} : \dot{D}\right) \geq 0.
\end{aligned} \tag{2.11}$$

Taking into account the expression of the conjugate variables, the dissipation term can be expressed as follows:

$$\mathcal{D} = \sum_{i=1}^{N_v} \boldsymbol{\sigma}^{vi} : \dot{\boldsymbol{\epsilon}}^{vi} + \boldsymbol{\sigma} : \dot{\boldsymbol{\epsilon}}^{vp} - R\dot{r} + Y\dot{D} \geq 0. \tag{2.12}$$

According to Generalized Standard Materials formalism (GSM), satisfying the Clausius-Duhem inequality requires defining the rate of internal state variables through dual dissipation potentials and indicative functions [106], which are introduced in the following.

A set of sub-potentials, Ω^{vi}, are introduced to derive the elementary viscoelastic strain rates, $\boldsymbol{\epsilon}^{vi}$, with respect to their associated thermodynamic forces, $\boldsymbol{\sigma}^{vi}$, such that:

$$\Omega^{vi}(\boldsymbol{\sigma}^{vi}, D) = \frac{1}{2}\boldsymbol{\sigma}^{vi} : \frac{\mathbb{V}^{vi\,-1}}{1-D} : \boldsymbol{\sigma}^{vi}, \tag{2.13}$$

where $\mathbb{V}^{vi}$ denotes the viscosity tensor of the $i\,th$ viscoelastic Kelvin-Voigt branch. For each Kelvin-Voigt branch, a characteristic time, τ^{vi}, can be identified, which corresponds to the viscous behavior of the considered branch. A single viscoelastic branch under a sudden stress, $\boldsymbol{\sigma}_0$, at time t_0 responds

through the following equation [114]:

$$\boldsymbol{\epsilon}^{vi}(t) = \boldsymbol{\epsilon}^{vi}_{\infty}\left[1 - exp\left(-\frac{t-t_0}{\tau^{vi}}\right)\right], \quad \text{with} \quad \boldsymbol{\epsilon}^{vi}_{\infty} = \mathbb{C}^{vi\,-1} : \boldsymbol{\sigma}_0, \tag{2.14}$$

with

$$\tau^{vi}\mathbb{I} = \mathbb{C}^{vi\,-1} : \mathbb{V}^{vi}, \quad \tau^{vi} = \frac{\eta^{vi}}{E^{vi}}, \tag{2.15}$$

therein the relations between the viscoelastic model parameters are expressed. The viscoelastic strain rates are derived through the derivation of Ω^{vi} with respect to the viscoelastic thermodynamic force:

$$\dot{\boldsymbol{\epsilon}}^{vi} = \frac{\partial \Omega^{vi}}{\partial \boldsymbol{\sigma}^{vi}} = \frac{\mathbb{V}^{vi\,-1}}{1-D} : \boldsymbol{\sigma}^{vi}. \tag{2.16}$$

According to the J_2-viscoplasticity theory [16], the viscoplastic evolution laws coupled with damage are derived using the normality rule by considering the following indicative function inspired from damage-plasticity law by Lemaitre [115]:

$$F = f(\boldsymbol{\sigma}, D, r) + f_D, \tag{2.17}$$

with

$$f_D = \frac{S_D}{(\beta_D + 1)(1-D)}\left(\frac{Y}{S_D}\right)^{\beta_D+1}, \tag{2.18}$$

where β_D and S_D are damage-related parameters, and f is given in (2.3). The latter model has been used primarily for ductile damage in metals, in which the damage grows slowly in the beginning and very rapidly in the final stages of loading. However, the damage progression is different in polymers, for whom the damage initiation is quite rapid at the beginning and then slowly grows thereafter [116]. For metals, the sign of β_D is positive yielding increasing damage rate with respect to plasticity. However, for polymers, the damage behavior can be captured by considering negative sign for β_D [20]. Figure 2.3 shows how the sign of β_D affects the damage growth. Considering the negative β_D in the present model, the damage-related function, f_D, can be negative if β_D is smaller than -1, but the dissipation sign is not affected and it stays zero or positive. In other words, thermodynamically speaking, there is no restriction about the sign of F as long as the mechanical dissipation stays zero or positive according to Clausius-Duhem inequality. The viscoplastic-damage evolution laws are derived as:

$$\begin{aligned} &\dot{r} = \dot{\lambda}, \qquad \dot{\boldsymbol{\epsilon}}^{vp} = \frac{\partial F}{\partial \boldsymbol{\sigma}}\dot{\lambda} = \boldsymbol{\Lambda}_{vp}\dot{\lambda}, \\ &\dot{D} = \frac{\partial F}{\partial Y}\dot{\lambda} = \left(\frac{Y}{S_D}\right)^{\beta_D}\frac{\dot{\lambda}}{1-D} = \Lambda_D\dot{\lambda}. \end{aligned} \tag{2.19}$$

The viscoplasticilty and rate dependency in the permanent deformation zone is modeled by expressing the rate of the hardening state variable with respect to the yield function, f:

$$\dot{r} = \langle \frac{f}{R_{vp}} \rangle_+^{1/P_{vp}}, \tag{2.20}$$

where "$\langle\,.\,\rangle_+$" denotes the Macaulay brackets, and R_{vp} and P_{vp} are respectively the viscoplastic resistance and exponent. Considering the above relations and the dissipation given by (2.12), it is easy to prove that the dissipation is always non-negative: for the first term, the viscoelastic strain rates are derived from the viscoelastic potential as (2.16), and its product with $\boldsymbol{\sigma}^{vi}$ can not be negative; for the second and third terms, they are non-negative values derived from the normality rule of the yield surface; for the third term, Y is always positive (see (2.10)), and the damage rate, $\dot{D}$, is derived from Λ_D and $\dot{\lambda}$ which is positive, so their product is always non-negative. This confirms the earlier discussion that dissipation is always non-negative no matter what the sign of f_D is.

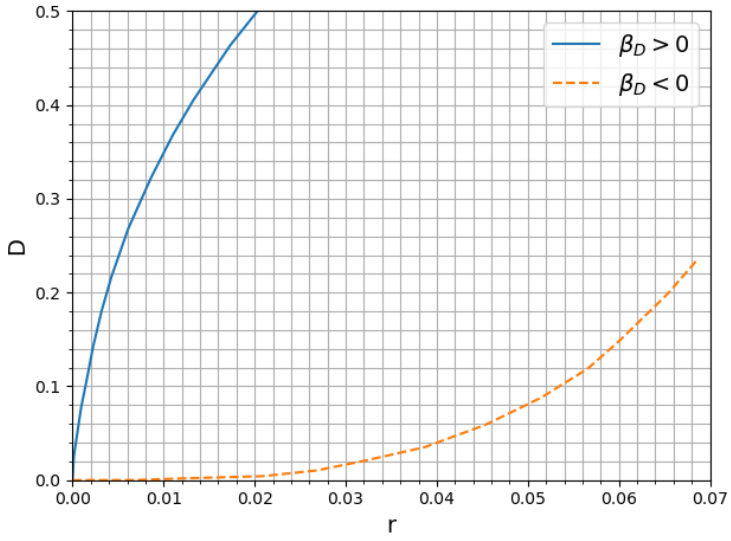

Figure 2.3: Effect of the sign of β_D on the damage growth with respect to hardening state variable.

2.3 Numerical implementation

The time discretization of the governing equations is implemented through a backward Euler scheme, based on which an arbitrary variable Ξ is updated from the time step n into the time step $n+1$ as $\Xi_{n+1} = \Xi_n + \Delta\Xi_{n+1}$. An iterative algorithm is required so as to solve the time discretized

equations. At the time step $n+1$ and the kth iteration, the iterative equations are expressed as $\Xi_{n+1}^{k+1} = \Xi_{n+1}^{k} + \delta\Xi_{n+1}^{k}$ and subsequently $\Delta\Xi_{n+1}^{k+1} = \Delta\Xi_{n+1}^{k} + \delta\Delta\Xi_{n+1}^{k}$. As a return mapping algorithm, "convex cutting plane" approach is employed to integrate the constitutive laws and update the state variables at each time step [16, 117]. To this end, the rate dependent constitutive relations are integrated through inelastic criteria whose nullity must be satisfied at time step n:

$$\boldsymbol{\phi}^{vi} = \frac{1}{1-D}\mathbb{V}^{vi-1} : \boldsymbol{\sigma}^{vi} = \mathbf{0}, \tag{2.21a}$$

$$\phi^{vp} = \dot{r} - \langle \frac{f}{R_{vp}} \rangle_{+}^{1/P_{vp}} = 0, \tag{2.21b}$$

where $\boldsymbol{\sigma}^{vi}$ is given in (2.10), and $\boldsymbol{\phi}^{vi}$ and ϕ^{vp} are respectively the viscoelastic and viscoplastic criteria derived from the constitutive relations. Since the viscoelastic deformation is always activated, its associated criteria, $\boldsymbol{\phi}^{vi}$, have to be always satisfied. However, the viscoplastic criterion is taken into account when the viscoplastic deformation appears, once the equivalent effective stress exceeds the elastic limit, R_0. Hence, the return mapping algorithm works in two steps: firstly, viscoelastic correction-prediction, and secondly, full correction.

2.3.1 Viscoelastic correction-prediction

As long as the plastic flow is not activated, the return mapping algorithm solely deals with the viscoelastic correction-prediction, in which only the elementary viscoelastic strains, $\boldsymbol{\epsilon}_{n+1}^{vi}$, at the time step $n+1$, evolve, and the rest of internal variables remain constant ($\delta r_{n+1} = \delta D_{n+1} = 0$ and $\delta\boldsymbol{\epsilon}_{n+1}^{vp} = \mathbf{0}$). The viscoelastic criteria converge to zero through the following iterative equation:

$$\boldsymbol{\phi}_{n+1}^{vi(k+1)} = \boldsymbol{\phi}^{vi(k)} + \delta\boldsymbol{\phi}_{n+1}^{vi(k)} = \mathbf{0}, \quad \text{with} \quad i = 1, ..., N_v. \tag{2.22}$$

For simplicity, the subscripts $n+1$ and superscripts k are ignored in the following equations and the related expansions. Considering (2.21a), the viscoelastic criteria increments, $\delta\boldsymbol{\phi}^{vi}$, are properly determined with respect to $\delta\boldsymbol{\epsilon}^{vi}$ and substituted in (2.22):

$$\boldsymbol{\phi}^{vi} - \mathbb{A}^{vi} : \sum_{j=1(j\neq i)}^{N_v} \delta\boldsymbol{\epsilon}^{vj} - \mathbb{B}^{v}i : \delta\boldsymbol{\epsilon}^{vi} = \mathbf{0}, \quad \text{with} \quad i = 1, ..., N_v, \tag{2.23}$$

where the related mathematical procedure of deriving (2.23) is expressed in detail in the appendix A. The expression (2.23) allows us to constitute a system of equations so as to update the viscoelastic

criteria in each iteration. The iteration process stops once all equations converge to zero. Calculating $\boldsymbol{\epsilon}^{vi}$ and subsequently $\boldsymbol{\sigma}$ and σ^{eq}, the yield function sign, $sgn(f)$, determines whether the material is subjected to the plastic deformation or it still remains within the viscoelastic domain. In other words, the equivalent stress, σ^{eq}, is smaller than the elastic limit, R_0, gives $f < 0$ which means there is no plastic flow, and the algorithm passes to the next time step. On the contrary, when $f > 0$, the material exhibits viscoplastic deformation which requires full correction via enforcing both viscoelastic and viscoplastic criteria to be zero, as expressed in the following section.

2.3.2 Full correction

In the full correction step, the variation of all internal state variable increments ($\delta\boldsymbol{\epsilon}^{vi}_{n+1}$, $\delta\boldsymbol{\epsilon}^{vp}_{n+1}$, δr_{n+1}) are taken into account, while the nullity of viscoelastic and viscoplastic criteria must be satisfied:

$$\begin{cases} \boldsymbol{\phi}^{vi(k+1)}_{n+1} = \boldsymbol{\phi}^{vi(k)}_{n+1} + \delta\boldsymbol{\phi}^{vi(k)}_{n+1} = \mathbf{0}, \quad \text{with} \quad i = 1, ..., N_v, \\ \phi^{vp(k+1)}_{n+1} = \phi^{vp(k)}_{n+1} + \delta\phi^{vp(k)}_{n+1} = 0. \end{cases} \tag{2.24}$$

Similar to the previous section for simplicity, k and $n+1$ are ignored for the following equations. Considering all internal variable increments, the viscoelastic and viscoplastic criteria increments are expressed with respect to $\delta\boldsymbol{\epsilon}^{vi}$ and δr and substituted into:

$$\begin{cases} \mathbb{A}^{vi} : \sum_{j=1(j\neq i)}^{N_v} \delta\boldsymbol{\epsilon}^{vj} + \mathbb{B}^{vi} : \delta\boldsymbol{\epsilon}^{vi} + \boldsymbol{B}^{gi}\delta r = \mathbf{0}, \\ \boldsymbol{A}^{vp} : \sum_{j=1}^{N_v} \delta\boldsymbol{\epsilon}^{vj} + B^{s}\delta r, \end{cases} \tag{2.25}$$

where the whole mathematical procedure of deriving (2.25) is expressed in detail in the appendix A. The internal variable increments and subsequently the inelastic deformations, $\boldsymbol{\epsilon}^{vp}$ and $\boldsymbol{\epsilon}^{vi}$, are then derived allowing to update the stress tensor for the next time step. Figure 2.4 shows the algorithm flowchart depicting the general overview of the numerical implementation and its interaction with the FE solver.

2.3.3 Tangent operator

The above algorithm updates the stress tensor at each time step using viscoelastic correction-prediction and full correction. The finite element solver, however, also requires the tangent operator to provide the new stress corresponding to the new strain. To this end, it is assumed that the nullity

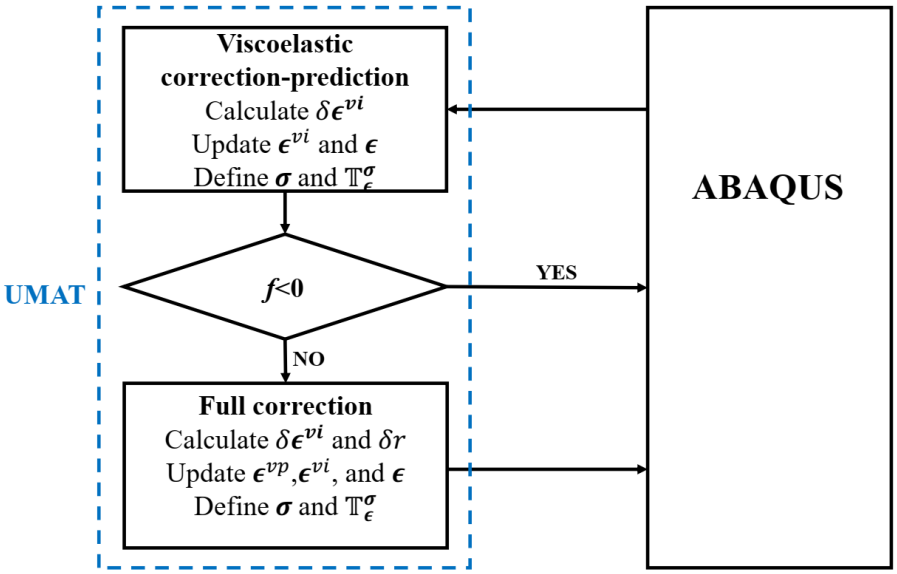

Figure 2.4: Flowchart of the numerical implementation and its interaction with the solver.

condition of viscoelastic and viscoplastic criteria is satisfied and the tangent operator updates the new stress tensor as:

$$d\boldsymbol{\sigma} = \mathbb{T}_{\boldsymbol{\epsilon}}^{\boldsymbol{\sigma}} : d\boldsymbol{\epsilon}. \tag{2.26}$$

The tangent operator, $\mathbb{T}_{\boldsymbol{\epsilon}}^{\boldsymbol{\sigma}}$, is calculated in both viscoelastic correction-prediction and full correction algorithm steps, and its derivation is presented in the appendix A.

2.4 Parametric study

2.4.1 Mechanical responses investigation using the 0D solver

In this section, the numerical implementation procedure, presented in the previous section, is developed as a UMAT subroutine. Here, for humid polyamide 66 conditioned at 50% Relative Humidity (RH50), some numerical examples are provided to investigate the effect of asymmetry parameter, m, on the model mechanical responses. These are extracted as stress-strain curves using a homemade 0D solver. The material properties and model parameters used in this example are listed in the table.2.1, in which 4 viscoelastic branches are considered. As discussed earlier, since damage in polymers starts very quickly, and then progresses slowly thereafter, β_D here has a negative value, which satisfies the damage behavior in the polymers [20].

First, the mechanical responses under monotonic strain-controlled tensile load and compression with $0.1\,s^{-1}$ are plotted as stress-strain curves and depicted in Figure 2.5. As observed, an increase in the asymmetry parameter, m, increases the stress level. This is more pronounced under compression, as expected. Mathematically speaking, this can be justified by the faster growth of the denominators of the stress invariants coefficients in the yield function in presence of m, which leads to negative yield function and plasticization at higher stress levels. To study this in a broader perspective, the variation of m is investigated under a single cycle of loading-unloading, and the results are plotted in Figure 2.6. A similar trend with respect to m is observed in the loading part. In the unloading phase, the curves slopes show less damage in the larger values of m, however, the plastic deformation is almost the same in all cases. The model is also subjected to tension-compression-unloading cycle, and its corresponding stress-strain curves are plotted as Figure 2.7. As seen, the influence of m in compression is more pronounced than in tensile loading. However, if the loading is reversed and starts with compression as compression-tension-unloading, the effect of m is bigger in the tension phase (see Figure 2.8). The above simple examples demonstrate the importance of m in tension-compression cyclic loads, in which the mechanical responses are affected in both tensile and compression phases, specially when the loading starts by compression.

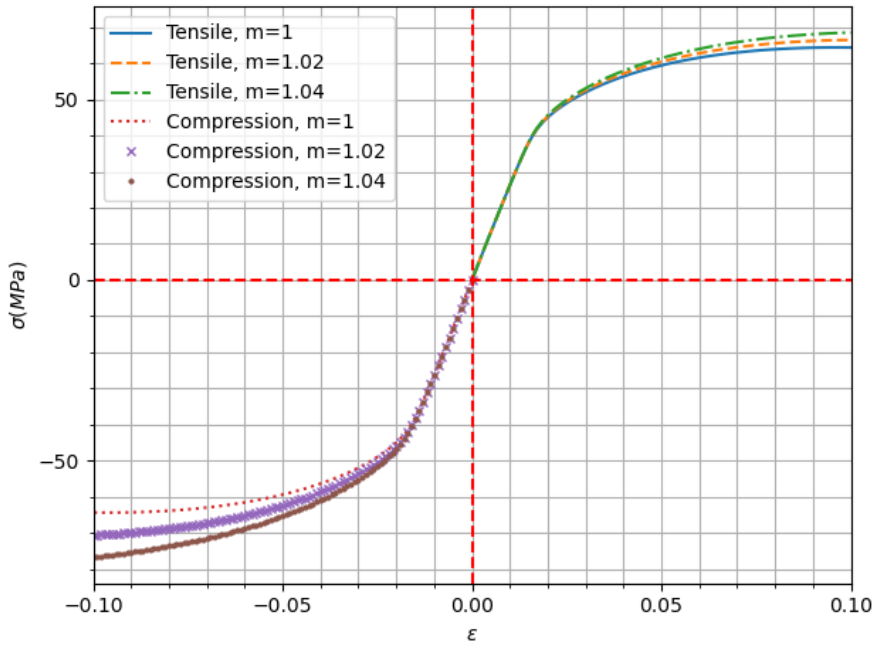

Figure 2.5: Variation of m and its influence on the material response under monotonic loading.

Table 2.1: Model parameters for humid polyamide 66 conditioned at RH50 and room temperature [1].

Mechanical feature	**parameter**	**Value (unit)**
Elastic properties:		
Young's modulus	E^e	2731 (MPa)
Poisson ratio	ν	0.3 (−)
Viscoelasticity:		
1^{st} branch:	E^{v1}	9751.44 (MPa)
	τ^{v1}	0.36 (s)
2^{nd} branch:	E^{v2}	19125.64 (MPa)
	τ^{v2}	6.72 (s)
3^{th} branch:	E^{v3}	30855.24 (MPa)
	τ^{v3}	6.38 (s)
4^{th} branch:	E^{v4}	6771.25 (MPa)
	τ^{v4}	128.49 (s)
Viscoplasticity coupled with damage:		
Elastic limit:	R_0	4.76 (MPa)
Hardening model:	H_m	1302.71 (MPa)
	H_p	0.8 (MPa)
Viscoplastic model:	R_{vp}	45.86 (MPa .s$^{P_{vp}}$)
	P_{vp}	0.07 (−)
Damage:	S_D	20.03 (MPa)
	β_D	−0.86 (−)

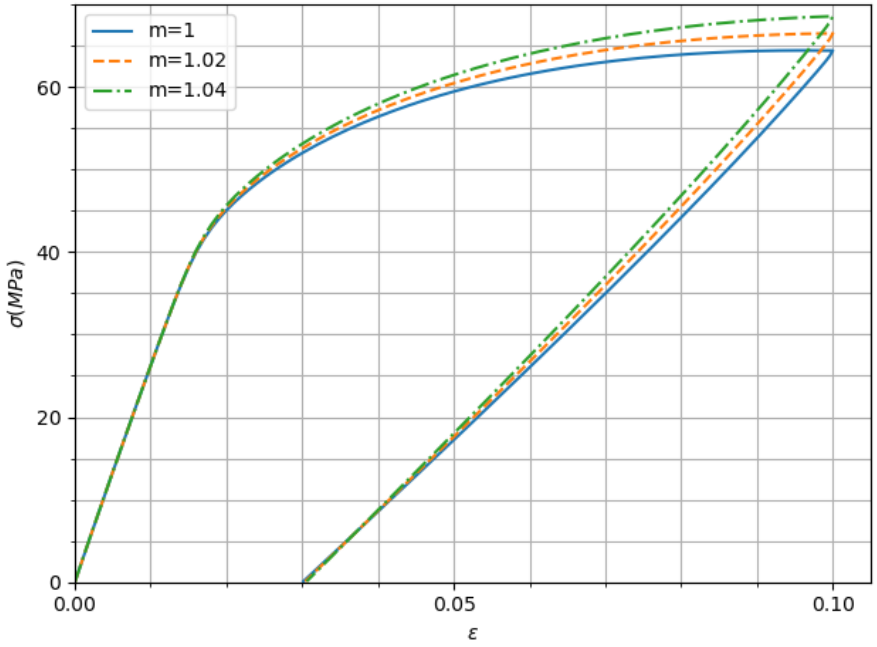

Figure 2.6: Variation of m and its influence on the material response under tension-unloading.

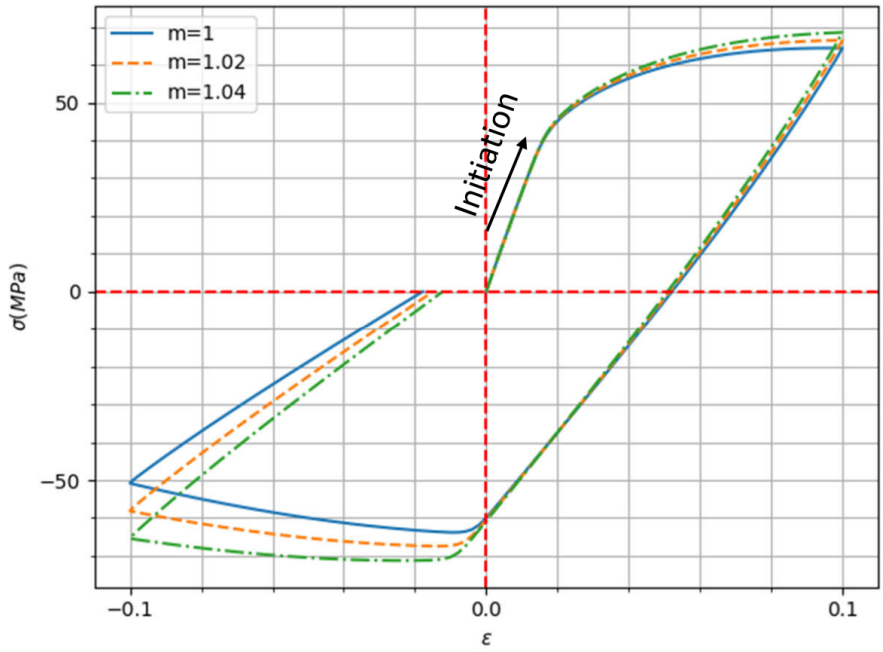

Figure 2.7: Variation of m and its influence on the material response under tension, compression, and unloading.

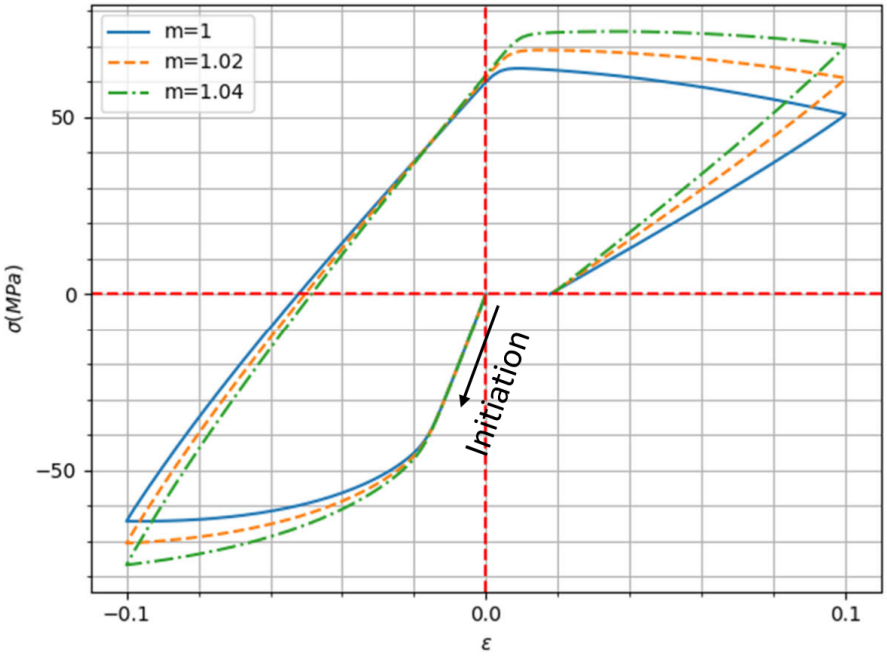

Figure 2.8: Variation of m and its influence on the material response under compression, tension, and again unloading.

2.4.2 3D model examples and parametric study

In this section, the unilateral notched plate and the plate with a hole are considered as 3D examples for the parametric study on self-heating and multi-axial loading. The model presented in the previous sections is implemented as UMAT, and ABAQUS is used as the solver.

2.4.2.1 Investigation of self-heating due to dissipative mechanisms

A unilateral notched plate is considered with the given dimensions and boundary conditions shown in Figure 2.9-a, which is subjected to different monotonic displacement-controlled loads with $0.3\,\mathrm{mm\,s^{-1}}$ and $3\,\mathrm{mm\,s^{-1}}$. The 3D damage and mechanical dissipation maps are extracted and shown in Figures 2.10 and 2.11 for $0.3\,\mathrm{mm\,s^{-1}}$ and $3\,\mathrm{mm\,s^{-1}}$ ($0.01\,\mathrm{s^{-1}}$ and $0.1\,\mathrm{s^{-1}}$ strain rates), respectively. As observed, the dissipation in different damage levels and loading rates is not big enough to change the temperature drastically through dissipative mechanisms. To verify this more precisely, the heat equation can be used to estimate the temperature level in the current example:

$$\rho c_p \dot{T} = -\boldsymbol{\nabla_x}.\boldsymbol{q} + \text{thermo-mechanical terms} + \mathcal{D}, \tag{2.27}$$

where ρ and c_p are the density and specific heat capacity, which are taken as $1.19 \times 10^{-3}\,\mathrm{g\,mm^{-3}}$ and $1590\,\mathrm{J(gK)^{-1}}$, respectively [89]. Should the self-heating due to mechanical dissipation be isolated, an approximate temperature increase due to the dissipative mechanisms can be estimated by $\mathcal{D}/(\rho\, c_p)$. Figure 2.11 shows that the maximum dissipation is $1.694 \times 10^{-2}\,\mathrm{GPa\,s^{-1}}$ in almost 60 % of damage under $3\,\mathrm{mm\,s^{-1}}$ loading rate. With this in mind, the approximate temperature rate in this case can be derived as:

$$\dot{T} = \frac{1.694\ \times 10^{-2}\,\mathrm{GPa\,s^{-1}}}{1.19\ \times 10^{-3}\,\mathrm{g\,mm^{-3}} 1590\,\mathrm{J(gK)^{-1}}} = 8.95\ \times 10^{-3}\,\mathrm{K\,s^{-1}}. \tag{2.28}$$

The above estimation shows that, more than 100 loading cycles, in the quasi-static condition, are required to increase the temperature for only 1 K. The cyclic response of thermoplastics is out of scope for the present study. Thus, the thermo-mechanical coupling can be safely neglected with a good accuracy in this study.

2.4.2.2 Asymmetric yield behavior under multi-axial loading

In this section, the effect of asymmetry parameter, m, is explored in a 3D case through the classic example of holed plate. Thanks to its symmetric structure, only 1/4 of the geometry is sufficient for the study of the whole structure (see Figure 2.9-b). Multi-axial displacement-controlled loading with $0.2\,\mathrm{mm\,s^{-1}}$ is imposed on the structure (compression in X-axis and tensile along Y-axis). First, it is considered that the yield behavior is symmetric, in which $m = 1$, and the results are compared when $m = 1.2$ and $m = 1.4$. Figure 2.12 demonstrates the 3D map of hardening state variable, r, which shows how the asymmetry parameter influences on the plasticity distribution. As observed, the hardening state variable profile is symmetric when $m = 1$, and it obviously becomes asymmetric for the values more than 1 ($m = \{1.2, 1.4\}$). Moreover, it is observed that the maximum hardening state variable is reduced by an increase in m. The same effect is seen in the damage profiles (see Figure 2.13). As seen, the damage level is decreased and asymmetry of the damage profile is enhanced by increasing in m.

2.5 Conclusion

In this chapter, the typical von Mises yield function was extended to the I_1-J_2 model, taking into account the pressure sensitivity and asymmetric yield behavior of humid polyamide 66 material.

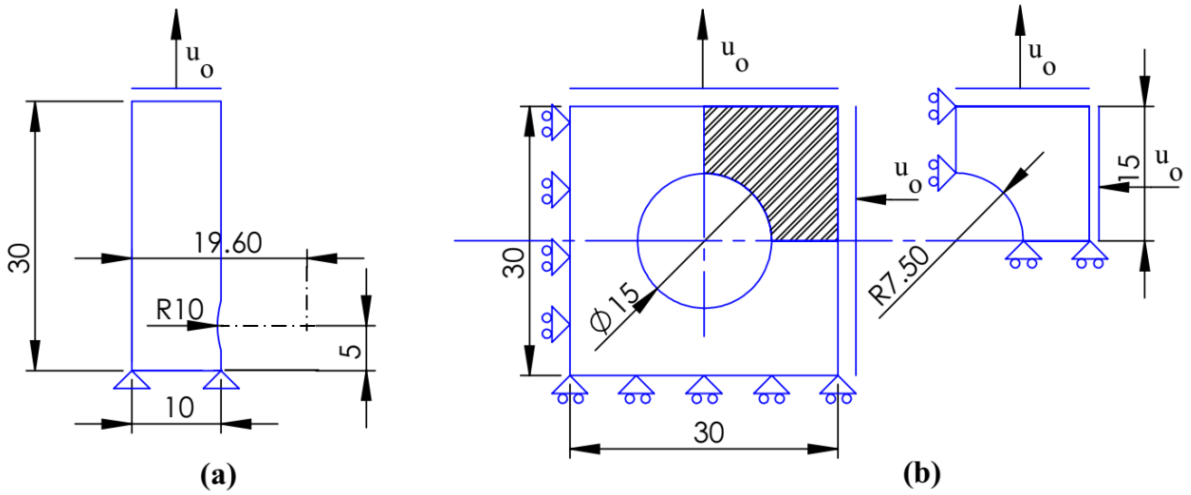

Figure 2.9: Dimension of the given structures with 1 mm of thickness: a) unilateral notched plate, b) 1/4 of the plate with a hole (all dimensions are in mm).

The corresponding thermodynamic framework was modified using the new yield function, based on which the constitutive laws were derived. A parametric study was carried out by conducting several numerical examples to investigate the effect of the asymmetry parameter and dissipative mechanisms on the mechanical responses. First, stress-strain curves obtained using the homemade 0D solver were studied under tensile and compressive loading conditions. Then, the unilateral notched plate, as a 3D example, was used to study dissipation under different loading rates at different damage levels, while the classical example of plate with a hole is employed to study the asymmetry parameter impact on the model behavior under multi-axial loading. The parametric study showed that the effect of the asymmetry parameter is of significant importance in tension-compression loading, specially when the loading starts with compression, and the increase of the asymmetry parameter clearly changes the damage and plasticity profiles under multi-axial loading. Investigation of the mechanical dissipation in the numerical examples revealed that the temperature change due to the dissipative mechanisms is negligible and the thermo-mechanical coupling can be neglected with good accuracy for the rest of this research work.

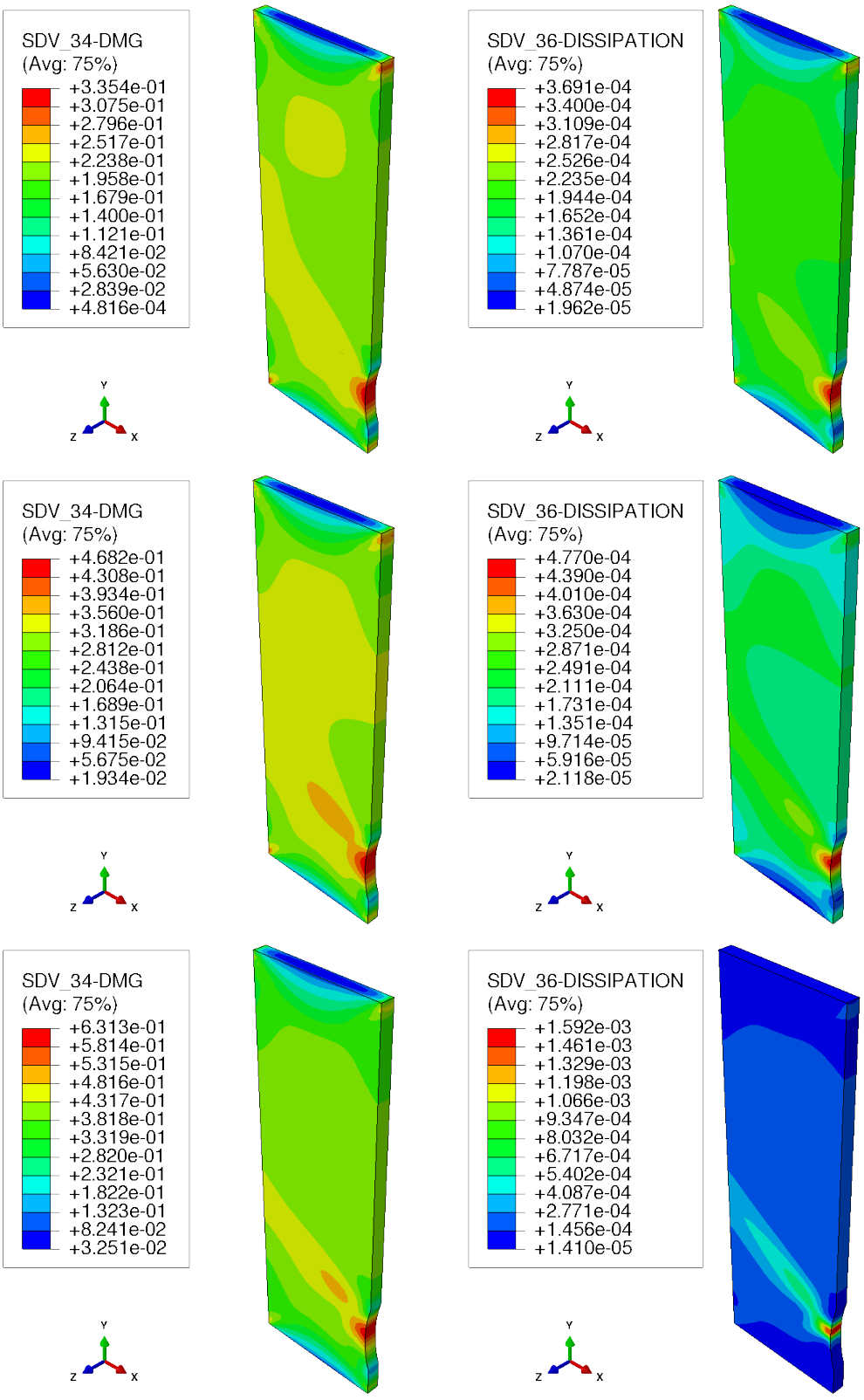

Figure 2.10: Damage and dissipation profiles under displacement-controlled monotonic load with $0.3\,\mathrm{mm\,s^{-1}}$ in three different damage levels when $m = 1$.

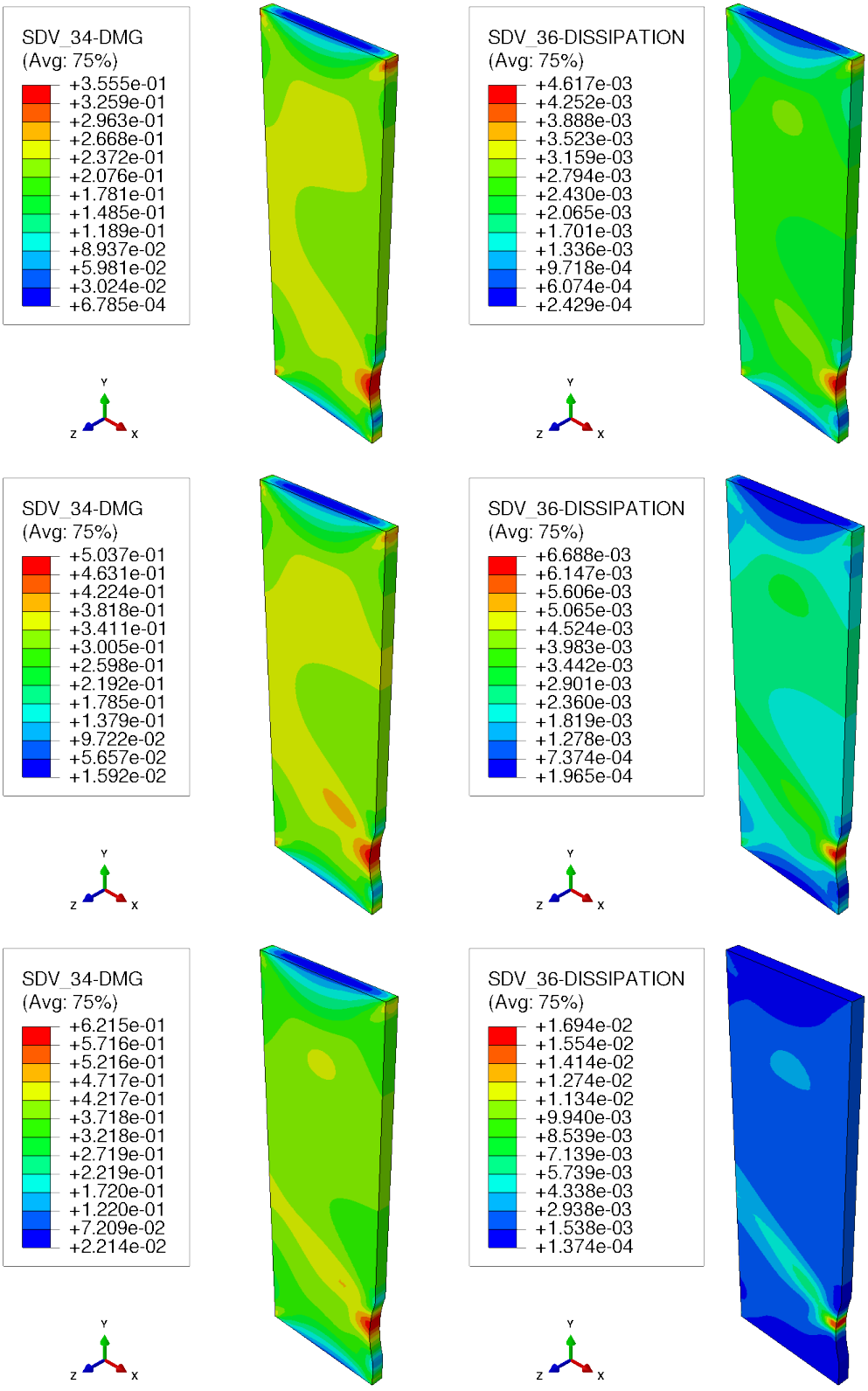

Figure 2.11: Damage and dissipation maps under displacement-controlled monotonic load with $3\,\mathrm{mm\,s^{-1}}$ in three different damage levels when $m = 1$.

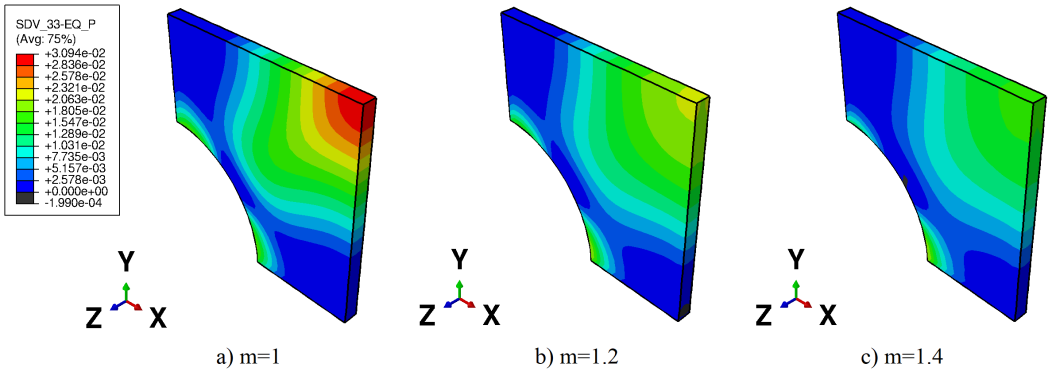

Figure 2.12: 3D maps of hardening state variable for 1/4 plate with a hole subjected to the multi-axial loading when a) $m = 1$, b) $m = 1.2$, and c) $m = 1.4$.

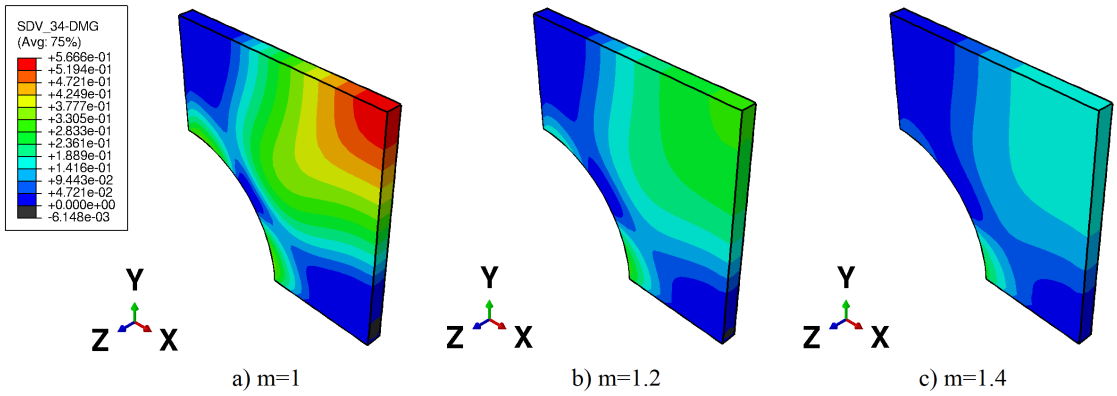

Figure 2.13: 3D maps of damage for 1/4 plate with a hole subjected to the multi-axial loading when a) $m = 1$, b) $m = 1.2$, and c) $m = 1.4$.

Chapter 3

Parameters identification and model validation based on the experimental data

Contenu

3.1 Introduction

In the previous chapter, a VEVPD model based on I_1-J_2 yield function accounting for hydrostatic pressure effect and tension-compression asymmetry was formulated and discussed through parametric studies. The parameters used in the numerical examples an the parametric study were considered from those calibrated for the symmetric von Mises-based model at RH50 [1, 14]. However, as explained in the general introduction, thermoplastics exhibit different mechanisms depending on environmental conditions.

The chemical structure of polyamides allows them to absorb water through the presence of amide groups up to their water saturation limit, depending on the environmental temperature. This makes them softer and more flexible through the interaction of hydrogen bonds and water molecules [118–120]. Many studies are available in the open literature that have investigated polyamides chemical structure and the corresponding reversible and irreversible reactions leading to change in their properties due to water absorption [120–122]. Water content has an inverse relation with the glass transition temperature of semi-crystalline polymers leading to a decrease it below room temperature. This leads to a change in physical properties from glassy to more flexible and rubbery with viscous behavior [123–126]. Young's modulus is the mechanical property most affected by relative humidity and decrease with increasing water content [127,128]. Increasing water content leads to a plasticizing effect, which amplifies inelastic mechanical responses, including viscoelasticity and viscoplasticity. In other words, the higher the relative humidity, the more plasticity plays a role in the damage mechanism. The rheological properties and the dominant mechanisms of polymers and composites under different hygro-thermo-mechanical states have been investigated experimentally in many studies [3, 129–131], and many constitutive laws have been presented in the literature [5, 10, 11, 14, 20, 105].

Two types of VEVPD models have been presented so far: based on the von Mises function assuming that thermoplastics are pressure-insensitive materials and on the I_1-J_2 function considering the effect of hydrostatic pressure and tension-compression asymmetry. According to our literature review, none of these models have been experimentally calibrated for different RH. The calibration procedure, loading types, and the corresponding sample shapes depends on the mechanisms to be identified. Thus, in the first step, dog bone samples are subjected to different types of loading at several rates, and the results are used to calibrate and validate the classical model based on the von Mises function, in which the

tension-compression asymmetry of the yield stress is ignored. In the second step, specially designed (diabolo) samples at several RH are subjected to monotonic tension-torsion tests at different rates, from which the asymmetry of the yield behavior in PA 66 is captured. The global force-displacement and torsion moment-rotation angle curves along with the data obtained from the dog bone samples are used to calibrate the new I_1-J_2-based model, in which the asymmetry parameter, m, is identified as a new parameter. The parameters identified in both models are studied as a function of RH, and the related trends are explored in order to derive an evolution function of these parameters with respect to RH.

Chapter 3 is structured as follows: in section 3.2, the designed experimental campaign is first expressed in detail, and the sample preparation procedure is stated. Then, the experimental results are explored and the material behavior is discussed under different RH and loading conditions. The obtained experimental data are applied to identify the von Mises-based model parameter set for each RH and the variation of the parameters is explored. In section 3.3, as the previous section the experimental campaign is stated and the experimental data are explored, then they are employed to identify and validate the I_1-J_2-based model.

3.2 Calibration and validation of the model based on von Mises yield function

3.2.1 Model parameters identification strategy

The VEVPD model is firstly considered based on the conventional von Mises yield function, in which pressure-sensitivity and yield asymmetry are neglected. In this case, three sets of parameters are required to be identified: elastic, viscoelastic, viscoplastic, and damage-related parameters (see Table 3.1). A proper experimental campaign is designed to capture all mechanisms and identify the related parameters at different RH, namely RH0%, RH25%, RH50%, RH65%, and RH80%. The viscoelastic model parameters, for the $i\,th$ branch, are related to each other through $\tau^{vi} = \eta^{vi}/E^{vi}$. This means η^{vi} is derived automatically after calibrating the other two parameters, E^{vi} and τ^{vi}. To investigate the effect of RH, considering the correlation between the viscoelastic parameters, the model parameters must be identified in constant viscoelastic characteristic times, τ^{vi}. For the model calibration, it is

enough to define cost function, $C^r(p)$, between the numerical and experimental responses:

$$C^r(p) = \sum_{k=1}^{N_p} w_k \left[\frac{m_k^{\text{num}}(p) - m_k^{\text{exp}}}{m_k^{\text{exp}}} \right]^2, \tag{3.1}$$

where p is the parameters values set, N_p denotes the number of data compared with each other, m_k^{num} and m_k^{exp} are the numerical and experimental quantities that have to be compared, respectively, and w_k is their corresponding weight in the calibration in the $k\,th$ point.

Table 3.1: Parameters of the VEVPD model based on von Mises yield function.

Mechanism	Parameters
Elastic	E, ν
Viscoelastic	$\{E^{vi}, \eta^{vi}, \tau^{vi}\}_{i=1,4}$
Viscoplastic	H_m, H_p, R_{vp}, P_{vp}
Damage	S_D, β_D

3.2.2 Experimental setup and procedure

3.2.2.1 Materials and sample preparation

The material used in this study is polyamide 66 supplied by DOMO Chemicals, which commercially known as A218 BK 34NG, and it is provided in rectangular injection-molded plates with 360 mm in length, 100 mm in width, and 3 mm in thickness nominal dimensions. To perform mechanical tensile tests, dog bone samples are cut using water jet hyperbar machining process, as shown in Figure 3.1-a. The samples dimensions are schematically displayed in Figure 3.1-b, including 96 mm overall length, 14 mm gauge width, and 3 mm in thickness. In order to control the water uptake ratio, the samples are placed in a conditioning chamber at temperature of 80 °C under dry environment to extract any residual humidity from the samples machining process. Figure 3.2 shows water uptake evolution with respect to time, in which a mass reduction is observed until its stabilization. The water content eventually gets around 0.3% (as the residual value).

To recondition at different RH, the samples are placed in the hygrometric chamber, Memmert HCP246 (Figure 3.3), at the corresponding temperature and humidity. The appropriate temperature and humidity is adjusted depending on the target RH and is performed in two phases: first, the

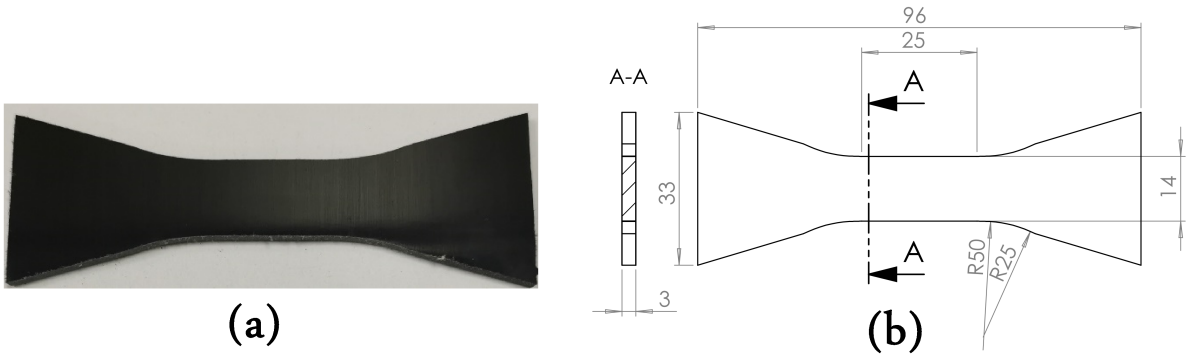

Figure 3.1: a) Dog bone sample; b) sample schematics and the corresponding dimensions (in mm).

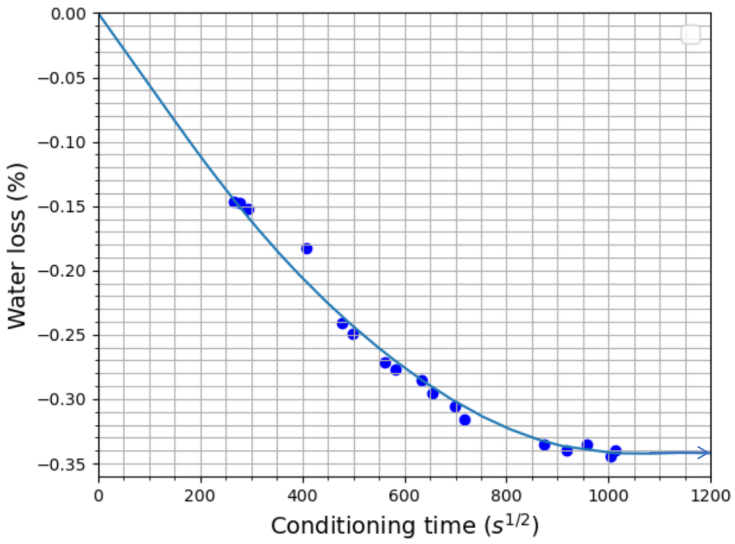

Figure 3.2: Water loss of the samples with respect to time in the initial drying procedure.

rapid water absorption with a higher conditioning temperature and RH to accelerate the water uptake process, and second, stabilization and homogenization of the humidity along the thickness of the sample to avoid any humidity concentration gradient, during which the temperature is reduced as close as possible to the ambient temperature and the considered RH. Different mass measurements are performed through the conditioning in order to verify the relative humidity evolution. The targeted RH is reached once the mass evolution is constant. Mass measurements are performed using a weighing device with a resolution of 0.1 mg. The conditioned samples are kept in hermetic envelopes to keep their water content constant. This also prevents undesirable thermomechanical effects by ensuring that the samples are at room temperature before the test.

Figure 3.3: a) Hygrometric chamber, Memmert HCP246; b) dog bone samples in the hygrometric chamber.

3.2.2.2 Mechanical tests

To calibrate and validate the VEVPD model based on the von Mises yield function, several mechanical tests are performed to capture the dominant mechanisms. To this end, time-dependent mechanisms are captured by monotonic tensile tests with three different displacement rates. The evolution of plasticity-induced ductile damage is identified using the loading-unloading test, and the

viscoelastic and viscoplastic mechanisms are captured by creep-recovery tests with two different stages of loading at 50 % and 70 % of the maximum force in the monotonic test, $F_{\max}$. The load is held for 5 min in the creep phase and 5 min in the recovery phase. Figure 3.4 shows the schematic diagrams of the above mechanical tests used in the calibration phase. Calibration is performed in several steps. In each step, the model parameters are identified and then used as initial values for the next step. In each step, experimental data are used as follows:

- 1st step: monotonic loading tests.
- 2nd step: monotonic loading tests and loading-unloading test.
- 3th step: monotonic loading tests, loading-unloading test, and creep-recovery test at 50 % $F_{\max}$.
- 4th step: monotonic loading tests, loading-unloading test, creep-recovery test at 50 % $F_{\max}$, and creep-recovery test at 70 % $F_{\max}$.

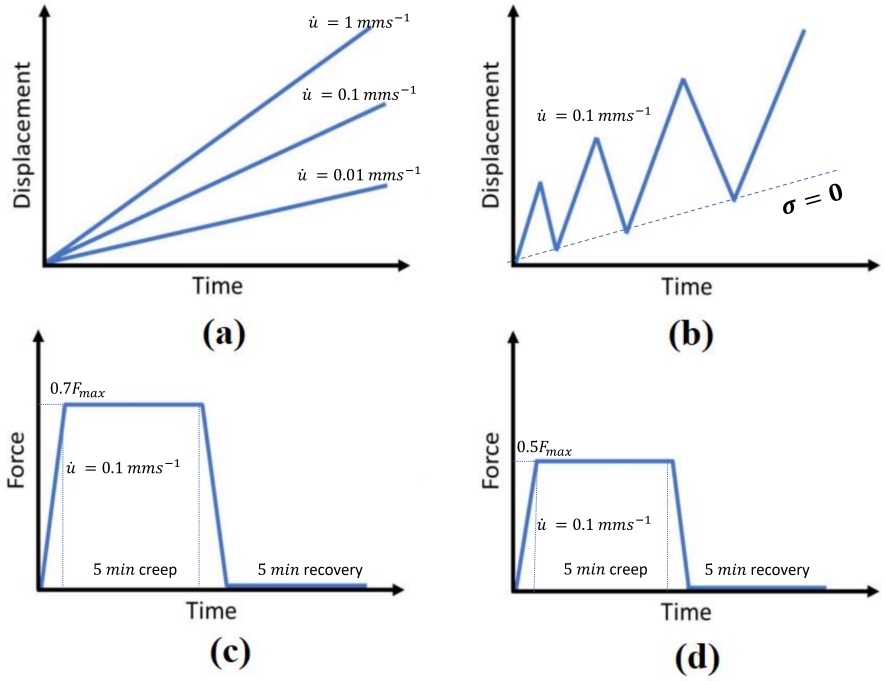

Figure 3.4: Schematics of the mechanical tests of the calibration phase: a) monotonic displacement-controlled tests, b) loading-unloading test with increasing displacement, c) creep-recovery test with 70 % of $F_{\max}$, d) creep-recovery test with 50 % of $F_{\max}$.

Figure 3.5 shows the schematic diagrams of the mechanical tests used in the validation phase.

For implementing the above mechanical tests, zwick-roell Z050, 50kN is employed. To obtain more accurate experimental data, a sample setting tool is designed to ensure the dog bone sample is aligned with the loading axes and there is no torsional moment (Figure 3.6). It should be mentioned that this tool is removed before starting the test. The displacement is measured using an extensometer with the gauge length of 25 mm (Figure 3.7), based on which the corresponding strain is calculated. It should be mentioned that engineering stress and strain are considered here. The stress is calculated based on the original cross-section, and the strain is the displacement of the material per unit length.

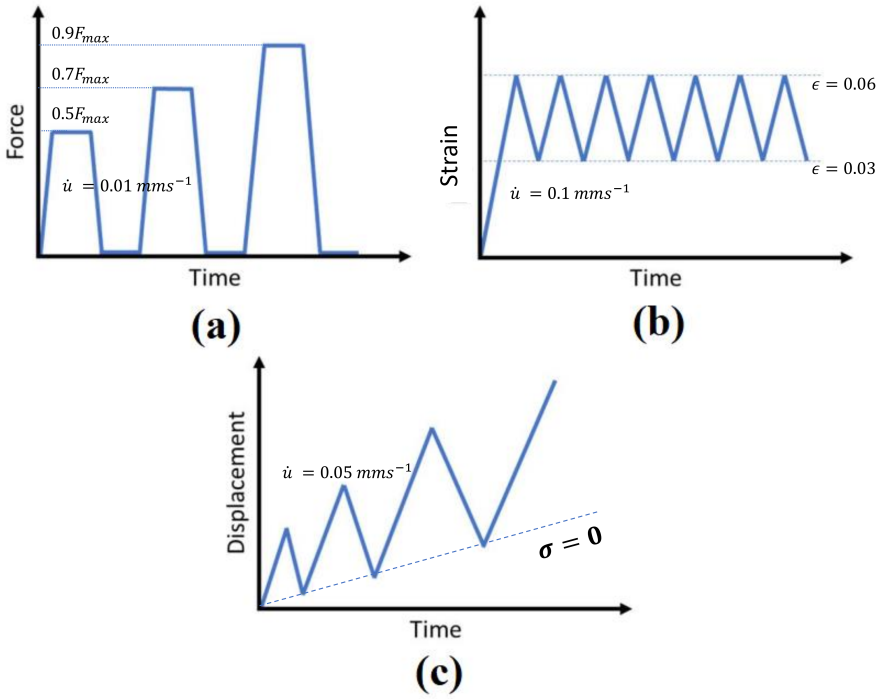

Figure 3.5: Schematics of the mechanical tests of the validation phase: a) Creep-recovery test at different steps, b) cyclic tension-tensile test, c) loading-unloading test with increasing displacement.

Since there are often some slight dimensional errors in the production process of polyamide plates and cutting into dog bone samples, the corresponding cross-section, A_s, is measured for each sample. To this end, the sample thickness, t_s, and the gauge width, w_s, are measured before all tests and listed in Table 3.2 and 3.3 for calibration and validation phases, respectively, in which monotonic, loading-unloading, and creep-recovery tests are abbreviated as "MT", "L-U", and "C-R".

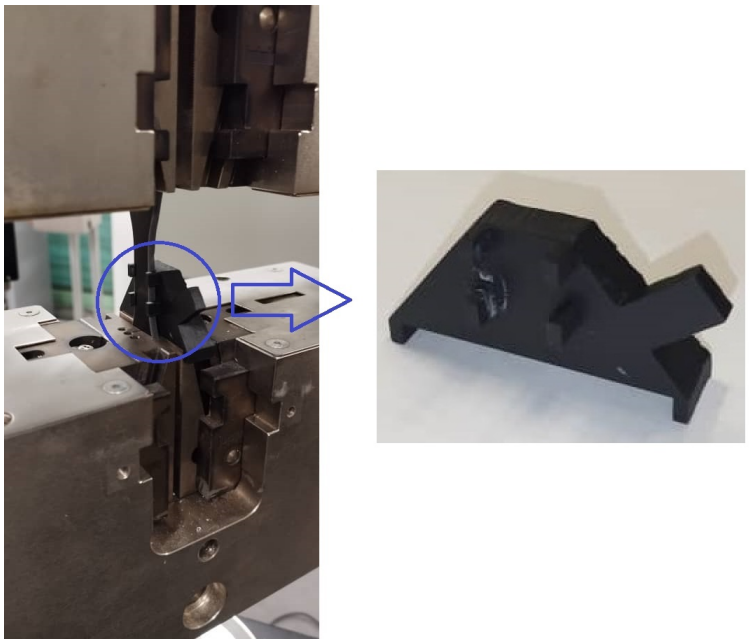

Figure 3.6: Sample setting tool for keeping the sample aligned with the loading axes.

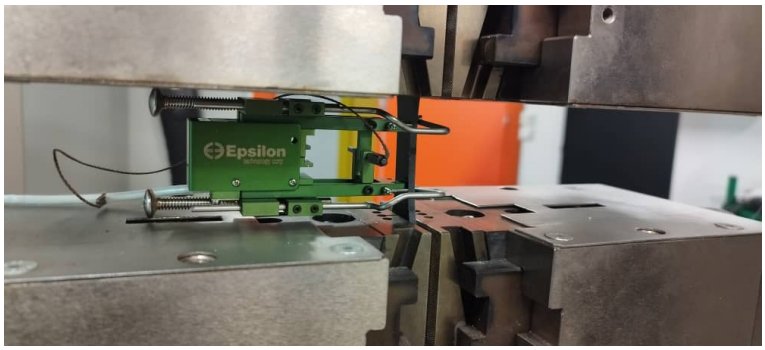

Figure 3.7: Measurement of displacement of dog bone samples using extensometer.

Table 3.2: Dog bone samples cross-section measurements at different RH in the calibration phase.

RH (%)	Test, loading rate ($\mathrm{mm\,s^{-1}}$)	t_s (mm)	w_s (mm)	A_s ($\mathrm{mm^2}$)
0	MT, 0.01	3.28	14.38	47.17
	MT, 0.1	3.33	14.37	47.85
	MT, 1	3.26	14.32	46.68
	L-U, 0.1	3.13	14.25	44.60
	C-R, 0.1 (50 %$F_{\max}$)	2.95	14.55	42.92
	C-R, 0.1 (70 %$F_{\max}$)	3.12	14.97	46.71
25	MT, 0.01	3.30	14.40	47.52
	MT, 0.1	3.28	14.33	47.00
	MT, 1	3.30	14.40	47.52
	L-U, 0.1	3.23	14.28	46.12
	C-R, 0.1 (50 %$F_{\max}$)	3.27	14.30	46.76
	C-R, 0.1 (70 %$F_{\max}$)	3.32	14.30	47.48
50	MT, 0.01	3.00	14.05	42.15
	MT, 0.1	3.10	14.08	43.65
	MT, 1	3.12	14.58	45.49
	L-U, 0.1	3.14	14.06	44.15
	C-R, 0.1 (50 %$F_{\max}$)	3.12	13.98	43.62
	C-R, 0.1 (70 %$F_{\max}$)	3.07	14.03	43.07
65	MT, 0.01	3.12	14.08	43.93
	MT, 0.1	3.15	14.09	44.38
	MT, 1	3.14	14.02	44.02
	L-U, 0.1	3.14	14.09	44.24
	C-R, 0.1 (50 %$F_{\max}$)	3.14	14.01	43.99
	C-R, 0.1 (70 %$F_{\max}$)	3.05	13.98	42.64
80	MT, 0.01	3.22	14.88	47.91
	MT, 0.1	3.27	14.83	48.49
	MT, 1	3.17	14.80	46.91
	L-U, 0.1	3.18	14.74	46.87
	C-R, 0.1 (50 %$F_{\max}$)	3.24	14.88	48.21
	C-R, 0.1 (70 %$F_{\max}$)	3.25	14.88	48.36

Table 3.3: Dog bone samples cross-section measurements at different RH in the validation phase.

RH (%)	Test, loading rate ($\mathrm{mm\,s^{-1}}$)	t_s (mm)	w_s (mm)	A_s ($\mathrm{mm^2}$)
0	C-R, 0.01	14.91	3.24	48.31
	Cyclic, 0.1	14.78	3.12	46.11
	L-U, 0.05	14.80	3.22	47.66
25	C-R, 0.01	14.33	3.26	46.71
	Cyclic, 0.1	15.01	3.21	48.18
	L-U, 0.05	14.35	3.3	47.35
50	C-R, 0.01	14.05	3.16	44.40
	Cyclic, 0.1	14.15	3.12	44.15
	L-U, 0.05	13.93	3.05	42.49
65	C-R, 0.01	14.08	3.15	44.35
	Cyclic, 0.1	14.06	3.14	44.15
	L-U, 0.05	13.92	3.05	42.46
80	C-R, 0.01	14.85	3.21	47.67
	Cyclic, 0.1	15.36	3.27	50.23
	L-U, 0.05	14.85	3.27	48.56

3.2.3 Experimental observations

In this section, the data obtained through the mechanical tests are studied, and the effect of loading rate and RH is investigated. The monotonic tests are performed in $0.01\,\mathrm{mm\,s^{-1}}$, $0.1\,\mathrm{mm\,s^{-1}}$, and $1\,\mathrm{mm\,s^{-1}}$ displacement rates ($4\times10^{-4}\,\mathrm{s^{-1}}$, $4\times10^{-3}\,\mathrm{s^{-1}}$, and $4\times10^{-2}\,\mathrm{s^{-1}}$ strain rates considering 25 mm gauge length), and the corresponding stress-strain curves are displayed in Figure 3.8. As observed, the increase in RH leads to a decrease in the stress level, and the material becomes softer, which confirms the notions in the previous sections about plasticization mechanism due to the increase of the water content. Moreover, the rate dependent mechanical response of the material yields higher stress level for faster loading rates (see Figure 3.8). Creep-recovery tests also shows the same behavior regarding the RH effect. Figures 3.9 and 3.10 display stress-time and strain-time curves considering 50% of $F_{\max}$ and 70% of $F_{\max}$, respectively. Since the maximum force level is reduced by increasing the relative humidity level (see Figure 3.8), the corresponding stress in the creep-recovery tests is also reduced, as expected (see Figure 3.9-a and 3.10-a). The strain in the creep-recovery test normally depends on both the corresponding stress and RH level. Figure 3.9-b shows no trend in terms of total strain and plastic strain level when the creep loading level is 50% of $F_{\max}$. However, when the creep loading level is 70% of $F_{\max}$, the plastic strain level increases by increasing RH. The maximum total

strain level also increases by increasing RH, except for RH80 which is at the same level as RH65. This means that, the effect of RH is more pronounced than the stress level in the creep-recovery results with 70% of $F_{\max}$. The effect of both stress level and RH can be also observed together in the stress-strain curves in Figures 3.11 and 3.12. Loading-unloading mechanical responses are plotted as stress-strain curves and depicted in Figure 3.13. As observed, increasing RH decreases the stress level, as expected. In the following section, the stress and strain values obtained from the present mechanical tests are used to identify the model parameters of the VEVPD model based on the von Mises yield function at different RH levels.

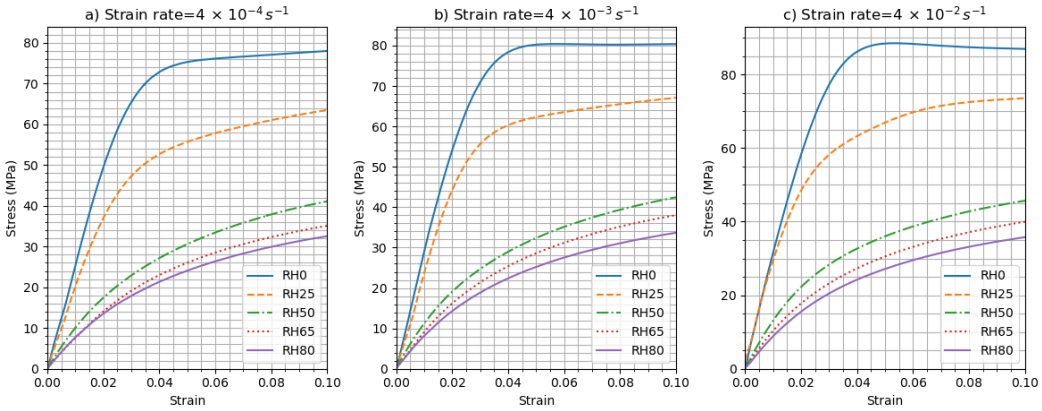

Figure 3.8: Stress-strain curves obtained from monotonic tensile tests on the dog bone samples.

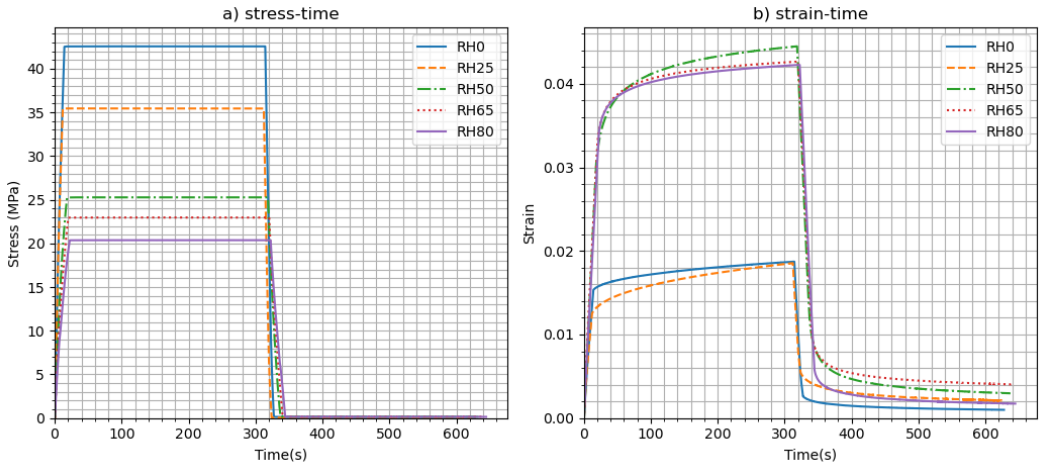

Figure 3.9: Stress-time and strain-time curves obtained from creep-recovery tests at different RH levels with 4 $\times 10^{-3}\,\mathrm{s}^{-1}$ strain rate and 50% of $F_{\max}$.

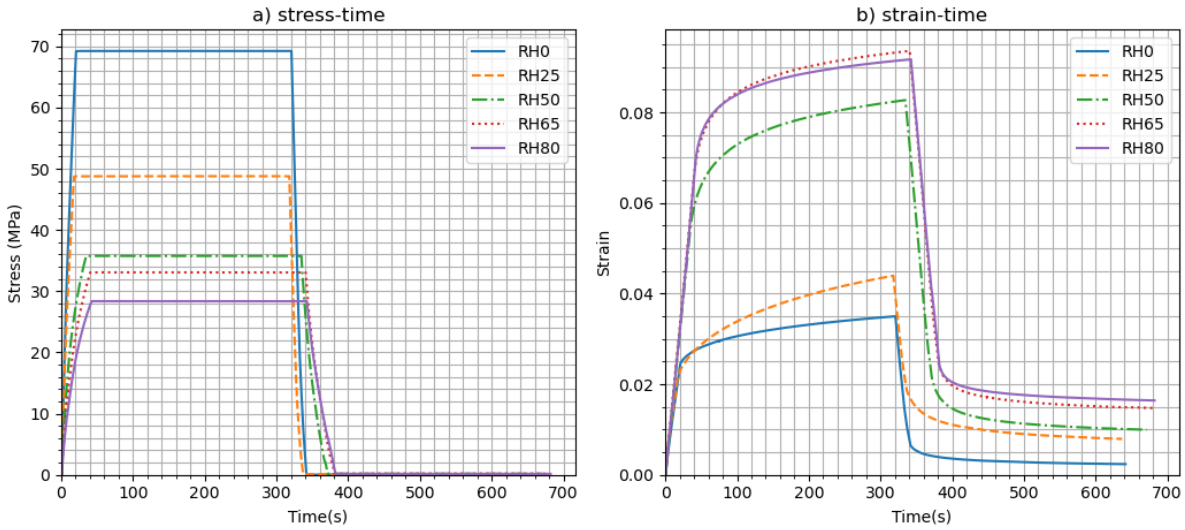

Figure 3.10: Stress-time and stress-time curves obtained from creep-recovery tests at different RH levels with $4 \times 10^{-3}\,\mathrm{s}^{-1}$ strain rate and 70% of $F_{\max}$.

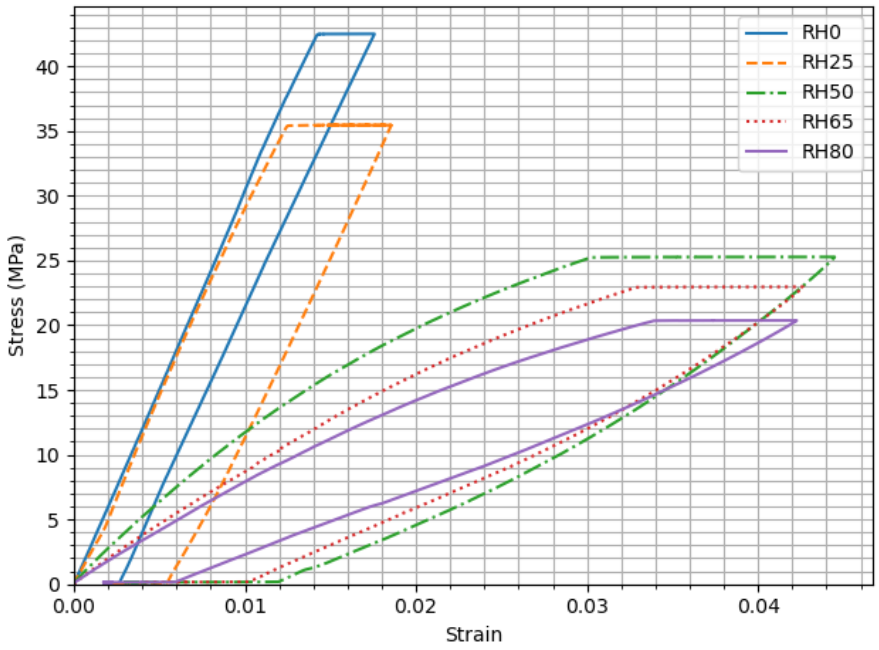

Figure 3.11: Stress-strain curves of creep-recovery tests at different RH levels with $4 \times 10^{-3}\,\mathrm{s}^{-1}$ strain rate and 50% of $F_{\max}$.

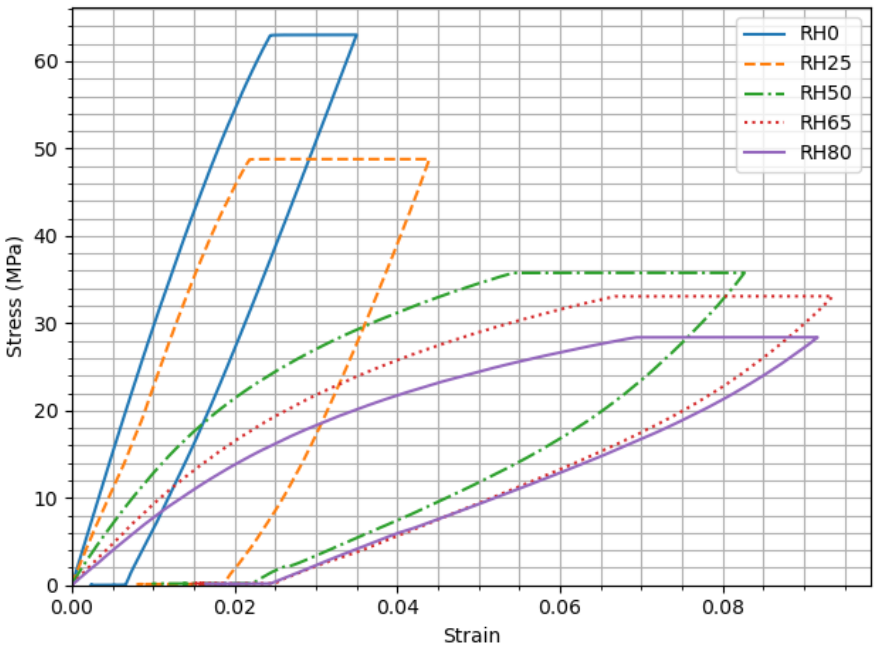

Figure 3.12: Stress-strain curves of creep-recovery tests at different RH levels with $4 \times 10^{-3}\,\mathrm{s}^{-1}$ strain rate and 70% of $F_{\max}$.

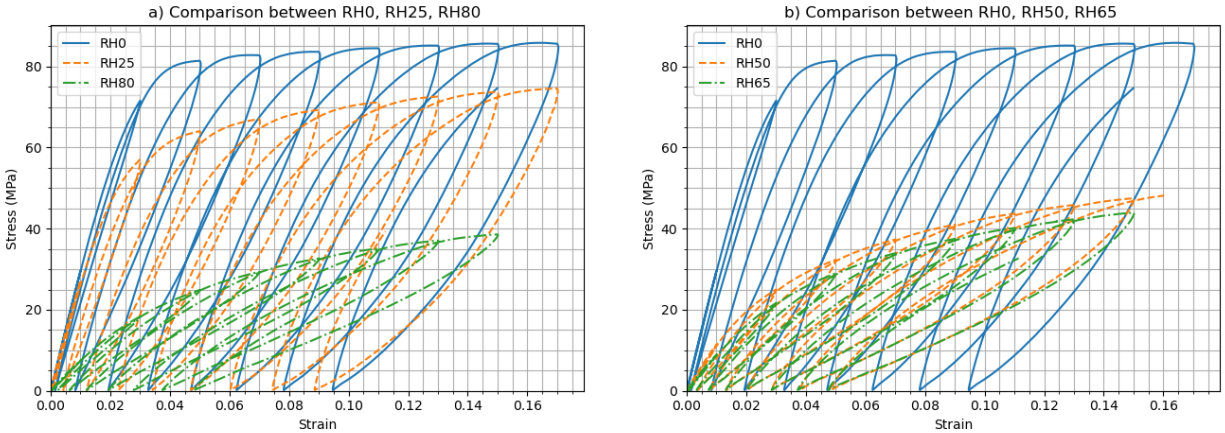

Figure 3.13: Stress-strain curves of loading-unloading test with increasing strain when the strain rate is $4 \times 10^{-3}\,\mathrm{s}^{-1}$.

3.2.4 Model calibration

The experimental data and the homemade 0D solver, mentioned in chapter 2, are used to identify the model parameters through an optimization algorithm, in which, the difference between the experimental and numerical variables (stress or strain depending on the loading conditions) is minimized to find the appropriate parameters fit to the model at the corresponding RH level. To this end, the cost function between the experimental and numerical results is formed as a multidimensional function based on the model parameters, and Nelder-Mead method is used to find the appropriate set of parameters minimizing it. Nelder-Mead approach operates directly by comparing the function values and does not rely on the derivatives. In this method, for an n-dimensional function, a geometrical shape called "simplex" consisting of $n+1$ vertices is defined in an n-dimensional domain, as $\mathbb{R}^n$, and each vertex represents a set of parameters. For example, for $n = 2$, the "simplex" is a triangle, for $n = 3$, the "simplex" is a tetrahedron, etc. After determining the initial simplex, at each iteration, the value of the cost function at each vertex is computed, then they are sorted and replaced by new values calculated using the steps defined by the algorithm. This process continues until the standard deviation of the function values at the simplex vertices gets close to zero as much as possible. More details about the algorithm and its formulations are given in [132, 133]. In this study, Nelder-Mead numerical approach is used through a Python standard library.

Figures 3.14 to 3.28 show the comparison between the calibrated numerical results and the experimental data. As observed, in the calibration procedure, it is tried to conduct the numerical results as close as possible to the experimental responses. However, the errors are relatively larger in the monotonic test with the highest displacement rate ($1\,\mathrm{mm\,s^{-1}}$), particularly at RH50 and RH65. Furthermore, in the loading-unloading tests (Figures 3.16, 3.19, 3.22, 3.25, and 3.28), the experimental data show larger hysteresis loops compared to the numerical results. This may be due to higher dissipation by viscoelastic mechanisms in the experiments [134]. The obtained identified parameters are listed in Table 3.4 and plotted with respect to RH as shown in Figure 3.29. As seen, the viscoelastic moduli have an aproximately decreasing trend by an increase in RH except E^{v4} which increases. Some of viscoplastic and damage-related parameters, H_p, R_{vp}, P_{vp}, and β_D can be fitted with increasing or decreasing trend lines. However, H_m, S_D, and R_0 does not follow any certain increasing or decreasing trend.

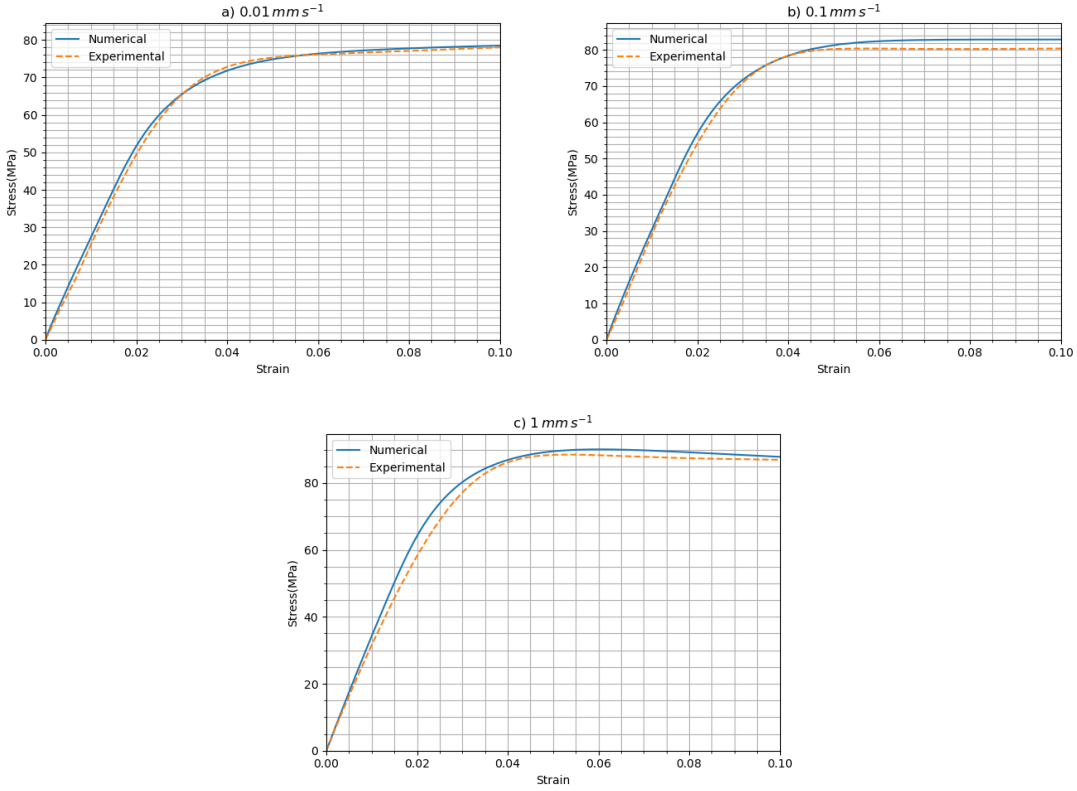

Figure 3.14: Calibration results for monotonic tests at RH0 under different loading rates: a) $0.01\,\mathrm{mm\,s^{-1}}$, b) $0.1\,\mathrm{mm\,s^{-1}}$, c) $1\,\mathrm{mm\,s^{-1}}$.

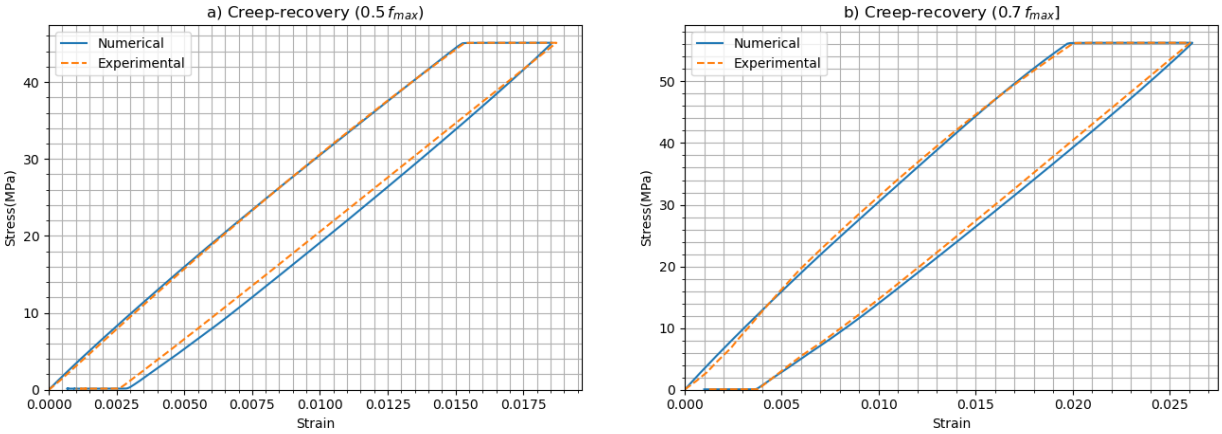

Figure 3.15: Calibration results for creep-recovery tests at RH0 under different loading levels: a) 50% of $F_{\max}$, b) 70% of $F_{\max}$.

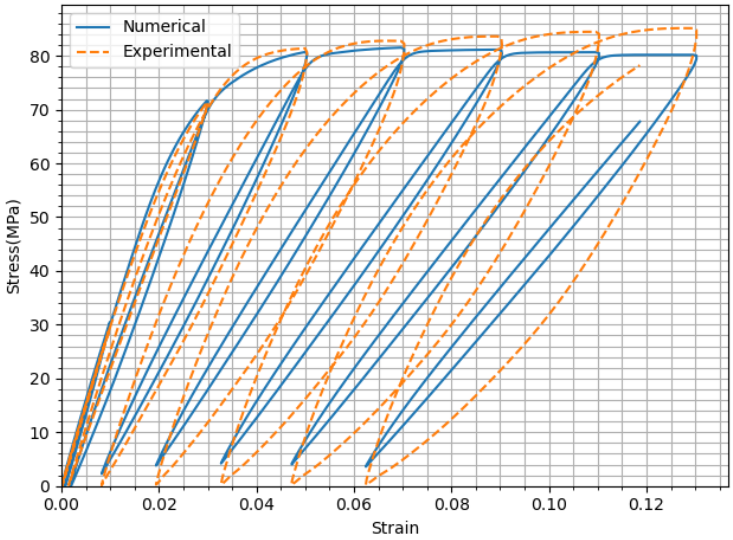

Figure 3.16: Calibration results for loading-unloading test at RH0.

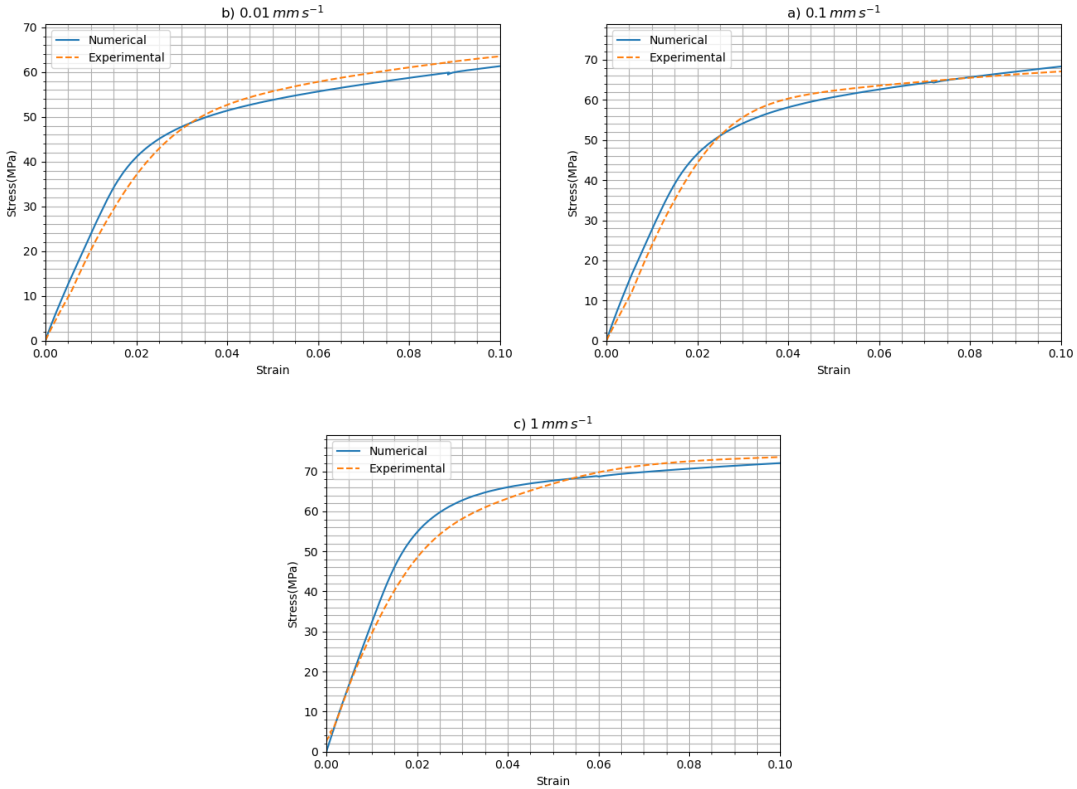

Figure 3.17: Calibration results for monotonic tests at RH25 under different loading rates: a) $0.01\,\mathrm{mm\,s^{-1}}$, b) $0.1\,\mathrm{mm\,s^{-1}}$, c) $1\,\mathrm{mm\,s^{-1}}$.

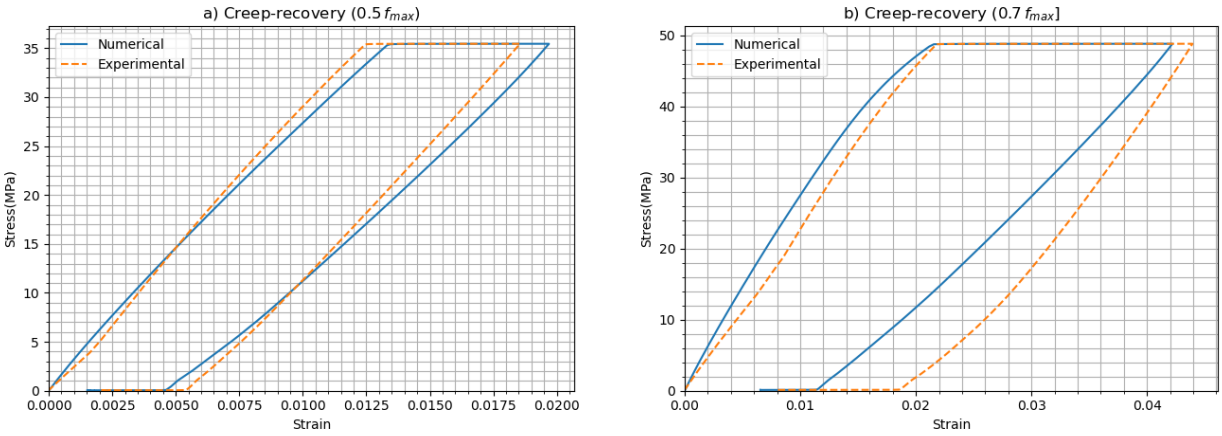

Figure 3.18: Calibration results for creep-recovery tests at RH25 under different loading levels: a) 50% of $F_{\max}$, b) 70% of $F_{\max}$.

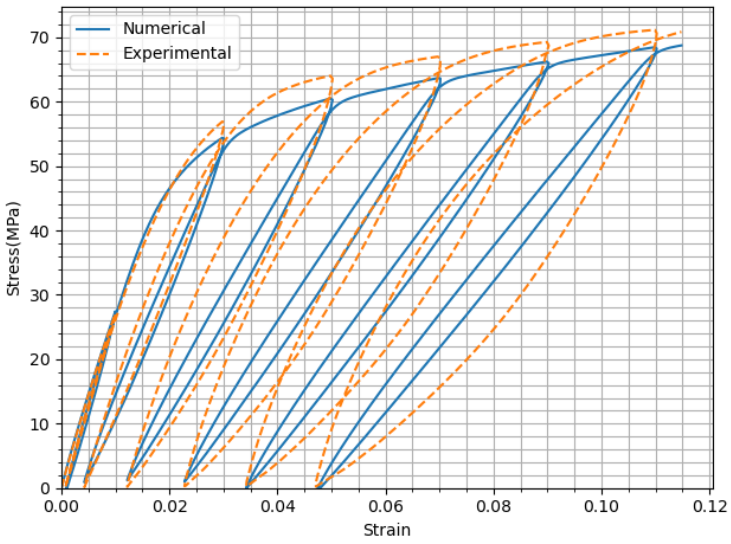

Figure 3.19: Calibration results for loading-unloading test at RH25.

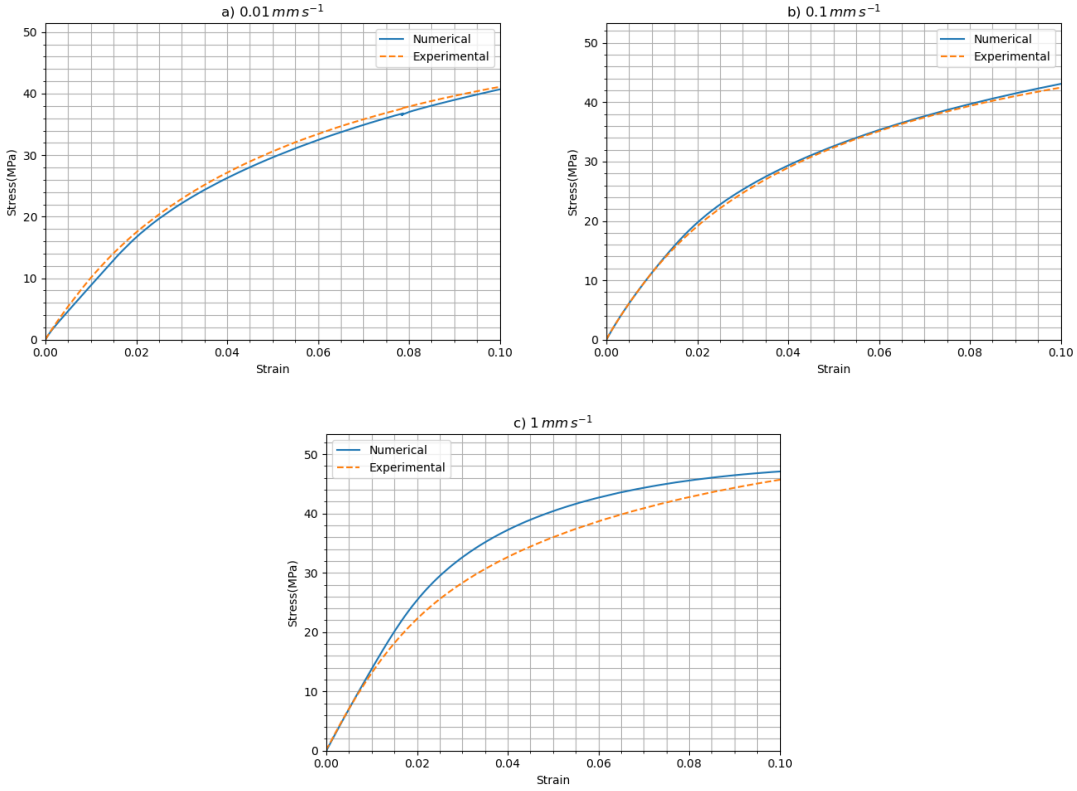

Figure 3.20: Calibration results for monotonic tests at RH50 under different loading rates: a) $0.01\,\mathrm{mm\,s^{-1}}$, b) $0.1\,\mathrm{mm\,s^{-1}}$, c) $1\,\mathrm{mm\,s^{-1}}$.

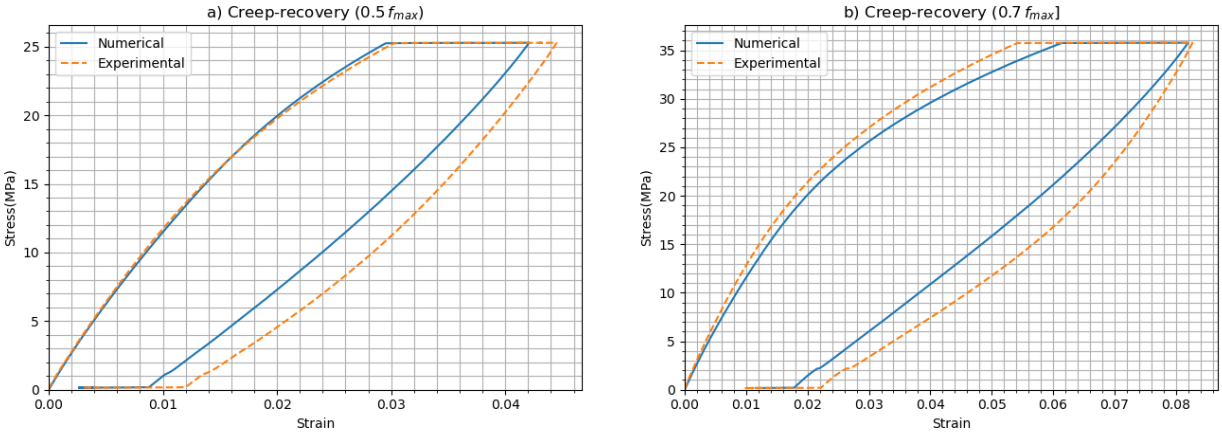

Figure 3.21: Calibration results for creep-recovery tests at RH50 under different loading levels: a) 50% of $F_{\max}$, b) 70% of $F_{\max}$.

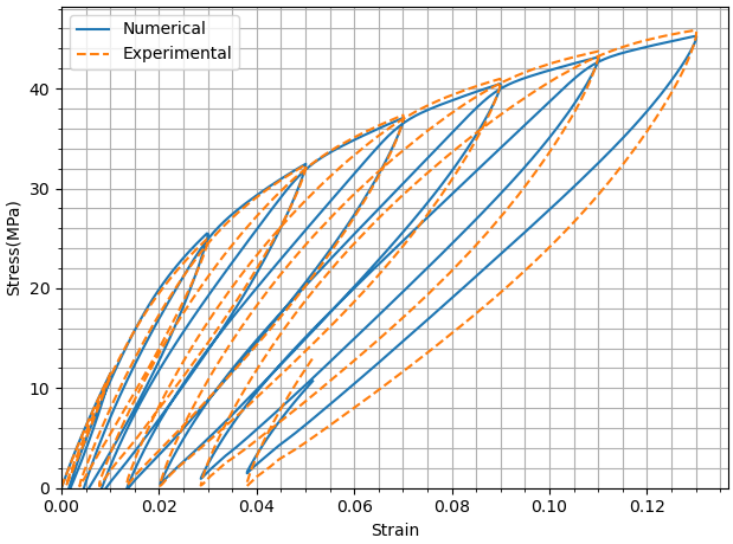

Figure 3.22: Calibration results for loading-unloading test at RH50.

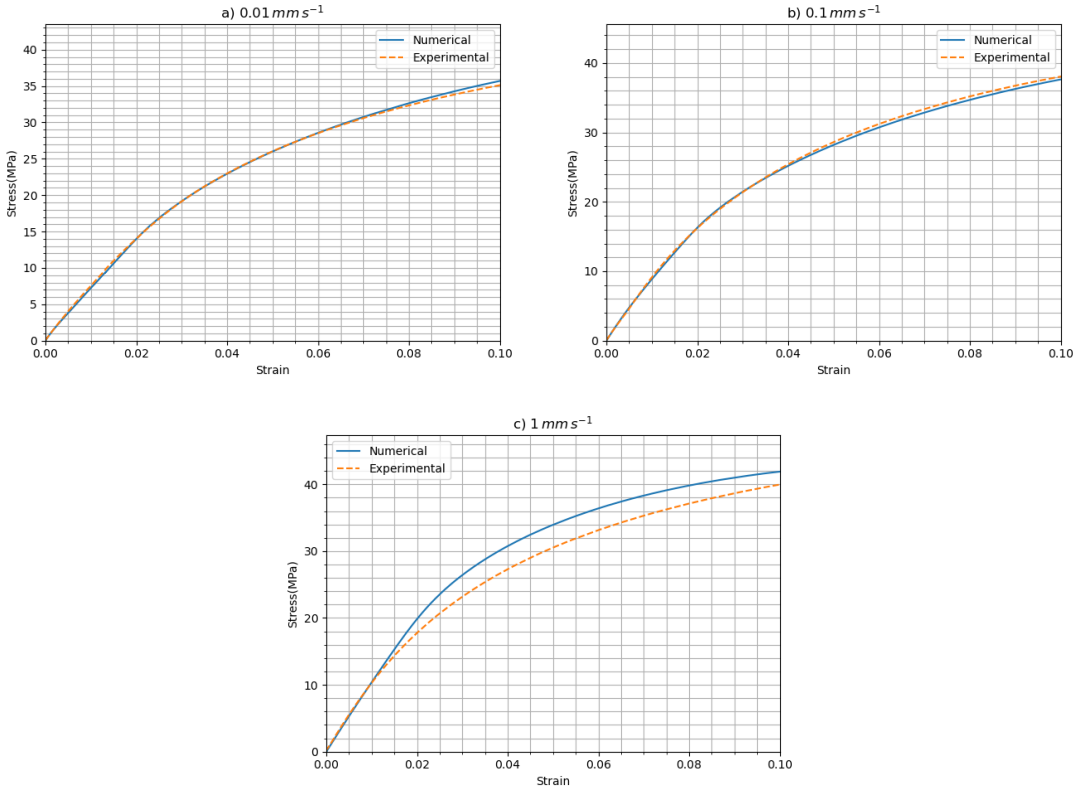

Figure 3.23: Calibration results for monotonic tests at RH65 under different loading rates: a) 0.01 mm s^{-1}, b) 0.1 mm s^{-1}, c) 1 mm s^{-1}.

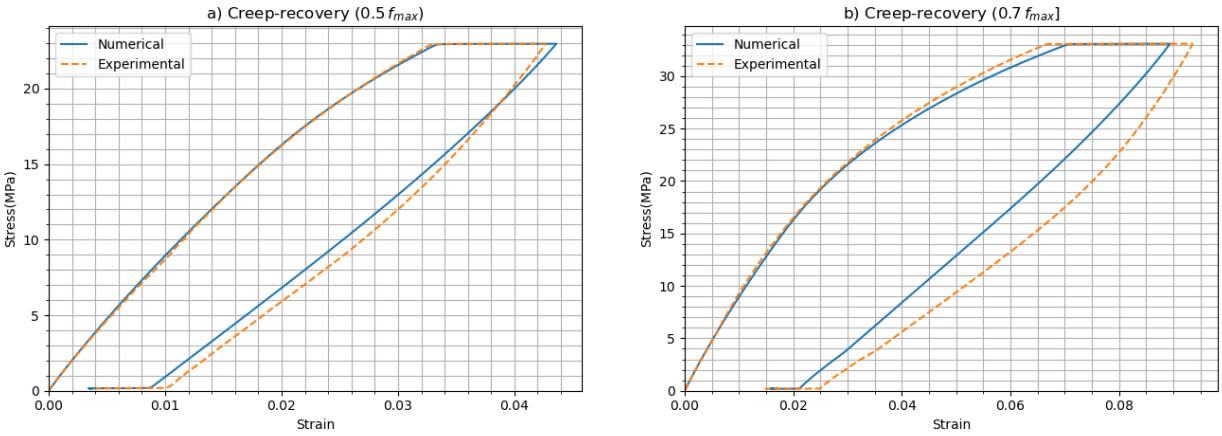

Figure 3.24: Calibration results for creep-recovery tests at RH65 under different loading levels: a) 50% of $F_{\max}$, b) 70% of $F_{\max}$.

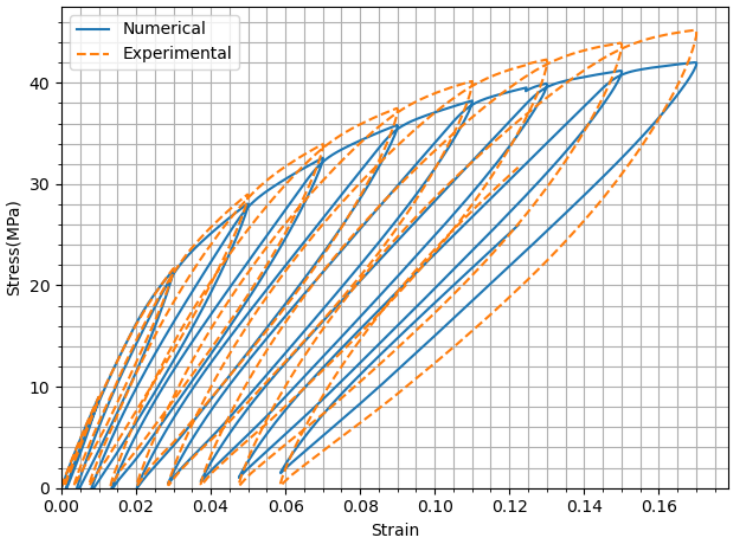

Figure 3.25: Calibration results for loading-unloading test at RH65.

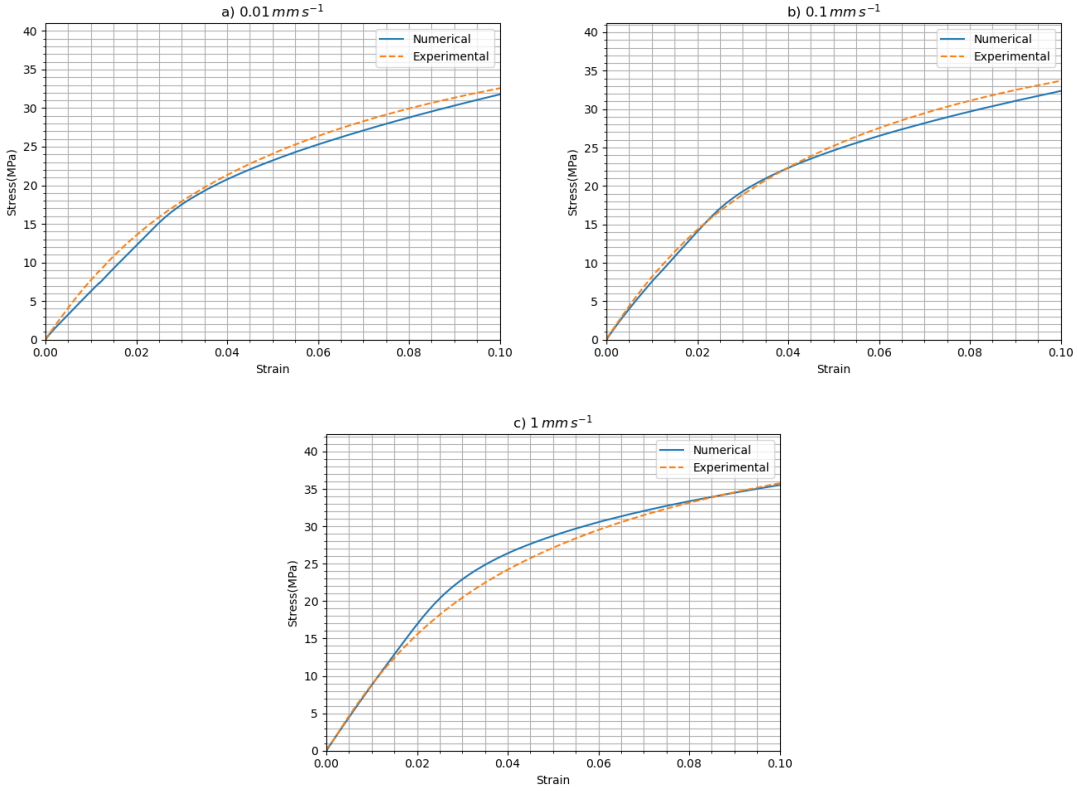

Figure 3.26: Calibration results for monotonic tests at RH80 under different loading rates: a) 0.01 mm s^{-1}, b) 0.1 mm s^{-1}, c) 1 mm s^{-1}.

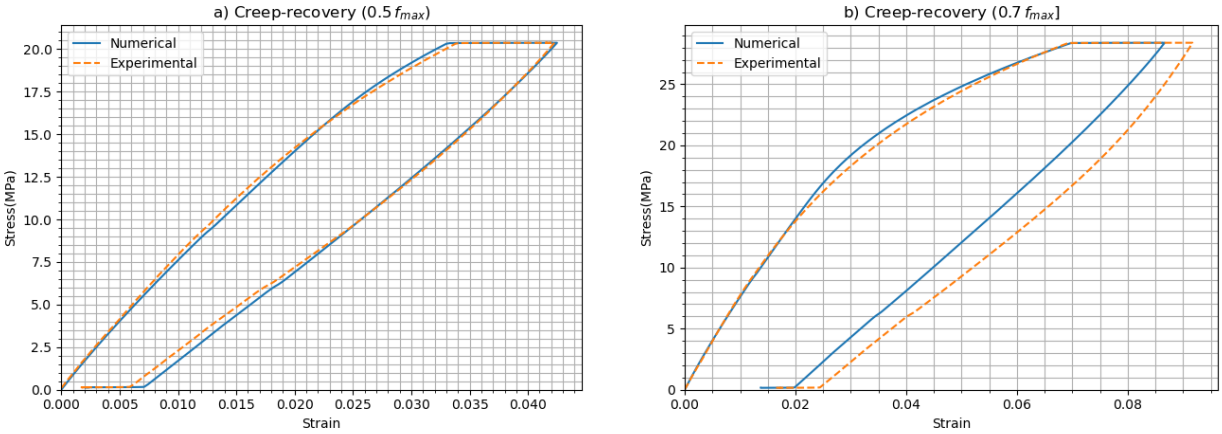

Figure 3.27: Calibration results for creep-recovery tests at RH80 under different loading levels: a) 50% of $F_{\max}$, b) 70% of $F_{\max}$.

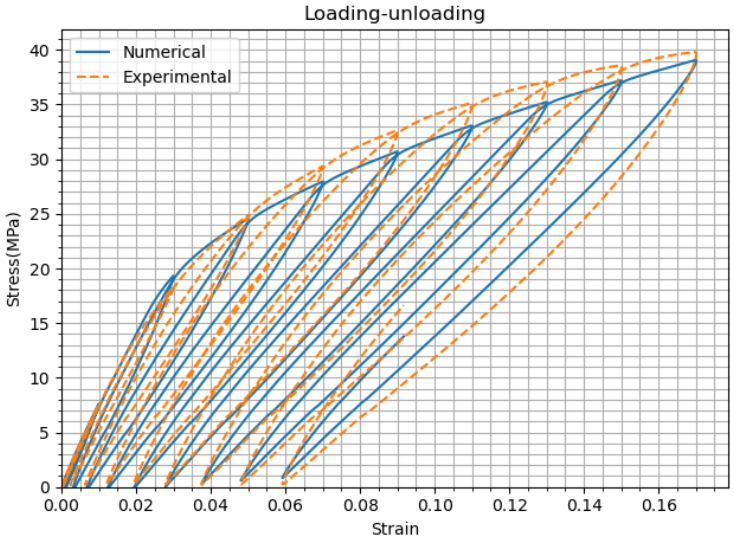

Figure 3.28: Calibration results for loading-unloading test at RH80.

Table 3.4: Calibrated parameters for the von Mises-based model at different RH levels.

Parameters	RH0	RH25	RH50	RH65	RH80
E (MPa)	3588.99	3577.91	1452.46	1088.50	918.80
ν $(-)$	0.3	0.3	0.3	0.3	0.3
E^{v1} (MPa)	37935.58	17702.06	18025.02	12116.62	9104.26
E^{v2} (MPa)	18202.36	13626.63	2350.54	2375.67	2400.77
E^{v3} (MPa)	46065.55	31916.05	17975.70	16002.66	10611.56
E^{V4} (MPa)	17947.79	6454.42	63073.45	67036.98	156679.06
τ^{v1} (s)	0.8	0.8	0.8	0.8	0.8
τ^{v2} (s)	8	8	8	8	8
τ^{v3} (s)	80	80	80	80	80
τ^{v4} (s)	800	800	800	800	800
H_m (MPa)	515.40	782.34	772.68	703.76	450.21
H_p $(-)$	0.33	0.48	0.59	0.67	0.60
R_{vp}(MPa.s$^{P_{vp}}$)	67.52	59.83	44.67	36.73	33.51
P_{vp} $(-)$	0.07	0.09	0.16	0.22	0.26
S_D (MPa)	8.87	7.22	13.60	16.57	6.02
β_D $(-)$	-2.77	-2.09	-1.28	-1.02	-1.56
R_0 (MPa)	20.20	13.89	8.77	11.86	14.08

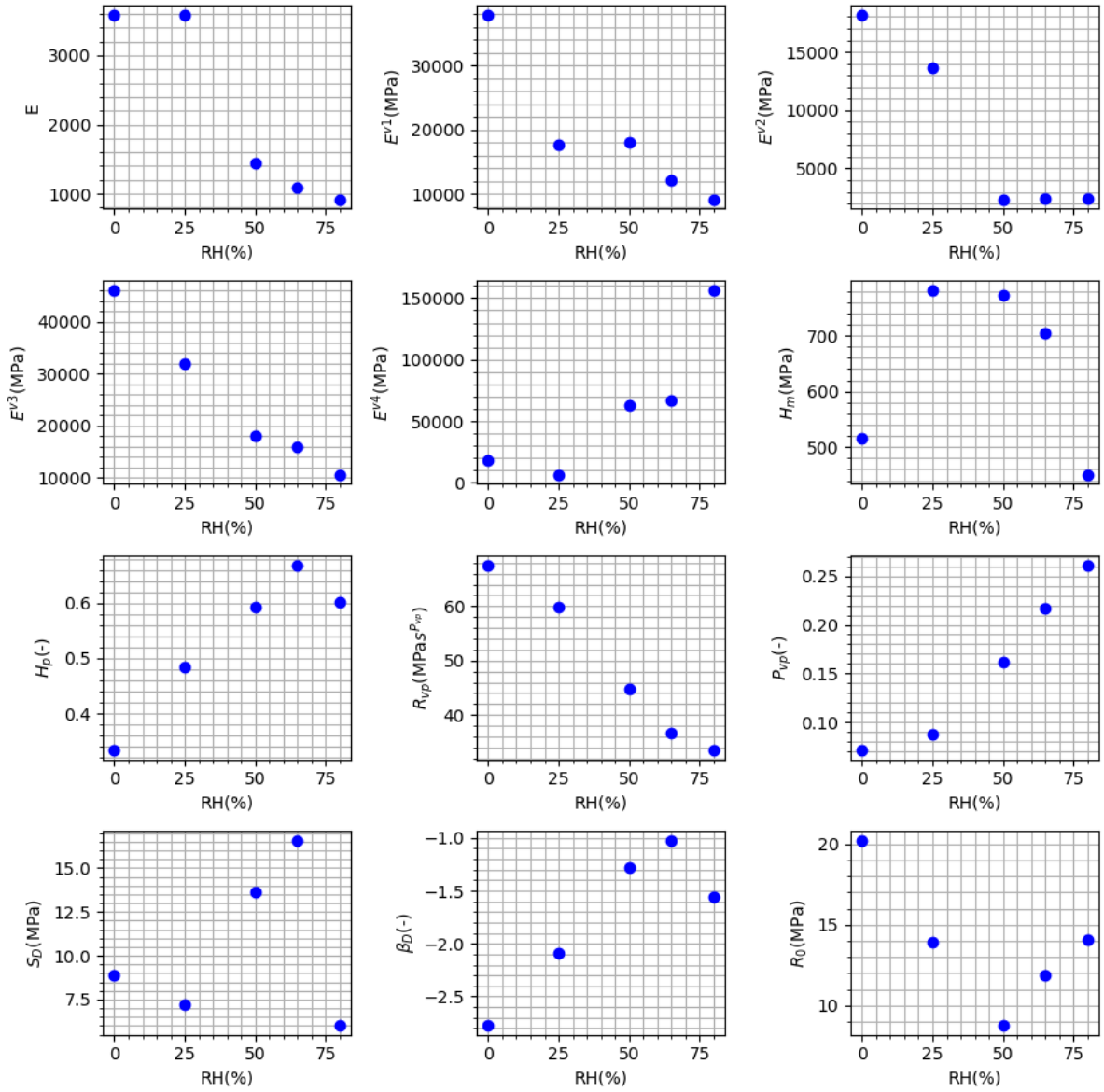

Figure 3.29: Model parameters variation with respect to RH.

3.2.5 Model validation

As indicated before, validation of the model identified in the previous section is implemented through stepped creep-recovery, cyclic, and loading-unloading tests in the small deformation zone (less than 10%), and the results are plotted and shown in Figures 3.30 to 3.34. As observed, the results are better validated when RH is more than 50%. However, the numerical results are closer to the experimental data for RH50 and RH65 (Figures 3.32 and 3.33). Here, the model based on the von Mises yield function is calibrated, and the model using the obtained parameters has been validated. In the following section, an experimental-numerical framework is developed to identify the I_1-J_2-based model parameters, presented in chapter 2.

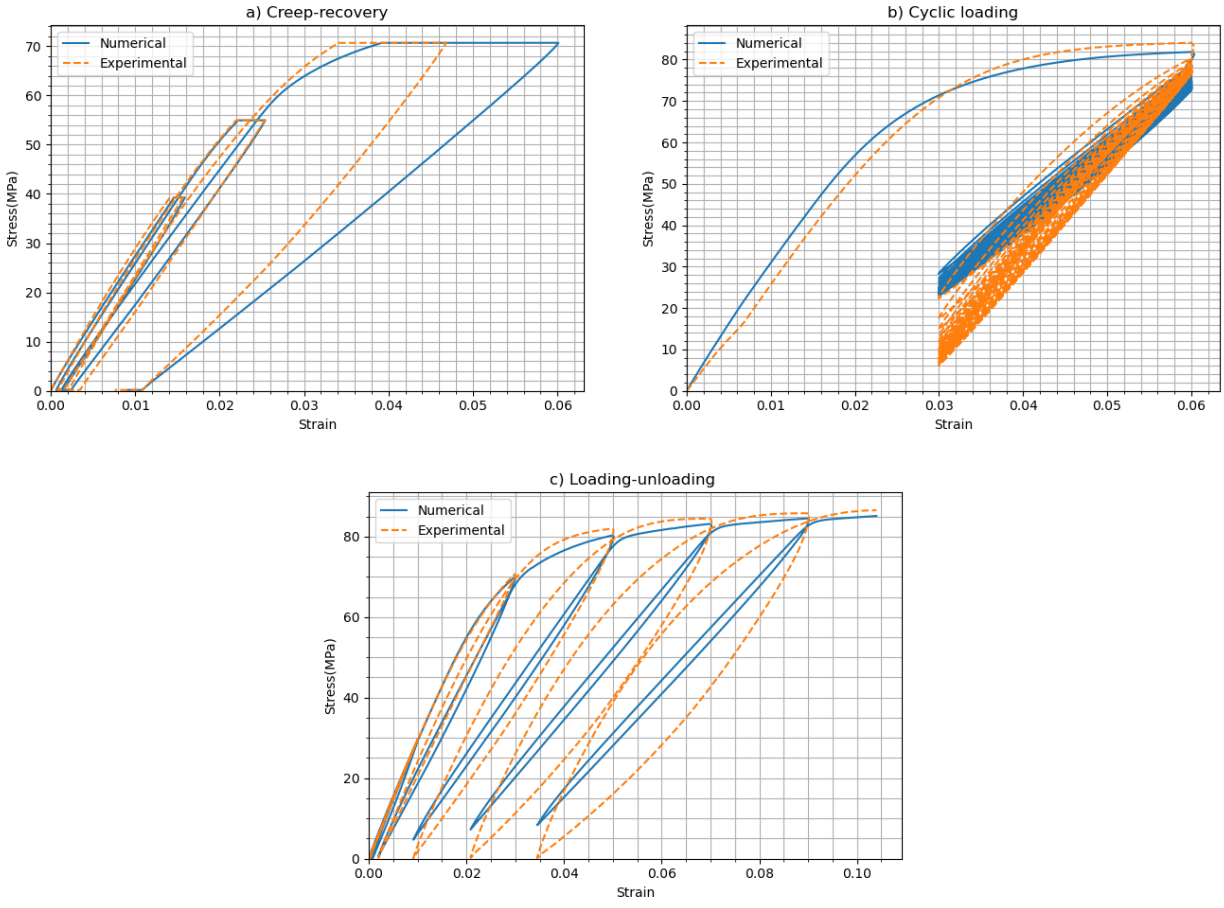

Figure 3.30: Validation results at RH0: a) Creep-recovery test with $0.01\,\mathrm{mm\,s^{-1}}$, b) cyclic loading with $0.1\,\mathrm{mm\,s^{-1}}$, c) loading-unloading with $0.05\,\mathrm{mm\,s^{-1}}$.

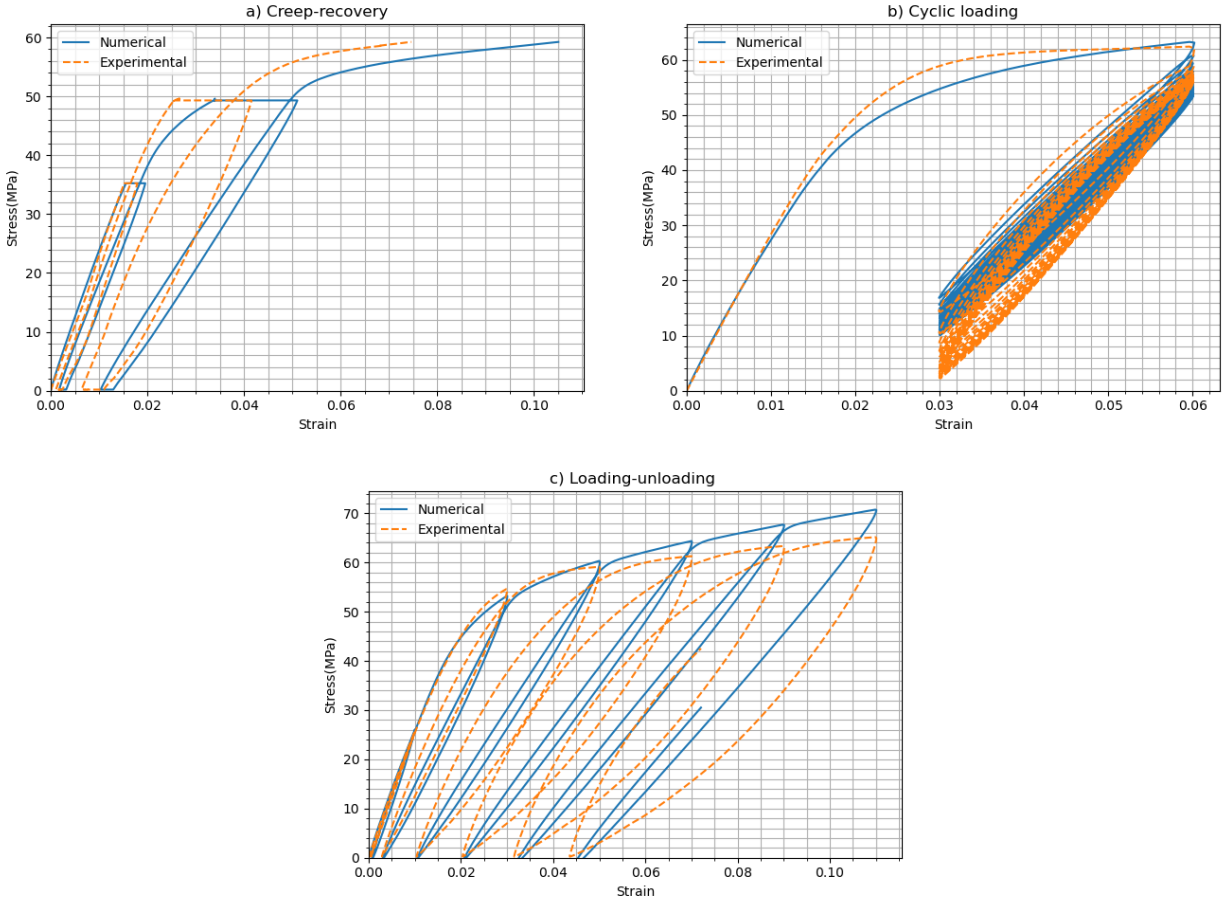

Figure 3.31: Validation results at RH25: a) creep-recovery test at RH25 with $0.01\,\mathrm{mm\,s^{-1}}$, b) cyclic loading with $0.1\,\mathrm{mm\,s^{-1}}$, c) loading-unloading with $0.05\,\mathrm{mm\,s^{-1}}$.

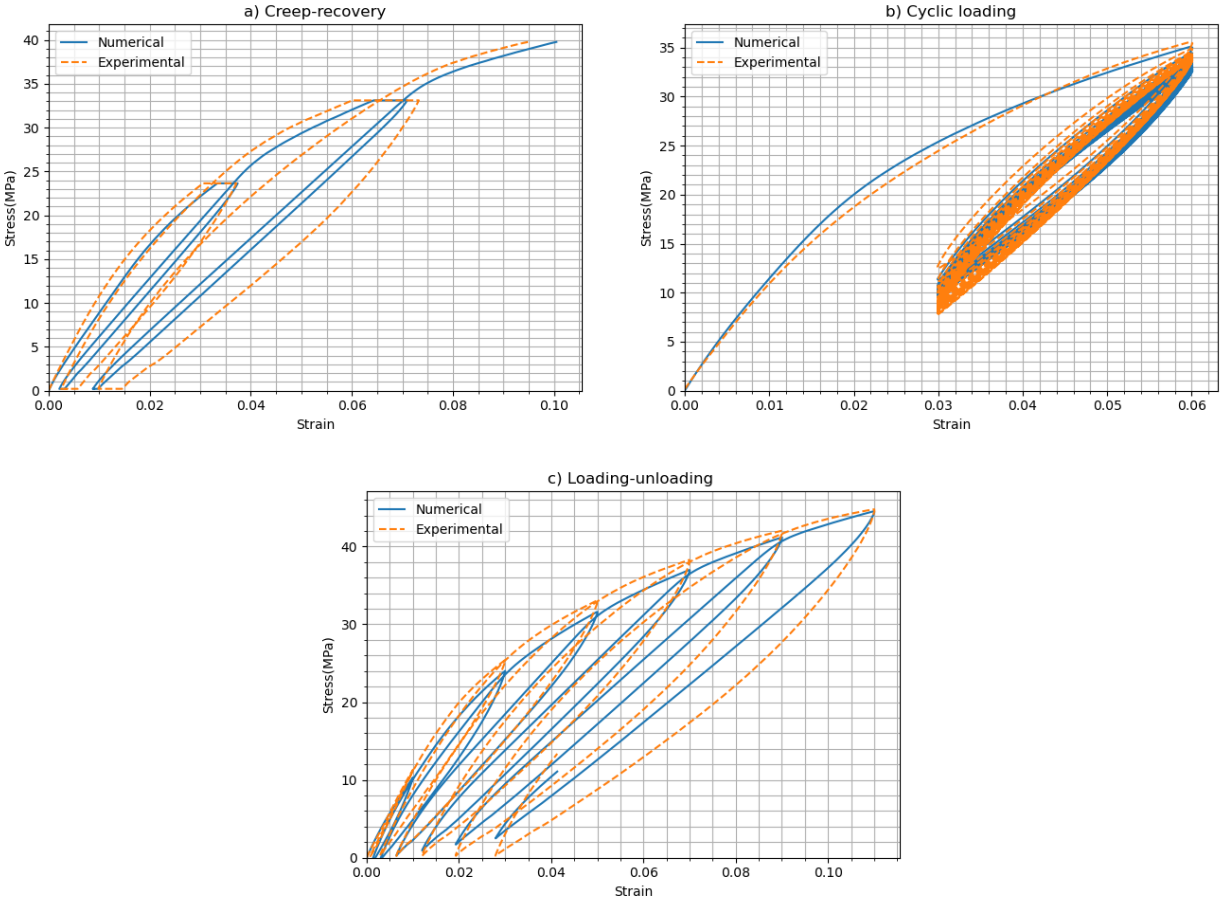

Figure 3.32: Validation results at RH50: a) creep-recovery test with $0.01\,\mathrm{mm\,s^{-1}}$, b) cyclic loading with $0.1\,\mathrm{mm\,s^{-1}}$, c) loading-unloading with $0.05\,\mathrm{mm\,s^{-1}}$.

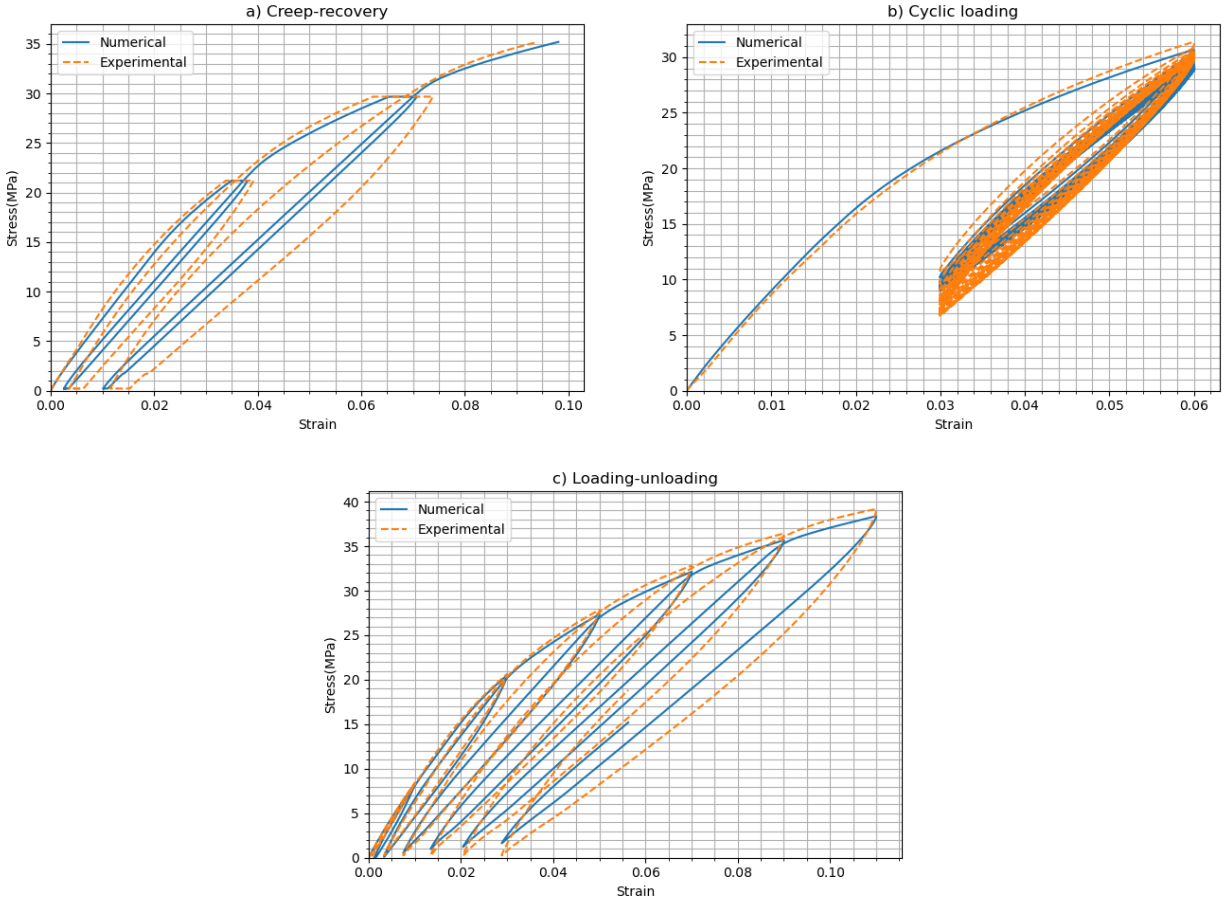

Figure 3.33: Validation results at RH65: a) creep-recovery test with $0.01\,\mathrm{mm\,s^{-1}}$, b) cyclic loading with $0.1\,\mathrm{mm\,s^{-1}}$, c) loading-unloading with $0.05\,\mathrm{mm\,s^{-1}}$.

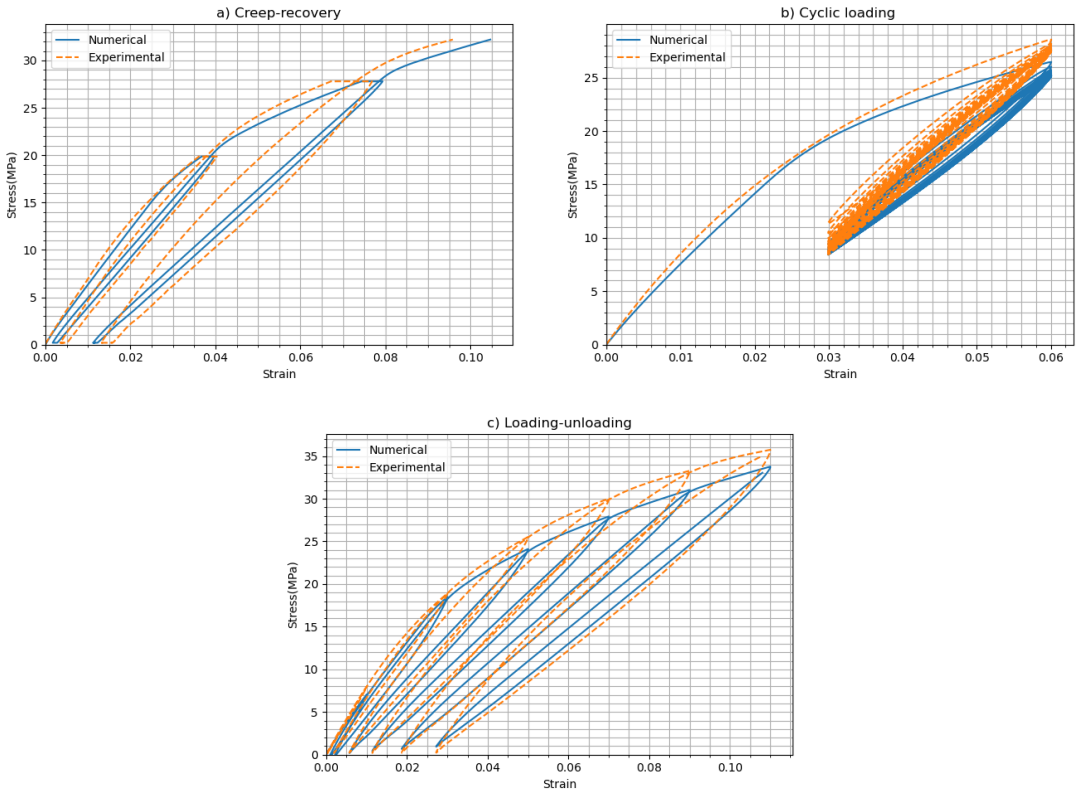

Figure 3.34: Validation results at RH80: a) creep-recovery test with $0.01\,\mathrm{mm\,s^{-1}}$, b) cyclic loading with $0.1\,\mathrm{mm\,s^{-1}}$, c) loading-unloading with $0.05\,\mathrm{mm\,s^{-1}}$.

3.3 Calibration and validation of the model based on I_1-J_2 yield function

Up to now, the model based on von Mises yield function has been calibrated and validated at different RHs using the mechanical tests, expressed in the previous sections. However, the latter model does not capture hydrostatic pressure effect and tension-compression asymmetry. To address this, a model based on I_1-J_2 yield function has been presented in chapter 2, which should be calibrated through tension-compression multi-axial tests, but imposing compressive loading on the thermoplastic specimens is quite complicated due to the buckling occurrence. With this in mind, diabolo specimens (Figure 3.35) are designed to perform tension-torsion tests as multi-axial loading instead of tension-compression. To this end, as dog bone samples, diabolo samples are also reconditioned at RH0, RH25, RH50, RH65, and RH80, and the mechanical tests are conducted using the zwick-roell hydraulic machine. Special grips have been designed to first fit to the machine and second keep the cylindrical shape of the specimen under tension-torsion loading (see Figure 3.36). Monotonic tension-torsion tests are performed when the loading in two directions are imposed at the same time with the rates of: i) $0.05\,\mathrm{mm\,s^{-1}}$ and $0.03^{\mathrm{o}}\,\mathrm{s^{-1}}$, ii) $0.5\,\mathrm{mm\,s^{-1}}$ and $0.3^{\mathrm{o}}\,\mathrm{s^{-1}}$, and iii) $5\,\mathrm{mm\,s^{-1}}$ and $3^{\mathrm{o}}\,\mathrm{s^{-1}}$. The data extracted from monotonic test with the second rate is applied in the calibration phase, and the two others are used for validation. The tension-torsion tests along with the tests implemented on the dog bone samples provides the experimental data for calibration and validation of the I_1-J_2-based model. Tables 3.5 and 3.6 briefly demonstrate the summary of the defined experimental campaign for calibration and validation, in which monotonic, loading-unloading, creep-recovery, and tension-torsion tests are abbreviated as MT, L-U, C-R, and T-T, respectively.

Table 3.5: Experimental campaign for the calibration phase of the I_1-J_2-based model.

RH (%)	Corresponding test	Tensile rate ($\mathrm{mm\,s^{-1}}$)	Torsion rate ($^{\mathrm{o}}\,\mathrm{s^{-1}}$)
0, 25, 50, 65 , 80	MT	0.01	-
	MT	0.1	-
	MT	1	-
	L-U	0.1	-
	C-R (50 %$F_{\max}$)	0.1	-
	C-R (70 %$F_{\max}$)	0.1	-
	T-T	0.5	0.3

Table 3.6: Experimental campaign for the validation phase of the I_1-J_2-based model.

RH (%)	Corresponding test	Tensile rate ($\mathrm{mm\,s^{-1}}$)	Torsion rate ($^{\circ}\,\mathrm{s^{-1}}$)
0, 25, 50, 65, 80	C-R	0.01	-
	Cyclic	0.1	-
	L-U	0.05	-
	T-T	0.05	0.03
	T-T	5	3

3.3.1 Experimental observations

As discussed before, water content affects the mechanical response of the material from rubber-like to glass-like behavior, which is confirmed through the experimental observations in previous sections. Figure 3.37 yields a better visual observation in this regard. As observed, Figure 3.37-a shows the brittle sample with RH0 shattered after being subjected to the tension-torsion load. However, in Figure 3.37-b, the sample with RH50 exhibits a ductile behavior along with plastic deformation which can be observed through white stickers before and after loading (see Figure 3.38). The monotonic tension-torsion tests, mentioned previously, are implemented, and the results are plotted as overall force-displacement and torsion moment-rotation angle at different RH (see Figures 3.39 and 3.40). As expected, the samples with lower RH reach higher stress levels. Here, the results for RH0 are not plotted due to high instability and brittle fraction as Figure 3.37-a.

(a)

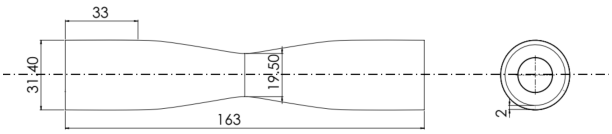

(b)

Figure 3.35: a) Diabolo sample; b) sample dimensions.

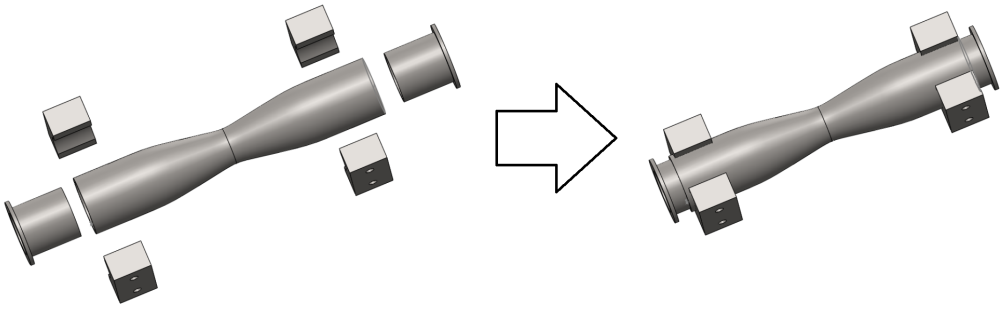

Figure 3.36: Assembly of grips and diabolo shape sample for tension-torsion tests.

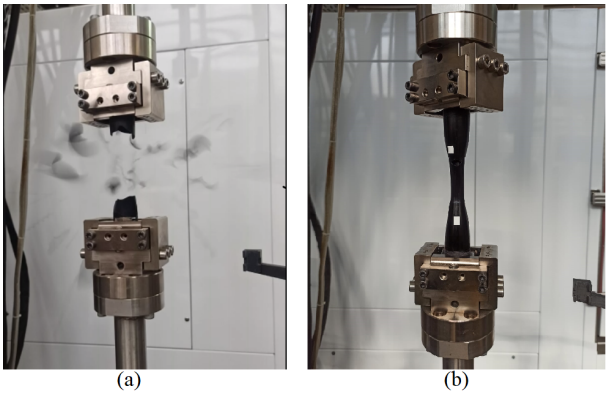

Figure 3.37: a) Tension-torsion test for diabolo at RH0; b) tension-torsion test for diabolo at RH50.

Figure 3.38: Plastic deformation and ductile damage at RH50 for the sample after tension-torsion test in comparison with the initial sample.

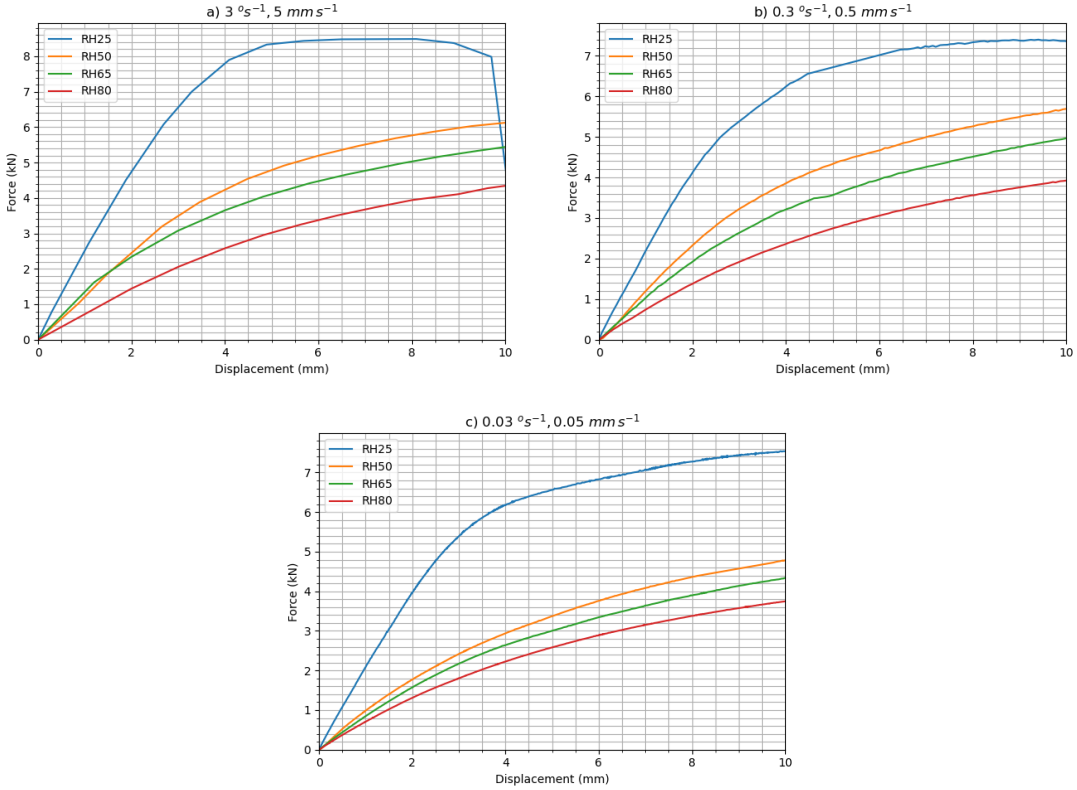

Figure 3.39: Force-displacement curves for monotonic tension-torsion tests in different loading rates: a) $5\,\mathrm{mm\,s^{-1}}$ and $3^{\mathrm{o}}\,\mathrm{s^{-1}}$, b) $0.5\,\mathrm{mm\,s^{-1}}$ and $0.3^{\mathrm{o}}\,\mathrm{s^{-1}}$, c) $0.05\,\mathrm{mm\,s^{-1}}$ and $0.03^{\mathrm{o}}\,\mathrm{s^{-1}}$.

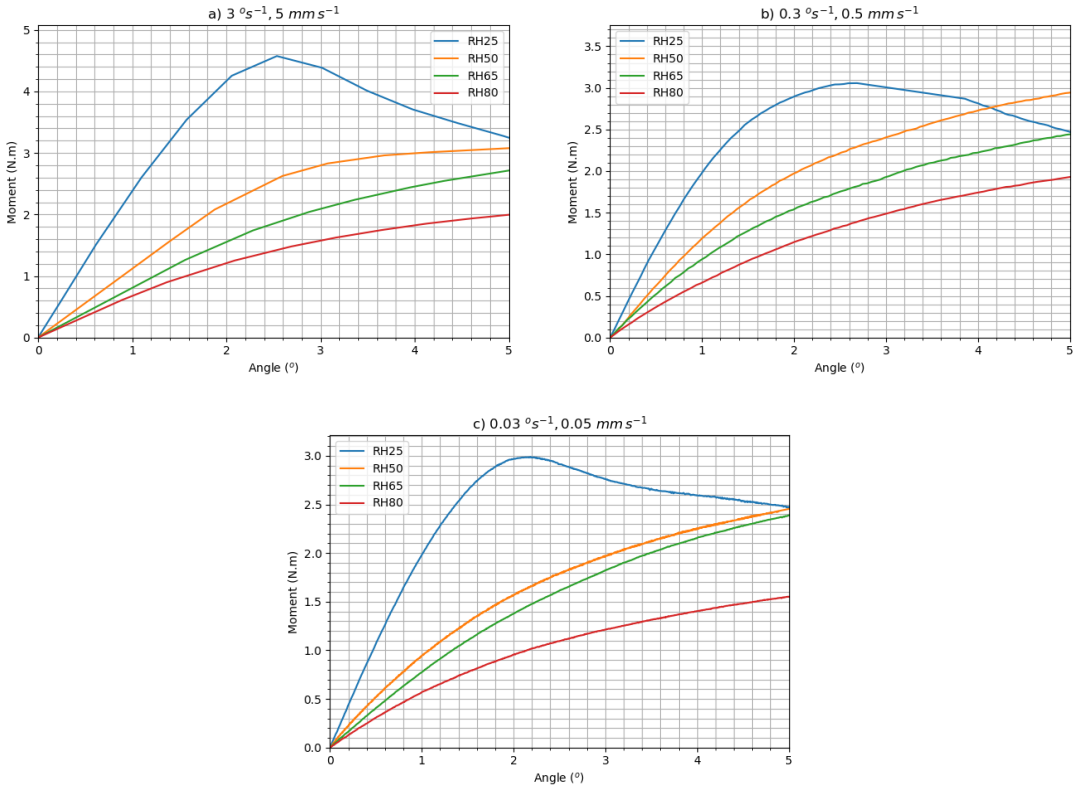

Figure 3.40: Torsion moment-rotation angle (in °) curves for monotonic tension-torsion tests in different loading rates: a) $5\,\mathrm{mm\,s^{-1}}$ and $3^{\mathrm{o}}\,\mathrm{s^{-1}}$, b) $0.5\,\mathrm{mm\,s^{-1}}$ and $0.3^{\mathrm{o}}\,\mathrm{s^{-1}}$, c) $0.05\,\mathrm{mm\,s^{-1}}$ and $0.03^{\mathrm{o}}\,\mathrm{s^{-1}}$.

3.3.2 I_1-J_2 model calibration

In this section, for the present model based on the I_1-J_2 yield function, the same parameters shown in Table 3.1 plus the asymmetry parameter, m, are identified. The calibration procedure is performed using the experimental data obtained from dog bone samples used in the calibration phase of von Mises-based model (section 3.2) and the new data from diabolo shape samples under monotonic tension-torsion test with $0.5\,\mathrm{mm\,s^{-1}}$ and $0.3^{\mathrm{o}}\,\mathrm{s^{-1}}$. Similar to the previous section, the Nelder-Mead optimization algorithm is used to minimize the cost function between the numerical and experimental results. Since the overall force-displacement and moment-angle experimental results are used in the optimization algorithm, it is required to use ABAQUS solver (with the implemented UMAT). To this end, the diabolo shape structure is designed and simulated under same boundary conditions in ABAQUS (see Figure 3.41-a). To reduce the calculation time, since the structure is symmetrical in the circumferential direction, only one slice is sufficient to analyze the whole structure (see Figure 3.41-b). With this in mind, a 10^{o} slice of the whole structure is considered and cyclic boundary conditions are set on it. The numerical results obtained on force and moment are 36 times lower than the whole structure output, so before being used in the optimization algorithm, they must be scaled to be comparable to the experimental data. Considering the validation results in the previous sections, the von Mises-based VEVPD model does not fit well to the experimental data for RH0 and RH25. In other words, the VEVPD model is not designed to predict mechanical responses at low RHs, particularly at RH0, when the material is glassy. Therefore, it is required to model their behavior considering a brittle damage. Thus, here, the data for RH0 and RH25 is excluded from the calibration procedure, and the parameters are identified for RH50, RH65, and RH80. The final calibration results are plotted as stress-strain, force-displacement, and torsion moment-rotation angle curves at RH50 and depicted in Figures 3.42 to 3.45, from which the identified parameters are listed in Table 3.7. As observed, the I_1-J_2-based model is in a good agreement with experimental results, particularly in force-displacement and torsion moment-rotation angle curves obtained from tension-torsion tests. The numerical results are produced using the von Mises and I_1-J_2 models are plotted to compare with the experiments on diabolo samples in Figure 3.45. As seen, the I_1-J_2-based model is better fit to the experimental data compared to von Mises, as expected. The asymmetry parameter, m, is identified as 1.05 for RH50, which is in a good range compared to other polymer types [44]. In the same way, for RH65, the I_1-J_2-based model is calibrated and the results are plotted and presented in Figures 3.46 to 3.49, and the

parameters are listed in Table 3.7. For RH65, the asymmetry parameter, m, is obtained as 1.00 which indicates that increasing RH leads to a symmetric yield behavior. Although the responses obtained from I_1-J_2-based model with $m = 1$ should be similar to those from the von Mises-based model, Figure 3.49 shows that the I_1-J_2-based model yields results relatively closer to the experimental data. This is due to the fact that for the I_1-J_2-based model, the experimental tension-torsion data are taken into account in the calibration procedure. The observed incompatibility between tensile tests on the dog bone samples and tension-torsion tests on the diabolo samples may be due to non-uniformity of water diffusion or to structural effects in the diabolo samples. This can have more impact at higher RH levels, particularly RH80, making it difficult to calibrate the model properly. For these latter reasons, the calibration procedure for RH80 does not provide desirable results for the I_1-J_2-based model.

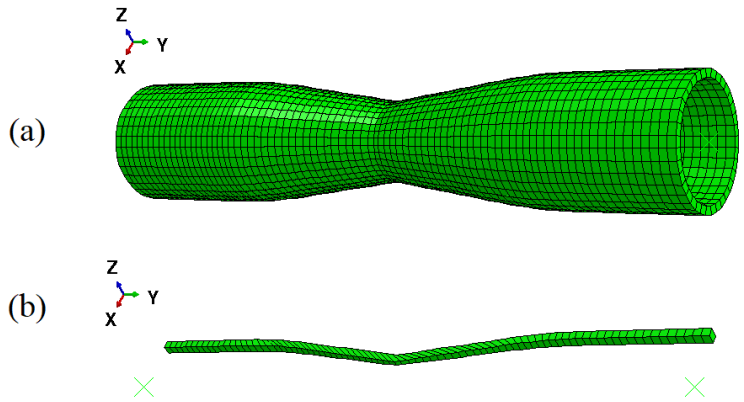

Figure 3.41: a) Complete diabolo; b) a sector of diabolo used in the simulation (10° or 1/36).

3.3.3 I_1-J_2-based model validation

In this section, the I_1-J_2-based model is validated using experimental data extracted from tension-torsion tests with $0.05\,\mathrm{mm\,s^{-1}}$; $0.03^{o}\,\mathrm{s^{-1}}$ and $5\,\mathrm{mm\,s^{-1}}$; $3^{o}\,\mathrm{s^{-1}}$, plus data from the creep-recovery, cyclic, and loading-unloading tests used in the validation phase of the von Mises-based model. The results for RH50 and RH65 are plotted and presented in Figures 3.50 to 3.55. As observed, the numerical results are mostly well validated by the creep-recovery, cyclic, and loading-unloading tests (Figure 3.50). However, for RH65, the cyclic test model result is relatively more distant from the experimental results (see Figure 3.53-b). For the tension-torsion tests, the I_1-J_2-based model is more accurate than the von Mises model (Figures 3.51, 3.52, 3.54, and 3.55), however, the differences are a bit higher under loading with a lower rate in $0.03\,^{o}\,\mathrm{s^{-1}}$ and $0.05\,\mathrm{mm\,s^{-1}}$. As mentioned before for the calibration

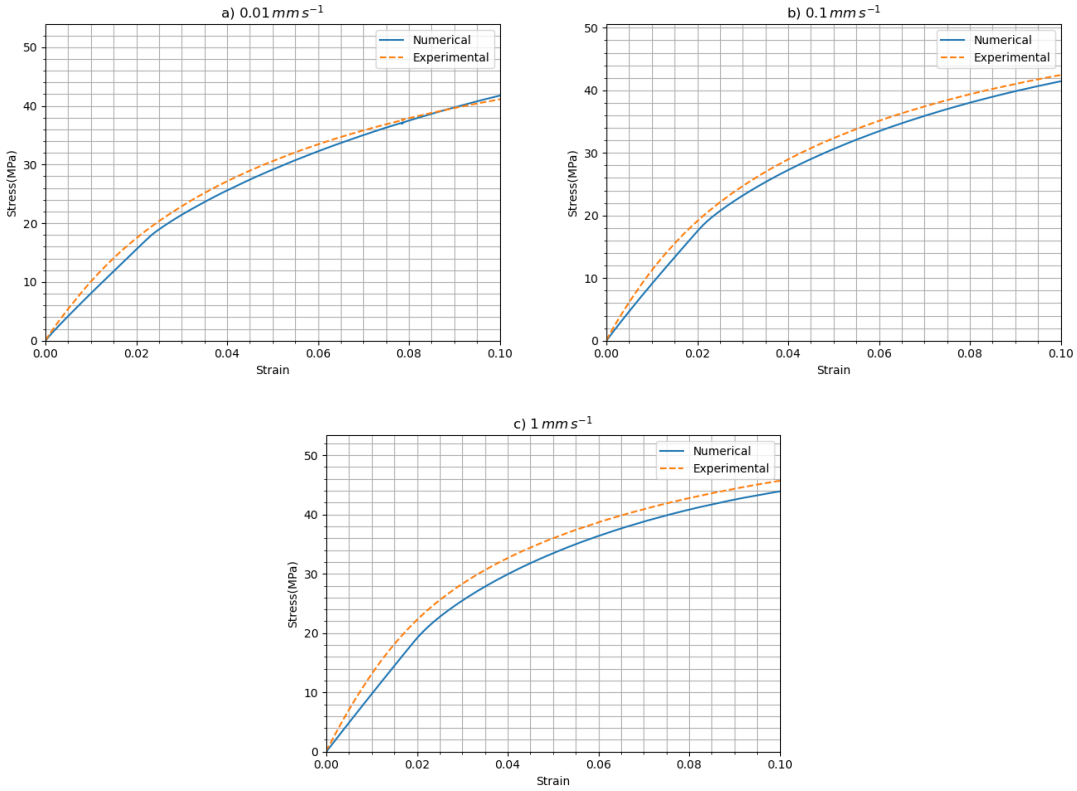

Figure 3.42: Calibration results for I_1-J_2-based model under monotonic tests at RH50 under different loading rates: a) 0.01 mm s^{-1}, b) 0.1 mm s^{-1}, c) 1 mm s^{-1}.

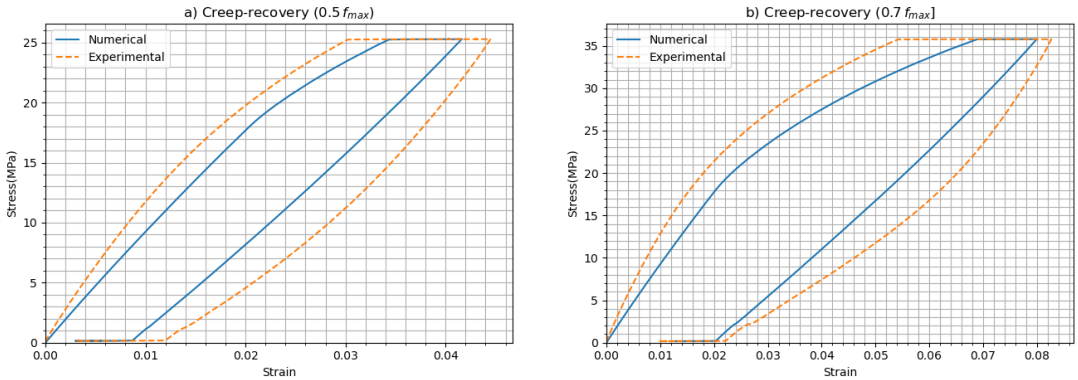

Figure 3.43: Calibration results for I_1-J_2-based model under creep-recovery tests at RH50 under different loading levels: a) 50% of $F_{\max}$, b) 70% of $F_{\max}$.

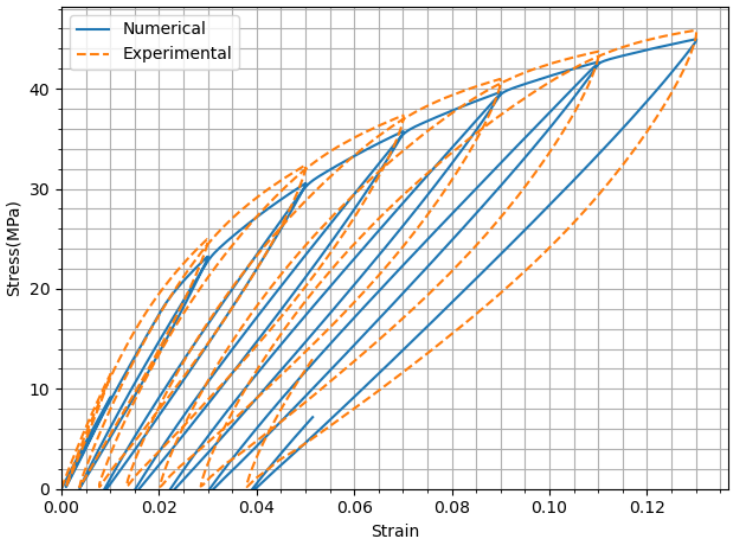

Figure 3.44: Calibration results for I_1-J_2-based model under loading-unloading tests at RH50.

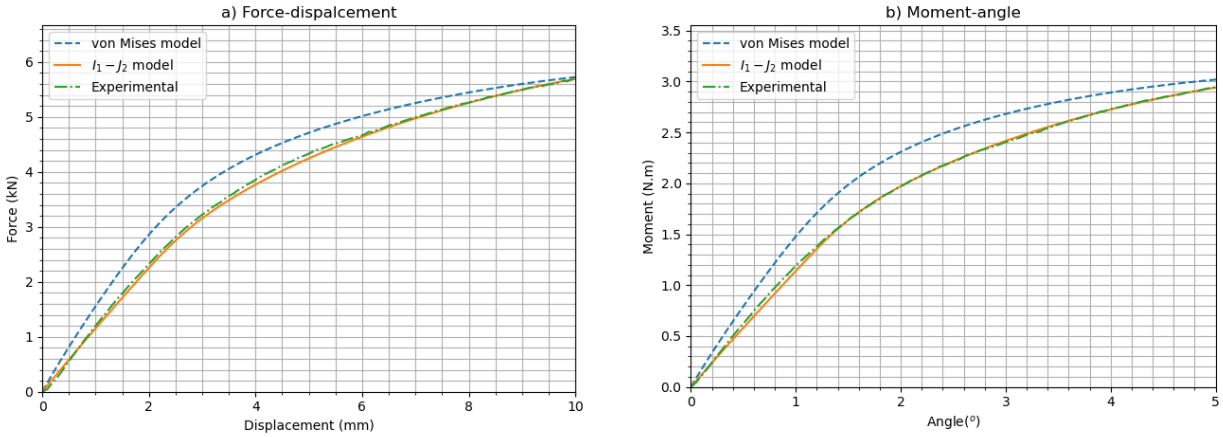

Figure 3.45: Calibration results for I_1-J_2-based model under tension-torsion test at RH50 with $0.3\,^{\circ}\,s^{-1}$ and $0.5\,mm\,s^{-1}$: a) force-displacement curves, b) torsion moment-rotation angle curves.

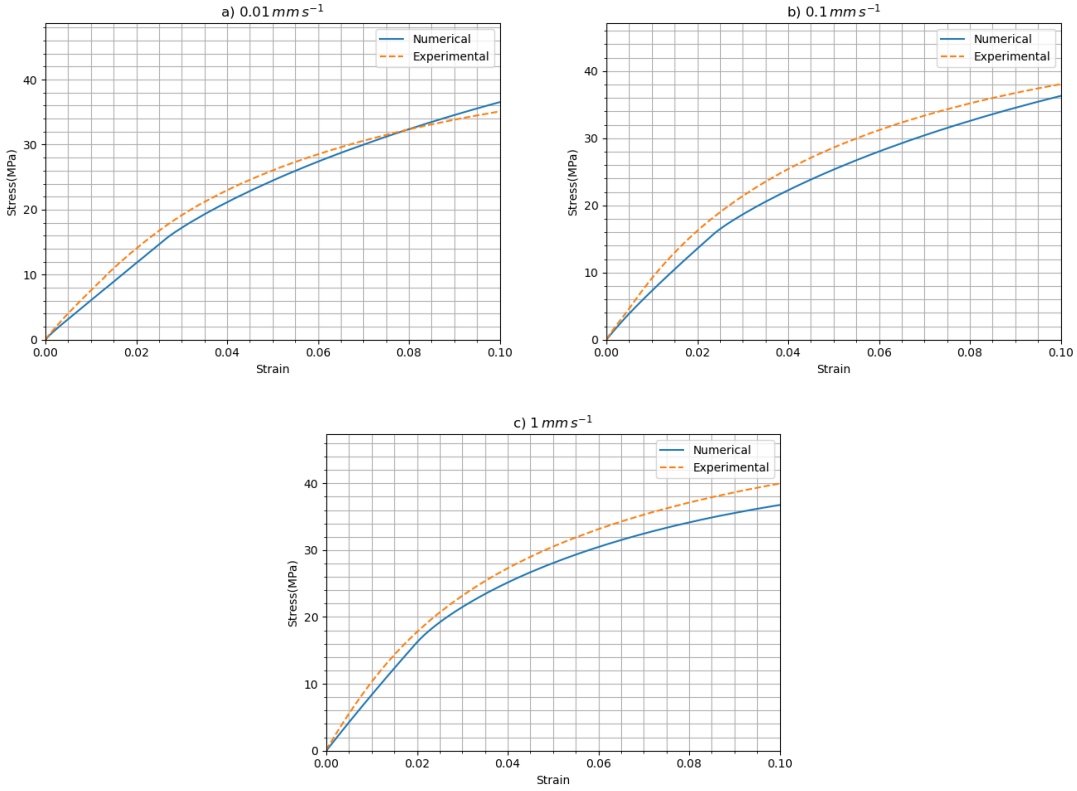

Figure 3.46: Calibration results for I_1-J_2-based model under monotonic tests at RH65 under different loading rates: a) 0.01 mm s^{-1}, b) 0.1 mm s^{-1}, c) 1 mm s^{-1}.

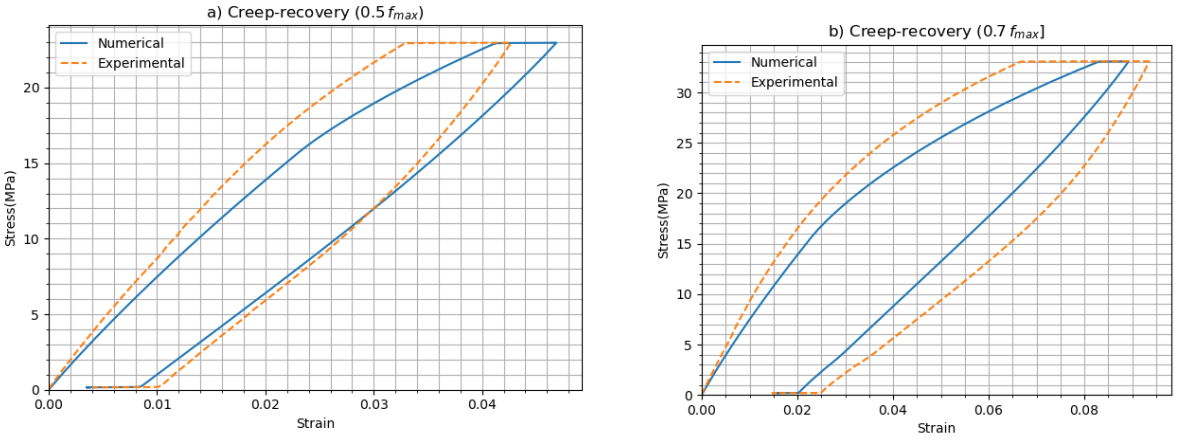

Figure 3.47: Calibration results for I_1-J_2-based model under creep-recovery tests at RH65 under different loading levels: a) 50% of $F_{\max}$, b) 70% of $F_{\max}$.

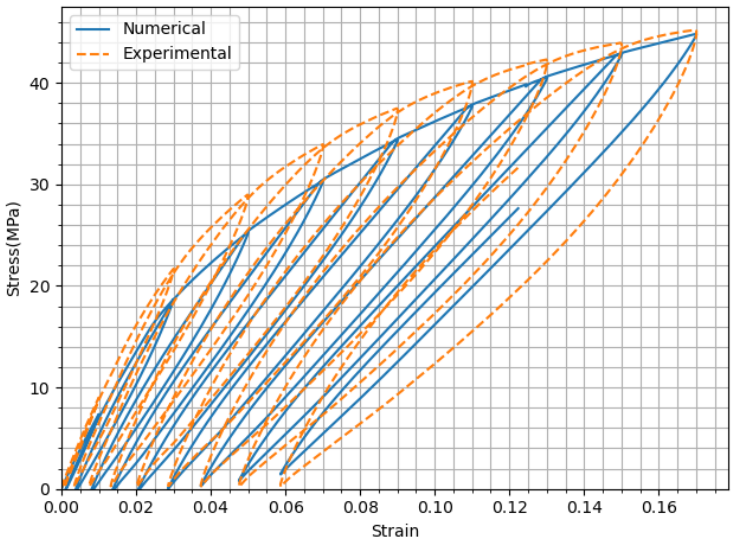

Figure 3.48: Calibration results for I_1-J_2-based model under loading-unloading tests at RH65.

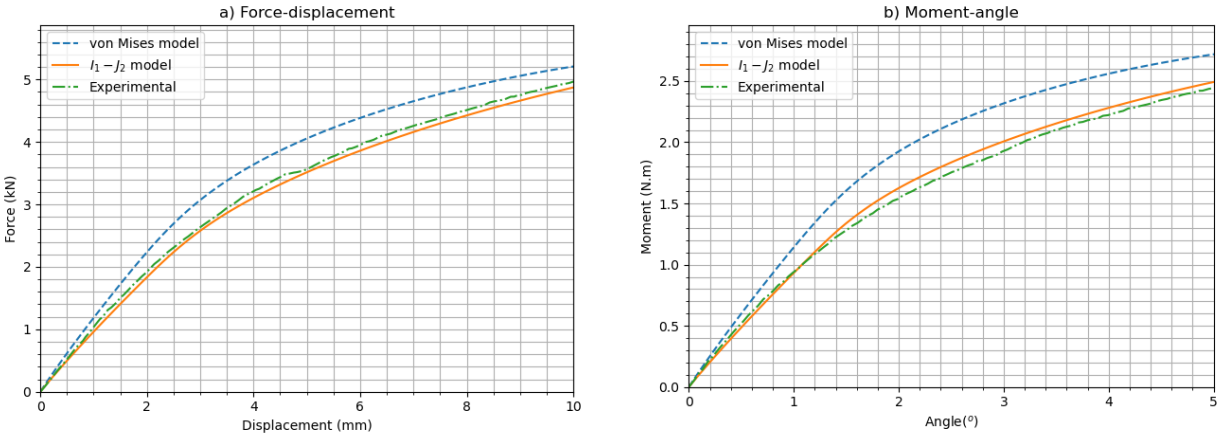

Figure 3.49: Calibration results for I_1-J_2-based model under tension-torsion test at RH65 with $0.3\,^{\circ}\,\mathrm{s}^{-1}$ and $0.5\,\mathrm{mm\,s}^{-1}$: a) force-displacement curves, b) torsion moment-rotation angle curves.

Table 3.7: Calibrated parameters for the I_1-J_2-based model at RH50 and RH65.

Parameters	RH50	RH65
E (MPa)	988.95	868.12
ν $(-)$	0.3	0.3
E^{v1} (MPa)	36396.15	12325.03
E^{v2} (MPa)	5765.97	2143.08
E^{v3} (MPa)	5924.76	19865.37
E^{V4} (MPa)	83879.34	131788.15
τ^{v1} (s)	0.8	0.8
τ^{v2} (s)	8	8
τ^{v3} (s)	80	80
τ^{v4} (s)	800	800
m	1.05	1.00
H_m (MPa)	996.82	566.07
H_p $(-)$	0.76	0.71
R_{vp}(MPa.s$^{P_{vp}}$)	24.82	21.02
P_{vp} $(-)$	0.37	0.48
S_D (MPa)	26.78	16.89
β_D $(-)$	-0.83	-0.81
R_0 (MPa)	17.04	15.70

phase, the responses obtained from I_1-J_2-based model at RH65 ($m = 1$) is closer to the experimental data than those from von Mises-based model because of the consideration of tension-torsion tests experimental data in the calibration procedure of the I_1-J_2-based model.

3.4 Conclusion

In this chapter, an experimental campaign has been conducted using two types of samples: dog bone and diaboo structure. The obtained experimental results have been discussed and implemented into a model parameters identification process. Dog bone samples were subjected to monotonic, cyclic, and creep-recovery mechanical tests. The effect of RH on the experimental data was studied. Increasing RH decreases the glass transition temperature, and the material then exhibits softer behavior at room temperature, as expected. The obtained experimental data were applied to identify the VEVPD model based on the von Mises yield function at different RH levels. The effect of RH on the model parameters was explored, which follows a more organized trend in the viscoelastic parameters. To capture the asymmetry in compressive and tensile yield strength, diabolo shape specimens were subjected to

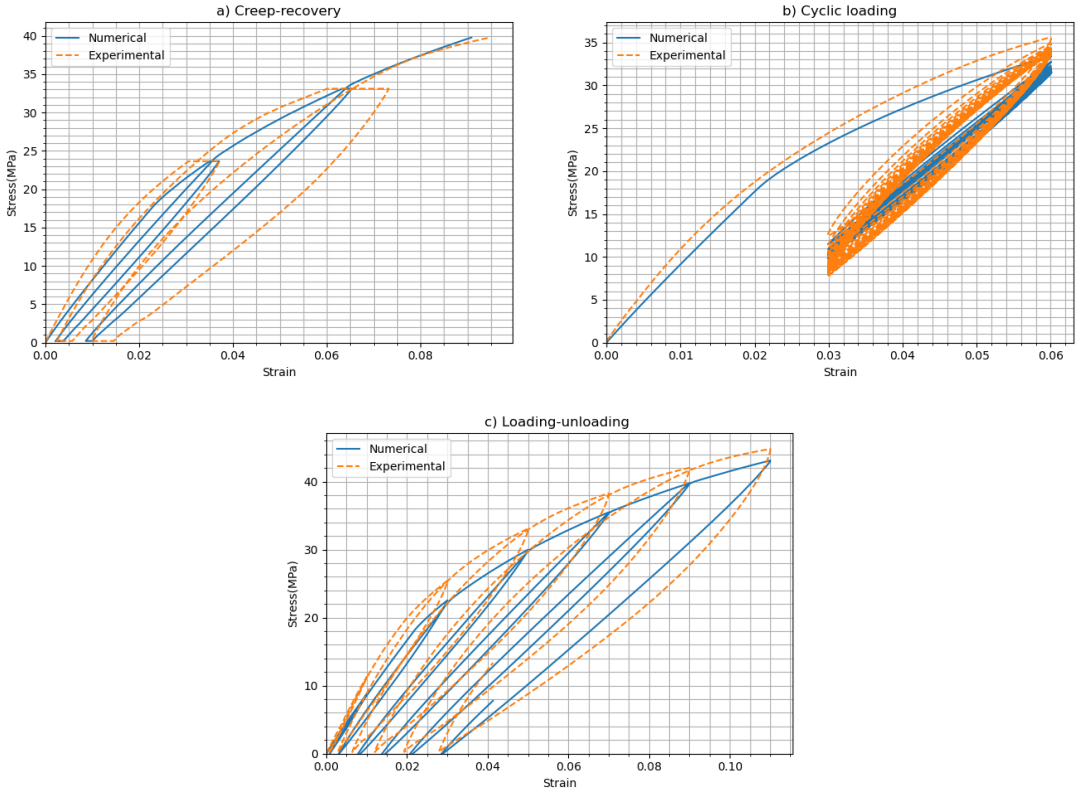

Figure 3.50: Validation results for I_1-J_2-based model at RH50: a) creep-recovery test with $0.1\,\mathrm{mm\,s^{-1}}$; b) cyclic loading with $0.1\,\mathrm{mm\,s^{-1}}$; c) loading-unloading with $0.05\,\mathrm{mm\,s^{-1}}$.

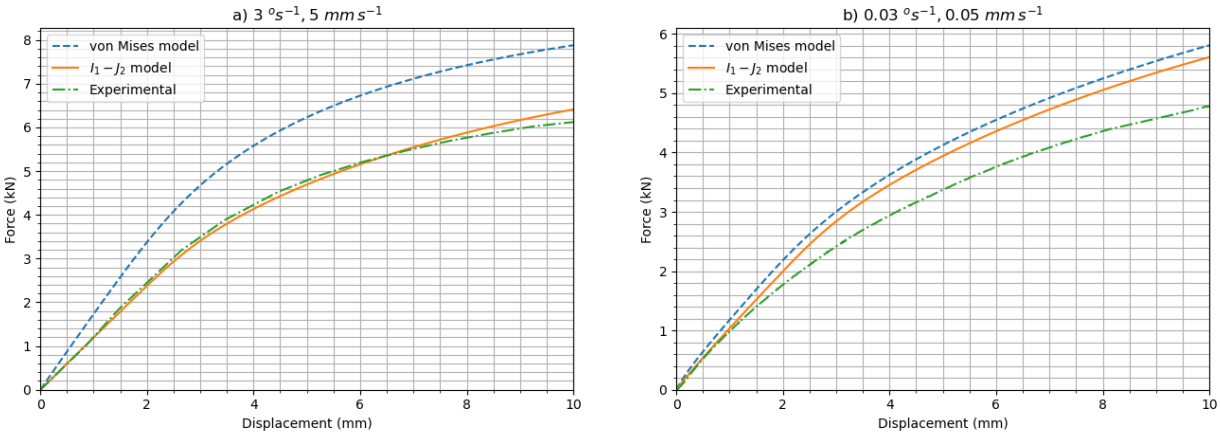

Figure 3.51: Force-displacement validation results for I_1-J_2-based model at RH50 under tension-torsion tests: a) $3\,^{\circ}\,\mathrm{s^{-1}}$ and $5\,\mathrm{mm\,s^{-1}}$, b) $0.03\,^{\circ}\,\mathrm{s^{-1}}$ and $0.05\,\mathrm{mm\,s^{-1}}$.

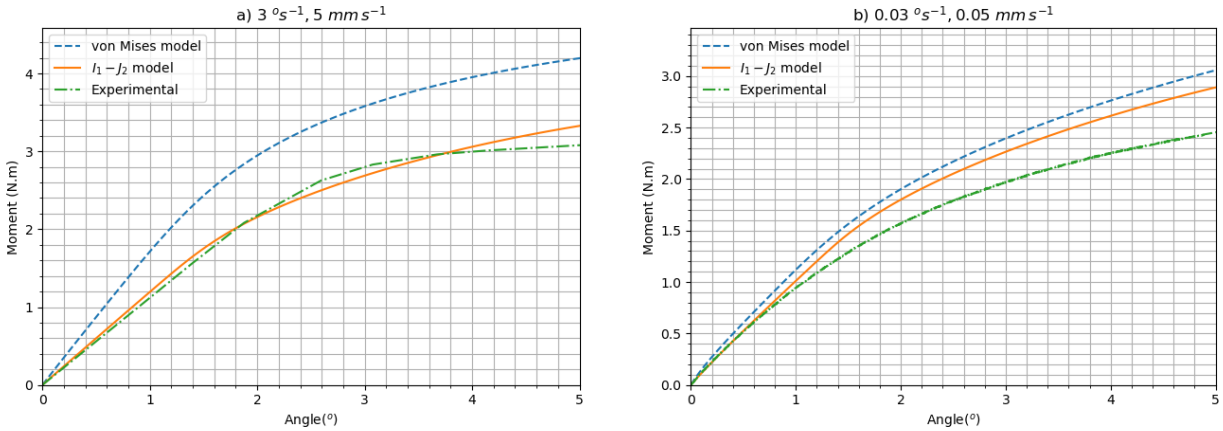

Figure 3.52: Torsion moment-rotation angle validation results for I_1-J_2-based model at RH50 under tension-torsion tests: a) $3\,^{\circ}\,\mathrm{s}^{-1}$ and $5\,\mathrm{mm\,s}^{-1}$, b) $0.03\,^{\circ}\,\mathrm{s}^{-1}$ and $0.05\,\mathrm{mm\,s}^{-1}$.

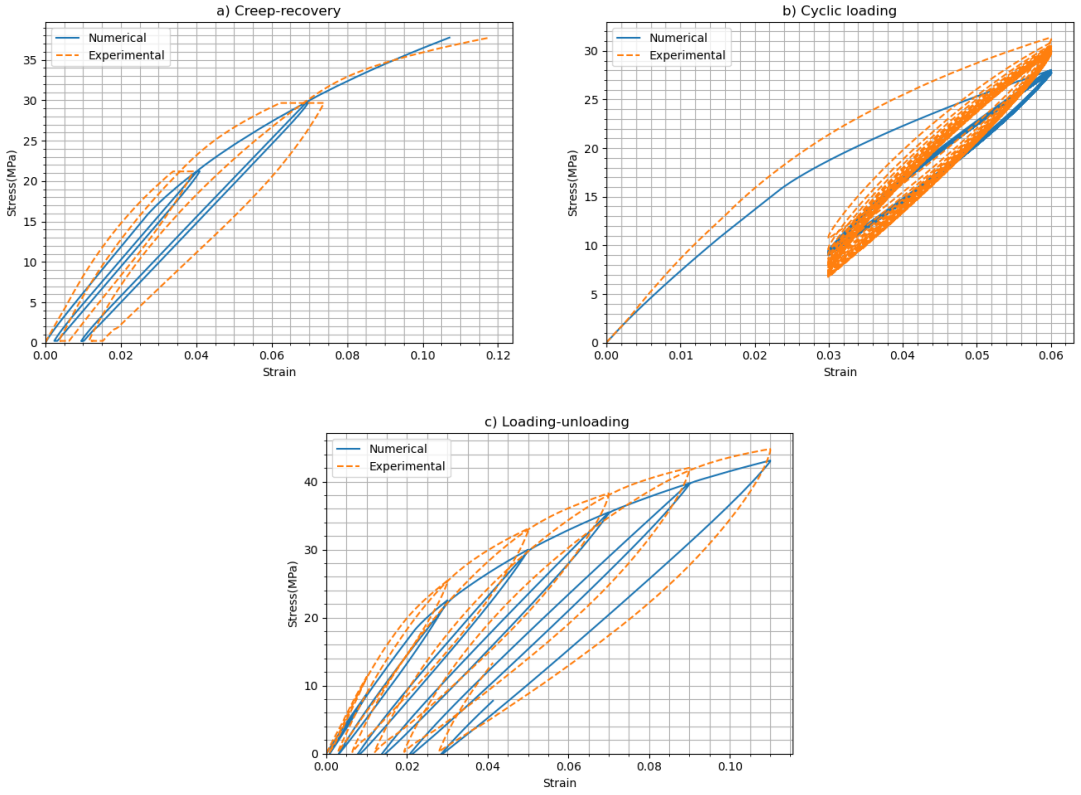

Figure 3.53: Validation results for I_1-J_2-based model at RH65: a) creep-recovery test with $0.1\,\mathrm{mm\,s}^{-1}$, b) cyclic loading with $0.1\,\mathrm{mm\,s}^{-1}$, c) loading-unloading with $0.05\,\mathrm{mm\,s}^{-1}$.

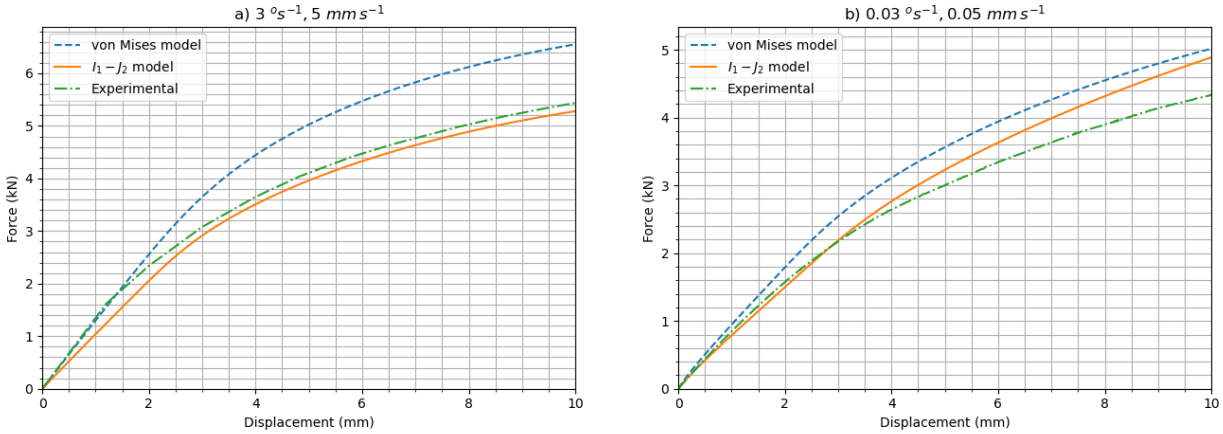

Figure 3.54: Force-displacement validation results for I_1-J_2-based model at RH65 under tension-torsion tests: a) $3\,^{\circ}\,\mathrm{s}^{-1}$ and $5\,\mathrm{mm\,s}^{-1}$, b) $0.03\,^{\circ}\,\mathrm{s}^{-1}$ and $0.05\,\mathrm{mm\,s}^{-1}$.

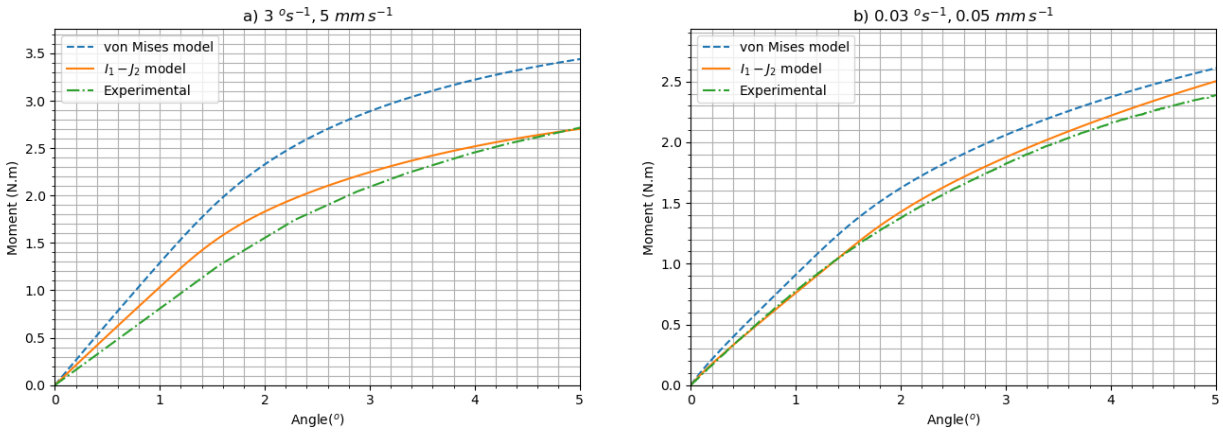

Figure 3.55: Torsion moment-rotation angle validation results for I_1-J_2-based model at RH65 under tension-torsion tests: a) $3\,^{\circ}\,\mathrm{s}^{-1}$ and $5\,\mathrm{mm\,s}^{-1}$, b) $0.03\,^{\circ}\,\mathrm{s}^{-1}$ and $0.05\,\mathrm{mm\,s}^{-1}$.

monotonic tension-torsion tests at different rates, and global force-displacement and moment-angle curves were extracted. The latter data, along with those obtained with dog bone samples, were used to identify the parameters of the VEVPD model based on the I_1-J_2 yield function, which also includes the asymmetry parameter, m. The calibration and validation results of the I_1-J_2-based model show that the latter model fits the tension-torsion test results better than the von Mises-based one. However, for higher RH, particularly RH80, the experimental results of diabolo and dog bone samples are not compatible leading to difficulties in I_1-J_2-based model calibration. This may be due to a non-uniform distribution of moisture on the diabolo and the complex geometry.

Chapter 4

Gradient enhanced nonlocal framework for thermoplastics

Contenu

4.1 Introduction

As discussed in previous chapters, predicting the behavior of glass-reinforced thermoplastics requires developing a proper multi-scale model capturing the nonlinear inelastic behaviors of the matrix and addressing the limitations of conventional models, namely pressure sensitivity, asymmetric yield behavior, and non-objective results in the computational model at high damage levels. By considering a new yield function I_1-J_2 in chapter 2, the effect of hydrostatic pressure and compression-tension asymmetry are captured. Furthermore, in chapter 3, identification of the model at different RH allows to study the effect of humidity on the model parameters and to predict the mechanical responses of thermoplastics at different water content levels. However, the local formulation framework is not yet capable of producing objective responses in computational models at highly damaged zones due to material softening.

Generally speaking, softening refers to the degradation of material strength by increasing in strain, which often occurs for polymers depending on RH and temperature. Mathematically speaking, this physical phenomenon leads to an ill-posed problem and consequently to numerical model instability and bifurcation in the computational models. In other words, finite element simulation models based on conventional local continuum frameworks exhibit non-physical and non-unique responses in the analysis of localized deformation models, and the corresponding shear band becomes increasingly more restricted by any mesh refinement.

In this chapter, the later model limitation in predicting the behavior of thermoplastics at high damage levels in the softening regime is discussed, for which a nonlocal framework is formulated, and its efficiency is explored compared to the conventional local continuum model. To this end, the constitutive model is formulated considering a gradient enhanced thermodynamic potential, function of local and nonlocal state variables. The model is formulated based on two different options for the nonlocal state variable: the first option considers nonlocal damage scalar, while the second considers nonlocal hardening state variable that drives the damage. An appropriate user-defined material subroutine is developed so as to define and to update the stress, the state variables, and the associated tangent moduli towards finite element structural computations. The analogy between the steady-state heat equation and the nonlocal gradient enhanced relation enables coupling the displacement and nonlocal fields within a finite element package code (i.e. ABAQUS). Structural analyses conducted on

polyamide 66 (PA66) material are presented to assess the efficiency of the developed nonlocal model. The capability of the model to capture efficiently the ductile damage localization and simulate the related fields is demonstrated when using the nonlocal hardening or damage state variable. This study for the first time combines viscoelasticity, viscoplasticity, and damage with nonlocal approaches, and can be considered as an initial step aiming at developing a constitutive formulation towards multi-scale analyses for polymer-based composites.

This chapter is organized as follows: in section 4.2, theoretical concepts including instability in local models due to the material softening and nonlocal approaches are presented. In section 4.3, the constitutive laws of the considered material are derived for both nonlocal damage and nonlocal hardening state variable. In section 4.4, the return mapping numerical approach as well as the nonlocal model implementation are established. In section 4.5, a parametric analysis is provided to explore the ductile damage development and mesh objectivity of the nonlocal model based on benchmark examples.

4.2 Theoretical background

4.2.1 Instability in local models due to softening

The instability of the model arises due to different kinds of factors, such as material type, geometrical and structural reasons, etc. In this work, considering the behavior of polyamide 66 as a semi-crystalline material, the strain softening at high damage level leads to the model instability and non-unique responses [50,62,135]. Mathematically speaking, the local conventional continuum model is stable until it reaches the bifurcation limit, which is defined through general bifurcation criterion [136]. The material is stable when it satisfies the inequality:

$$\dot{\epsilon}_{ij}\dot{\sigma}_{ij} > 0, \quad \text{or} \quad \dot{\epsilon}_{ij}\, C^{e}_{ijkl}\, \dot{\epsilon}_{kl} > 0, \tag{4.1}$$

where C^{e}_{ijkl} denotes the tensor of the corresponding tangent modulus. The above criterion, (4.1), requires a definite fourth order positive tangent modulus. Thus, the bifurcation limit can be expressed as:

$$\dot{\epsilon}_{ij}\, C^{e}_{ijkl}\, \dot{\epsilon}_{kl} = 0, \quad \text{or} \quad \det(\mathbb{C}^{e}) = 0. \tag{4.2}$$

Beyond the bifurcation limit, tangent modulus is not positive definite anymore, and it causes non-physical and meaningless results as zero dissipated energy and the non-unique responses in the FE

computational models. As a matter of fact, the tendency for releasing the least amount of inelastic stored energy during the failure leads to internal variables localization into narrowest areas [50, 51], which leads to non-objective solutions when refining the mesh in the computational models. To address this issue, the local model is often modified using the nonlocal framework as a form of "localization limiters", in which the length scale is included so as to derive objective responses [52, 53].

4.2.2 Nonlocal approaches

Different nonlocal approaches are reported in the open literature. Some authors apply the integral form in which the local variable is replaced by its nonlocal counterpart derived by a weighted average over the corresponding neighborhood [54–58]. In this manner, nonlocal variables depend not only on their local positions but also on their weighted average in the whole body (see Figure 4.1).

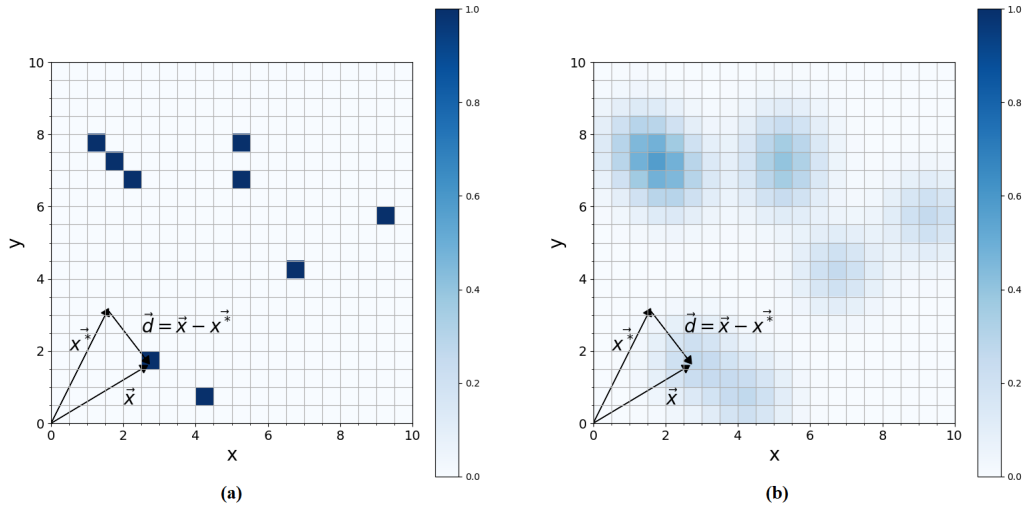

Figure 4.1: a) Schematic of the local model in a 2D spatial field; b) schematic of the nonlocal model using the integral form formulation.

The Taylor expansion of the integral nonlocal formulation yields to gradient enhanced forms that are more simple to implement into finite element codes compared to the integral one, and the interaction between local and nonlocal variables are defined through their gradients [58–62]. In addition, other methods based on phase field, micromorphic, and peridynamics approaches are also widely employed in the literature, for which more detailed information is available in [63–65, 69, 70, 137]. In reference to what is mentioned above, there are two types of nonlocal gradient models: explicit and implicit forms.

The first one is derived through the Taylor expansion of the nonlocal integral formulation [76, 138]. The second one is another simplification of the integral form, deduced from the explicit one, for which solutions are often in a good agreement with the classical integral type [60, 139, 140].

Regarding the choice of the nonlocal variable, many approaches in the open literature consider plastic deformation, equivalent strain, damage, etc. as nonlocal variables [54, 77, 141–143]. In this connection, Saanouni and Hamed presented a nonlocal micromorphic model based on various nonlocal variables and used the micromorphic damage variable to characterize the material behavior in the softening phase [63]. To ensure a proper connection between local and nonlocal variables, several options can be adopted. Indeed, the chosen local variable can be either enforced to behave as its nonlocal counterpart through Kuhn-Tucker conditions [140] or directly replaced by the nonlocal variable in the constitutive laws [144]. As an efficient alternative, one can propose a thermodynamically based extended framework, in which the free energy is enhanced with a nonlocal term including the nonlocal variable and its gradient [62, 72, 135, 145].

This work proposes a thermodynamically based nonlocal framework for semi-crystalline polyamides formulated under small deformation and rotation assumption. It performs a parametric study to investigate the capability of the gradient enhanced model in yielding mesh objective and physically meaningful solutions within the highly damaged zones under softening, which considers the nonlinear rheology of the material including all inelastic mechanisms (viz. viscoelasticity at different time scales, VE, viscoplasticity, VP, ductile damage, D, etc.). It also introduces the nonlocal hardening state variable to address the damage localization in a VEVPD model, where its efficiency is justified compared to the nonlocal damage. Since the framework is developed for polyamide materials, the goal is to adopt the model in multi-scale analyses. For fiber-reinforced composites, the deformation levels are usually small, thus it is reasonable to develop the present nonlocal framework using small deformations/rotations hypothesis.

4.3 Gradient enhanced constitutive modeling

The I_1-J_2 VEVPD model presented in the first chapter is used in this chapter in a similar way. However, since for the nonlocal model there are no experimental data yet, for more simplicity, here the asymmetry parameter, m, in the I_1-J_2 model is set to one which gives the classical von Mises function.

Although the material is considered symmetric, this does not affect the main objective, which is to address the instability and non-uniqueness in the computational model. In this section, first the corresponding extended thermodynamic framework is presented by introducing the nonlocal variable, φ^{nl} , and the constitutive laws are expressed with new additional nonlocal terms. Considering the dominant mechanisms, we determine the internal variable from which the nonlocal variable is derived.

4.3.1 Thermodynamically based Euler-Lagrange equations

The nonlocal variable, φ^{nl}, is derived from its local counterpart, φ, which is introduced into the thermodynamic framework by dividing the thermodynamic potential, Ψ, into two parts: local, Ψ^l, and nonlocal, Ψ^{nl} [62, 72]:

$$\Psi(\boldsymbol{\epsilon}, \{\chi_i\}_{i=2,N}, \varphi, \varphi^{nl}, \boldsymbol{\nabla_x}\varphi^{nl}) = \Psi^l(\boldsymbol{\epsilon}, \{\chi_i\}_{i=2,N}, \varphi) + \Psi^{nl}(\varphi, \varphi^{nl}, \boldsymbol{\nabla_x}\varphi^{nl}), \tag{4.3}$$

where $\boldsymbol{\epsilon}$ is the total strain tensor, and $\{\chi_i\}_{i=2,N}$ is the set of internal state variables which can be scalar or tensorial. Since, two different cases with distinct nonlocal variables are considered. The thermodynamical state of the polyamide is described by the following internal variables:

- two different options for the first two state variables are considered:

$$\varphi = \chi_1 = r, \quad D = \chi_2, \quad \text{or} \quad \varphi = \chi_1 = D, \quad r = \chi_2, \tag{4.4}$$

- the viscoplastic deformation, $\boldsymbol{\epsilon}^{vp} = \boldsymbol{\chi}_3$,

- considering N_v Kelvin-Voigt branches, the elementary viscoelastic strains are assigned as $\{\boldsymbol{\epsilon}^{vi}\}_{i=1,N_v} = \{\boldsymbol{\chi}_i\}_{i=4,N}$.

Similar to chapter 2, the local part of the thermodynamic potential, Ψ^l, is divided into the elastic part, Ψ^e, the set of viscoelastic potentials, $\{\Psi^{vi}\}_{i=1,N_v}$, and viscoplastic free energy, Ψ^{vp}:

$$\Psi^l(\boldsymbol{\epsilon}, \boldsymbol{\epsilon}^{vp}, \{\boldsymbol{\epsilon}^{vi}\}_{i=1,N_v}, r, D) = \Psi^e(\boldsymbol{\epsilon}, \boldsymbol{\epsilon}^{vp}, \{\boldsymbol{\epsilon}^{vi}\}_{i=1,N_v}, D) + \sum_{i=1}^{N_v} \Psi^{vi}(\boldsymbol{\epsilon}^{vi}, D) + \Psi^{vp}(r), \tag{4.5}$$

with

$$\Psi^e = \frac{1}{2}\left(\boldsymbol{\epsilon} - \sum_{i=1}^{N_v} \boldsymbol{\epsilon}^{vi} - \boldsymbol{\epsilon}^{vp}\right) : (1-D)\mathbb{C}^e : \left(\boldsymbol{\epsilon} - \sum_{i=1}^{N_v} \boldsymbol{\epsilon}^{vi} - \boldsymbol{\epsilon}^{vp}\right), \tag{4.6a}$$

$$\Psi^{vi} = \frac{1}{2}\boldsymbol{\epsilon}^{vi} : (1-D)\mathbb{C}^{vi} : \boldsymbol{\epsilon}^{vi}, \quad \text{for} \quad i = 1, N_v, \tag{4.6b}$$

$$\Psi^{vp} = \int_0^r R(\alpha) d\alpha. \tag{4.6c}$$

The nonlocal thermodynamic potential expressed as a function of the nonlocal variable, its spatial gradient, and its local counterpart is defined as [72]:

$$\Psi^{nl}(\varphi, \varphi^{nl}, \boldsymbol{\nabla}_{\boldsymbol{x}}\varphi^{nl}) = \frac{\xi^{nl}}{2}\left|\left|\boldsymbol{\nabla}_{\boldsymbol{x}}\varphi^{nl}\right|\right|^2 + \frac{1}{2}\gamma^{nl}(\varphi - \varphi^{nl})^2, \tag{4.7}$$

where the operator "||.||" denotes the second norm (quadratic), and ξ^{nl} and γ^{nl} are the nonlocal gradient and nonlocal interaction parameters respectively which are considered positive. The gradient parameter ξ^{nl} determines the degree of regularization governing the nonlocal part of the free energy and is derived from the internal length scale incorporating the microstructural effects into the model [62, 135, 145]. The nonlocal parameter γ^{nl} is assigned to ensure that i) the local variable behaves as closely as possible to its nonlocal counterpart, and ii) the performed analyses are mesh objective. The nonlocal parameters implicitly introduce the nonlocal length scale, l^{nl}, into the model, which is defined as:

$$l^{nl} = \sqrt{\frac{\xi^{nl}}{\gamma^{nl}}}. \tag{4.8}$$

Considering the above thermodynamic potential, the equilibrium equations are obtained using the minimum potential energy postulate. Accordingly, the total potential energy, Π, in a reference domain, $\mathcal{B}$, is the sum of external, $-\Pi_{ext}$, and internal, Π_{int}, potential energies:

$$\Pi = \Pi_{int} - \Pi_{ext} = \int_{\mathcal{B}} \Psi(\boldsymbol{\epsilon}, \{\chi_i\}_{i=2,N}, \varphi, \varphi^{nl}, \boldsymbol{\nabla}_{\boldsymbol{x}}\varphi^{nl}) \mathrm{d}V - \int_{\mathcal{B}} \boldsymbol{u} \cdot \boldsymbol{f}_b \mathrm{d}V - \int_{\partial\mathcal{B}} \boldsymbol{u} \cdot \boldsymbol{f}_s \mathrm{d}S, \tag{4.9}$$

where $\boldsymbol{f}_b$ and $\boldsymbol{f}_s$ are respectively the external force per unit volume and external force per unit surface, and $\boldsymbol{u}$ denotes the associated displacement field. The minimum potential energy postulate allows to write:

$$\{\boldsymbol{u}, \varphi^{nl}\} = \arg[\min_{\boldsymbol{u}, \varphi^{nl} \in \mathcal{B}}(\Pi)]. \tag{4.10}$$

Accordingly, the differential of the potential energy with respect to the displacement field, $\boldsymbol{u}$, and the nonlocal variable, φ^{nl}, is set to zero:

$$\delta_{\boldsymbol{u}}\Pi = \int_{\mathcal{B}} \frac{\partial \Psi}{\partial \boldsymbol{\epsilon}} : (\frac{\partial \boldsymbol{\epsilon}}{\partial \boldsymbol{u}}) \, \mathrm{d}V - \int_{\mathcal{B}} \boldsymbol{f}_b . \delta\boldsymbol{u} \mathrm{d}V - \int_{\partial\mathcal{B}} \boldsymbol{f}_s . \delta\boldsymbol{u} \, \mathrm{d}S = 0, \tag{4.11a}$$

$$\delta_{\varphi^{nl}}\Pi = \int_{\mathcal{B}} \left[\xi^{nl}\boldsymbol{\nabla_x}\varphi^{nl}.\boldsymbol{\nabla_x}\delta\varphi^{nl} - \gamma^{nl}(\varphi - \varphi^{nl})\delta\varphi^{nl}\right] \mathrm{d}V = 0. \tag{4.11b}$$

Based on the small deformations assumption, the strain tensor can be replaced by the symmetrical gradient of the displacement field $\boldsymbol{\nabla_x}^{\mathrm{sym}}\boldsymbol{u}$. Substituting it into (4.11a) and using the Gauss-Ostrogradski theorem results in:

$$-\int_{\mathcal{B}} (\boldsymbol{\nabla_x}\cdot\boldsymbol{\sigma})\cdot\delta\boldsymbol{u}\,\mathrm{d}V + \int_{\partial\mathcal{B}} (\boldsymbol{\sigma}\cdot\boldsymbol{n})\cdot\delta\boldsymbol{u}\,\mathrm{d}S - \int_{\mathcal{B}} \boldsymbol{f}_b\cdot\delta\boldsymbol{u}\,\mathrm{d}V - \int_{\partial\mathcal{B}} \boldsymbol{f}_s\cdot\delta\boldsymbol{u}\,\mathrm{d}S = 0. \tag{4.12}$$

Using Gauss-Ostrogradski theorem, (4.11b) is expanded as:

$$\int_{\partial\mathcal{B}} \xi^{nl}\boldsymbol{\nabla_x}\varphi^{nl}\delta\varphi^{nl}.\boldsymbol{n}\,\mathrm{d}S - \int_{\mathcal{B}} \xi^{nl}\boldsymbol{\nabla_x}^2\varphi^{nl}\delta\varphi^{nl}\,\mathrm{d}V - \int_{\mathcal{B}} \gamma^{nl}(\varphi - \varphi^{nl})\delta\varphi^{nl}\,\mathrm{d}V = 0. \tag{4.13}$$

From (4.12) and (4.13), the Euler-Lagrange equations with the associated boundary conditions are derived:

- stress equilibrium:

$$\boldsymbol{\nabla_x}\cdot\boldsymbol{\sigma} + \boldsymbol{f}_b = 0, \quad \forall\, x\in\mathcal{B}, \quad \boldsymbol{\sigma}\cdot\boldsymbol{n} - \boldsymbol{f}_s = \boldsymbol{0}, \quad \forall\, x\in\partial\mathcal{B}, \tag{4.14}$$

- nonlocal balance equation:

$$\xi^{nl}\boldsymbol{\nabla_x}^2\varphi^{nl} + \gamma^{nl}(\varphi - \varphi^{nl}) = 0, \quad \forall\boldsymbol{x}\in\mathcal{B}, \quad \boldsymbol{\nabla_x}\varphi^{nl}\cdot\boldsymbol{n} = 0 \quad \forall\boldsymbol{x}\in\partial\mathcal{B}. \tag{4.15}$$

4.3.2 State and evolution laws

The conjugate state variables, $\{A_i\}_{i=1,N}$, can be derived from the partial derivative of the thermodynamic potential with respect to the internal state variables, $\{\chi_i\}_{i=1,N}$, as follows (given in the 2):

$$A_i = \frac{\partial\Psi}{\partial\chi_i}, \quad \text{with}, \quad i = 1, ..., N. \tag{4.16}$$

Aside this, the partial derivatives of the nonlocal term, ψ^{nl}, lead to the following nonlocal conjugate state variables:

$$Y_{\varphi^{nl}} = \frac{\partial\Psi}{\partial\varphi^{nl}}, \quad \boldsymbol{Y}_{\boldsymbol{\nabla_x}\varphi^{nl}} = \frac{\partial\Psi}{\partial\boldsymbol{\nabla_x}\varphi^{nl}}. \tag{4.17}$$

Accordingly, using the rate form of the free energy, the intrinsic mechanical dissipation inequality is expressed by:

$$\mathcal{D} = P_m - \dot{\Psi} \geq 0, \tag{4.18}$$

where P_m is the sum of strain and nonlocal energy rates such that:

$$P_m = \boldsymbol{\sigma} : \dot{\boldsymbol{\epsilon}} + Y_{\varphi^{nl}} \dot{\varphi}^{nl} + \boldsymbol{Y}_{\boldsymbol{\nabla_x}\varphi^{nl}} \cdot \boldsymbol{\nabla_x} \dot{\varphi}^{nl}. \tag{4.19}$$

According to the state laws (given in the chapter 2) and substituting into (4.18), the dissipation is expanded to:

$$\mathcal{D} = \boldsymbol{\sigma} : \dot{\boldsymbol{\epsilon}} + Y_{\varphi^{nl}} \dot{\varphi}^{nl} + \boldsymbol{Y}_{\boldsymbol{\nabla_x}\varphi^{nl}} \cdot \boldsymbol{\nabla_x} \dot{\varphi}^{nl} - \left(\frac{\partial \Psi}{\partial \boldsymbol{\epsilon}} : \dot{\boldsymbol{\epsilon}} + \sum_{i=1}^{N} \frac{\partial \Psi}{\chi_i} : \dot{\chi}_i + Y_{\varphi^{nl}} \dot{\varphi}^{nl} + \boldsymbol{Y}_{\boldsymbol{\nabla_x}\varphi^{nl}} \cdot \boldsymbol{\nabla_x} \dot{\varphi}^{nl} \right). \tag{4.20}$$

From (4.20), the nonlocal terms can be canceled out, and the dissipation is expressed as:

$$\mathcal{D} = \sum_{i=1}^{N_v} \boldsymbol{\sigma}^{vi} : \dot{\boldsymbol{\epsilon}}^{vi} + \boldsymbol{\sigma} : \dot{\boldsymbol{\epsilon}}^{vp} - R\,\dot{r} + Y\,\dot{D} \geq 0, \quad \text{with} \quad -Y = \frac{\partial \Psi}{\partial D}. \tag{4.21}$$

According to the Generalized Standard Materials formalism, GSM, the evolution laws are derived through convex dual dissipation and indicative functions [106], which are expressed in detail in the chapter 2.

In order to capture the damage localization and to address the mesh sensitivity during FE computations, the nonlocal model is formulated based on two different nonlocal variable cases: the first considers the nonlocal damage, D^{nl}, as the nonlocal variable by enhancing the damage release energy, Y, while the second considers the nonlocal hardening state variable, r^{nl}, by modifying the hardening function, R. The constitutive laws related to both cases are derived in the following sections.

4.3.3 Case 1: nonlocal damage variable

Replacing φ^{nl} by D^{nl} in (4.7), the nonlocal free energy can be re-expressed as:

$$\Psi^{nl}(D, D^{nl}, \boldsymbol{\nabla_x} D^{nl}) = \frac{\xi^{nl}}{2} \left\| \boldsymbol{\nabla_x} D^{nl} \right\|^2 + \frac{1}{2} \gamma^{nl} (D - D^{nl})^2. \tag{4.22}$$

According to the state laws, the damage release energy, Y, can be decomposed as:

$$-Y = \frac{\partial \Psi}{\partial D} = -Y^l - Y^{nl}, \quad \text{with} \quad -Y^l = \frac{\partial \Psi^l}{\partial D} \quad \text{and} - Y^{nl} = \frac{\partial \Psi^{nl}}{\partial D}, \tag{4.23}$$

where the local part, Y^l, is obtained as:

$$Y^l = \frac{1}{2} \left(\boldsymbol{\epsilon} - \sum_{i=1}^{N_v} \boldsymbol{\epsilon}^{vi} - \boldsymbol{\epsilon}^{vp} \right) : \mathbb{C}^e : \left(\boldsymbol{\epsilon} - \sum_{i=1}^{N_v} \boldsymbol{\epsilon}^{vi} - \boldsymbol{\epsilon}^{vp} \right). \tag{4.24}$$

The nonlocal term, Y^{nl}, is given by:

$$Y^{nl} = -\gamma^{nl}(D - D^{nl}). \tag{4.25}$$

Y^{nl} is often a negative value added to the positive Y^{l} [62]. In certain instances, the total Y becomes negative and violates the positivity of the dissipation. This can be prevented through considering only the positive part of Y in the damage related indicative function, f_D, as follows:

$$f_D = \frac{S_D}{(\beta_D + 1)(1 - D)} \left(\frac{\langle Y \rangle_+}{S_D} \right)^{\beta_D + 1} \frac{\dot{\lambda}}{1 - D}. \tag{4.26}$$

Substituting (4.26) into the damage evolution law (given in chapter 2) yields:

$$\dot{D} = \frac{1 + \mathrm{sgn}(Y)}{2} \left(\frac{\langle Y \rangle_+}{S_D} \right)^{\beta_D} \frac{\dot{\lambda}}{1 - D}, \tag{4.27}$$

where "sgn(.)" and "$\langle\, . \,\rangle_+$" denote the sign function and Macaulay bracket, respectively.

4.3.4 Case 2: nonlocal hardening state variable

In the second case, the nonlocal hardening state variable, r^{nl}, can be adopted to limit the damage localization within the softening zones. Thus, substituting the nonlocal hardening state variable, r^{nl}, into the thermodynamic potential, Ψ, in (4.7) leads to:

$$\Psi^{nl}(r, r^{nl}, \boldsymbol{\nabla_x} r^{nl}) = \frac{\xi^{nl}}{2} \left|\left| \boldsymbol{\nabla_x} r^{nl} \right|\right|^2 + \frac{1}{2}\gamma^{nl}(r - r^{nl})^2. \tag{4.28}$$

It is worth mentioning that since the damage evolution is derived by the evolution of the hardening state variable, r, the nonlocal hardening state variable, r^{nl}, also affects the ductile damage implicitly. Substituting the above nonlocal energy (4.28) into (4.7), the hardening state function is enhanced with the nonlocal term, R^{nl}, as follows:

$$R(r) = \frac{\partial \Psi}{\partial r} = R^{l} + R^{nl}, \tag{4.29}$$

with:

$$R^{l} = H_m \, r^{H_p}, \quad R^{nl} = \frac{\partial \Psi^{nl}}{\partial r} = \gamma^{nl}(r - r^{nl}). \tag{4.30}$$

As indicated above, the constitutive laws are modified by introducing the nonlocal variables in two given cases and summarized in Table 4.1. Considering (4.29) and (4.30), if r^{nl} gets much larger than its local counterpart, r, then there is a possibility that the total hardening function becomes negative. However, as the next sections show, in all the analyses performed, this has not occurred.

Table 4.1: Modified associated variables in presence of the nonlocal variables along with the related evolution laws.

State variables	Associated variables	Evolution laws
Nonlocal damage, D^{nl}	$Y = Y^l + Y^{nl}$,	$\dot{D} = \frac{\partial F}{\partial Y}\dot{\lambda} = \left(\frac{Y}{S_D}\right)^{\beta_D} \frac{\dot{\lambda}}{1-D}$
	$Y^{nl} = -\gamma^{nl}(D - D^{nl})$	-
	$Y_{\varphi^{nl}} = \frac{\partial \Psi}{\partial D^{nl}} = \gamma^{nl}(D - D^{nl})$	-
	$\boldsymbol{Y}_{\boldsymbol{\nabla_x}\varphi^{nl}} = \frac{\partial \Psi}{\partial \boldsymbol{\nabla_x} D^{nl}} = \xi^{nl}\boldsymbol{\nabla_x} D^{nl}$	-
	$R = R^l$	$\dot{r} = \dot{\lambda}$
Nonlocal hardening state variable, r^{nl}	$Y = Y^l$	$\dot{D} = \frac{\partial F}{\partial Y}\dot{\lambda} = \left(\frac{Y}{S_D}\right)^{\beta_D} \frac{\dot{\lambda}}{1-D}$
	$Y_{\varphi^{nl}} = \frac{\partial \Psi}{\partial r^{nl}} = \gamma^{nl}(r - r^{nl})$	-
	$\boldsymbol{Y}_{\boldsymbol{\nabla_x}\varphi^{nl}} = \frac{\partial \Psi}{\partial \boldsymbol{\nabla_x} r^{nl}} = \xi^{nl}\boldsymbol{\nabla_x} r^{nl}$	-
	$R = R^l + R^{nl}$, $R^{nl} = \gamma^{nl}(r - r^{nl})$	$\dot{r} = \dot{\lambda}$

4.4 Numerical implementation

The nonlocal constitutive laws are implemented numerically through "convex cutting plane" return mapping algorithm, as presented in the chapter 2. However, gradient enhanced field development within the FE package code ABAQUS requires a nonlocal balance equation as well as the stress equilibrium. In order to impose the additional Euler-Lagrange equation into a commercial FE code like ABAQUS, two different ways are available: first, developing a user-defined element (UEL) [62,145], and second, using the analogy between nonlocal and steady state heat equations when the nonlocal variable is a scalar [135, 146].

4.4.1 Finite element implementation

Under this approach, the considered UMAT employs a UEL subroutine to form a proper system of equations in a linearized version. To do so, the equations are derived in their weak form and linearized using the corresponding shape functions and B-matrices. In the sequel, we consider an

isoparametric 2D element with four nodes (the geometry and displacement shape functions are equal) whose interpolation functions are introduced as:

$$\boldsymbol{u} = \sum_{i=1}^{n} N_u^i \boldsymbol{z}_u^i, \quad \boldsymbol{\epsilon} = \sum_{i=1}^{n} \boldsymbol{B}_u^i \boldsymbol{z}_u^i, \quad \varphi^{nl} = \sum_{i=1}^{n} N_\varphi^i z^i, \quad \boldsymbol{\nabla}_x \varphi^{nl} = \sum_{i=1}^{n} \boldsymbol{B}_\varphi^i z_\varphi^i, \tag{4.31}$$

and subsequently:

$$\delta\boldsymbol{u} = \sum_{i=1}^{n} N_u^i \delta\boldsymbol{z}_u^i, \quad \delta\boldsymbol{\epsilon} = \sum_{i=1}^{n} \boldsymbol{B}_u^i \delta\boldsymbol{z}_u^i, \quad \delta\varphi^{nl} = \sum_{i=1}^{n} N_\varphi^i \delta z_\varphi^i, \quad \boldsymbol{\nabla}_x \delta\varphi^{nl} = \sum_{i=1}^{n} \boldsymbol{B}_\varphi^i \delta z_\varphi^i, \tag{4.32}$$

where $\boldsymbol{z}_u^i$ (for $n = 4$: $i = 1, 2, 3, 4$) are the displacement nodal values; N_u^i (scalar) and B_u^i (vector) respectively denote shape functions and the B matrix. The iterative equations considering the nullity of residuals equilibrium are constituted as:

$$\begin{cases} \boldsymbol{r}_u + \delta\boldsymbol{r}_u = 0 \\ \boldsymbol{r}_\varphi + \delta\boldsymbol{r}_\varphi = 0 \end{cases}, \tag{4.33}$$

with

$$\begin{cases} \delta\boldsymbol{r}_u = K_{uu}\delta\boldsymbol{z}_u + K_{u\varphi}\delta\boldsymbol{z}_\varphi \\ \delta\boldsymbol{r}_u = K_{\varphi u}\delta\boldsymbol{z}_u + K_{\varphi\varphi}\delta\boldsymbol{z}_\varphi \end{cases}, \tag{4.34}$$

and

$$\begin{cases} \boldsymbol{r}_u = \{\boldsymbol{r}_u^1, \boldsymbol{r}_u^2, ..., \boldsymbol{r}_u^n\} \\ \boldsymbol{r}_\varphi = \{r_\varphi^1, r_\varphi^2, ..., r_\varphi^n\} \\ \boldsymbol{z}_u = \{\boldsymbol{z}_u^1, \boldsymbol{z}_u^2, ..., \boldsymbol{z}_u^n\} \\ \boldsymbol{z}_\varphi = \{z_\varphi^1, z_\varphi^2, ..., z_\varphi^n\} \end{cases}. \tag{4.35}$$

(4.33) is written as:

$$\begin{bmatrix} \boldsymbol{K}_{uu} & \boldsymbol{K}_{u\varphi} \\ \boldsymbol{K}_{\varphi u} & \boldsymbol{K}_{\varphi\varphi} \end{bmatrix} \begin{Bmatrix} \delta\boldsymbol{z}_u \\ \delta\boldsymbol{z}_\varphi \end{Bmatrix} = - \begin{Bmatrix} \boldsymbol{r}_u \\ r_\varphi \end{Bmatrix}, \tag{4.36}$$

where the tangent operators are derived as:

$$\boldsymbol{K}_{uu} = \frac{\partial \boldsymbol{r}_u}{\partial \boldsymbol{z}_u}, \quad \boldsymbol{K}_{u\varphi} = \frac{\partial \boldsymbol{r}_u}{\partial \boldsymbol{z}_\varphi}, \quad \boldsymbol{K}_{\varphi u} = \frac{\partial \boldsymbol{r}_\varphi}{\partial \boldsymbol{z}_u}, \quad \boldsymbol{K}_{\varphi\varphi} = \frac{\partial \boldsymbol{r}_\varphi}{\partial \boldsymbol{z}_\varphi}. \tag{4.37}$$

4.4.1.1 Stress equilibrium right hand side vector

As mentioned before, in the section 4.3.1, the strong form of stress equilibrium in the absence of surface traction, $\boldsymbol{f}_s$, is expressed as (4.14). Based on the minimum potential energy postulate, a minimization problem can be defined, as expressed in detail in section 4.3.1, and the weak form of the stress equilibrium is obtained as follows:

$$\int_{\mathcal{B}} \boldsymbol{\sigma} : \delta\boldsymbol{\epsilon} \mathrm{d}V + \int_{\mathcal{B}} \boldsymbol{f}_b \cdot \delta\boldsymbol{u} \, \mathrm{d}V = 0. \tag{4.38}$$

Substituting (4.32) into (4.38) yields:

$$\int_{\mathcal{B}} \boldsymbol{\sigma} : \sum_{i=1}^{n} \boldsymbol{B}_u^i \delta \boldsymbol{z}_u^i \mathrm{d}V + \int_{\mathcal{B}} \boldsymbol{f}_b \cdot \sum_{i=1}^{n} N_u^i \delta \boldsymbol{z}_u^i \mathrm{d}V = \boldsymbol{0}, \tag{4.39}$$

where can be reduced to nodal residuals as:

$$\boldsymbol{r}_u^i = \int_{\mathcal{B}} \left(\boldsymbol{B}_u^i\right)^T : \boldsymbol{\sigma} \mathrm{d}V + \int_{\mathcal{B}} \boldsymbol{f}_b N_u^i \mathrm{d}V. \tag{4.40}$$

One can consider the first and second terms respectively as the right hand side vector (RHS keyword in ABAQUS) and external forces.

4.4.1.2 Nonlocal equation right hand side vector

According to (4.18), the weak form of the nonlocal balance equation is expressed as:

$$\int_{\mathcal{B}} \left[\xi^{nl} \boldsymbol{\nabla}_x \varphi^{nl} . \boldsymbol{\nabla}_x \delta\varphi^{nl} - \gamma^{nl}(\varphi - \varphi^{nl})\delta\varphi^{nl}\right] \mathrm{d}V. \tag{4.41}$$

Substituting (4.32) into (4.41) yields:

$$\int_{\mathcal{B}} \left[\xi^{nl} \boldsymbol{\nabla}_x \varphi^{nl} . \sum_{i=1}^{n} \boldsymbol{B}_\varphi^i \delta z_\varphi^i - \gamma^{nl}(\varphi - \varphi^{nl}) \sum_{i=1}^{n} N_\varphi^i \delta z_\varphi^i\right] \mathrm{d}V = 0. \tag{4.42}$$

The nonlocal nodal residual is derived as:

$$r_\varphi^i = \int_{\mathcal{B}} \left[(\boldsymbol{B}_\varphi^i)^T . \xi^{nl} \boldsymbol{\nabla}_x \varphi^{nl} - \gamma^{nl}(\varphi - \varphi^{nl}) N_\varphi^i\right] \mathrm{d}V, \tag{4.43}$$

where yields the right hand side vector used in the UEL subroutine for the nonlocal equation.

4.4.2 Nonlocal and heat equations analogy

In this approach, the nonlocal fields are developed in a fully coupled temperature-displacement frame without developing a special UEL. Assuming the steady state heat equation, the following analogy is derived:

$$K_c \boldsymbol{\nabla_x}^2 \theta + h_g = 0 \quad \leftrightarrows \quad \xi^{nl} \boldsymbol{\nabla_x}^2 \varphi^{nl} + \gamma^{nl}(\varphi - \varphi^{nl}) = 0, \tag{4.44}$$

$$\boldsymbol{q} \cdot \boldsymbol{n} = 0 \quad \leftrightarrows \boldsymbol{\nabla_x} \varphi^{nl} \cdot \boldsymbol{n} = 0, \tag{4.45}$$

where K_c denotes the heat conduction, h_g is the heat sources, and $\boldsymbol{q}$ is the heat flux vector derived from the Fourier's law:

$$\boldsymbol{q} = -K_c \boldsymbol{\nabla}_{\boldsymbol{x}} \theta. \tag{4.46}$$

The thermomechanical tangent operators can be also defined within the UMAT subroutine (for ABAQUS versions after 2020) [147]. As another option, HETVAL as an auxiliary user subroutine is employed to allow definition of the heat flux, heat sources, and interaction between internal state variables and the thermal field. In the present study, the HETVAL subroutine is adopted by replacing the temperature and its associated fields with the nonlocal scalar variable and the analogous fields.

4.4.3 Tangent operators

The UMAT subroutine, within the nonlocal framework, not only requires the tangent stiffness tensor $\mathbb{T}^{\boldsymbol{\sigma}}_{\boldsymbol{\epsilon}}$, but also the associated nonlocal tangent operators. Thus, considering the stress equilibrium, the stress increment, $\Delta\boldsymbol{\sigma}$, is given by:

$$\Delta\boldsymbol{\sigma} = \mathbb{T}^{\boldsymbol{\sigma}}_{\boldsymbol{\epsilon}} : \Delta\boldsymbol{\epsilon} + \boldsymbol{T}^{\boldsymbol{\sigma}}_{\varphi^{nl}} \Delta\varphi^{nl}, \tag{4.47}$$

where $\mathbb{T}^{\boldsymbol{\sigma}}_{\boldsymbol{\epsilon}}$ denotes the nonlocal tangent modulus. The computation of the tangent stiffness tensor, $\mathbb{T}^{\boldsymbol{\sigma}}_{\boldsymbol{\epsilon}}$, is described in appendix A. In the nonlocal formulation, (4.15), the increment of $\gamma^{nl}(\varphi - \varphi^{nl})$ is expressed as follows:

$$\Delta\left[\gamma^{nl}(\varphi - \varphi^{nl})\right] = \boldsymbol{T}^{h}_{\epsilon} : \Delta\boldsymbol{\epsilon} + T^{h}_{\varphi^{nl}} \Delta\varphi^{nl}, \tag{4.48}$$

where $\boldsymbol{T}^{h}_{\boldsymbol{\epsilon}}$ and $T^{h}_{\varphi^{nl}}$ denote the nonlocal tangent operators. Technically speaking, HETVAL subroutine, among all nonlocal tangent operators indicated in (4.47) and (4.48), solely demands for $T^{h}_{\varphi^{nl}}$. Also, the same aspect can be considered for the UEL subroutine, and the other two tangent operators are automatically approximated. Thus, besides $\mathbb{T}^{\boldsymbol{\sigma}}_{\boldsymbol{\epsilon}}$, only the derivative of $\gamma^{nl}(\varphi - \varphi^{nl})$ with respect to the nonlocal variable is calculated as:

$$T^{h}_{\varphi^{nl}} = -\gamma^{nl}. \tag{4.49}$$

The return mapping algorithm including viscoelastic correction-prediction and its interactions with the solver and HETVAL or the corresponding UEL is summarized as a flowchart depicted in Figure 4.2.

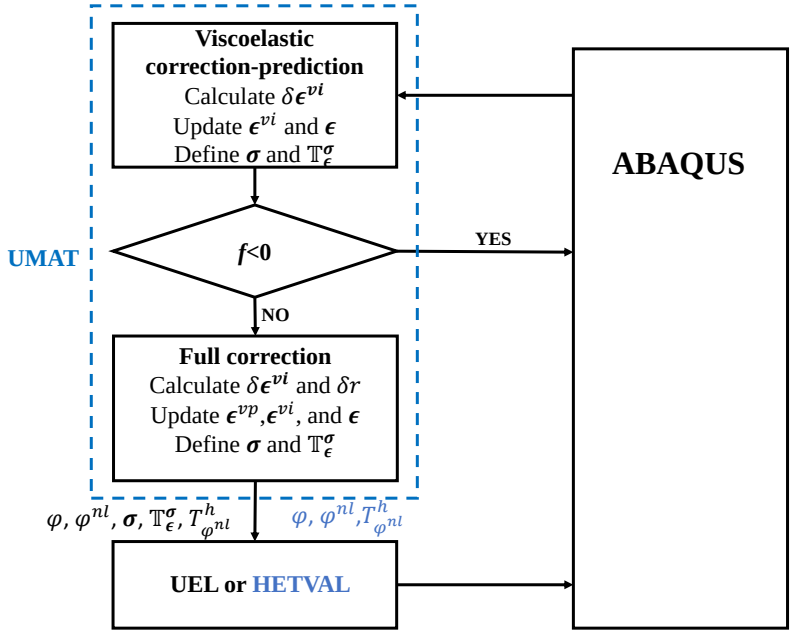

Figure 4.2: Flowchart of return mapping implementation on UMAT and its interaction with the FE solver and HETVAL or UEL subroutine.

4.5 Results and discussions

In this section, first, the given methodologies (UMAT-HETVAL and UEL-UMAT) for nonlocal framework implementation on the FE model is investigated, and then, the model is examined using a unilaterally notched rectangular plate and an asymmetrically double notched structure, whose dimensions are depicted in Figure 4.3. In all examples, the material properties are those of the polyamide 66, which have been earlier calibrated as a local VEVPD model (given in the first chapter). As already indicated, to perform a nonlocal analysis in a ductile damage model, the nonlocal variable may be derived from the damage variable, D, or from the hardening state variable, r. In this research, the first step consists of the nonlocal damage variable, D^{nl}. The first step is formulated to investigate the unilaterally notched plate under monotonic displacement controlled tensile loading, then its efficiency in controlling the damage localization is discussed. As the second step, the model derived from the nonlocal hardening state variable, r^{nl}, is applied on the structure considering the same loading conditions, and the results are compared with the latter case (related to D^{nl}). Moreover, the influences of the

nonlocal parameters, ξ^{nl} and γ^{nl}, on the damage localization are explored through a parametric study. As another numerical example, the asymmetrically double notched structure is used so as to examine the efficiency of the nonlocal model in a more complex geometry case. The nonlocal framework can be switched to the local model simply by setting the nonlocal parameters ξ^{nl} and γ^{nl}, to zero, which enables comparing the responses with those using the nonlocal model. Technically speaking, in highly nonlinear systems, the finite element solver often requires decreasing the time increments to achieve convergent solutions in the "unstable deformation zones". However, in some cases, as in the present study, instabilities in the form of material softening cause sudden changes in the stiffness tensor in the global equilibrium equation of the computational model. In such cases, the time steps become too small and the analysis never ends or converges. To address this issue, a viscous term is added to the global equilibrium that damps sudden changes in the stiffness tensor, as an artificial inertia. In this respect, the "automatic stabilization" in the finite element solver provides a viscous term with respect to the displacement in the global equilibrium equation, which is employed in the present work.

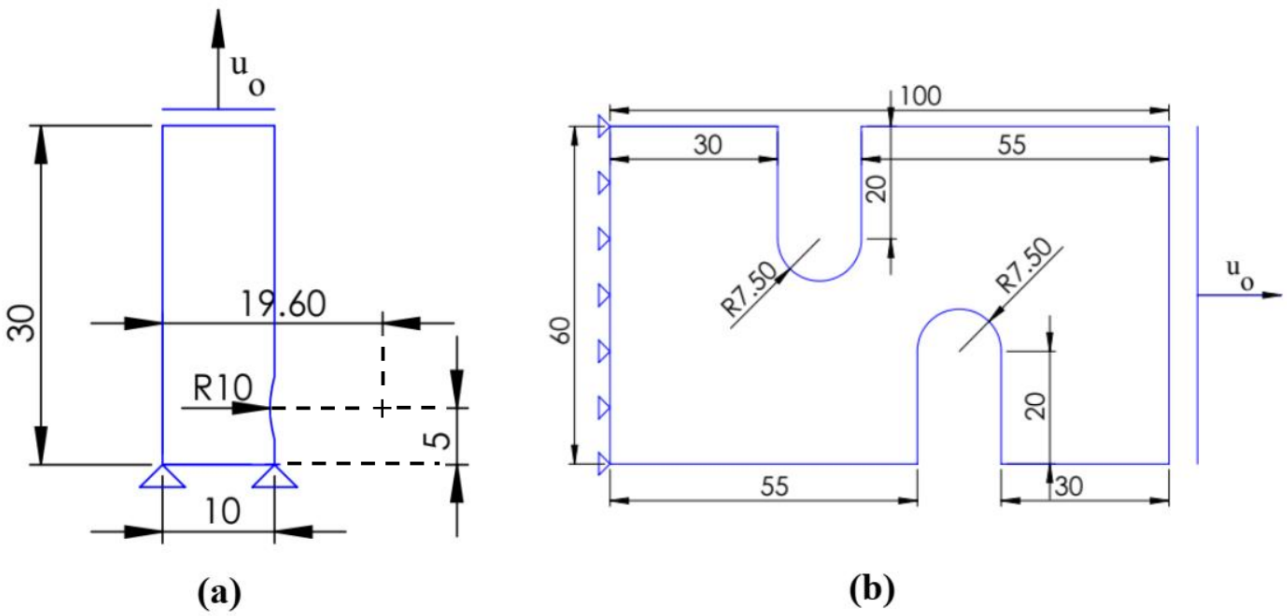

Figure 4.3: Dimensions of the considered structures and the given boundary conditions: a) unilaterally notched plate, b) asymmetrically double notched plate.

4.5.1 UMAT-HETVAL and UMAT-UEL methodologies: results and comparison

In this section, the presented nonlocal framework is implemented on the FE computational model using UEL-UMAT and UMAT-HETVAL which are expressed in the previous sections. To this end, the unilateral notched plate (Figure 4.3), under displacement-controlled monotonic tensile load ($\dot{u}_0 = 1.5\,\mathrm{mm\,s^{-1}}$), is considered, and the nonlocal framework is based on the nonlocal hardening state variable, r^{nl}. For more simplicity, the 2D four nodes plane strain element type (CPE4 for UMAT-UEL and CPE4T for UMAT-HETVAL) is employed. The results are plotted as force displacement curves and depicted in the Figure 4.4. As seen, the responses are strongly in agreement and approximately no difference is observable. With this in mind, UMAT-HETVAL and UEL-UMAT methodologies yield same responses, however, using HETVAL and thermo-mechanical analogy has some advantages as: less amount of programming, no visualization difficulties, being more computationally efficient. Hence, in this research, it is preferred that UMAT-HETVAL approach is used for the rest of examples.

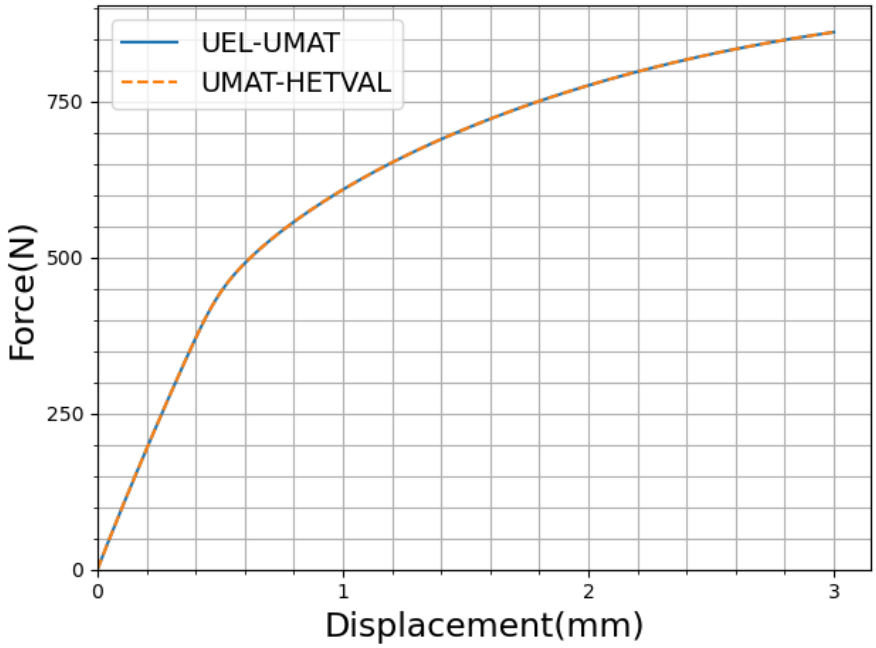

Figure 4.4: Comparison between UEL-HETVAL and UMAT-HETVAL approaches through force-displacement curves ($\xi^{nl} = 20\,\mathrm{kN}$, $\gamma^{nl} = 5\,\mathrm{GPa}$).

4.5.2 Efficiency evaluation of nonlocal models based on D^{nl} and r^{nl}

In this part, the unilaterally notched plate (Figure 4.3) is considered under tensile loading to evaluate the efficiency of the nonlocal model based on two presented cases: based on D^{nl} and r^{nl}. To this end, the damage analysis is initially performed using the 4 nodes plane strain fully coupled temperature displacement element type (CPE4T in Abaqus package) in different mesh sizes (300, 602, and 1200 elements). A reference point is set on the plate whose displacement is tied with the upper side allowing to plot the force vs. displacement responses. This aims at extracting more precise information regarding the hardening and softening mechanisms as well as the model behavior beyond the material instability limits. In terms of boundary conditions, the plate is subjected to a monotonic displacement-controlled tensile load with a rate of $\dot{u}_0 = 3\,\mathrm{mm}s^{-1}$ from one side, and the displacement components are set to zero at the other side (see Figure 4.3). As already indicated, firstly, the nonlocal analysis is performed based on D^{nl} and is compared with the local model results. The responses are extracted as the force-displacement curves in Figure 4.5 for the local and nonlocal models with different values of γ^{nl} when the structure is meshed by 1200 elements. As previously mentioned, γ^{nl} controls the interaction between D and D^{nl} via the nonlocal associated damage variable Y^{nl} (see Table 4.1). As observed, introducing nonlocal parameters in this case leads to faster failures compared to the local model. In other words, as the level of interaction with the nonlocal variable increases, the model becomes more unstable and fails earlier.

From the same analysis, force-displacement curves are plotted for several levels of ξ^{nl} at a constant value of γ^{nl} in Figure 4.6. As seen, variation of ξ^{nl} almost has no influence on the material responses because γ^{nl} is not sufficiently large to make a strong interaction between D and D^{nl}, and on the other hand, for the reasons mentioned above, introducing the nonlocal parameters makes the model more unstable than the local framework, and higher values of γ^{nl} are not feasible because the model fails too early.

Figure 4.7 provides the damage distribution resulted from the nonlocal damage model in three given mesh sizes, in which the damage, as expected, is localized into the crack zone restricted to a single row of elements as the smallest possible area. Since the damage is coupled with plasticity, and the damage rate is directly related to the hardening state variable rate, $\dot{r}$, based on the given evolution laws, the damage localization may stem from the localization of r. Concerning this, the

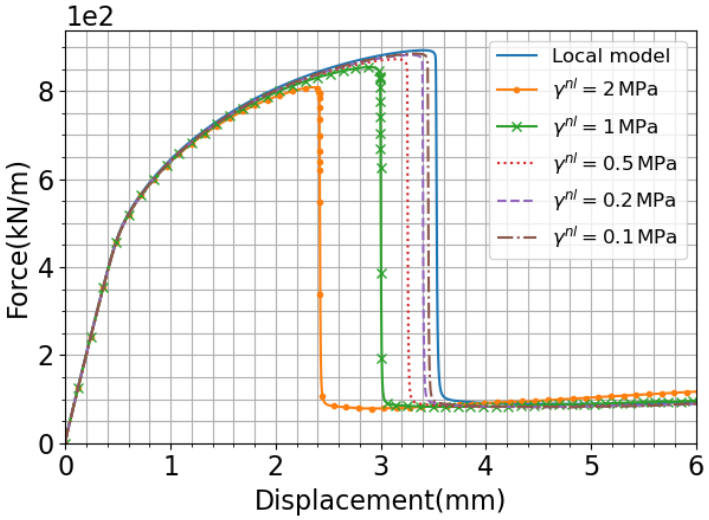

Figure 4.5: Force-displacement curves for the unilaterally notched plate and comparison between local and nonlocal damage models responses for different values of γ^{nl} when $\xi^{nl} = 2\,\mathrm{kN}$ under uniaxial monotonic tensile loading with the displacement rate $\dot{u}_0 = 3\,\mathrm{mm\,s^{-1}}$; the nonlocal model is based on D^{nl}.

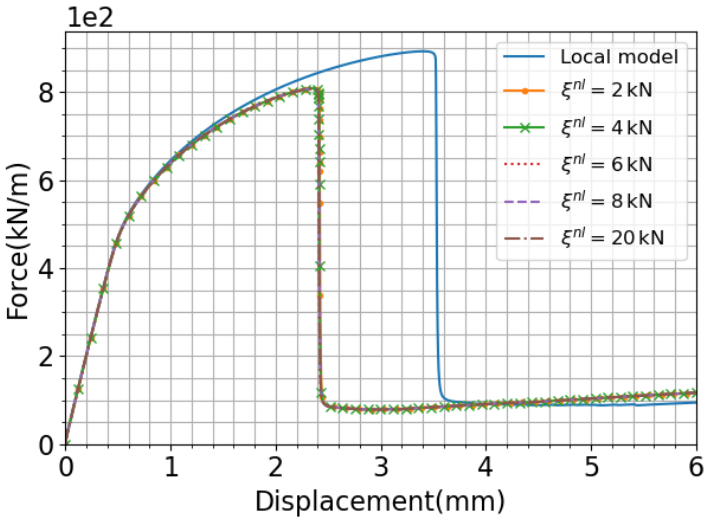

Figure 4.6: Force-displacement curves for the unilaterally notched plate and comparison between local and nonlocal models responses for different values of ξ^{nl} when $\gamma^{nl} = 2\,\mathrm{MPa}$ under uniaxial monotonic tensile loading with the displacement rate $\dot{u}_0 = 3\,\mathrm{mm\,s^{-1}}$; the nonlocal model is based on D^{nl}.

distribution of r, for the nonlocal damage model ($\xi^{nl} = 2\,\text{kN}$, $\gamma^{nl} = 2\,\text{MPa}$), is extracted and depicted as Figure 4.8. As shown, the hardening state variable is localized into the crack and exhibits mesh sensitivity by refining the mesh, which consequently leads to damage localization. Regarding this, it can be concluded that the nonlocal variable deriving from r may properly address the damage mesh sensitivity in the FE computations, which is discussed as follows.

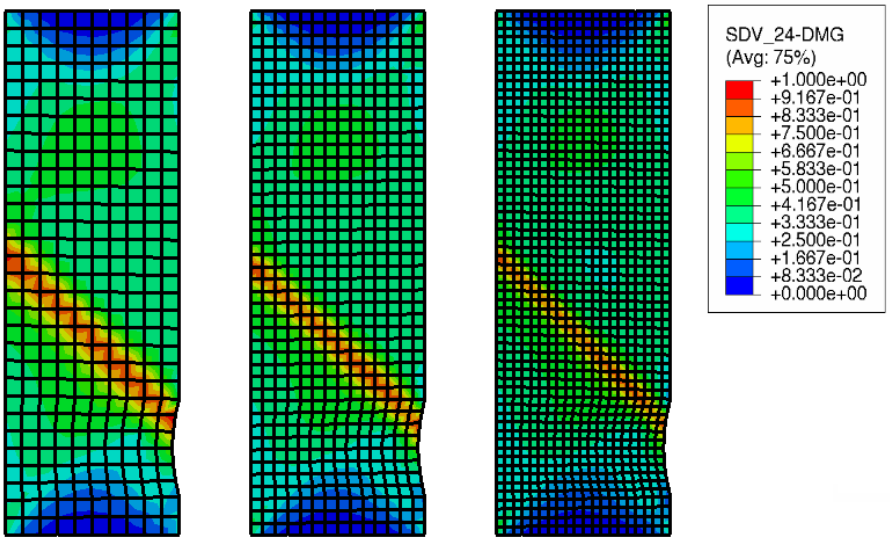

Figure 4.7: Damage distribution of the unilaterally notched plate using the nonlocal damage model ($\xi^{nl} = 2\,\text{kN}$, $\gamma^{nl} = 2\,\text{MPa}$) under uniaxial monotonic tensile loading with the displacement rate $\dot{u}_0 = 3\,\text{mm}\,\text{s}^{-1}$ (three mesh refinements, $N_E = \{300;\ 602 \text{ or } 1200\}$); the nonlocal model is based on D^{nl}.

As the second option, the nonlocal variable is derived from r, and the nonlocal free energy dictates the nonlocal term R^{nl} into the hardening function, R, as indicated in (4.28) and (4.29). The model is implemented on the considered geometry under same loading and boundary conditions, with the first option. To observe the interaction between local and nonlocal variables (r and r^{nl}), the unilaterally notched structure under tensile load with $\dot{u}_0 = 3\,\text{mm}\,\text{s}^{-1}$ is analyzed, then considering the localization time in the local model, the 2D maps of the hardening state variable using the local and nonlocal models (based on r^{nl}) are compared with the distribution of the nonlocal variable in the same time increment (Figure 4.9). As seen, r is localized in the local model (Figure 4.9-a) while r and r^{nl} on the nonlocal model show no localization or shear band at this stage (Figure 4.9-b,c). The responses are also exported with respect to γ^{nl} as force-displacement curves in Figure 4.10. As observed, the softening zone in the nonlocal responses is more extended compared to those predicted by the local

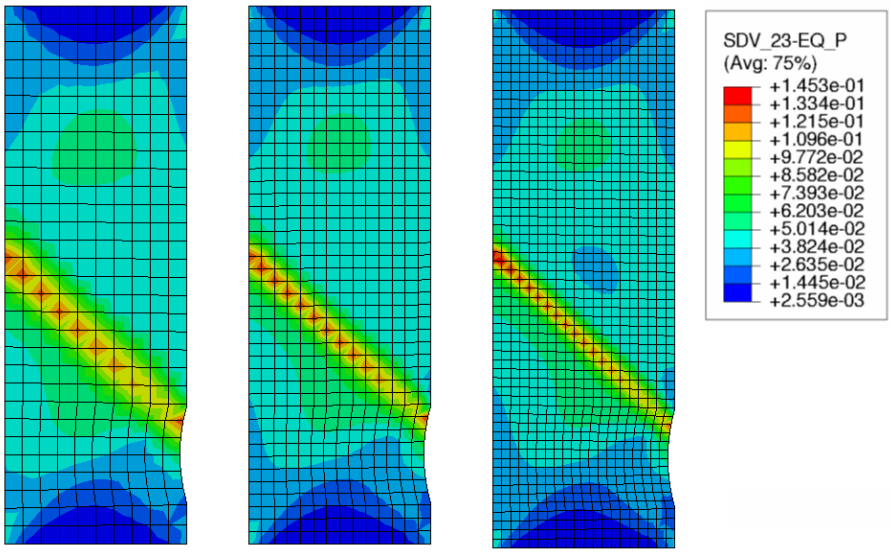

Figure 4.8: Distribution of the hardening state variable, r, in the unilaterally notched plate using the nonlocal damage model ($\xi^{nl} = 2\,\text{kN}$, $\gamma^{nl} = 2\,\text{MPa}$) under uniaxial monotonic tensile loading with the displacement rate $\dot{u}_0 = 3\,\text{mm}\,\text{s}^{-1}$ (three mesh refinements, $N_E = \{300;\ 602 \text{ or } 1200\}$); the nonlocal model is based on D^{nl}.

model and subsequently they drop more smoothly. However, after a certain level of the γ^{nl}, its increase does not yield a significant variation in responses nor in the failure points.

The damage distribution contours show a clearer view of the influence of γ^{nl} on the damage profile (Figure 4.11). As shown, the bigger the value of γ^{nl} is, the wider damaged area evolves surrounding the crack zone. The model is also examined for different ξ^{nl} in a constant level of interaction ($\gamma^{nl} = 5\,\text{GPa}$) and is depicted in Figure 4.12. The mesh sensitivity is decreased by an increase in ξ^{nl}, and the softening zone becomes smoother, which leads to failure in higher deformation levels. The aforementioned notion is confirmed with the damage distribution contours in three different mesh sizes $N_E = \{300;\ 602 \text{ or } 1200\}$ for several values of ξ^{nl} (see Figure 4.13). In the local model contour, as seen also earlier, the damage is localized into a single row of elements and shows mesh sensitivity by changing the mesh size. This issue is addressed by introducing the nonlocal parameters into the model. The damage in the vicinity of the crack is progressively evolved by an increase in ξ^{nl}, and the damage profile remains identical for different mesh sizes in the higher level of γ^{nl}.

In order to investigate how the nonlocal model affects and governs the damage development within the structure prior and after the force peak, three spots are taken into consideration: I) the first spot at 90% of the peak prior to it, II) the second spot at the peak, and III) the third one at its 80%

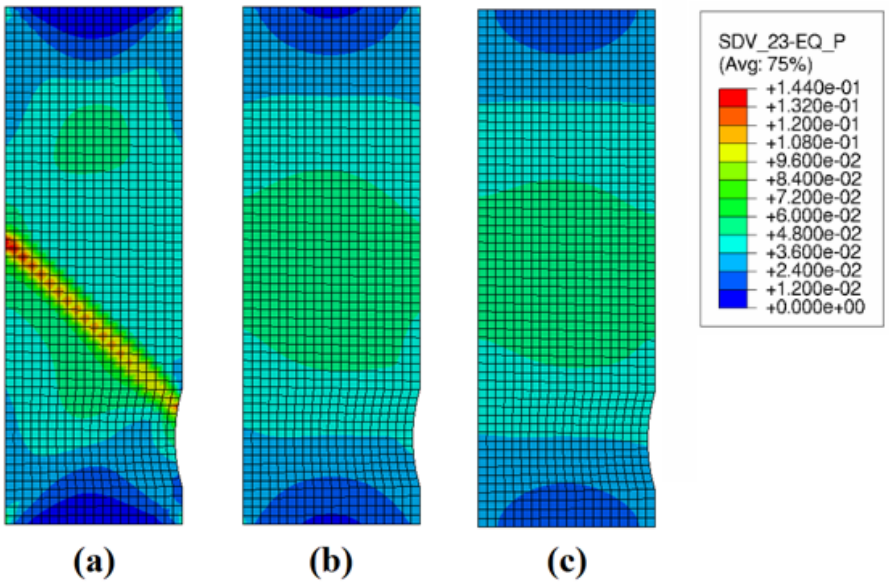

Figure 4.9: Local and nonlocal variables 2D maps under monotonic tensile loading: a) hardening state variable distribution using the local model, b) hardening state variable distribution using the nonlocal model when $\gamma^{nl} = 5\,\text{GPa}$ and $\xi^{nl} = 6\,\text{kN}$, and c) nonlocal variable using the nonlocal model when $\gamma^{nl} = 5\,\text{GPa}$ and $\xi^{nl} = 6\,\text{kN}$; the nonlocal model is based on r^{nl}.

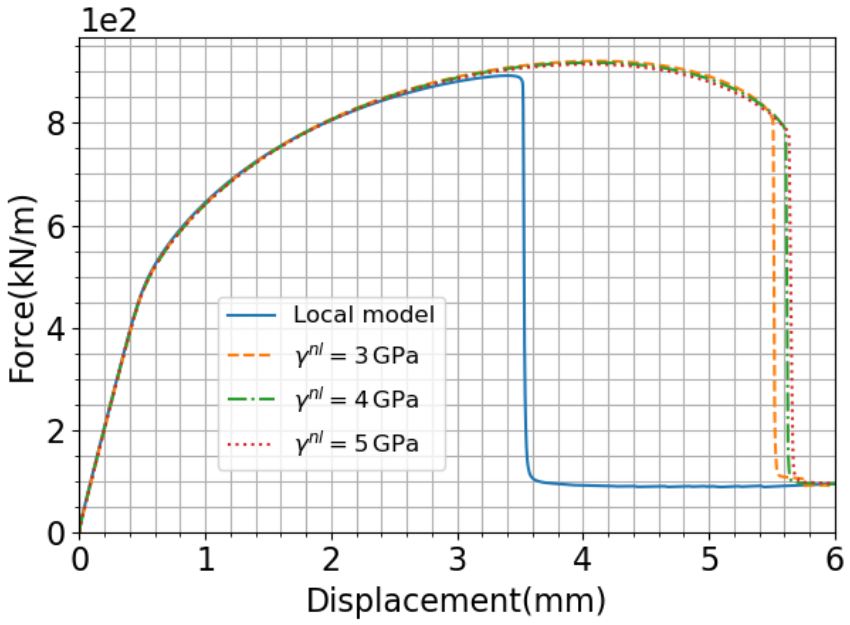

Figure 4.10: Force-displacement curves for the unilaterally notched plate and comparison between local and nonlocal models responses for different values of γ^{nl} when $N_E = 1200$, $\xi^{nl} = 6\,\text{kN}$, and $\dot{u}_0 = 3\,\text{mm}\,\text{s}^{-1}$; the nonlocal model is based on r^{nl}.

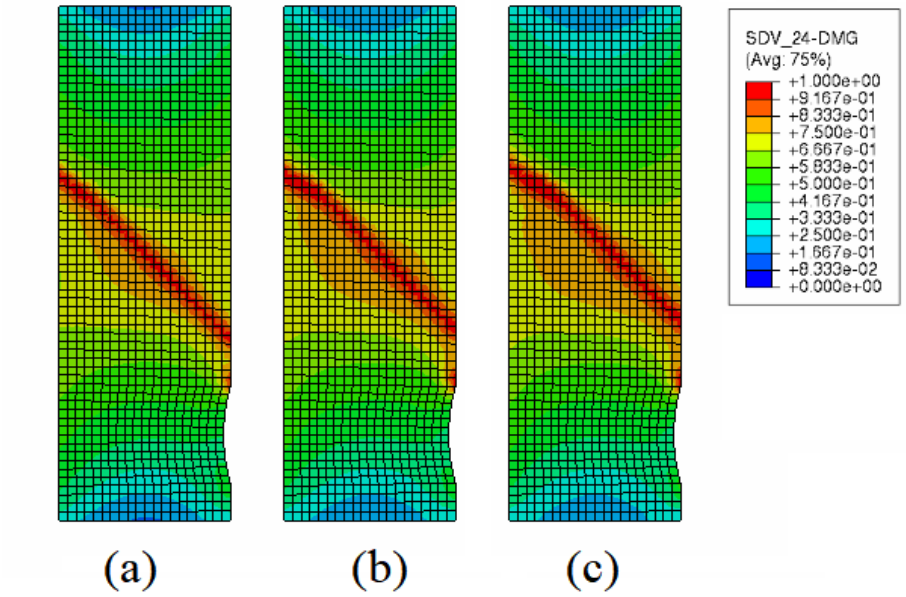

Figure 4.11: Damage distribution in the unilaterally notched plate under tensile loading ($\dot{u}_0 = 3\,\mathrm{mm\,s^{-1}}$) with 1200 elements using: a) nonlocal model when $\xi^{nl} = 6\,\mathrm{kN}$ and $\gamma^{nl} = 3\,\mathrm{GPa}$, b) nonlocal model when $\xi^{nl} = 6\,\mathrm{kN}$ and $\gamma^{nl} = 4\,\mathrm{GPa}$, and c) nonlocal model when $\xi^{nl} = 6\,\mathrm{kN}$ and $\gamma^{nl} = 5\,\mathrm{GPa}$; the nonlocal model is based on r^{nl}.

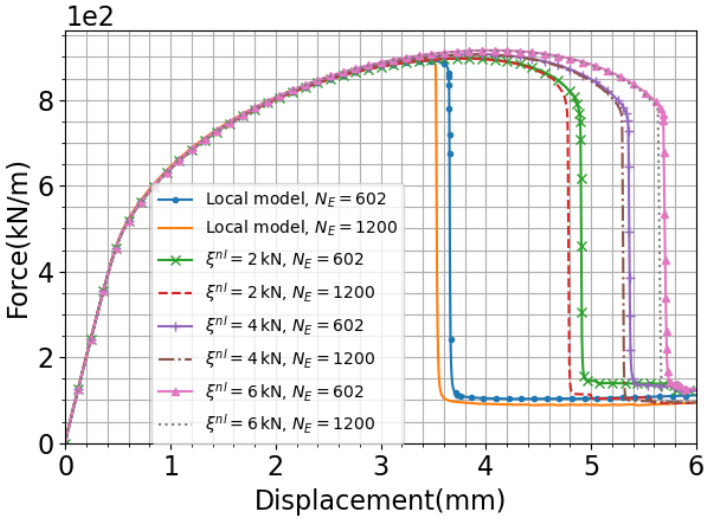

Figure 4.12: Force-displacement curves for unilaterally notched plate and comparison between local and nonlocal models responses for different values of ξ^{nl} when $N_E = \{602, 1200\}$, $\gamma^{nl} = 5\,\mathrm{GPa}$, and $\dot{u}_0 = 3\,\mathrm{mm\,s^{-1}}$. By increasing the value of ξ^{nl}, the analysis converges better for different mesh sizes; the nonlocal model is based on r^{nl}.

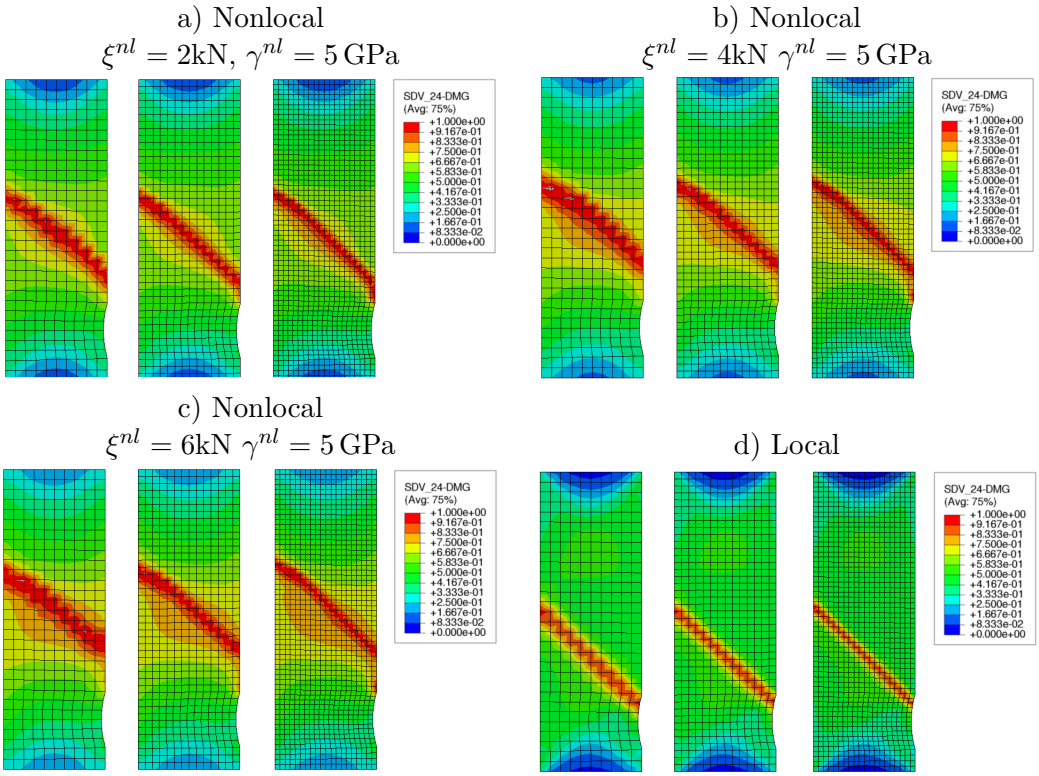

Figure 4.13: Damage distribution in the unilaterally notched plate meshed by 300, 602, and 1200 elements using nonlocal model with $\gamma^{nl} = 5$ GPa and a) $\xi^{nl} = 2$ kN, b) $\xi^{nl} = 4$ kN, c) $\xi^{nl} = 6$ kN, and comparison with d) local model; the nonlocal model is based on r^{nl}.

after the peak, at which the damage distributions are compared for the local and nonlocal models and illustrated in the Figure 4.14 and Figure 4.15. As observed, as the material approaches the instability region, the discrepancies in damage distributions between the local and nonlocal models become more pronounced, particularly after the force peak.

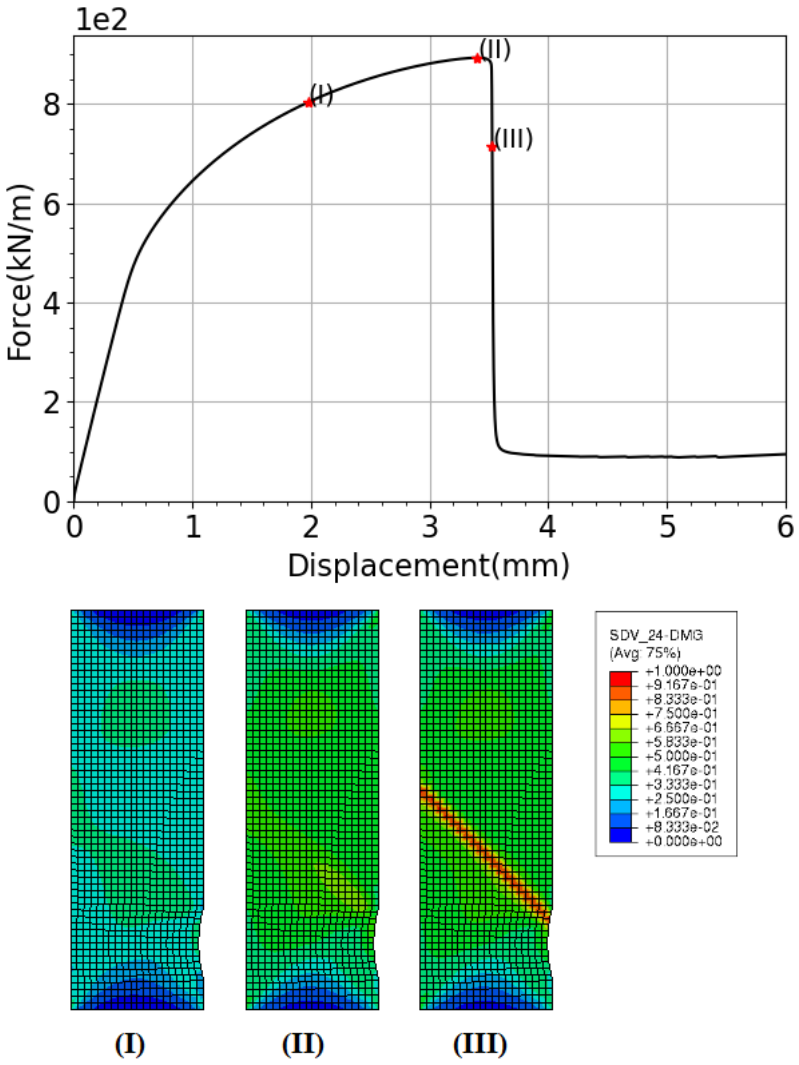

Figure 4.14: Damage distribution using the local model: I) before the maximum force and at 90 percent of the peak, II) at the maximum force, III) after the maximum force and at 80 percent of the peak.

As the material is defined through the VEVPD rheological model, the change in the loading rate necessarily affects the material behavior and the related damage distribution. Following this, the structure is subjected to different loading rates and the force-displacement curves are explored for

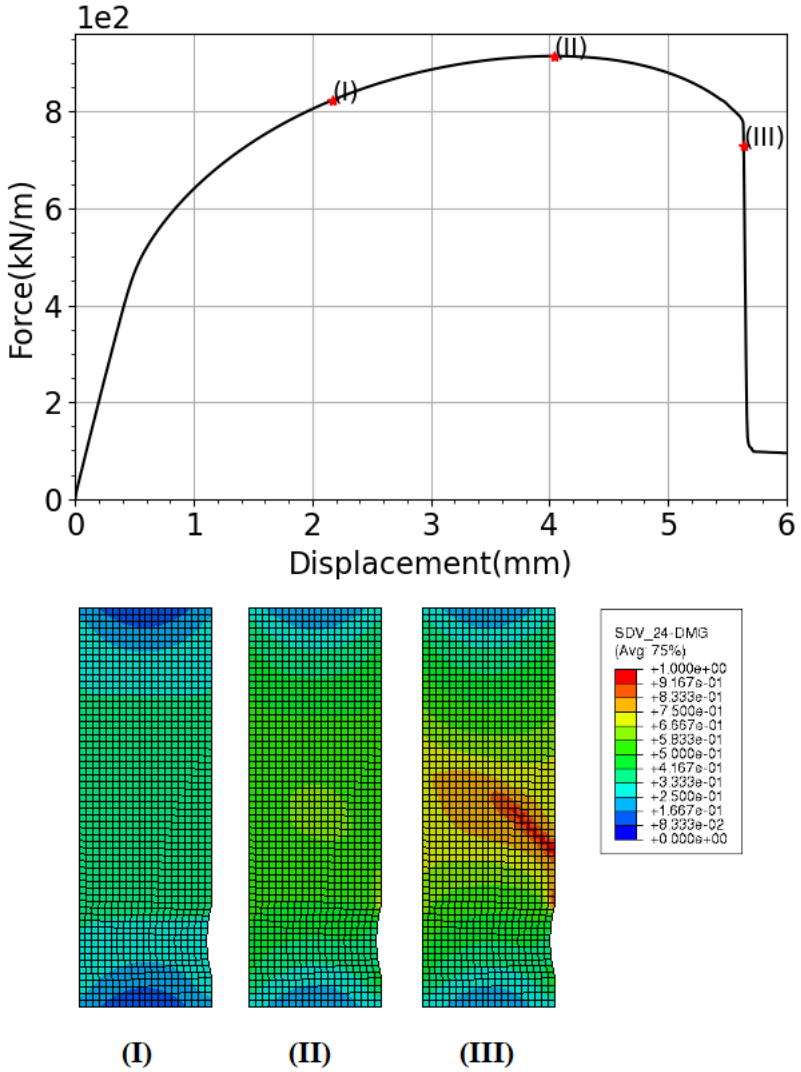

Figure 4.15: Damage distribution using the nonlocal model with $\xi^{nl} = 6\,\text{kN}$ and $\gamma^{nl} = 5\,\text{GPa}$: I) before the maximum force and at 90 percent of the peak, II) at the maximum force, III) after the maximum force and at 80 percent of the peak; the nonlocal model is based on r^{nl}.

local and nonlocal models in the Figure 4.16 and Figure 4.17. As observed, the curves obtained from the local case are mostly affected by the loading rate in the hardening zone, and their failure point is slightly shifted forward by an increase in the rate (see Figure 4.16). However, the rate effect is more significant in the nonlocal model, particularly at the failure points, where the higher rate yields sharper softening regions and subsequent earlier failures (see Figure 4.17). The damage distribution is extracted for $\dot{u}_0 = 2,5\text{mm}\,s^{-1}$ and presented in the Figure 4.18. As seen, for the local model, no difference is observable under given loading rates. However, in the nonlocal model, the damaged region surrounding the crack is slightly reduced and localized toward the crack by an increase in the displacement rate.

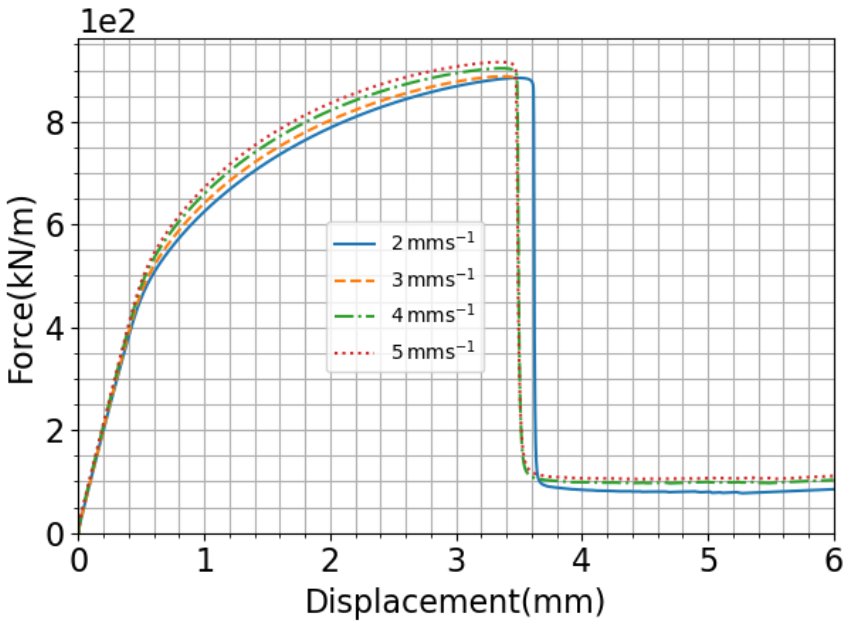

Figure 4.16: Force-displacement curves obtained from the local model for unilaterally notched plate under different loading rates.

In order to capture the effects of transverse deformation in the thickness direction, the unilaterally notched structure is studied in a 3D setup considering a thickness of 1 mm. The structure is meshed using the 8 nodes thermally coupled brick element type (C3D8T). In terms of the boundary conditions, all displacement components are bounded at the bottom, and a monotonic tensile load ($\dot{u}_0 = 3\,\text{mm}s^{-1}$) is set to the top. The damage analysis results are extracted as contours and depicted in Figure 4.19. As observed, the crack inclination is decreased compared to the plane strain case, which it is reduced

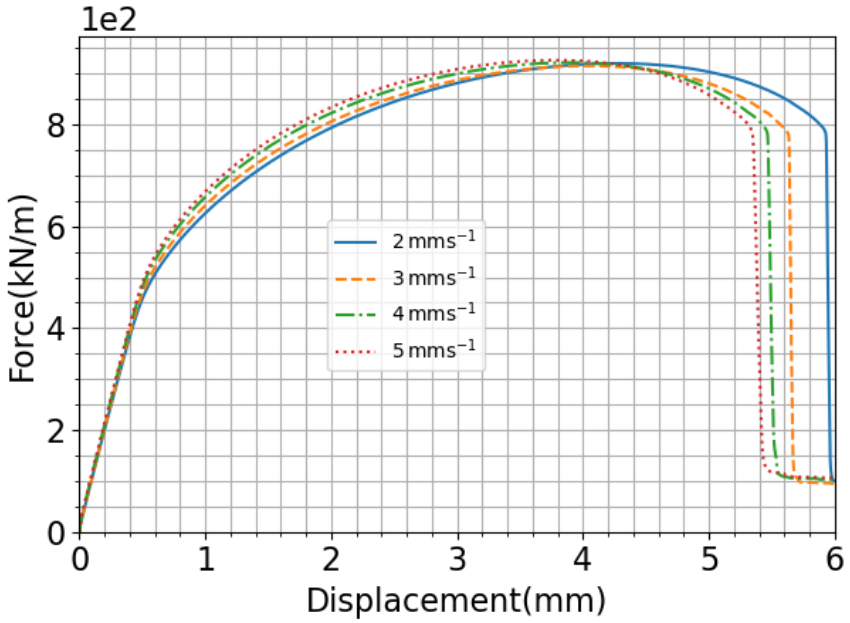

Figure 4.17: Force-displacement curves obtained from the nonlocal model (with $\xi^{nl} = 6\,\text{kN}$ and $\gamma^{nl} = 5\,\text{GPa}$) for the unilaterally notched plate under different loading rates; the nonlocal model is based on r^{nl}.

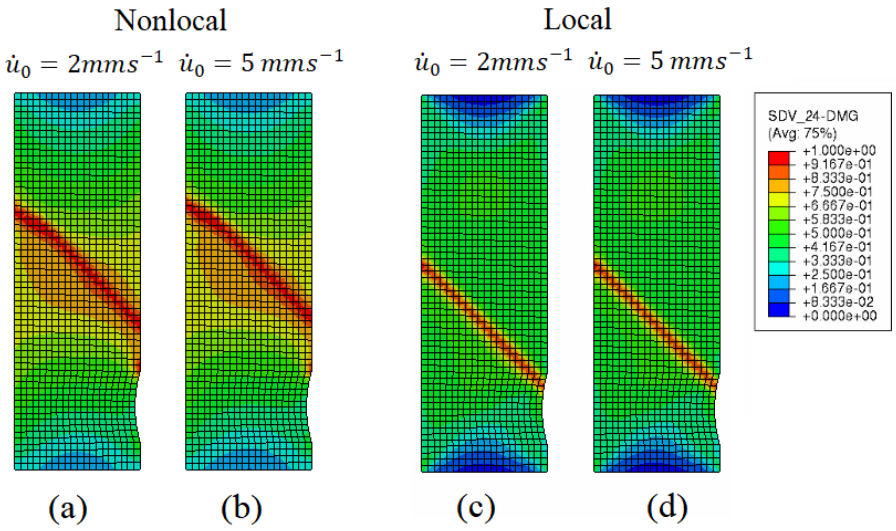

Figure 4.18: Damage distribution in the unilaterally notched plate with 1200 elements using nonlocal model when $\xi^{nl} = 6\,\text{kN}$ and $\gamma^{nl} = 5\,\text{GPa}$ under the displacement rates: a) $\dot{u}_0 = 2\,\text{mm}\,\text{s}^{-1}$, b) $\dot{u}_0 = 5\,\text{mm}\,\text{s}^{-1}$ and using the local model under displacement rates: c) $\dot{u}_0 = 2\,\text{mm}\,\text{s}^{-1}$, d) $\dot{u}_0 = 5\,\text{mm}\,\text{s}^{-1}$; the nonlocal model is based on r^{nl}.

more drastically for the nonlocal model (see Figure 4.19-a).

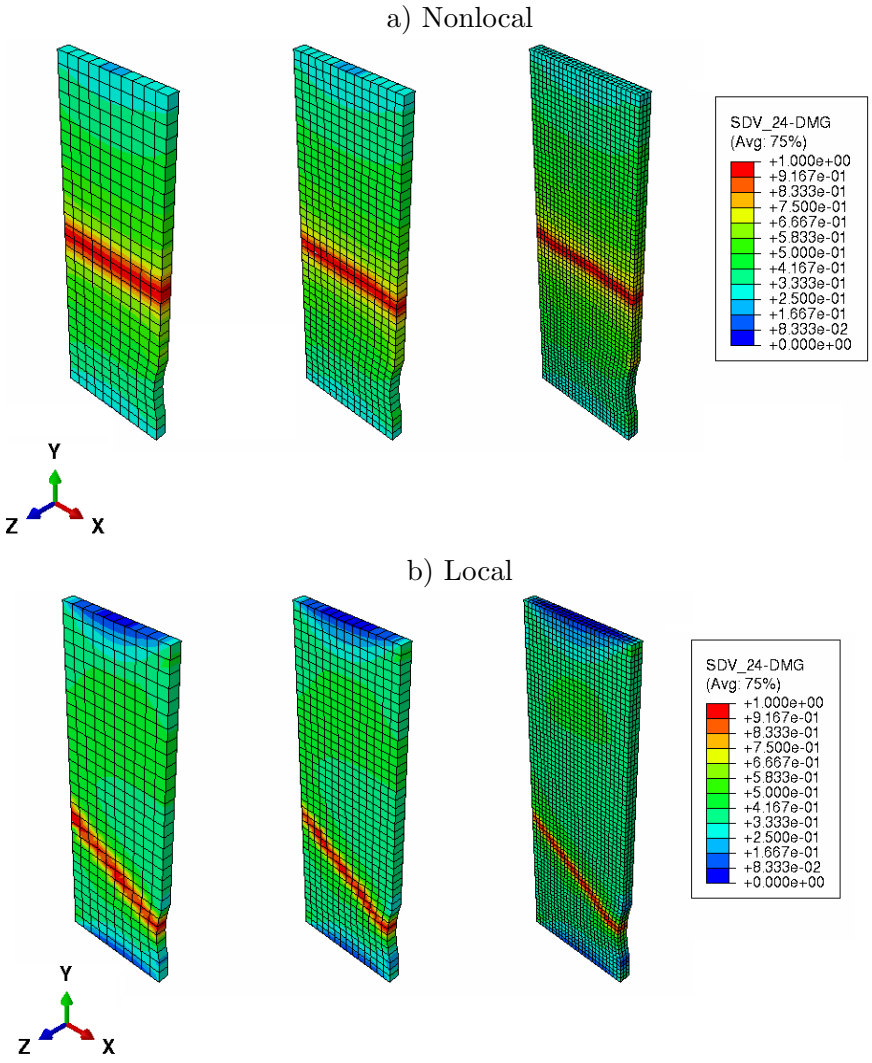

Figure 4.19: Damage distribution in the unilaterally notched plate with 300, 602, and 5625 elements using: a) nonlocal model when $\xi^{nl} = 6\,\text{kN}$ and $\gamma^{nl} = 5\,\text{GPa}$, b) local model; the nonlocal model is based on r^{nl}.

4.5.3 Asymmetrically double notched rectangular plate

Based on the results and discussions in the previous section, the nonlocal model employing r^{nl} works more efficiently than the first option using D^{nl}. In fact, based on the VEVPD constitutive laws, the damage is induced by plasticity, and not inverse. With this in mind, the nonlocal damage, D^{nl}, does not address the plasticity localization and subsequently the non-unique and non-physical responses.

Thus, here, the use of r^{nl} is preferred to implement as the nonlocal model on the asymmetrically double notched structure (Figure 4.3). For the 2D case, the structure is meshed via 3 and 4 nodes plane strain temperature-displacement elements (CPE3T, CPE4T) in two mesh sizes ($N_E = 1555, 6346$). The plate is subjected to the monotonic uniaxial tensile load with $\dot{u}_0 = 3\,\mathrm{mm}s^{-1}$ from the right side, and the displacement at the left side is bounded to zero. The damage contours are extracted for the local and nonlocal models with $\xi^{nl} = \{4\,\mathrm{kN}, 6\,\mathrm{kN}\}$ and displayed in Figure 4.20 As seen, an increase in ξ^{nl} leads to change in the damage profile and thicken the shear band (Figure 4.20-a and Figure 4.20-b). While, for the local case (Figure 4.20-c), the damage is mostly localized into the crack zone and shows the tendency to occupy the minimum possible area. The aforementioned structure with a thickness of 1 mm, under the same loading and boundary conditions, is examined through the 3D element, C3D8T. The damage distribution is provided for the local and nonlocal model ($\xi^{nl} = 6\,\mathrm{kN}$,$\gamma^{nl} = 3\,\mathrm{GPa}$) and shown in the Figure 4.21. In the 3D case, the damage localization is well addressed. In comparison with the 2D case, since the damage profile is also distributed in thickness, it affects the damage growth in other directions, and the corresponding profile seems less diffused with a narrower crack zone in the X-Y plane.

4.6 Conclusion

A gradient enhanced thermodynamically based framework was proposed towards investigating the PA66 mechanical behavior in the highly damaged levels and address the spurious damage localization leading to the macroscopic failure as well as the consequent mesh sensitivity in the FE computations. To this end, the Thermodynamics of Irreversible Processes (TIP) and the Generalized Standard Materials (GSM) formalism were employed to derive the constitutive equations. A specific nonlocal formulation for the thermodynamic potential was considered and then enhanced based on two cases regarding the nonlocal state variable: nonlocal damage, and nonlocal hardening state variable. The constitutive laws were integrated through the "convex cutting plane" as a return mapping algorithm and implemented within the finite element framework through a user-defined material subroutine. Two methodologies have been studied to implement the nonlocal model: UEL-UMAT and HETVAL-UMAT. In the first approach, the appropriate system of equations was defined by the UEL subroutine, and in the second approach, the analogy between the steady state heat equation and the nonlocal formulation allowed to introduce the nonlocal equation implicitly in the FE solver. The responses are

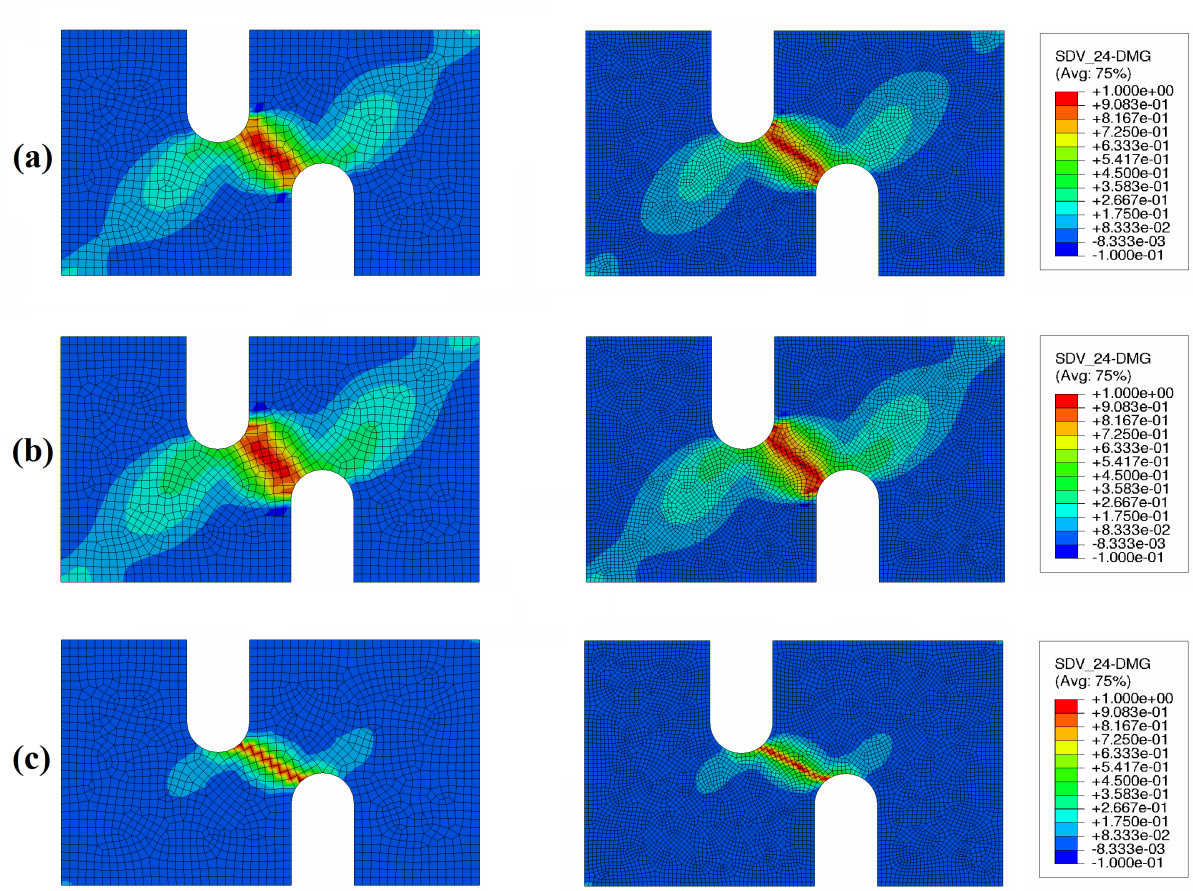

Figure 4.20: Damage distribution in the asymmetrically double notched plate under uniaxial tensile load with the displacement rate $\dot{u}_0 = 10\,\mathrm{mm\,s^{-1}}$ meshed by 1555 and 6346 elements using the nonlocal model with $\gamma^{nl} = 3\,\mathrm{GPa}$ and a) $\xi^{nl} = 4\,\mathrm{kN}$, b) $\xi^{nl} = 6\,\mathrm{kN}$ and comparison with c) local model; the nonlocal model is based on r^{nl}.

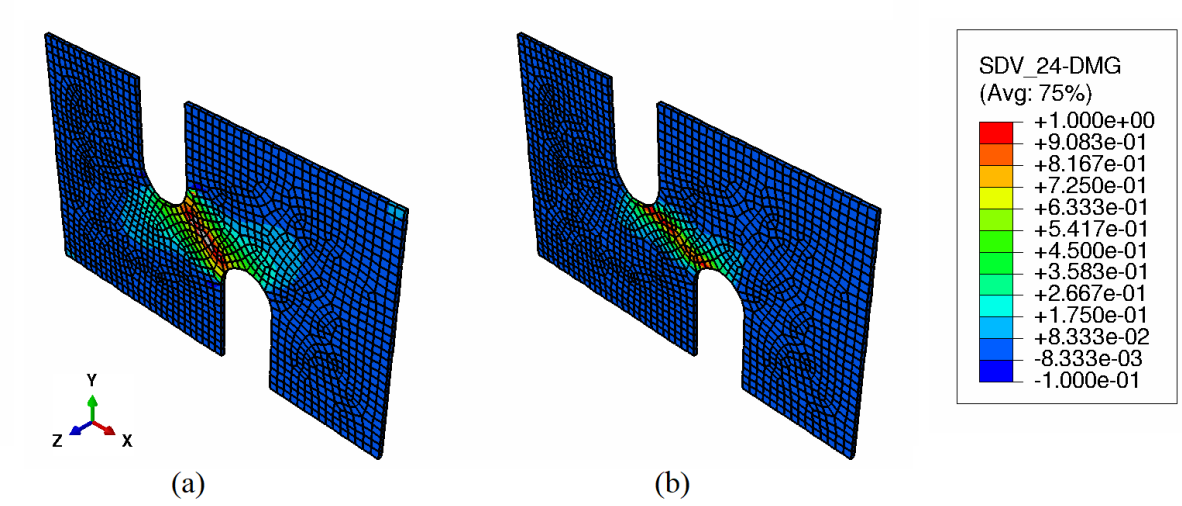

Figure 4.21: Damage distribution in the asymmetrically double notched plate under uniaxial tensile load with the displacement rate $\dot{u}_0 = 10\,\mathrm{mm\,s^{-1}}$ meshed by 6444 elements using a) Local model, and b) Nonlocal model with $\gamma^{nl} = 3\,\mathrm{GPa}$ and $\xi^{nl} = 6\,\mathrm{kN}$; the nonlocal model is based on r^{nl}.

identical in both implementation methodologies, but the use of the steady state heat equation analogy is cheaper computationally, particularly when the nonlocal variable is scalar. Considering two nonlocal variable cases, numerical examples were presented to perform a parametric study and examine the nonlocal model efficiency in controlling the damage localization. Investigation of the numerical examples revealed that employing D^{nl} as the nonlocal variable does not enable the model to control the damage localization while a spurious plasticity localization appears during the material softening. In fact, due to the formulations of the VEVPD constitutive model, damage is induced by plasticity, and the plasticity localization leads to the damage localization. With this in mind, the nonlocal damage is not able to address the plasticity localization, but the opposite is possible. It implies that the nonlocal hardening state variable addresses non-unique mesh sensitive results in both the damage and plasticity. The nonlocal model based on r^{nl} yielded mesh objective responses and exhibited the capability of investigating the material behavior in higher levels of damage during material softening stages. The mesh objectivity of the results is improved for the higher values of the nonlocal parameters γ^{nl} and ξ^{nl}. However, beyond a certain level of nonlocal parameters, no significant effect on the solutions is observed, which is due to the size of structure.

Chapter 5

Nonlocal multi-scale framework for glass reinforced thermoplastics

Contenu

5.1 Introduction

In the previous chapters, the VEVPD model based on von Mises yield function was modified to a I_1-J_2 model accounting for the effect of hydrostatic pressure and tension-compression asymmetry. The effect of RH was also studied experimentally, and the model parameters were identified which allow modeling the mechanical responses of thermoplastics with different water contents. Furthermore, non-physical model responses in modeling of severely damaged material were addressed using the nonlocal gradient enhanced framework. However, the main objective of this research is to develop a proper multi-scale framework for glass reinforced thermoplastics capturing the nonlocal phenomena and addressing the computational instability due to the localization of internal state variables. The overall behavior of glass reinforced thermoplastics at the macroscopic scale is affected by the matrix phase at microscale which exhibits nonlinear viscoelastic viscoplastic rheology with plasticity-induced ductile damage. Softening of the matrix phase due to the high level damage leads to the localization of the internal state variable and, consequently, structural instability and difficulties in the computational model. To address this problem, one may propose to extend the nonlocal gradient enhanced framework to a multi-scale model, in which an appropriate homogenization framework is developed to conduct unique overall mechanical responses in composites.

This chapter utilizes the nonlocal model, presented in chapter 4, into the multi-scale framework aimed at predicting the mechanical response of long glass fiber reinforced polyamide composites. To treat numerically material instabilities at severe damage levels, an internal length scale is introduced within the model through a gradient enhanced framework that controls the non-physical localization of state variables and the consequent early model failures. To do so, a viscoelastic viscoplastic phenomenological model is adopted to capture the matrix phase nonlinear response at the microscale, then an appropriate homogenization approach is considered to provide the overall response of the composite, in which the gradient enhanced framework is formulated at the macroscale. As a result, a consistent homogenization model capable of capturing nonlocal phenomena is introduced and implemented into a commercial finite element software, which addresses the non-physical responses of the local model and exhibits higher stability.

This chapter is structured as follows: in section 5.2, the theoretical framework is presented. First, the nonlinear inelastic behavior of the matrix phase and the corresponding constitutive laws

are discussed, and then an appropriate multi-scale scheme is introduced, based on which the Mori-Tanaka/TFA homogenization framework is applied and formulated. In section 5.3, the model is first validated with a multi-layered structure, then the application of the framework is justified with a numerical example, and finally, several examples are investigated as parametric studies.

5.2 Theoretical background

5.2.1 Multi-scale homogenization

To investigate the global mechanical behavior of composite structures, it is necessary to model them as homogeneous materials based on multi-scale homogenization theories [77, 89, 148–162]. Multi-scale homogenization framework addresses the composite behavior at both the macro and micro scales. It considers the mechanisms of the composite constituents as well as their geometry characteristics and configurations in the microstructure, based on which the overall mechanical behavior of the composite is interpreted as a homogeneous material at the macroscale. In this connection, many finite element based homogenization and mean field approaches are proposed in the literature. From a technical prospect, mean field models are computationally less expensive than finite element-based approaches, which has made their application more popular. Mori-Tanaka approach is among the most widely used of mean field techniques and was first applied to elastic models [163], and then extended to investigate nonlinear inelastic mechanisms [2, 148, 164–167].

5.2.1.1 Mori-Tanaka approach

Considering a heterogeneous material, the different inclusions in the matrix have interactions with each other depending on their material type, size, shape and orientation. The communication between the inclusions is established by the strain and stress corresponding to the matrix around them. According to Mori-Tanaka, while the physical properties may change in the material, the surrounding average strain, $\boldsymbol{\epsilon}_0$, and stress, $\boldsymbol{\sigma}_0$, can give a good approximation in the considered field, when the number of inhomogeneities is large enough. This concept is illustrated schematically in Figure 5.1 , in which the average strain is approximated for an arbitrary inclusion with elastic stiffness, $\mathbb{L}_r$ and its surrounding matrix with elastic stiffness, $\mathbb{L}_0$. With this in mind, it can be also assumed that replacing only one inclusion by the matrix phase with a large number of inclusions does not affect the overall

elastic behavior. Thus, the $r\,th$ inhomogeneity can be considered as an elipsoidal inclusion in a uniform matrix subjected to $\boldsymbol{\sigma}_0$ and $\boldsymbol{\epsilon}_0$. Hence, the strain of $r\,th$ inhomogeneity can be derived as [168]:

$$\boldsymbol{\epsilon}_r = \mathbb{T}_r : \boldsymbol{\epsilon}_0, \quad \text{with} \quad \mathbb{T}_r = [\mathbb{I} + \mathbb{S}_r : \mathbb{L}_0^{-1} : [\mathbb{L}_r - \mathbb{L}_0]]^{-1}, \tag{5.1}$$

where $\mathbb{T}_r$ denotes the interaction tensor, $\mathbb{S}_r$ is the Eshelby tensor based on the inclusion shape (aspects ratios), and $\mathbb{L}_0$ and $\mathbb{L}_r$ denote the elastic stiffness tensors of matrix and $r\,th$ inclusion, respectively. Considering the volume fractions of matrix, V_0^f, and the $r\,th$ inclusion, V_f^r, the following can be derived for the overall strain, $\bar{\boldsymbol{\epsilon}}$:

$$\bar{\boldsymbol{\epsilon}} = \left[V_0^f \mathbb{I} + \sum_{r=1}^{N} V_r^f \mathbb{T}_r\right] : \boldsymbol{\epsilon}_0 \quad \text{or} \quad \boldsymbol{\epsilon}_0 = \left[V_0^f \mathbb{I} + \sum_{r=1}^{N} V_r^f \mathbb{T}_r\right]^{-1} : \bar{\boldsymbol{\epsilon}}. \tag{5.2}$$

Considering the above equation, the $r\,th$ inclusion strain is derived as:

$$\boldsymbol{\epsilon}_r = \mathbb{A}_r : \bar{\boldsymbol{\epsilon}}, \quad \text{with} \quad \mathbb{A}_r = \mathbb{T}_r : \left[V_0^f \mathbb{I} + \sum_{r=1}^{N} V_r^f \mathbb{T}_r\right]^{-1}, \tag{5.3}$$

where $\mathbb{A}_r$ is the concentration tensor of the $r\,th$ inclusion.

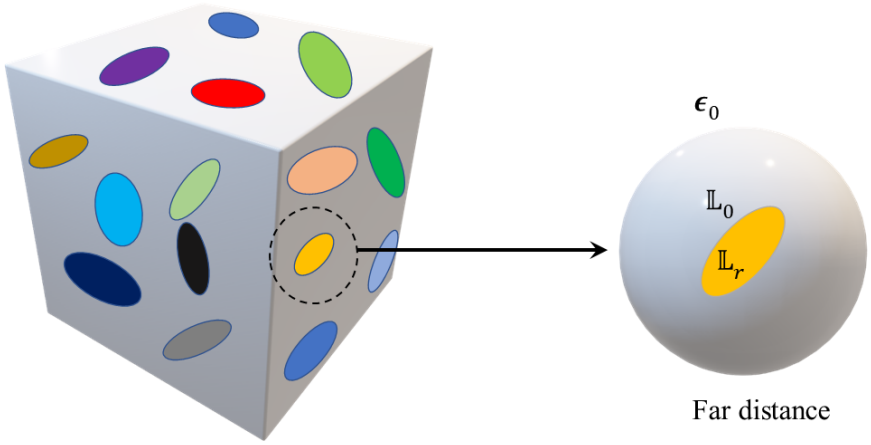

Figure 5.1: Schematics for Mori-Tanaka assumptions [2].

Many researchers extended this framework to also obtain the global stiffness using the material properties of the constituents [168–170]. For the nonlinear materials, Transformation Field Analysis (TFA) allows estimating the overall behavior of the composite when the matrix phase exhibits inelastic mechanisms. However, some shortcomings have been reported in the literature regarding the classical model, related to stiff predicted response due to inability to capture properly the inelastic strains,

especially in the matrix phase. To resolve this issue, several techniques have been proposed in the literature, among them the isotropization technique [104], a method involving the Linear Comparison Composite (LCC) [171] and an approach considering a coating layer with increased inelastic strains [36,92]. However, typical multi-scale models are incapable of providing accurate results at high damage levels; numerical instabilities in small zones appear as non-physical responses leading to early numerical model failure. To this end, nonlocal approaches are proposed to capture the mechanical behavior in severely damaged regions. Thus, prior to any multi-scale development, the relationship between the nonlocal length scale, l^{nl}, and the RVE size, l^{ε}, as well as its impact on the microscopic and macroscopic response should be investigated. This is the topic of the following section.

5.2.2 Multi-scale modeling

This section discusses the nonlocal multi-scale framework for the aforementioned composite. In a composite medium exhibiting nonlocal phenomena, three sizes are of great importance: the global size of the structure, L, the RVE size, l^{ε}, and the nonlocal length scale, l^{nl}, of the matrix phase. Assuming that the RVE size is always much smaller than the actual size of the structure ($L \gg l^{\varepsilon}$), two different cases will be examined:

- first, when the RVE size is sufficiently larger or comparable with the nonlocal length scale ($l^{nl} \leq l^{\varepsilon}$ or l^{nl} in the same order with l^{ε}),
- second, when the length scale is much bigger than the RVE size ($l^{nl} \gg l^{\varepsilon}$), but l^{nl} is still less that L.

To illustrate the differences between the two cases in terms of homogenized response, several examples of a fiber composite medium will be discussed. For this composite, the RVE is periodic and appears in two different settings: first, as a single periodic unit cell, and second, as a group of periodic unit cells (Figure 5.2). The fibers are assumed long, unidirectional, elastic, and made of glass, while the matrix phase is of the PA 66 material, whose constitutive law has been described in chapters 2 and 4. For each case, the damage behavior is studied and the analysis is performed using a commercial finite element tool. Quadratic tetrahedral elements are used in the finite element models, and the numerical implementation of the nonlocal model is expressed in the following sections. For computational reasons, both the matrix and the fibers are assumed to have the same ξ^{nl}, but the γ^{nl} parameter of the fibers is

considered zero. The latter hypothesis ensures that the nonlocal field does not present jumps inside the fiber, but also it does not affect its response. The FE size for all these studied cases is approximately 0.05 mm, whereas the RVE size is 1 mm $\times$ 1 mm $\times$ 0.1mm.

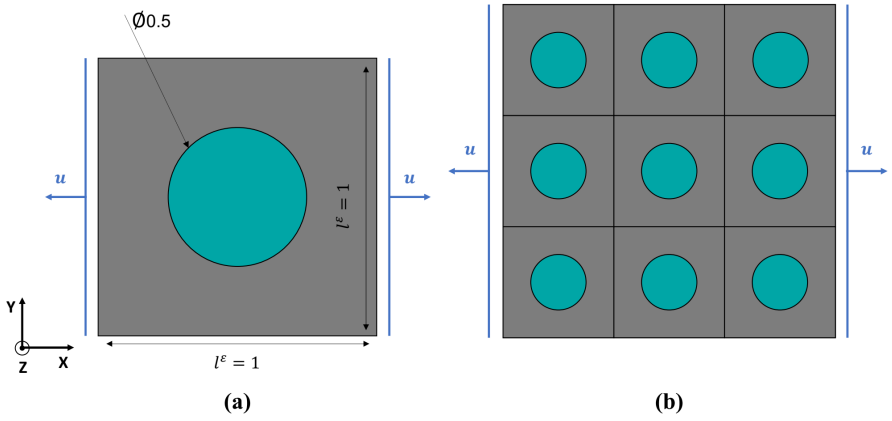

Figure 5.2: Loading conditions ($\dot{u} = 0.1\,\mathrm{mms}^{-1}$) and the dimensions corresponding to: a) single long fiber reinforced RVE, b) a group of RVEs (dimensions are based on mm); the thickness for both cases is 0.1 mm.

5.2.2.1 Case 1: $l^{nl} \leq l^{\varepsilon}$ or l^{nl} in the same order with l^{ε}

In this case, the nonlocal length scale, l^{nl}, is assumed to be smaller than or in the same order with the RVE size, l^{ε}. This assumption implies that the nonlocal length scale is not present explicitly at the macroscale and only appears at the microscale. Accordingly, the multi-scale system of equations can be derived using asymptotic expansion as:

- macroscale:

$$\frac{\partial \bar{\sigma}_{ij}}{\partial \bar{x}_i} = 0 \quad \text{with} \quad \langle \sigma_{ij}^{(0)} \rangle = \bar{\sigma}_{ij}, \tag{5.4}$$

- microscale:

$$\begin{cases} \dfrac{\partial \sigma_{ij}^{(0)}}{\partial x_i} = 0, \\ \xi^{nl} \dfrac{\partial}{\partial x_i} \left(\dfrac{\partial r^{nl}}{\partial x_i} \right) + \gamma^{nl} \left(r - r^{nl} \right) = 0, \end{cases} \tag{5.5}$$

where the symbols, "$\bar{.}$" and "$\langle . \rangle$", are the macroscopic variable and the average on the microscopic unit cell volume respectively, and "$.^{(0)}$" denotes the zero order terms of the corresponding asymptotic

expansion. The deriving procedure is fully expressed in appendix B where besides the zero order terms, higher order terms are also introduced. It is noted that such case may be problematic from a homogenization point of view, as reported in the literature [95].

As a first example, the periodic boundary conditions are applied on a single RVE and a group of RVEs when $l^{nl} = 0.01\, l^{\varepsilon}$, and the resulting damage profiles are extracted in Figure 5.3. As seen, the damage profiles are not identical and uniform in the RVEs set, and it is not clear which one illustrates the true damage behavior, arising questions whether the RVE is representative. As the second example, the same analysis is performed when $l^{nl} = 0.1\, l^{\varepsilon}$, and the 3D maps of damage are depicted in Figure 5.4. As observed, by increasing the ratio of l^{nl}/l^{ε}, the damage profiles become almost uniform in the RVEs group, and the damage stays within the RVE and concentrates around the fiber.

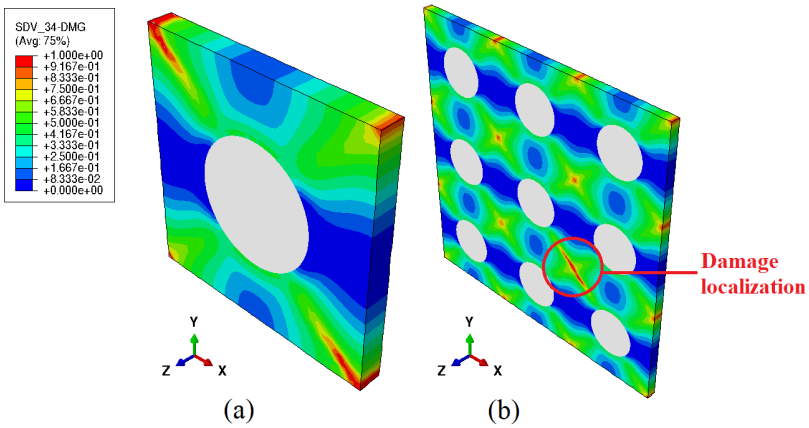

Figure 5.3: Damage profile under $0.1\,\mathrm{mms}^{-1}$ monotonic loading rate when $l^{nl} = 0.01\, l^{\varepsilon}$ ($l^{nl} < l^{\varepsilon}$): a) single long fiber reinforced RVE, b) a group of RVEs. Element size is set to 0.05 mm.

5.2.2.2 Case 2: $l^{nl} \gg l^{\varepsilon}$

As the second case, the nonlocal length scale is assumed to be much larger than the RVE size. Therefore, the nonlocal equation does not appear at the micro level and passes through the macroscale. Based on the asymptotic expansion given in appendix B, it is shown that the scale separation has a more "classical" formalism, and the governing equations at the macro and micro scales are expressed as follows:

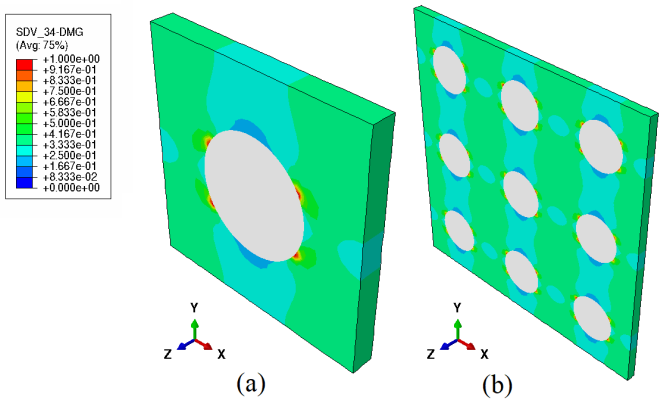

Figure 5.4: Damage profile under $0.1\,\mathrm{mms}^{-1}$ monotonic loading rate when $l^{nl} = 0.1\,l^{\varepsilon}$ ($l^{nl} < l^{\varepsilon}$): a) single long fiber reinforced RVE, b) a group of RVEs. Element size is set to 0.05 mm.

- macroscale:

$$\begin{cases} \dfrac{\partial \bar{\sigma}_{ij}}{\partial \bar{x}_i} = 0 \quad \text{with} \quad \langle \sigma_{ij}^{(0)} \rangle = \bar{\sigma}_{ij}, \\ \\ \xi^{nl} \dfrac{\partial}{\partial \bar{x}_i} \left(\dfrac{\partial r^{nl(0)}}{\partial \bar{x}_i} \right) + \langle \gamma^{nl} r^{(0)} \rangle - \langle \gamma^{nl} \rangle r^{nl(0)} = 0, \end{cases} \tag{5.6}$$

- microscale

$$\frac{\sigma_{ij}^{(0)}}{\partial x_i} = 0. \tag{5.7}$$

Similar example with the previous one, considering this time $l^{nl} = 100\,l^{\varepsilon}$, allows to study the damage growth within the RVEs (see Figure 5.5). As observed, the RVEs damage profiles are identical, so the RVE is representative.

According to the above results, it can be concluded that the second case ($l^{nl} \gg l^{\varepsilon}$) is more compatible with the multi-scale framework than the first one because the RVE is representative, and it satisfies the periodicity assumption and the classical scale separation formalism. Furthermore, this assumption allows the nonlocal variable to be identical throughout the RVE, whereas smaller length scales lead to non-uniform nonlocal variable, r^{nl}, at the microscale. This fact is confirmed through 3D maps of the nonlocal variable, r^{nl}, depicted in Figure 5.6. Uniform nonlocal variable within the RVE makes the model compatible with the mean field homogenization frameworks, in which the material properties in the RVE vary by phase. In addition, the second case is more acceptable physically

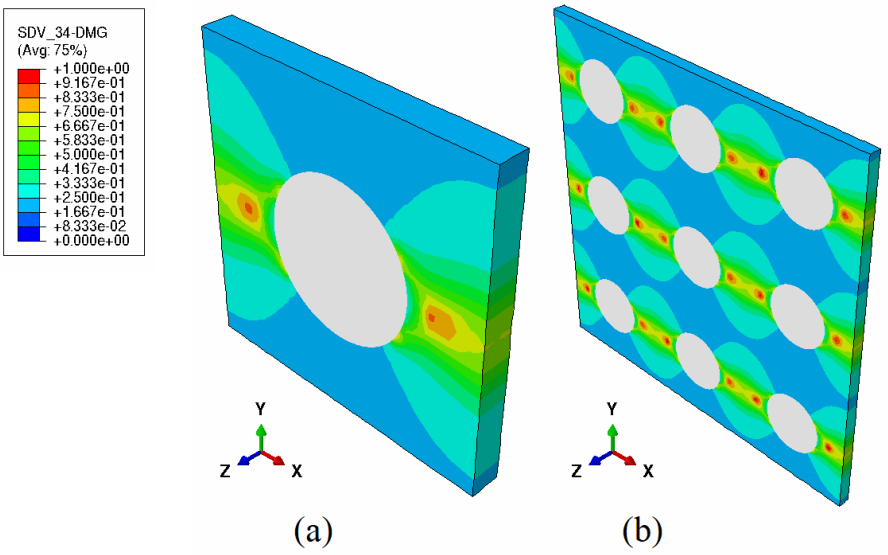

Figure 5.5: Damage profile under $0.1\,\mathrm{mms}^{-1}$ monotonic loading rate when $l^{nl} = 100\,l^{\varepsilon}$ ($l^{nl} \gg l^{\varepsilon}$): a) single long fiber reinforced RVE, b) a group of RVEs. Element size is set to 0.05 mm.

because the localization of state variables, particularly damage, is a problem often observed at the macroscale failure.

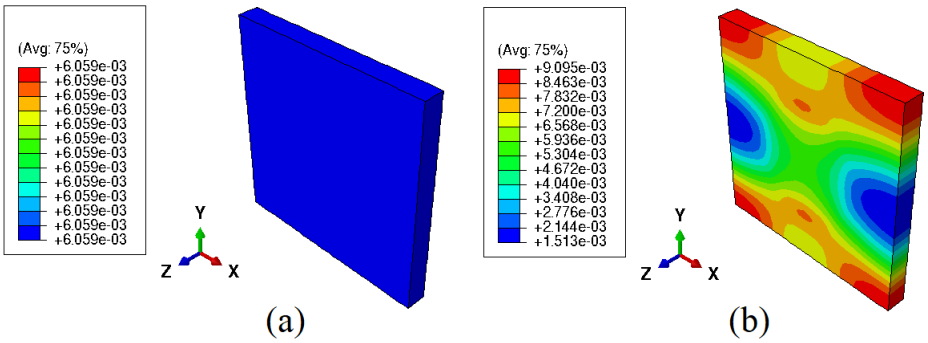

Figure 5.6: Nonlocal variable, r^{nl}, profile under periodic boundary conditions when: a) $l^{nl} = 100\,l^{\varepsilon}$, b) $l^{nl} = 0.1\,l^{\varepsilon}$.

It is worth mentioning that, according to nonlocal analyses standards [140, 147], for $l^{nl} = 0.1\,l^{\varepsilon}$ and $l^{nl} = 100\,l^{\varepsilon}$, the FE size is sufficiently small compared to the length scales. However, for the lowest l^{nl} case, this FE size is relatively large. An additional analysis with much finer mesh leads to qualitatively similar results, confirming thus the derived conclusions of the study.

5.2.3 Mori-Tanaka/TFA framework

Since the focus of this research is the failure at the macrostructure, the second case (i.e. $l^{nl} \gg l^{\varepsilon}$) is considered in the sequel of this chapter to develop the multi-scale framework. The conclusions reached from the asymptotic expansion homogenization approach, specially with regard to the macroscale and microscale problems, can be adopted for other micromechanics schemes. Mori-Tanaka/TFA homogenization approach is used here to model overall mechanical responses of glass fiber reinforced polyamide 66. Since the current work is an attempt to establish a general framework and there is no experimental comparison, the classical Mori-Tanaka/TFA framework without inelasticity related modifications is adopted here. The proposed theory can be easily extended to adopt a correction on the plastic strains level. Mori-Tanaka/TFA method suggests splitting the total macroscopic stress into two parts, elastic and inelastic [36, 90]:

$$\bar{\boldsymbol{\sigma}} = \bar{\boldsymbol{\sigma}}^{r} + \bar{\boldsymbol{\sigma}}^{in} = \bar{\mathbb{C}}^{sec} : \bar{\boldsymbol{\epsilon}} + \bar{\boldsymbol{\sigma}}^{in}, \tag{5.8}$$

where $\bar{\mathbb{C}}^{sec}$ is the 4th order overall secant tensor, and the superscripts ".^{e}" and ".^{in}" respectively denote the elastic and inelastic parts of the variable. Based on the extended Eshelby's problem the inclusion deformation, $\boldsymbol{\epsilon}_1$ is defined as [172]:

$$\boldsymbol{\epsilon}_1 = \mathbb{T}_1 : \boldsymbol{\epsilon}_0 + \mathbb{T}_1^{p} : \boldsymbol{\sigma}_0^{in} - \mathbb{T}_1^{p} : \boldsymbol{\sigma}_1^{in}, \tag{5.9}$$

with

$$\mathbb{T}_1 = \left[\mathbb{I} + \mathbb{P} : (\mathbb{C}_1^{sec} - \mathbb{C}_0^{sec})\right]^{-1}, \quad \mathbb{T}_1^{p} = \mathbb{T}_1 : \mathbb{P}, \quad \mathbb{P} = \mathbb{S}\left(\mathbb{C}_0^{sec}\right) : \mathbb{C}_0^{sec-1}, \tag{5.10}$$

where $\mathbb{S}$ and $\mathbb{P}$ are the 4th order Eshelby and polarization tensors, respectively; here, the subscripts, ".$_0$" and ".$_1$", denote the matrix and inclusion variables, and $\mathbb{T}_1$ and $\mathbb{T}_1^{p}$ are the elastic and inelastic interaction tensors, respectively. The macroscopic strain, $\bar{\boldsymbol{\epsilon}}$, for a composite material whose RVE constitutes from the matrix phase and one single inclusion is expressed as:

$$\bar{\boldsymbol{\epsilon}} = V_0^{f}\boldsymbol{\epsilon}_0 + V_1^{f}\boldsymbol{\epsilon}_1, \tag{5.11}$$

where V_0^f and V_1^f are the matrix and inclusion volume fractions respectively. Substituting 5.9 into 5.11 yields:

$$\bar{\boldsymbol{\epsilon}} = V_0^f \boldsymbol{\epsilon}_0 + V_1^f \left(\mathbb{T}_1 : \boldsymbol{\epsilon}_0 + \mathbb{T}_1^p : \boldsymbol{\sigma}_0^{in} - \mathbb{T}_1^p : \boldsymbol{\sigma}_1^{in} \right), \tag{5.12}$$

where it can be rewritten as:

$$\bar{\boldsymbol{\epsilon}} = \left(V_0^f \mathbb{I} + V_1^f \mathbb{T}_1 \right) : \boldsymbol{\epsilon}_0 + V_1^f \left(\mathbb{T}_1^p : \boldsymbol{\sigma}_0^{in} - \mathbb{T}_1^p : \boldsymbol{\sigma}_1^{in} \right). \tag{5.13}$$

Thus, the matrix deformation can be expressed as:

$$\boldsymbol{\epsilon}_0 = \mathbb{A}_0 : \bar{\boldsymbol{\epsilon}} + \mathbb{A}_0^p : \boldsymbol{\sigma}_0^{in} + \mathbb{A}_1^p : \boldsymbol{\sigma}_1^{in}, \tag{5.14}$$

with the concentration tensors being given by the formulas:

$$\mathbb{A}_0 = \left[V_0^f \mathbb{I} + V_1^f \mathbb{T}_1 \right]^{-1}, \quad \mathbb{A}_0^p = -V_1^f \mathbb{A}_0 : \mathbb{T}_1^p, \quad \mathbb{A}_1^p = \mathbb{A}_0 : V_1^f \mathbb{T}_1^p. \tag{5.15}$$

The inclusion deformation is also derived by substituting 5.14 into 5.9:

$$\boldsymbol{\epsilon}_1 = \mathbb{A}_1 : \bar{\boldsymbol{\epsilon}} + \mathbb{A}_0^f : \boldsymbol{\sigma}_0^{in} + \mathbb{A}_1^f : \boldsymbol{\sigma}_1^{in}, \tag{5.16}$$

with

$$\mathbb{A}_1 = \mathbb{T}_1 : \mathbb{A}_0, \quad \mathbb{A}_0^f = \mathbb{T}_1 : \mathbb{A}_0^p + \mathbb{T}_1^p, \quad \mathbb{A}_1^f = \mathbb{T}_1 : \mathbb{A}_1^p - \mathbb{T}_1^p. \tag{5.17}$$

The overall stiffness for the present two phase composite is defined as [90]:

$$\bar{\mathbb{C}}^{sec} = V_0^f \mathbb{C}_0^{sec} : \mathbb{A}_0 + V_1^f \mathbb{C}_1^{sec} : \mathbb{A}_1. \tag{5.18}$$

Since the glass fibers are considered elastic, $\boldsymbol{\sigma}_1^{in} = \mathbf{0}$, and the $\mathbb{A}_1^p$ and $\mathbb{A}_1^f$ concentration tensors can be omitted in the computational procedure. Moreover, the secant modulus, $\mathbb{C}_1^{sec}$, coincides with the elastic modulus of the reinforcement.

The next section deals with the numerical implementation of the present multi-scale model, combining the VEVPD matrix phase, the homogenization scheme, and the nonlocal framework.

5.3 Numerical implementation

The numerical implementation consists of three different stages: first, the microscale inelastic mechanisms in the matrix phase are computed and updated using a VEVPD subroutine, second, the micromechanical model subroutine providing the global stress tensor and secant modulus, and third, the nonlocal part implemented at the macroscopic scale using the analogy between heat and nonlocal equations through HETVAL subroutine. The interaction between the stages mentioned above and the associated inputs and outputs are briefly presented as a flowchart in Figure 5.7. The following sections discuss each part of the implementation procedure in more detail.

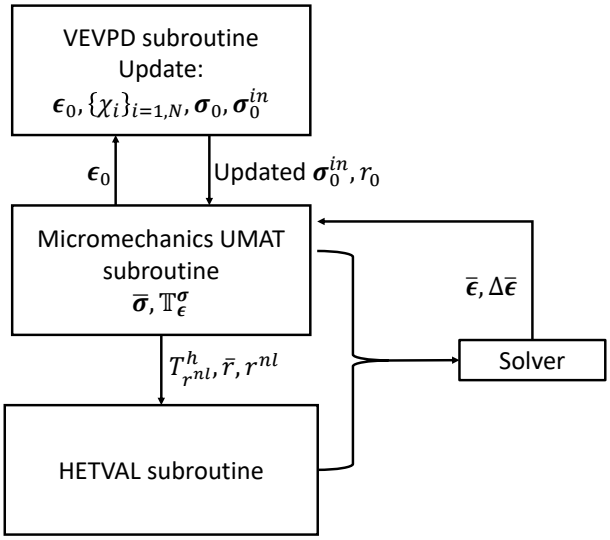

Figure 5.7: Flowchart of the numerical implementation in ABAQUS FE software for a composite structure. It should be mentioned that the HETVAL subroutine only needs $T_h^{r^{nl}}$, as the associated nonlocal tangent operator.

5.3.1 VEVPD model numerical implementation

As already expressed in chapter 2, the VEVPD numerical model is discretized in time based on an implicit backward Euler scheme compatible with the FE solver inputs in time steps. The associated subroutine takes the total deformation of the matrix phase, $\boldsymbol{\epsilon}_0$, at the time step n, and the corresponding deformation variation, $\Delta\boldsymbol{\epsilon}_0$, at the time step $n+1$, as inputs and produces the inelastic stress, $\boldsymbol{\sigma}_0^{in}$, and the secant modulus of the matrix phase, $\mathbb{C}_0^{sec}$, as outputs. For updating the internal

state variables and calculating the inelastic stress, an iterative process is designed based on the "convex cutting plane" return mapping algorithm [16, 117]. As an efficient method, the algorithm is divided into two steps: viscoelastic correction-prediction and full correction. At the first stage, no plasticity or damage is taken into account, and the deformation is governed by viscoelasticity. Therefore, only the total strain and viscoelastic strain elements vary under deformation. Once the equivalent stress, σ^{eq}, exceeds the material elastic limit, R_0 ($f > 0$), the viscoplasticity and the related ductile damage are activated, and a full correction is required to update the state variables including viscoplastic strain, hardening state variables, and viscoelastic strains. More detailed description of the numerical implementation of the VEVPD model can be found in [14].

5.3.2 Micromechanics model algorithm

The objective of the micromechanical model is to provide the solver with the overall stress and secant modulus tensors in macroscopic scale. To this end, the micromechanical subroutine passes the matrix phase strain tensor, $\boldsymbol{\epsilon}_0$ and its corresponding variation, $\Delta\boldsymbol{\epsilon}_0$, to the VEVPD tool which yields the inelastic stress tensor, $\boldsymbol{\sigma}_0^{in}$. Since the matrix deformation depends on the inelastic mechanisms (equation (5.14)), an iterative algorithm is adopted to calculate the inelastic stress tensor. Table 5.1 provides the detailed description of the numerical micromechanical UMAT as an algorithm box. Also, Figure 5.7 illustrates how the numerical tools are inter-connected.

5.3.3 Nonlocal model setup within the ABAQUS FE software

As mentioned in the previous sections, the nonlocal phenomena appear and are integrated at the macroscopic scale. In this regard, the nonlocal strategy uses ξ^{nl} and $\langle\gamma^{nl}\rangle$ as nonlocal parameters. Also, it passes as inputs to the solver: the average local quantity, $\langle\gamma^{nl}\, r\rangle$, and the nonlocal variable, r^{nl}, as well as the associated tangent operators. In this respect, since the present gradient enhanced model contains the nonlocal balance equation as well as the stress equilibrium, an additional degree of freedom must be defined as the nonlocal field. To this end, similar to chapter 4 HETVAL subroutine is used to introduce the nonlocal field to the FE model.

Table 5.1: Algorithm box: Micromechanics iteration algorithm

1- Recover stress and state variables at the time step, n:
$\boldsymbol{\epsilon}_0^{vp(n)}, \boldsymbol{\epsilon}_0^{vi(n)}, D_0^n, r_0^n, \boldsymbol{\epsilon}_0^n, \boldsymbol{\epsilon}_1^n, \boldsymbol{\sigma}_0^n, \boldsymbol{\sigma}_0^{in(n)}$ with $(i = 1, .., N_v)$.
2- Calculate secant modulus tensors:
$\mathbb{C}_0^{sec}$, $\mathbb{C}_1^{sec}$.
3- Calculate concentration tensors based on $\mathbb{C}_0^{sec}$, $\mathbb{C}_1^{sec}$:
$\mathbb{A}_0$, $\mathbb{A}_0^p$, $\mathbb{A}_1$.
5- Compute $\Delta\boldsymbol{\epsilon}_0$ using concentration tensors:
$\Delta\boldsymbol{\epsilon}_0 = \boldsymbol{\epsilon}_0^{n+1} - \boldsymbol{\epsilon}_0^n = \mathbb{A}_0 : (\bar{\boldsymbol{\epsilon}} + \Delta\bar{\boldsymbol{\epsilon}}) + \mathbb{A}_0^p : \boldsymbol{\sigma}_0^{in} - \boldsymbol{\epsilon}_0^n$.
Start iterative process.
6- Run VEVPD subroutine and update:
$\boldsymbol{\epsilon}_0^{vp(n)}, \boldsymbol{\epsilon}_0^{vi(n)}, D_0^n, r_0^n, \boldsymbol{\epsilon}_0^n, \boldsymbol{\epsilon}_1^n, \boldsymbol{\sigma}_0^n, \boldsymbol{\sigma}_0^{in(n)}$ with $(i = 1, .., N_v)$.
7- Update secant modulus tensor, $\mathbb{C}_0^{sec}$, and concentration tensors:
$\mathbb{A}_0$, $\mathbb{A}_0^p$, $\mathbb{A}_1$.
8- Update $\Delta\boldsymbol{\epsilon}_0$ and $\Delta\boldsymbol{\epsilon}_1$ corresponding to iteration step $k+1$:
$\Delta\boldsymbol{\epsilon}_0^{k+1} = \boldsymbol{\epsilon}_0^{n+1} - \boldsymbol{\epsilon}_0^n = \mathbb{A}_0 : (\bar{\boldsymbol{\epsilon}} + \Delta\bar{\boldsymbol{\epsilon}}) + \mathbb{A}_0^p : \boldsymbol{\sigma}_0^{in} - \boldsymbol{\epsilon}_0^n$,
$\Delta\boldsymbol{\epsilon}_1^{k+1} = (\Delta\bar{\boldsymbol{\epsilon}} - V_0^f \Delta\boldsymbol{\epsilon}_0)/V_1^f$.
9- Update concentration tensors.
10- if $\left||\Delta\boldsymbol{\epsilon}_0^{k+1} - \Delta\boldsymbol{\epsilon}_0^k|\right| + \left||\Delta\boldsymbol{\epsilon}_1^{k+1} - \Delta\boldsymbol{\epsilon}_1^k|\right| \leq R^{tol}$,
update $\boldsymbol{\epsilon}_0$, $\boldsymbol{\epsilon}_1$, $\boldsymbol{\sigma}_0$, $\boldsymbol{\sigma}_1$, $\bar{\boldsymbol{\sigma}}$, and continue at 11,
else set $k = k + 1$ and return to 6,
11- Compute the tangent modulus (stiffness tensors) of each phase,
12- Calculate concentration tensors using the tangent moduli of the phases,
13- Compute the overall stiffness tensor using (5.18). For the next step (n+1), continue at 1.

5.3.4 Tangent operators

Based on the governing equations (5.6), the increment of the overall stress and the associated nonlocal term is expressed as:

$$\Delta\bar{\boldsymbol{\sigma}} = \mathbb{T}^{\boldsymbol{\sigma}}_{\boldsymbol{\epsilon}} : \Delta\bar{\boldsymbol{\epsilon}} + \boldsymbol{T}^{\boldsymbol{\sigma}}_{r^{nl}}\,\Delta r^{nl}, \tag{5.19a}$$

$$\Delta\left[\langle\gamma^{nl}r\rangle - \langle\gamma^{nl}\rangle r^{nl}\right] = \boldsymbol{T}^{h}_{\epsilon} : \Delta\bar{\boldsymbol{\epsilon}} + T^{h}_{r^{nl}}\,\Delta r^{nl}, \tag{5.19b}$$

with

$$\Delta\left[\langle\gamma^{nl}r\rangle - \langle\gamma^{nl}\rangle r^{nl}\right] = V_0^f\gamma_0^{nl}\left(\Delta r - \Delta r^{nl}\right), \tag{5.20}$$

where $\mathbb{T}^{\boldsymbol{\sigma}}_{\bar{\varepsilon}}$ denotes the overall stiffness tensor computed using (5.18) by substituting the phases tangent moduli and the corresponding concentration tensors, and it is passed to the solver through the UMAT subroutine. In terms of nonlocal parameters in the inclusion phase, since the inclusion is considered elastic, the parameter γ_1^{nl} is considered zero in the nonlocal equation, however ξ^{nl} term is assumed to be uniform in whole of the RVE. Here, $\boldsymbol{T}^{\boldsymbol{\sigma}}_{r^{nl}}$, $\boldsymbol{T}^{h}_{\epsilon}$, and $T^{h}_{r^{nl}}$ are the associated nonlocal tangent operators, of which only $T^{h}_{r^{nl}}$ is required by HETVAL, and simply derived as:

$$T^{h}_{r^{nl}} = -\langle\gamma^{nl}\rangle = -(V_0^f\gamma_0^{nl} + V_1^f\cancelto{0}{\gamma_1^{nl}}) = -V_0^f\gamma_0^{nl}. \tag{5.21}$$

5.4 Results and discussion

In this section, the overall mechanical responses of the proposed multi-scale model are studied under small deformation assumption (up to 10%). The matrix phase material properties given in [1], and the inclusions are made of glass (elastic phase) with Young's modulus, $E^g = 72000\,\text{MPa}$, and Poisson's ratio, $\nu^g = 0.22$. Since, there is no experimental data yet, the model is first validated by a multi-layered structure (unilateral notched body) then is examined for a long glass fiber reinforced composite structure (notched plate). Finally, the influences of different parameters are explored as a parametric study for an asymmetrically double notched structure.

5.4.1 Preliminary validation of the nonlocal model against full-structure solution for multi-layered composite

The validity of the suggested Mori-Tanaka/TFA framework can be investigated using a multi-layered model [173]. In this respect, a unilateral notched body is considered (Figure 5.8-a). Initially, the proposed homogenization scheme is implemented on the structure subjected to a monotonic load on the external surfaces normal to Y-axis, then the obtained results are compared to a complete structural model without homogenization (Figure 5.9-a), consisting of 100 RVEs. In terms of boundary conditions, the base of the structure is fixed and the monotonic load is imposed from above (Figure 5.8-a). Each RVE is constituted from a polymer layer in the middle and two glass layers at the sides, in which the glass volume fraction is set as 20 percent (see Figure 5.9). The number of layers determines the size of RVE which should be much smaller than the considered length scale as discussed in the past sections. Here, the nonlocal parameters are given as $\gamma^{nl} = 5\,\text{GPa}$ (for the matrix) and $\xi^{nl} = 600\,\text{kN}$ ($l^{nl^2} = \xi^{nl}/\gamma^{nl}$), while the ratio between length scale and the RVE size is derived based on the number of RVEs in the structure which means $l^{nl}/l^{\varepsilon} \approx 36.51$. Figure 5.10 shows the distribution of von Mises stress and damage in the multi-layered structure and exhibits how the combination of the glass and PA 66 layers responds under loading. The responses of both models under the same boundary conditions are extracted as displacement-force curves in Figure 5.11. As observed, there is a good agreement between the two analyses.

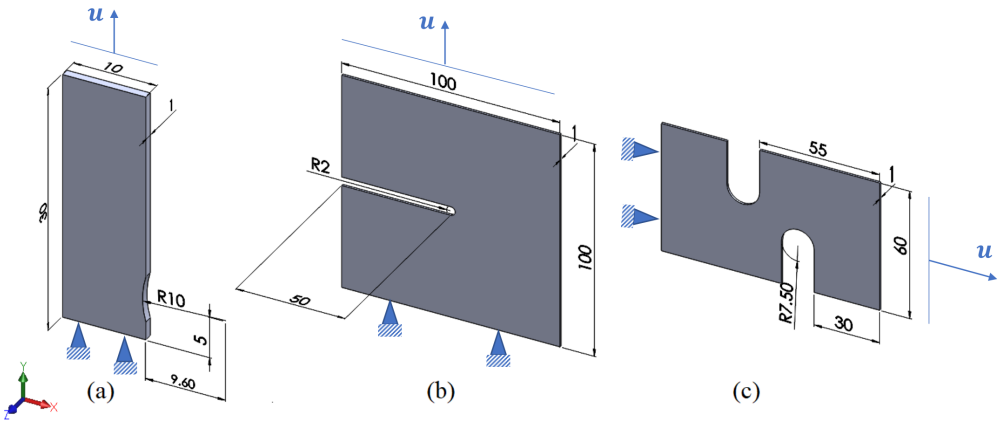

Figure 5.8: Geometrical dimensions and the corresponding boundary conditions of: a) unilateral notched plate, b) plate with a long notch, c) asymmetrically double notched structure.

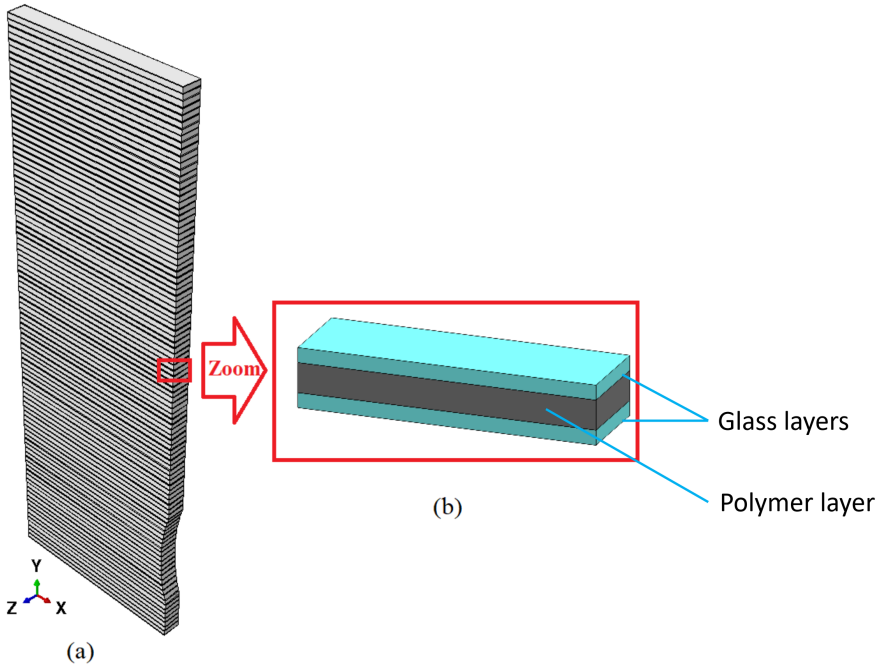

Figure 5.9: a) Multi-layered unilateral structure; b) zoom view and configuration of each RVE. The element type is the coupled temperature-displacement brick element (C3D8T)

.

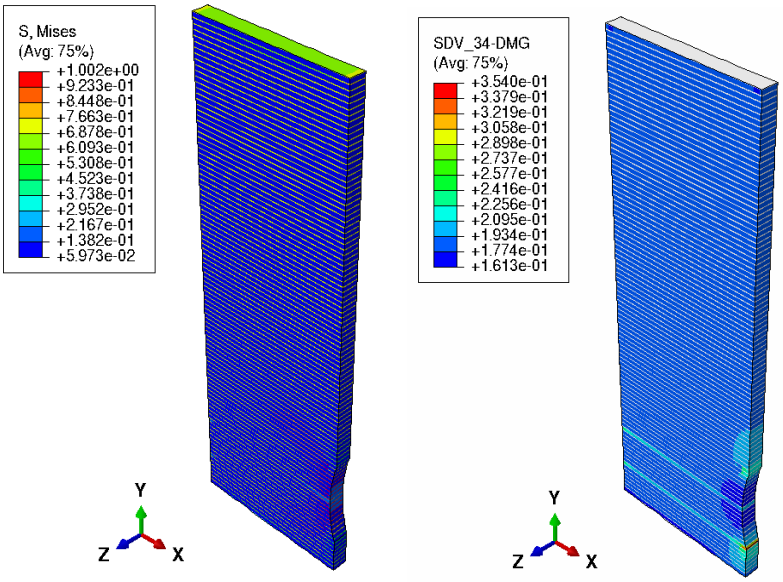

(a) von Mises stress 3D map (b) Damage 3D map

Figure 5.10: 3D maps of von Mises stress and damage under $5\,\mathrm{mm s^{-1}}$ monotonic loading rate in the multi-layered structure when $l^{nl}/l^{\varepsilon} \approx 36.51$. The element type is the coupled temperature-displacement brick element (C3D8T).

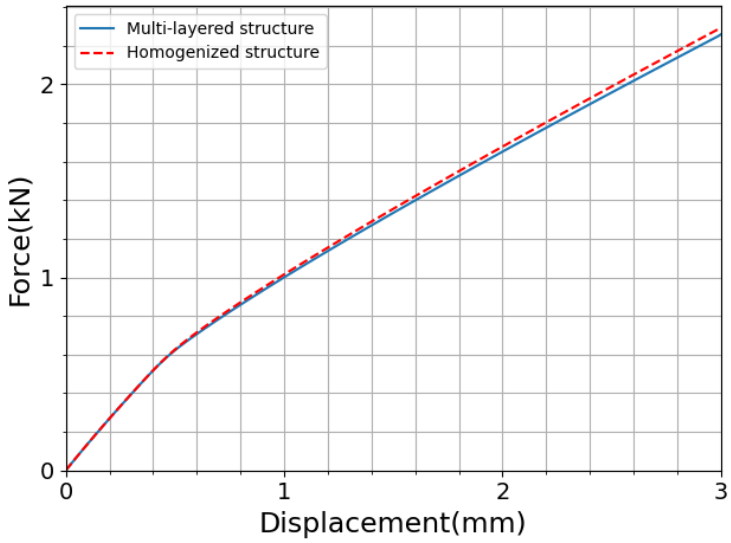

Figure 5.11: Force-displacement curve under $1.5\,\mathrm{mm\,s^{-1}}$ monotonic tensile loading for multi-layered and homogenized unilateral notched structure using the nonlocal framework when $l^{nl}/l^{\varepsilon} \approx 36.51$, $\xi^{nl} = 600\,\mathrm{kN}$, and $\gamma^{nl} = 5\,\mathrm{GPa}$.

5.4.2 Comparison of local and nonlocal models for long glass fiber reinforced structure

In this section, a composite notched plate is subjected to a monotonic tensile test, whose dimensions are given in Figure 5.8-b. The composite is considered as unidirectional long glass fiber reinforced polyamide 66 with the RVE given in Figure 5.2, and its overall mechanical behavior is estimated using the latter homogenization framework based on single fiber RVEs, oriented in Z-direction. The given structure is pulled from the upper side and fixed at the bottom, and the displacement controlled loading rate is assigned to $5\,\mathrm{mm\,s^{-1}}$ (5.8-b). Based on the present specified boundary conditions, local and nonlocal models are implemented on a commercial finite element software, and the mechanical responses are investigated. Figure 5.12 compares the force-displacement curves between local and nonlocal models. As shown, after some point, the nonlinear part of the curves in the local and nonlocal continuum models diverge, and the local model fails at a lower force level while the nonlocal model keeps evolving in a more stable way. Figure 5.13 shows the 3D maps of the matrix damage for the local and nonlocal models. As observed, in local models, the damage is localized in the crack zone passing through the structure. However in the nonlocal model, the damage remains around the notch region. In other words, the nonlocal model yields more stable responses in the small deformation zone compared the local framework. The notched plate is considered under the same boundary conditions, and the subsequent analysis is performed with different values of the nonlocal parameters when the nonlocal length scale is held constant. The resulting 3D damage maps are presented in Figure 5.14 for four sets of nonlocal parameters. As observed, changing the nonlocal parameters can invert the damage patterns. Consequently, the proposed model can lead to different damage profiles. Verification of the correct nonlocal parameters can be achieved through proper calibration against experimental data.

5.4.3 Parametric study

In this section, a parametric study is conducted to explore the effect of nonlocal parameters, volume fraction, and loading rates. To this end, an asymmetrically double notched structure is considered, whose dimensions are given in Figure 5.8-c. The boundary conditions are imposed on the external surfaces normal to X-axis. The displacement field is set to zero on one side, and a displacement controlled load is applied on the other side (Figure 5.8-c). As the previous section, the homogenization

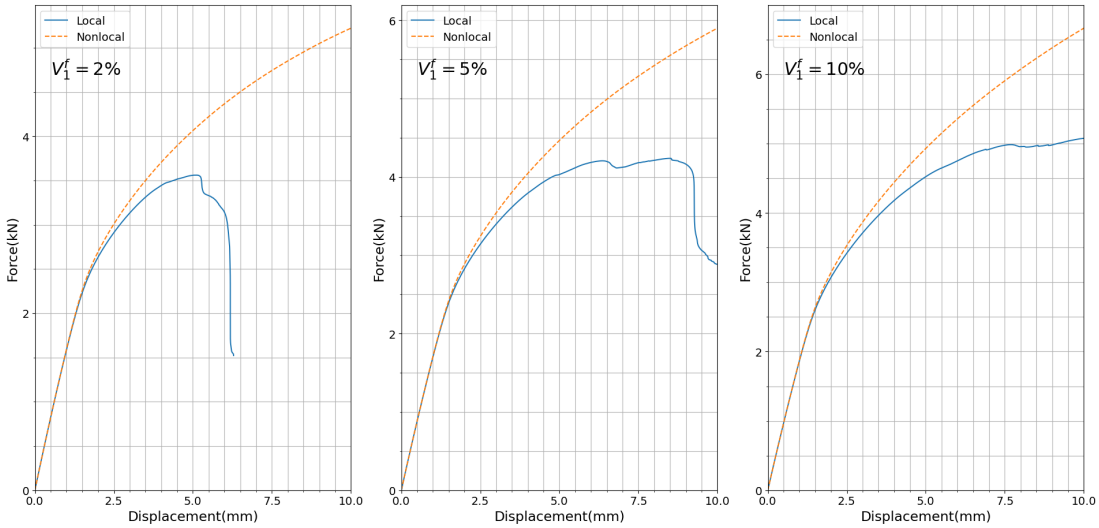

Figure 5.12: Force-displacement curves for the composite notched plate under $5\,\mathrm{mm\,s^{-1}}$ monotonic tensile loading using local and nonlocal models with $\xi^{nl} = 80\,\mathrm{kN}$ and $\gamma^{nl} = 5\,\mathrm{GPa}$ when $V_1^f = 2\%$, $V_1^f = 5\%$, and $V_1^f = 10\%$. The element type is the coupled temperature-displacement brick element (C3D8T).

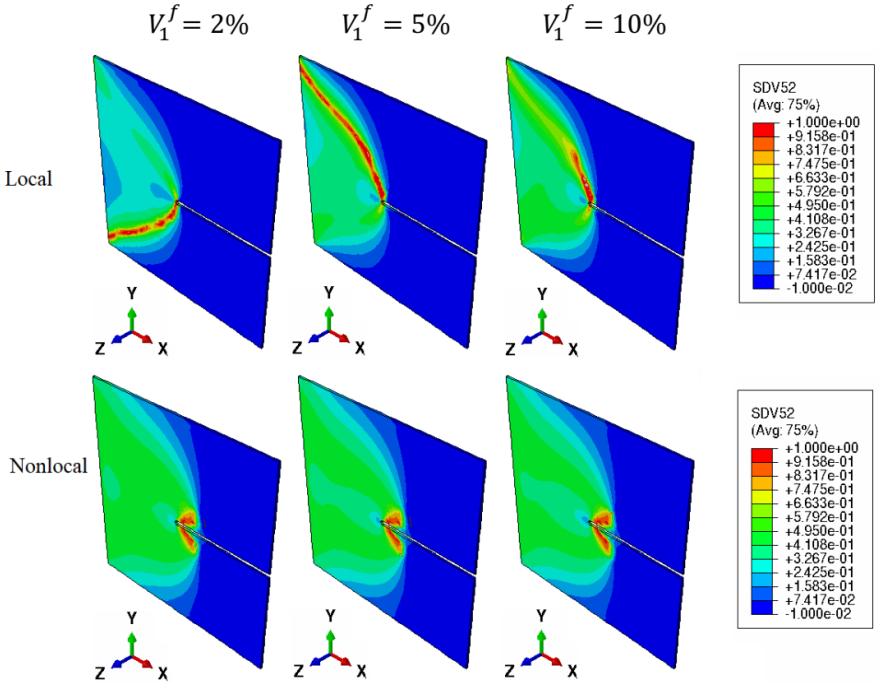

Figure 5.13: Matrix damage distribution in the notched plate under $5\,\mathrm{mm\,s^{-1}}$ monotonic tensile loading using local and nonlocal models with $\xi^{nl} = 80\,\mathrm{kN}$ and $\gamma^{nl} = 5\,\mathrm{GPa}$ when $V_1^f = 2\%$, $V_1^f = 5\%$, and $V_1^f = 10\%$.

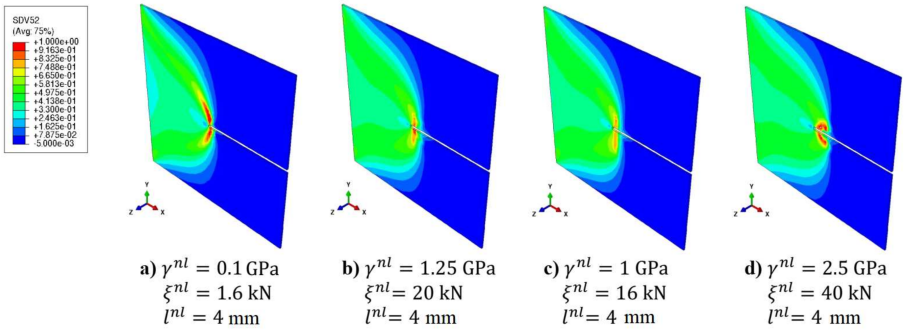

Figure 5.14: Matrix damage profile under $5\,\mathrm{mm\,s^{-1}}$ monotonic tensile loading using the nonlocal model with different ξ^{nl} and γ^{nl} when the length scale is constant ($l^{nl} = 4\,\mathrm{mm}$). The element type is the coupled temperature-displacement brick element (C3D8T).

framework is implemented based on the RVEs containing unidirectional long glass fibers, parallel to Z-axis, and the responses are conducted in different cases and compared with each other. Figure 5.15 shows the force-displacement curves in the different glass fiber volume fractions under the loading rate of $5\,mm\,\mathrm{s^{-1}}$ ($\gamma^{nl} = 5\,\mathrm{GPa}$, $\xi^{nl} = 80\,\mathrm{kN}$). As expected, the higher the volume fraction of glass fibers, the stiffer the structure becomes. Figure 5.16 shows more clearly how the volume fraction affects the stress level in the structure. As seen, for higher volume fractions, higher von Mises stress values are observed, and there is a stress concentration around the notches. For the latter analysis, the matrix damage profile also is shown in Figure 5.17, and the damage is mostly localized around the notches. Since the matrix phase is a viscoelastic viscoplastic material, the loading rate influences the material responses. In this respect, results at different loading rates are extracted for the composite with 10 percent glass fiber volume fraction, and the nonlocal parameters are given as $\gamma^{nl} = 5\,\mathrm{GPa}$ and $\xi^{nl} = 80\,\mathrm{kN}$ (see Figure 5.18). As observed, higher loading rates lead to higher slope curves and stiffer material behavior. However, the loading rate effect is more pronounced when the rate is increased to $50\,\mathrm{mm\,s^{-1}}$. Figures 5.15, 5.16, 5.17, and 5.18 imply that the impact of inclusion volume fraction and the loading rate on the composite mechanical behavior conforms to the expectations, and the present nonlocal framework does not violate them.

As discussed in the previous section, the nonlocal approach addresses early model failures and provides more stable results. The efficiency of the nonlocal scheme depends on the considered length scale controlled by the nonlocal parameters, γ^{nl} and ξ^{nl}. To study the influence of γ^{nl}, several analyses under $5\mathrm{mm\,s^{-1}}$ loading rate for different values of γ^{nl} are performed when ξ^{nl} is maintained constant

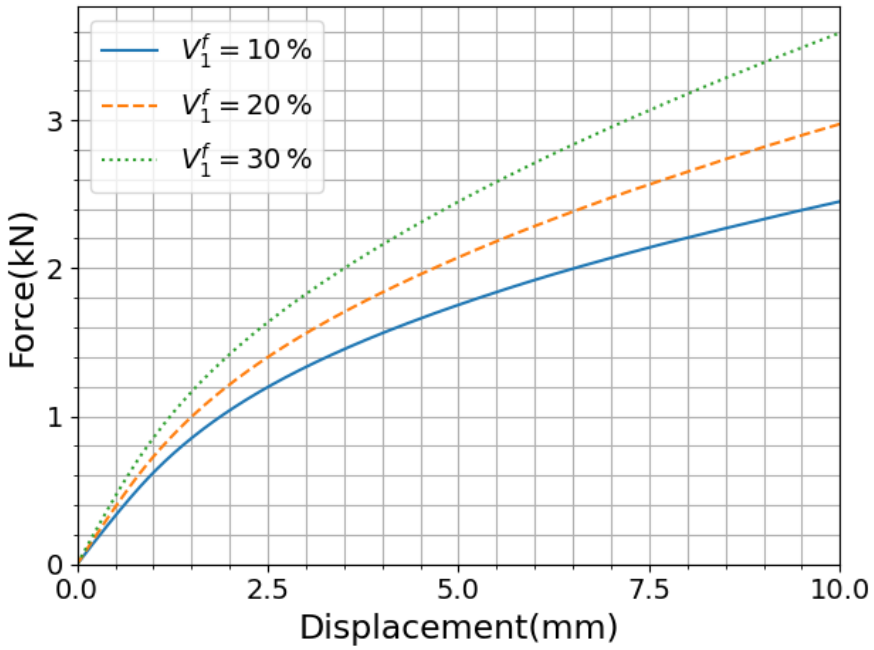

Figure 5.15: Force-displacement curves for the asymmetrically notched composite structure under 5 $\mathrm{mm\,s^{-1}}$ loading rate in different glass volume fractions ($\gamma^{nl} = 5\,\mathrm{GPa}$, $\xi^{nl} = 80\,\mathrm{kN}$).

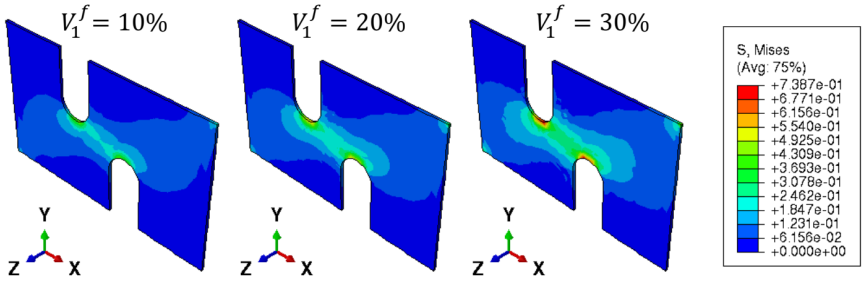

Figure 5.16: Von Mises stress distribution under 5 $\mathrm{mm\,s^{-1}}$ loading rate for the asymetrically notched structure with $\gamma^{nl} = 5\,\mathrm{GPa}$ and $\xi^{nl} = 80\,\mathrm{kN}$ when $V_1^f = 10\%$, $V_1^f = 20\%$, and $V_1^f = 30\%$.

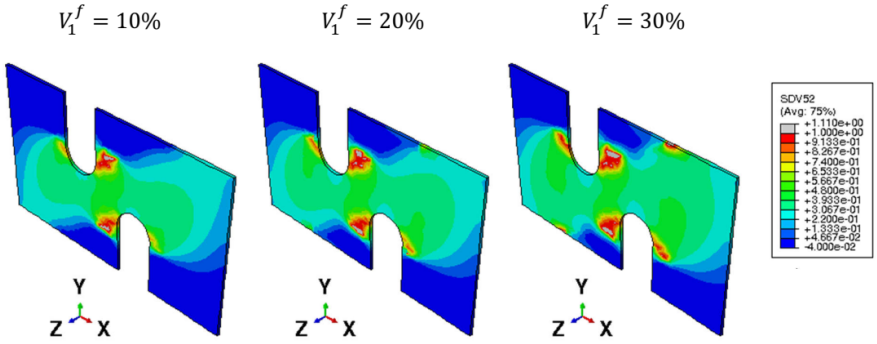

Figure 5.17: Matrix damage distribution under $5\,\mathrm{mm\,s^{-1}}$ loading rate for the asymetrically notched structure with $\gamma^{nl} = 5\,\mathrm{GPa}$ and $\xi^{nl} = 80\,\mathrm{kN}$ when $V_1^f = 10\%$, $V_1^f = 20\%$, and $V_1^f = 30\%$.

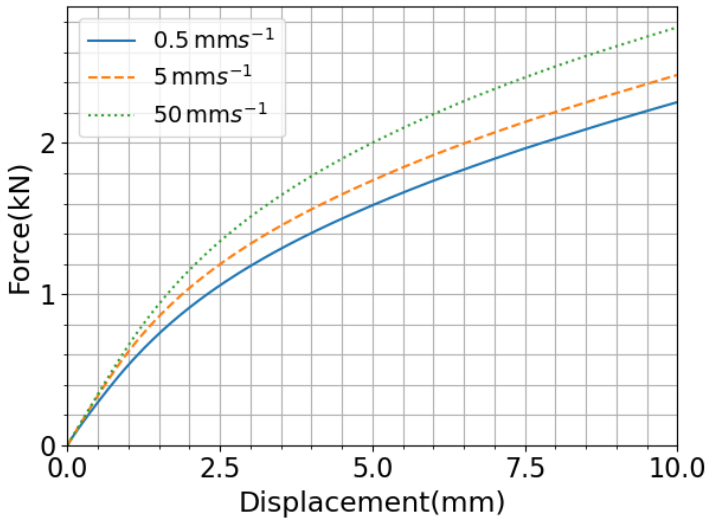

Figure 5.18: Force-displacement curves for the asymmetrically notched composite structure with $\gamma^{nl} = 5\,\mathrm{GPa}$ and $\xi^{nl} = 80\,\mathrm{kN}$ when $V_1^f = 10\%$.

at 80 kN, and the results are extracted as force-displacement curves in Figure 5.19. One can see that the effect of γ^{nl} is much smaller in its higher values. In other words, beyond a certain level of γ^{nl}, the differences in the curves become negligible. Figure 5.20 shows the effect of γ^{nl} in three different volume fractions, and as shown, its impact in all volume fractions is similar. By keeping $\gamma^{nl} = 5\,\text{GPa}$, the influence of ξ^{nl} is studied through several analyses under the same boundary conditions. Figure 5.21 provides the force-displacement curves in several values of ξ^{nl} for three different volume fractions of glass fiber. As observed, for larger values of ξ^{nl} the model is stiffer and its impact does not change by increasing the glass fiber volume fraction.

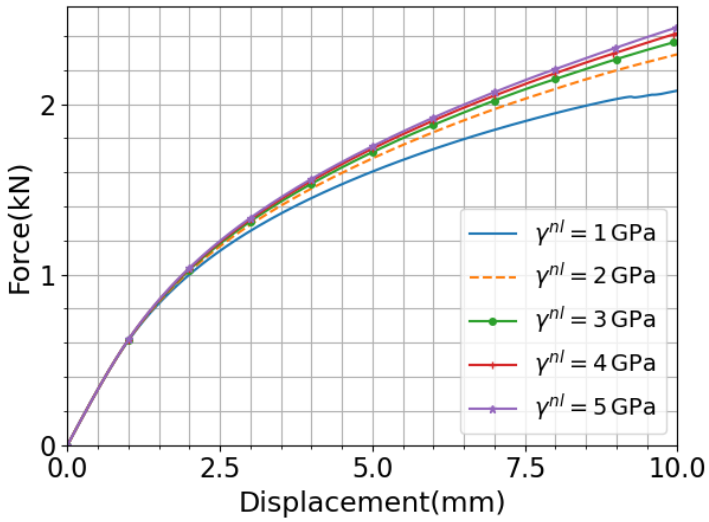

Figure 5.19: Force-displacement curves for the asymmetrically notched composite structure under 5 $\text{mm}\,\text{s}^{-1}$ loading rate in different γ^{nl} with $\xi^{nl} = 80\,\text{kN}$ when $V_1^f = 10\%$.

5.5 Conclusion

In this chapter, the shortcoming of the conventional multi-scale models regarding the physical characterization of composites undergoing high level damage was addressed by a gradient enhanced nonlocal approach. In the microscale, the matrix phase constitutive laws have been derived using the thermodynamics of irreversible processes and the generalized standard material formalism. To provide an appropriate multi-scale framework, the relationship between the nonlocal length scale and RVE size has been discussed, and the Mori-Tanaka/TFA approach has been implemented for homogenization when $l^{nl} \gg l^{\varepsilon}$, based on which the nonlocal approach is implemented at the macroscale. To develop

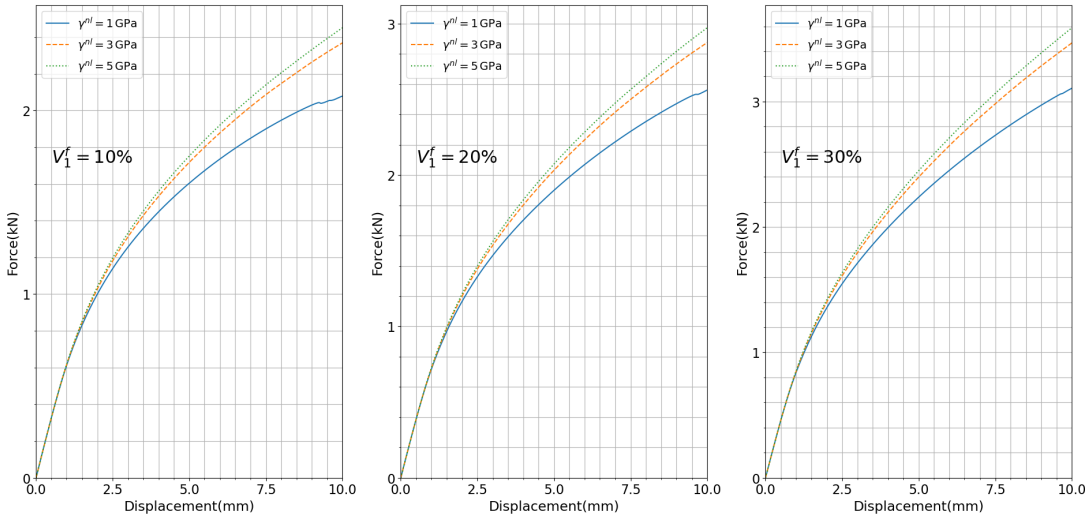

Figure 5.20: Force-displacement curves for the asymmetrically notched composite structure under 5 $\text{mm}\,\text{s}^{-1}$ loading rate in different γ^{nl} with $\xi^{nl} = 80\,\text{kN}$ when $V_1^f = 10\%$, $V_1^f = 20\%$, and $V_1^f = 30\%$.

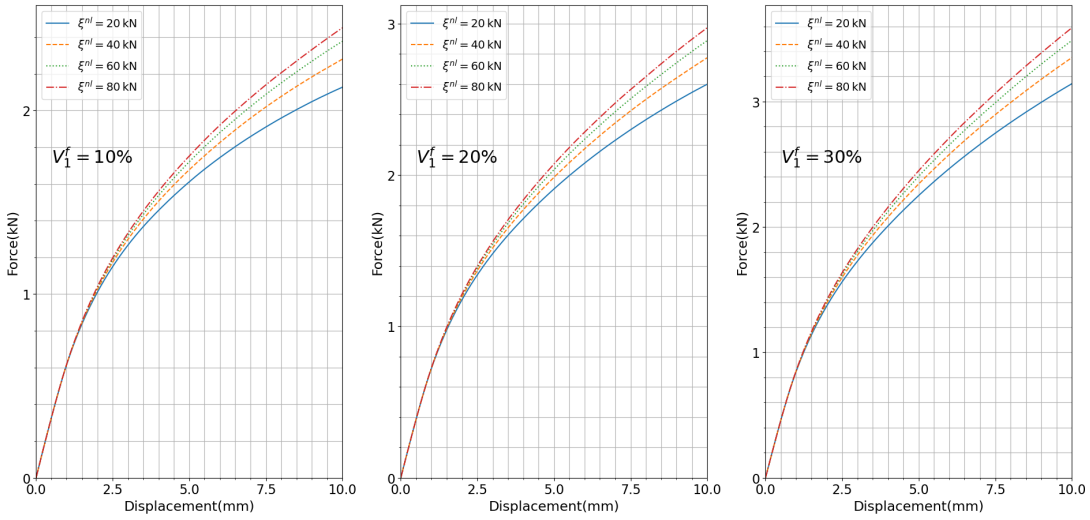

Figure 5.21: Force-displacement curves for the asymmetrically notched composite structure under 5 $\text{mm}\,\text{s}^{-1}$ loading rate in different ξ^{nl} with $\gamma^{nl} = 5\,\text{GPa}$ when $V_1^f = 10\%$, $V_1^f = 20\%$, and $V_1^f = 30\%$.

the nonlocal field within the FE tool, an analogy between the steady state heat flux equation and the gradient enhanced relationship was considered, which allowed using the fully coupled temperature displacement package in ABAQUS. The numerical examples presented in this study express the capability of the nonlocal model to fully characterize the composite material behavior in high damage levels under small deformation assumption. The resulting responses imply the good performance of the gradient enhanced thermodynamic model as a nonlocal approach in glass reinforced semi-crystalline polymers.

Chapter 6

Conclusions and perspectives

6.1 Conclusions

The scope of the thesis was to study the nonlinear behavior of polyamide 66 and its related composites, taking into account environmental conditions, pressure-sensitive behavior, and damage. In these materials, high level of damage is accompanied by softening leading to ill-posed problems and non-unique results in the computational models. Moreover, they exhibit tension-compression asymmetry when undergoing non-proportional loading and high sensitivity to environmental conditions, particularly humidity. In the present work, a viscoelastic viscoplastic damageable model (VEVPD) was presented, in which the hydrostatic pressure effect and tension-compression asymmetry is included. An experimental campaign was designed to study the dominant mechanisms and identify the parameters of the proposed framework. Then, the model was improved using the nonlocal gradient enhanced approach to obtain unique responses for the heavily damaged material. This was extended to a multi-scale framework for modeling the composite behavior. In the following, the outcomes are briefly listed for each chapter.

First, in chapter 2, the phenomenological VEVPD model developed in our group by Praud et al. [14] was extended to a more advanced model accounting for tension-compression asymmetry and hydrostatic pressure effect characterizing semi-crystalline polymers. A parametric study using 0D and 3D solvers was performed, and the effect of the tension-compression asymmetry parameter, m, on the stress-strain curves and damage profiles under different boundary conditions was investigated. The parametric study revealed that the asymmetry parameter effect is more significant when the material undergoes multi-axial or cyclic tension-compression loading. This leads to asymmetric profiles of the

internal state variables, such as damage or plasticity, and increase of asymmetry in the stress-strain curves under cyclic loading.

In chapter 3, an experimental campaign was designed and performed, in which dog bone samples with different water contents were subjected to mechanical tests including monotonic load, loading-unloading, and creep-recovery. This allowed investigating the variation of the mechanical response from rubbery-like to glassy-like by reconditioning the polyamide 66 material at different Relative Humidity (RH) conditions. The mechanical tests showed time-dependent strain along with creep, and ductile damage depending on the sample water uptake represented by different RH conditioning levels. The experimental data obtained from dog bone samples was employed to identify the von Mises-based model. Indeed, prior to this study, the von Mises-based VEVPD model had only been calibrated and validated for PA66 at RH50 [14]. In this study, for the first time the VEVPD model based on von Mises yield function was calibrated and validated for PA66 with RH0, RH25, RH65, and RH80. The validation results reveal that the VEVPD model provides accurate predictions for high RH level namely: RH50, RH65, RH80. In addition to capture the tension-compression asymmetry, tension-torsion tests were implemented on the diabolo-type specimens. The obtained global force-displacement and moment-angle curves were used to calibrate the I_1-J_2-based model. The asymmetry parameter identified in RH50 ($m = 1.05$) indicates that the compressive yield strength is slightly higher than the tensile yield strength. However, for RH65, the asymmetry parameter was identified as $m = 1.00$, which can be interpreted as symmetric behavior. This main result confirmed that the polyamide 66 response is highly depend on the RH.

To address the non-physical responses in high levels of damage, chapter 4 presented an extension of the local continuum model to a nonlocal framework through the gradient enhanced approach. In terms of nonlocal variable, two options were investigated: nonlocal damage and nonlocal hardening state variable that is driving the damage accumulation. Parametric studies show that the nonlocal damage model does not yield the desired physical results because the plasticity-related localization is not addressed. However, the gradient enhanced model based on the nonlocal hardening state variable is more efficient and leads to unique responses, as it implicitly accounts for the damage localization. Thus, the limitation of the local continuum model in characterizing the material behavior exhibiting severe damaged areas was addressed by using the gradient enhanced model with the nonlocal variable derived from the hardening state variable. Moreover, both UMAT-UEL and UMAT-HETVAL tools

were used to implement the nonlocal framework on the computational model, and they conducted same responses. However, UMAT-HETVAL is less computationally expensive when the nonlocal fields are scalar variables, as in the present study.

In chapter 5, the nonlocal model was extended to a multi-scale framework. The multi-scale model in different cases was investigated, and the magnitude of the nonlocal length scale versus the RVE size for nonlocal regularization was discussed. The investigations revealed that the homogenization becomes complex and the RVE is not representative when the length scale is comparable or smaller than the RVE size. Considering the length scale much larger than the RVE size, a proper nonlocal Mori-Tanaka/TFA framework was formulated for the first time. The multi-scale model was validated with a full-structure multi-layered composite finite element model, and a parametric study was performed to investigate its efficiency. For different types of composite structures, the results of the parametric study demonstrate that the responses of the nonlocal model were found more stable at a high damage level compared to the local model, as expected.

6.2 Perspectives

Until now, hydrostatic pressure and tension-compression asymmetry have been taken into account in modeling the behavior of thermoplastics as pressure-sensitive materials through the I_1-J_2 yield function. In addition, multi-axial mechanical tension-torsion tests were performed in chapter 3, which allowed calibration of the model accounting for the asymmetric yield behavior. However, as shown through the parametric analysis presented in chapter 2, the model subjected to cyclic tension-compression loading exhibits more pronounced asymmetric responses, whereas the experimental data obtained in chapter 3 are extracted from monotonic multi-axial loading. Thus, the present VEVPD based on the I_1-J_2 function should be calibrated for more general cases by designing performing additional experimental test configurations including multi-axial cyclic tests. Moreover, since the present model also captures the hydrostatic pressure, it can be better evaluated through mechanical tests under internal hydrostatic pressure, such as water-filled cylindrical samples. In that sense, tension-torsion-internal pressure would be an appropriate test configuration to enrich the experimental database for the identification.

Although the local model has been calibrated and validated at different RHs, it does not provide

sufficient agreement with experiments for RH0 and RH25. In other words, the model does not take into account certain active mechanisms at low RH, such as brittle damage or almost rate-independent response of thermoplastics at low extent of water content. This can be addressed by developing an elasto-viscoplastic model with brittle damage decoupled from plasticity [143,174,175]. In addition, the nonlocal framework has not yet been calibrated, and the nonlocal parameters and subsequently the length scale are still unknown. Therefore, nonlocal phenomena in thermoplastics and composites and the effect of RH on their behavior under high damage levels are the issues that have not been sufficiently investigated. To this end, a mixed numerical-experimental framework should be designed to identify the nonlocal length scale at different RH, for which local average measurements and compact tension tests are proposed in the literature depending on the active mechanisms in the material [141,176].

In the present work, the nonlocal multi-scale model was developed for composites with unidirectional long fiber inclusions, and its effectiveness in addressing nonlocal phenomena was evaluated through a parametric study. The orientation and shape of the inclusions in the composites can be accounted for in the model through micromechanical or finite element-based multi-scale models. An experimental study on reconditioned composites at different RH would also provide useful information about active and dominant mechanisms, based on which the multi-scale model can be modified and extended. Although there have been some experimental studies about the RH effect on PA66 composites in the literature [177], this can be a novel research to also study the effect of RH on nonlocal parameters and length scale in comparison with experimental data.

To predict the long-term mechanical responses of composites, a variety of environmental factors must be considered based on operating conditions, such as contact with water or chemical solvents, exposure to high or low temperatures, etc. For example, glass-reinforced thermoplastics used in the automotive industry are in permanent contact with chemical solvents, such as antifreeze (a mixture of water and ethylene glycol), which affects their mechanical behavior, and the nonlinear inelastic mechanisms are strongly affected, resulting in glassy to rubbery and less or more time-dependent behavior [178]. These operating conditions are often along with high temperature, such as the composites used in the cooling radiators [179]. Thus, the model needs to include more environmental factors and extended to chemico-mechanical coupling. To calibrate such a comprehensive model, the experimental data can be extracted from the mechanical tests implemented on samples reconditioned under different temperatures and aging conditions (glycol, water, etc.).

In this work, the VEVPD model has been validated and calibrated for different RH levels. In a more general context, it is possible to design and calibrate data-driven models that can lead to computationally less expensive predictions of the material behavior. [180, 181]. Generating a large enough database using the identified constitutive law, the physical based model can be replaced by a data-driven framework. The latter should be capable of providing the mechanical responses at arbitrary loading conditions and RH. The developed model using data-driven framework can be employed in Virtual/Augmented Reality (VR/AR) solutions to conduct real time responses in a digital, virtual, and hybrid twin [182].

Bibliography

[1] A. Benaarbia, G. Chatzigeorgiou, B. Kiefer et F. Meraghni, "A fully coupled thermo-viscoelastic-viscoplastic-damage framework to study the cyclic variability of the taylor-quinney coefficient for semi-crystalline polymers," *International Journal of Mechanical Sciences*, vol. 163, p. 105128, 11 2019.

[2] G. Chatzigeorgiou, F. Meraghni et N. Charalambakis, *Multiscale Modeling Approaches for Composites*. Elsevier, 2022.

[3] M. Arif, N. Saintier, F. Meraghni, J. Fitoussi, Y. Chemisky et G. Robert, "Multiscale fatigue damage characterization in short glass fiber reinforced polyamide-66," *Composites Part B: Engineering*, vol. 61, p. 55–65, 5 2014.

[4] M. Boyce, D. Parks et A. Argon, "Large inelastic deformation of glassy polymers. part i: rate dependent constitutive model," *Mechanics of Materials*, vol. 7, n°. 1, p. 15–33, 9 1988.

[5] E. Arruda et M. Boyce, "A three-dimensional constitutive model for the large stretch behavior of rubber elastic materials," *Journal of The Mechanics and Physics of Solids*, vol. 41, n°. 2, p. 389–412, 1993.

[6] C. Buckley et D. Jones, "Glass-rubber constitutive model for amorphous polymers near the glass transition," *Polymer*, vol. 36, n°. 17, p. 3301–3312, 1995.

[7] T. A. Tervoort, R. J. M. Smit, W. A. M. Brekelmans et L. E. Govaert, "A constitutive equation for the elasto-viscoplastic deformation of glassy polymers," *Mechanics of Time-Dependent Materials*, vol. 1, n°. 3, p. 269–291, 1997.

[8] L. Govaert, P. Timmermans et W. Brekelmans, "The influence of intrinsic strain softening on strain localization in polycarbonate: modeling and experimental validation," *Journal of Engineering Materials and Technology*, vol. 122, n°. 2, p. 177–185, 2000.

[9] E. Klompen, T. Engels, L. Govaert et H. Meijer, "Modeling of the postyield response of glassy polymers: influence of thermomechanical history," *Macromolecules*, vol. 38, n°. 16, p. 6997–7008, 8 2005.

[10] A. Launay, M. Maitournam, Y. Marco, I. Raoult et F. Szmytka, "Cyclic behaviour of short glass fibre reinforced polyamide: Experimental study and constitutive equations," *International Journal of Plasticity*, vol. 27, n°. 8, p. 1267–1293, 8 2011.

[11] N. Billon, "New constitutive modeling for time-dependent mechanical behavior of polymers close to glass transition: Fundamentals and experimental validation," *Journal of Applied Polymer Science*, vol. 125, n°. 6, p. 4390–4401, 3 2012.

[12] A. Maurel-Pantel, E. Baquet, J. Bikard, J.-L. Bouvard et N. Billon, "A thermo-mechanical large deformation constitutive model for polymers based on material network description: Application to a semi-crystalline polyamide 66," *International Journal of Plasticity*, vol. 67, p. 102–126, 2015.

[13] T. Zink, L. Kehrer, V. Hirschberg, M. Wilhelm et T. Böhlke, "Nonlinear schapery viscoelastic material model for thermoplastic polymers," *Journal of Applied Polymer Science*, vol. 139, n°. 17, p. 52028, 2022.

[14] F. Praud, G. Chatzigeorgiou, J. Bikard et F. Meraghni, "Phenomenological multi-mechanisms constitutive modelling for thermoplastic polymers, implicit implementation and experimental validation," *Mechanics of Materials*, vol. 114, p. 9–29, 11 2017.

[15] A. Benaarbia, A. Chrysochoos et G. Robert, "Influence of relative humidity and loading frequency on the pa6.6 cyclic thermomechanical behavior: part i. mechanical and thermal aspects," *Polymer Testing*, vol. 40, p. 290–298, 12 2014.

[16] J. C. Simo et T. J. Hughes, *Computational inelasticity*. Springer Science & Business Media, 2006, vol. 7.

[17] G. Papanicolaou et S. Zaoutsos, *Viscoelastic constitutive modeling of creep and stress relaxation in polymers and polymer matrix composites.* Elsevier, 2011, p. 3–59.

[18] C. Rodas, F. Zaïri et M. Naït-Abdelaziz, "A finite strain thermo-viscoelastic constitutive model to describe the self-heating in elastomeric materials during low-cycle fatigue," *Journal of The Mechanics and Physics of Solids*, vol. 64, n°. 64, p. 396–410, 2014.

[19] B. Miled, I. Doghri et L. Delannay, "Coupled viscoelastic–viscoplastic modeling of homogeneous and isotropic polymers: Numerical algorithm and analytical solutions," *Computer Methods in Applied Mechanics and Engineering*, vol. 200, n°. 47-48, p. 3381–3394, 2011.

[20] A. Krairi et I. Doghri, "A thermodynamically-based constitutive model for thermoplastic polymers coupling viscoelasticity, viscoplasticity and ductile damage," *International Journal of Plasticity*, vol. 60, p. 163–181, 2014.

[21] R. Rivlin, *Integral representations of constitutive equations.* Springer New York, 1983, vol. 22, p. 1615–1622.

[22] A. Pipkin et T. Rogers, "A non-linear integral representation for viscoelastic behaviour," *Journal of the Mechanics and Physics of Solids*, vol. 16, n°. 1, p. 59–72, 1 1968.

[23] J. Chaboche et G. Rousselier, "On the plastic and viscoplastic constitutive equations—part i: rules developed with internal variable concept," *Journal of Pressure Vessel Technology*, vol. 105, n°. 2, p. 153–158, 5 1983.

[24] E. Contesti et G. Cailletaud, "Description of creep-plasticity interaction with non-unified constitutive equations: application to an austenitic stainless steel," *Nuclear Engineering and Design*, vol. 116, n°. 3, p. 265–280, 9 1989.

[25] J. L. Chaboche, "A review of some plasticity and viscoplasticity constitutive theories," *International Journal of Plasticity*, vol. 24, n°. 10, p. 1642–1693, 10 2008.

[26] R. Barrett, P. O'donoghue et S. Leen, "An improved unified viscoplastic constitutive model for strain-rate sensitivity in high temperature fatigue," *International Journal of Fatigue*, vol. 48, p. 192–204, 3 2013.

[27] G. Cailletaud et K. Saï, "Study of plastic/viscoplastic models with various inelastic mechanisms," *International Journal of Plasticity*, vol. 11, n°. 8, p. 991–1005, 1 1995.

[28] V. Velay, G. Bernhart et L. Penazzi, "Cyclic behavior modeling of a tempered martensitic hot work tool steel," *International Journal of Plasticity*, vol. 22, n°. 3, p. 459–496, 3 2006.

[29] G. Kang, Q. Kan, J. Zhang et Y. Liu, "Constitutive modeling for uniaxial time-dependent ratcheting of ss304 stainless steel," *Key Engineering Materials*, vol. 340-341, p. 817–822, 6 2007.

[30] A. Benaarbia, J. Rouse et W. Sun, "A thermodynamically-based viscoelastic-viscoplastic model for the high temperature cyclic behaviour of 9–12100–121, 8 2018.

[31] H. Tresca, "Memoire sur l'écoulement des solides à de forte pressions," *Acad. Sci. Paris*, vol. 2, n°. 1, p. 59, 1864.

[32] R. v. Mises, "Mechanik der festen körper im plastisch-deformablen zustand," *Nachrichten von der Gesellschaft der Wissenschaften zu Göttingen, Mathematisch-Physikalische Klasse*, vol. 1913, p. 582–592, 1913.

[33] C. A. Coulomb, "Essai sur une application des regles de maximis et minimis a quelques problemes de statique relatifs a l'architecture (essay on maximums and minimums of rules to some static problems relating to architecture)," 1973.

[34] D. C. Drucker et W. Prager, "Soil mechanics and plastic analysis or limit design," *Quarterly of applied mathematics*, vol. 10, n°. 2, p. 157–165, 1952.

[35] M. Nachtane, F. Meraghni, G. Chatzigeorgiou, L. Harper et F. Pelascini, "Multiscale viscoplastic modeling of recycled glass fiber-reinforced thermoplastic composites: Experimental and numerical investigations," *Composites Part B: Engineering*, vol. 242, p. 110087, 2022.

[36] Q. Chen, G. Chatzigeorgiou et F. Meraghni, "Extended mean-field homogenization of viscoelastic-viscoplastic polymer composites undergoing hybrid progressive degradation induced by interface debonding and matrix ductile damage," *International Journal of Solids and Structures*, vol. 210, p. 1–17, 2021.

[37] D. Morin, G. Haugou, B. Bennani et F. Lauro, "Experimental characterization of a toughened epoxy adhesive under a large range of strain rates," *Journal of Adhesion Science and Technology*, vol. 25, n°. 13, p. 1581–1602, 1 2011.

[38] L. Dufour, B. Bourel, F. Lauro, G. Haugou et N. Leconte, "A viscoelastic-viscoplastic model with non associative plasticity for the modelling of bonded joints at high strain rates," *International Journal of Adhesion and Adhesives*, vol. 70, p. 304–314, 10 2016.

[39] G. H. B. Donato et M. Bianchi, "Pressure dependent yield criteria applied for improving design practices and integrity assessments against yielding of engineering polymers," *Journal of Materials Research and Technology*, vol. 1, n°. 1, p. 2–7, 2012.

[40] S. Olufsen, A. Clausen et O. Hopperstad, "Influence of stress triaxiality and strain rate on stress-strain behaviour and dilation of mineral-filled pvc," *Polymer Testing*, vol. 75, p. 350–357, 5 2019.

[41] J. P. Manaia, F. A. Pires, A. M. De Jesus et S. Wu, "Mechanical response of three semi crystalline polymers under different stress states: Experimental investigation and modelling," *Polymer Testing*, vol. 81, p. 106156, 2020.

[42] R. Raghava, R. Caddell et G. Yeh, "The macroscopic yield behaviour of polymers," *Journal of Materials Science*, vol. 8, n°. 2, p. 225–232, 2 1973.

[43] Y. Lee et J. Ghosh, "The significance of j3 to the prediction of shear bands," *International Journal of Plasticity*, vol. 12, n°. 9, p. 1179–1197, 1996.

[44] E. Ghorbel, "A viscoplastic constitutive model for polymeric materials," *International Journal of Plasticity*, vol. 24, n°. 11, p. 2032–2058, 11 2008.

[45] A. L. Gurson, "Continuum theory of ductile rupture by void nucleation and growth: Part i—yield criteria and flow rules for porous ductile media," 1977.

[46] P. Raghavan et S. Ghosh, "A continuum damage mechanics model for unidirectional composites undergoing interfacial debonding," *Mechanics of materials*, vol. 37, n°. 9, p. 955–979, 2005.

[47] C. Chu et A. Needleman, "Void nucleation effects in biaxially stretched sheets," 1980.

[48] V. Tvergaard et A. Needleman, "Effects of nonlocal damage in porous plastic solids," *International Journal of Solids and Structures*, vol. 32, n°. 8-9, p. 1063–1077, 1995.

[49] J. Koplik et A. Needleman, "Void growth and coalescence in porous plastic solids," *International Journal of Solids and Structures*, vol. 24, n°. 8, p. 835–853, 1988.

[50] J. Pamin, "Gradient plasticity and damage models: a short comparison," *Computational Materials Science*, vol. 32, n°. 3-4, p. 472–479, 1994.

[51] A. Benaarbia, A. Chrysochoos et G. Robert, "Kinetics of stored and dissipated energies associated with cyclic loadings of dry polyamide 6.6 specimens," *Polymer Testing*, vol. 34, p. 155–167, 4 2014.

[52] Z. Bažant, "Instability, ductility, and size effect in strain-softening concrete," *Journal of the Engineering Mechanics Division*, vol. 102, n°. 2, p. 331–344, 4 1976.

[53] Z. Bažant et F. Lin, "Nonlocal smeared cracking model for concrete fracture," *Journal of Structural Engineering*, vol. 114, n°. 11, p. 2493–2510, 11 1988.

[54] G. Pijaudier-cabot et Z. Bažant, "Nonlocal damage theory," *Journal of Engineering Mechanics*, vol. 113, n°. 10, p. 1512–1533, 10 1987.

[55] M. Jirásek, Jirásek, M, Jirásek, M, S. Rolshoven et P. Grassl, "Nonlocal models for damage and fracture: Comparison of approaches," *International Journal for Numerical and Analytical Methods in Geomechanics*, vol. 35, n°. 6, p. 653–670, 1998.

[56] M. Jirásek, "Objective modeling of strain localization," *Revue Française de Génie Civil*, vol. 6, n°. 6, p. 1119–1132, 1 2002.

[57] M. Jirásek, S. Rolshoven et P. Grassl, "Size effect on fracture energy induced by non-locality," *International Journal for Numerical and Analytical Methods in Geomechanics*, vol. 28, n°. 78, p. 653–670, 6 2004.

[58] M. Jirásek, "Nonlocal damage mechanics," *Revue européenne de génie civil*, vol. 11, n°. 7-8, p. 993–1021, 10 2007.

[59] Z. Bažant, T. Belytschko et T. Chang, "Continuum theory for strain-softening," *Journal of Engineering Mechanics*, vol. 110, n°. 12, p. 1666–1692, 12 1984.

[60] R. Peerlings, M. Geers, D. Borst et W. Brekelmans, "A critical comparison of nonlocal and gradient-enhanced softening continua," *International Journal of Solids and Structures*, vol. 38, n°. 44, p. 7723–7746, 2001.

[61] S. Forest, "Micromorphic approach for gradient elasticity, viscoplasticity, and damage," *Journal of Engineering Mechanics*, vol. 135, n°. 3, p. 117–131, 3 2009.

[62] B. Dimitrijevic et K. Hackl, "A regularization framework for damage-plasticity models via gradient enhancement of the free energy," *International Journal for Numerical Methods in Biomedical Engineering*, vol. 27, n°. 8, p. 1199–1210, 2011.

[63] K. Saanouni et M. Hamed, "Micromorphic approach for finite gradient-elastoplasticity fully coupled with ductile damage: Formulation and computational aspects," *International Journal of Solids and Structures*, vol. 50, n°. 14-15, p. 2289–2309, 7 2013.

[64] C. Miehe, M. Hofacker et F. Welschinger, "A phase field model for rate-independent crack propagation: Robust algorithmic implementation based on operator splits," *Computer Methods in Applied Mechanics and Engineering*, vol. 199, n°. 45, p. 2765–2778, 2010.

[65] C. Miehe, F. Aldakheel et A. Raina, "Phase field modeling of ductile fracture at finite strains: A variational gradient-extended plasticity-damage theory," *International Journal of Plasticity*, vol. 84, p. 1–32, 2016.

[66] R. de Borst et C. V. Verhoosel, "Gradient damage vs phase-field approaches for fracture: Similarities and differences," *Computer Methods in Applied Mechanics and Engineering*, vol. 312, p. 78–94, 2016.

[67] J.-Y. Wu et V. P. Nguyen, "A length scale insensitive phase-field damage model for brittle fracture," *Journal of the Mechanics and Physics of Solids*, vol. 119, p. 20–42, 2018.

[68] F. Praud, T. Schmitt, O. Zabeida, S. Maïza, L. Martinu et M. Lévesque, "Phase field fracture models to predict crack initiation and propagation in anti-reflective coatings," *Thin Solid Films*, vol. 736, p. 138920, 2021.

[69] S. Silling, "Reformulation of elasticity theory for discontinuities and long-range forces," *Journal of The Mechanics and Physics of Solids*, vol. 48, n°. 1, p. 175–209, 2000.

[70] S. Silling et R. Lehoucq, *Peridynamic theory of solid mechanics.* Elsevier, 2010, vol. 44, p. 73–168.

[71] A. C. Eringen, *Nonlocal continuum field theories.* Springer, 2002.

[72] S. Forest, "Nonlinear regularization operators as derived from the micromorphic approach to gradient elasticity, viscoplasticity and damage," *Proceedings of the Royal Society A: Mathematical, Physical and Engineering Sciences*, vol. 472, n°. 2188, p. 20150755, 2009.

[73] A. A. Griffith, "Vi. the phenomena of rupture and flow in solids," *Philosophical transactions of the royal society of london. Series A, containing papers of a mathematical or physical character*, vol. 221, n°. 582-593, p. 163–198, 1921.

[74] S. A. Silling et R. B. Lehoucq, "Peridynamic theory of solid mechanics," *Advances in applied mechanics*, vol. 44, p. 73–168, 2010.

[75] G. Borino, B. Failla et F. Parrinello, "A symmetric nonlocal damage theory," *International Journal of Solids and Structures*, vol. 40, n°. 13-14, p. 3621–3645, 2003.

[76] R. Engelen, M. Geers et F. Baaijens, "Nonlocal implicit gradient-enhanced elasto-plasticity for the modelling of softening behaviour," *International Journal of Plasticity*, vol. 19, n°. 4, p. 403–433, 4 2003.

[77] L. Wu, L. Noels, L. Adam et I. Doghri, *Non-local damage-enhanced mfh for multiscale simulations of composites.* Springer New York, 2013, p. 115–121.

[78] J. D. Eshelby, *The determination of the elastic field of an ellipsoidal inclusion, and related problems.* Springer Netherlands, 1957, vol. 241, p. 209–229.

[79] Z. Hashin, "The elastic moduli of heterogeneous materials," HARVARD UNIV CAMBRIDGE MA, Rapport technique, 1960.

[80] Z. a. Hashin et S. Shtrikman, "On some variational principles in anisotropic and nonhomogeneous elasticity," *Journal of the Mechanics and Physics of Solids*, vol. 10, n°. 4, p. 335–342, 1962.

[81] Z. Hashin et S. Shtrikman, "A variational approach to the theory of the elastic behaviour of multiphase materials," *Journal of the Mechanics and Physics of Solids*, vol. 11, n°. 2, p. 127–140, 1963.

[82] R. Hill, "Elastic properties of reinforced solids: some theoretical principles," *Journal of the Mechanics and Physics of Solids*, vol. 11, n°. 5, p. 357–372, 1963.

[83] M. Berveiller et A. Zaoui, "An extension of the self-consistent scheme to plastically-flowing polycrystals," *Journal of the Mechanics and Physics of Solids*, vol. 26, n°. 5-6, p. 325–344, 1978.

[84] R. Masson et A. Zaoui, "Self-consistent estimates for the rate-dependentelastoplastic behaviour of polycrystalline materials," *Journal of the Mechanics and Physics of Solids*, vol. 47, n°. 7, p. 1543–1568, 1999.

[85] I. Doghri, L. Brassart, L. Adam et J.-S. Gérard, "A second-moment incremental formulation for the mean-field homogenization of elasto-plastic composites," *International Journal of Plasticity*, vol. 27, n°. 3, p. 352–371, 2011.

[86] S. Mercier et A. Molinari, "Homogenization of elastic–viscoplastic heterogeneous materials: Self-consistent and mori-tanaka schemes," *International Journal of Plasticity*, vol. 25, n°. 6, p. 1024–1048, 2009.

[87] F. Feyel et J.-L. Chaboche, "Fe2 multiscale approach for modelling the elastoviscoplastic behaviour of long fibre sic/ti composite materials," *Computer methods in applied mechanics and engineering*, vol. 183, n°. 3-4, p. 309–330, 2000.

[88] S. B. Lee, R. Lebensohn et A. D. Rollett, "Modeling the viscoplastic micromechanical response of two-phase materials using fast fourier transforms," *International Journal of Plasticity*, vol. 27, n°. 5, p. 707–727, 2011.

[89] E. Tikarrouchine, G. Chatzigeorgiou, F. Praud, B. Piotrowski, Y. Chemisky et F. Meraghni, "Three-dimensional fe2 method for the simulation of non-linear, rate-dependent response of composite structures," *Composite Structures*, vol. 193, p. 165–179, 6 2018.

[90] G. J. Dvorak et Y. Benveniste, "On transformation strains and uniform fields in multiphase elastic media," *Proceedings of the Royal Society of London. Series A: Mathematical and Physical Sciences*, vol. 437, n°. 1900, p. 291–310, 1992.

[91] S. Kruch et J.-L. Chaboche, "Multi-scale analysis in elasto-viscoplasticity coupled with damage," *International Journal of Plasticity*, vol. 27, n°. 12, p. 2026–2039, 2011.

[92] M. Barral, G. Chatzigeorgiou, F. Meraghni et R. Léon, "Homogenization using modified mori-tanaka and tfa framework for elastoplastic-viscoelastic-viscoplastic composites: theory and numerical validation," *International Journal of Plasticity*, vol. 127, p. 102632, 2020.

[93] G. Chatzigeorgiou, "Study of multilayered composites through periodic homogenization and mori–tanaka methods," *Mechanics of Materials*, vol. 164, p. 104110, 2022.

[94] R. Bharali, F. Larsson et R. Jänicke, "Computational homogenisation of phase-field fracture," *European Journal of Mechanics-A/Solids*, vol. 88, p. 104247, 2021.

[95] F. Fantoni, A. Bacigalupo, M. Paggi et J. Reinoso, "A phase field approach for damage propagation in periodic microstructured materials," *International Journal of Fracture*, vol. 223, n°. 1, p. 53–76, 2020.

[96] V. Kouznetsova, M. G. Geers et W. M. Brekelmans, "Multi-scale constitutive modelling of heterogeneous materials with a gradient-enhanced computational homogenization scheme," *International journal for numerical methods in engineering*, vol. 54, n°. 8, p. 1235–1260, 2002.

[97] S. Forest, F. Pradel et K. Sab, "Asymptotic analysis of heterogeneous cosserat media," *International Journal of Solids and Structures*, vol. 38, n°. 26-27, p. 4585–4608, 2001.

[98] A. Benaarbia, A. Chrysochoos et G. Robert, "Thermomechanical analysis of the onset of strain concentration zones in wet polyamide 6.6 subjected to cyclic loading," *Mechanics of Materials*, vol. 99, p. 9–25, 8 2016.

[99] O. Hasan et M. C. Boyce, "A constitutive model for the nonlinear viscoelastic viscoplastic behavior of glassy polymers," *Polymer Engineering & Science*, vol. 35, n°. 4, p. 331–344, 1995.

[100] R. A. Schapery, "Nonlinear viscoelastic and viscoplastic constitutive equations based on thermodynamics," *Mechanics of Time-Dependent Materials*, vol. 1, n°. 2, p. 209–240, 1997.

[101] R. K. Abu Al-Rub, A. H. Tehrani et M. K. Darabi, "Application of a large deformation nonlinear-viscoelastic viscoplastic viscodamage constitutive model to polymers and their composites," *International Journal of Damage Mechanics*, vol. 24, n°. 2, p. 198–244, 2015.

[102] J. Wang, L. Peng, Y. Deng, X. Lai, M. Fu et J. Ni, "A finite strain thermodynamically-based constitutive modeling and analysis of viscoelastic-viscoplastic deformation behavior of glassy polymers," *International Journal of Plasticity*, vol. 122, p. 135–163, 2019.

[103] M. Haddad, I. Doghri et O. Pierard, "Viscoelastic-viscoplastic polymer composites: Development and evaluation of two very dissimilar mean-field homogenization models," *International Journal of Solids and Structures*, vol. 236, p. 111354, 2022.

[104] I. Doghri et A. Ouaar, "Homogenization of two-phase elasto-plastic composite materials and structures: Study of tangent operators, cyclic plasticity and numerical algorithms," *International Journal of Solids and structures*, vol. 40, n°. 7, p. 1681–1712, 2003.

[105] A. Benaarbia, Y. Rae et W. Sun, "Unified viscoplasticity modelling and its application to fatigue-creep behaviour of gas turbine rotor," *International Journal of Mechanical Sciences*, vol. 136, p. 36–49, 2 2018.

[106] B. Halphen et Q. Nguyen, "On the generalized standards materials (in french)," *Journal de Mécanique*, vol. 14, p. 39–63, 1975.

[107] P. Germain, P. Suquet et Q. Nguyen, "Continuum thermomechanics," *ASME Transactions Series E Journal of Applied Mechanics*, vol. 50, p. 1010–1020, 1983.

[108] M. Gudimetla et I. Doghri, "A finite strain thermodynamically-based constitutive framework coupling viscoelasticity and viscoplasticity with application to glassy polymers," *International Journal of Plasticity*, vol. 98, p. 197–216, 11 2017.

[109] L. Kachanov, "Time of the rupture process under creep conditions. izvestiia akademii nauk sssr, otdelenie teckhnicheskikh nauk," vol. 8, p. 26–31, 1958.

[110] Y. Rabotnov, *Creep rupture*. Springer Berlin Heidelberg, 1968, p. 342–349.

[111] J. L. Chaboche, "Thermodynamic formulation of constitutive equations and application to the viscoplasticity and viscoelasticity of metals and polymers," *International Journal of Solids and Structures*, vol. 34, n°. 18, p. 2239–2254, 6 1997.

[112] I. Ward, "Review: The yield behaviour of polymers," *Journal of Materials Science*, vol. 6, n°. 11, p. 1397–1417, 11 1971.

[113] K. Pae et S. Bhateja, "The effects of hydrostatic pressure on the mechanical behavior of polymers," *Journal of Macromolecular Science, Part C*, vol. 13, n°. 1, p. 1–75, 1 1975.

[114] N. S. Ottosen et M. Ristinmaa, *The mechanics of constitutive modeling.* Elsevier, 2005.

[115] J. Lemaitre, "Coupled elasto-plasticity and damage constitutive equations," *Computer methods in applied mechanics and engineering*, vol. 51, n°. 1-3, p. 31–49, 1985.

[116] F. Detrez, S. Cantournet et R. Seguela, "Plasticity/damage coupling in semi-crystalline polymers prior to yielding: Micromechanisms and damage law identification," *Polymer*, vol. 52, n°. 9, p. 1998–2008, 2011.

[117] M. Qidwai et D. Lagoudas, "Numerical implementation of a shape memory alloy thermomechanical constitutive model using return mapping algorithms," *International Journal for Numerical Methods in Engineering*, vol. 47, n°. 6, p. 1123–1168, 2 2000.

[118] A. Ishisaka, et M. Kawagoe, "Examination of the time–water content superposition on the dynamic viscoelasticity of moistened polyamide 6 and epoxy," *Journal of Applied Polymer Science*, vol. 93, n°. 2, p. 560–567, 2004.

[119] V. Bellenger, A. Tcharkhtchi et P. Castaing, "Thermal and mechanical fatigue of a pa66/glass fibers composite material," *International journal of Fatigue*, vol. 28, n°. 10, p. 1348–1352, 2006.

[120] V. Venoor, J. H. Park, D. O. Kazmer et M. J. Sobkowicz, "Understanding the effect of water in polyamides: a review," *Polymer Reviews*, vol. 61, n°. 3, p. 598–645, 2021.

[121] G. B. Kauffman, "Wallace hume carothers and nylon, the first completely synthetic fiber," *Journal of Chemical Education*, vol. 65, n°. 9, p. 803, 1988.

[122] J. Brydson, *Polyamides and polyimides.* Butterworth-Heinemann Oxford, 1999.

[123] A. Apinis, A. Y. Galvanovskii *et al.*, "The effect of the moisture content on the transition temperatures of polycaproamide," *Polymer Science USSR*, vol. 17, n°. 1, p. 46–51, 1975.

[124] K. Pramoda et T. Liu, "Effect of moisture on the dynamic mechanical relaxation of polyamide-6/clay nanocomposites," *Journal of Polymer Science Part B: Polymer Physics*, vol. 42, n°. 10, p. 1823–1830, 2004.

[125] M. Broudin, P.-Y. Le Gac, V. Le Saux, C. Champy, G. Robert, P. Charrier et Y. Marco, "Water diffusivity in pa66: Experimental characterization and modeling based on free volume theory," *European Polymer Journal*, vol. 67, p. 326–334, 2015.

[126] P. Y. Le Gac, M. Arhant, M. Le Gall et P. Davies, "Yield stress changes induced by water in polyamide 6: Characterization and modeling," *Polymer Degradation and Stability*, vol. 137, p. 272–280, 2017.

[127] H. Reimschuessel, "Relationships on the effect of water on glass transition temperature and young's modulus of nylon 6," *Journal of Polymer Science: Polymer Chemistry Edition*, vol. 16, n°. 6, p. 1229–1236, 1978.

[128] H. Obeid, A. Clément, S. Fréour, F. Jacquemin et P. Casari, "On the identification of the coefficient of moisture expansion of polyamide-6: Accounting differential swelling strains and plasticization," *Mechanics of Materials*, vol. 118, p. 1–10, 2018.

[129] E. M. Arruda, M. C. Boyce et R. Jayachandran, "Effects of strain rate, temperature and thermomechanical coupling on the finite strain deformation of glassy polymers," *Mechanics of Materials*, vol. 19, n°. 2-3, p. 193–212, 1995.

[130] A. Bergeret, I. Pires, M. Foulc, B. Abadie, L. Ferry et A. Crespy, "The hygrothermal behaviour of glass-fibre-reinforced thermoplastic composites: a prediction of the composite lifetime," *Polymer testing*, vol. 20, n°. 7, p. 753–763, 2001.

[131] I. Carrascal, J. Casado, J. Polanco et F. Gutiérrez-Solana, "Absorption and diffusion of humidity in fiberglass-reinforced polyamide," *Polymer composites*, vol. 26, n°. 5, p. 580–586, 2005.

[132] J. A. Nelder et R. Mead, "A simplex method for function minimization," *The computer journal*, vol. 7, n°. 4, p. 308–313, 1965.

[133] S. Singer et J. Nelder, "Nelder-Mead algorithm," *Scholarpedia*, vol. 4, n°. 7, p. 2928, 2009, revision #91557.

[134] Q. Chen, G. Chatzigeorgiou, G. Robert et F. Meraghni, "Viscoelastic-viscoplastic homogenization of short glass-fiber reinforced polyamide composites (pa66/gf) with progressive interphase and matrix damage: New developments and experimental validation," *Mechanics of Materials*, vol. 164, p. 104081, 2022.

[135] R. Ostwald, E. Kuhl et A. Menzel, "On the implementation of finite deformation gradient-enhanced damage models," *Computational Mechanics*, vol. 64, n°. 3, p. 847–877, 2 2019.

[136] M. Neilsen et H. Schreyer, "Bifurcations in elastic-plastic materials," *International Journal of Solids and Structures*, vol. 30, n°. 4, p. 521–544, 1993.

[137] R. De Borst et C. Verhoosel, "Gradient damage vs phase-field approaches for fracture: Similarities and differences," *Computer Methods in Applied Mechanics and Engineering*, vol. 312, p. 78–94, 12 2016.

[138] R. Abu Al-Rub et G. Voyiadjis, "Analytical and experimental determination of the material intrinsic length scale of strain gradient plasticity theory from micro- and nano-indentation experiments," *International Journal of Plasticity*, vol. 20, n°. 6, p. 1139–1182, 6 2004.

[139] R. De Borst, M. Geers, R. Peerlings et A. Benallal, *Some remarks on gradient and nonlocal damage theories*. Elsevier, 1998, vol. 46, p. 223–236.

[140] A. Seupel, G. Hütter et M. Kuna, "An efficient fe-implementation of implicit gradient-enhanced damage models to simulate ductile failure," *Engineering Fracture Mechanics*, vol. 199, p. 41–60, 8 2018.

[141] M. Geers, R. Borst, W. Brekelmans et R. Peerlings, "Validation and internal length scale determination for a gradient damage model: application to short glass-fibre-reinforced polypropylene," *International Journal of Solids and Structures*, vol. 36, n°. 17, p. 2557–2583, 6 1999.

[142] A. Simone, H. Askes et L. Sluys, "Incorrect initiation and propagation of failure in non-local and gradient-enhanced media," *International Journal of Solids and Structures*, vol. 41, n°. 2, p. 351–363, 1 2004.

[143] T. Brepols, S. Wulfinghoff et S. Reese, "Gradient-extended two-surface damage-plasticity: Micromorphic formulation and numerical aspects," *International Journal of Plasticity*, vol. 97, p. 64–106, 10 2017.

[144] M. Geers, R. Peerlings, W. Brekelmans et R. De Borst, "Phenomenological nonlocal approaches based on implicit gradient-enhanced damage," *Acta Mechanica*, vol. 144, n°. 1-2, p. 1–15, 3 2000.

[145] B. Kiefer, T. Waffenschmidt, L. Sprave et A. Menzel, "A gradient-enhanced damage model coupled to plasticity—multi-surface formulation and algorithmic concepts," *International Journal of Damage Mechanics*, vol. 27, n°. 2, p. 253–295, 2018.

[146] C. Hortig, "Local and non-local thermomechanical modeling and finite-element simulation of high-speed cutting," Thèse de doctorat, Dortmund, Techn. Univ., Diss., 2010, 2010.

[147] Y. Navidtehrani, C. Betegón et E. Martínez-Pañeda, "A unified abaqus implementation of the phase field fracture method using only a user material subroutine," *Materials*, vol. 14, n°. 8, p. 1913, 2021.

[148] C. Mareau, V. Favier, B. Weber, A. Galtier et M. Berveiller, "Micromechanical modeling of the interactions between the microstructure and the dissipative deformation mechanisms in steels under cyclic loading," *International Journal of Plasticity*, vol. 32-33, n°. 33, p. 106–120, 5 2012.

[149] P. Ponte-Castaneda, "The effective mechanical properties of nonlinear isotropic composites," *J. Mech. Phys. Solids*, vol. 39, p. 45–e71, 1991.

[150] K. Terada et N. Kikuchi, "A class of general algorithms for multi-scale analyses of heterogeneous media," *Computer Methods in Applied Mechanics and Engineering*, vol. 190, n°. 40-41, p. 5427–5464, 7 2001.

[151] F. Meraghni, F. Desrumaux et M. Benzeggagh, "Implementation of a constitutive micromechanical model for damage analysis in glass mat reinforced composite structures," *Composites Science and Technology*, vol. 62, n°. 16, p. 2087–2097, 12 2002.

[152] B. Love et R. Batra, "Determination of effective thermomechanical parameters of a mixture of two elastothermoviscoplastic constituents," *International Journal of Plasticity*, vol. 22, n°. 6, p. 1026–1061, 6 2006.

[153] P. Suquet, "Four exact relations for the effective relaxation function of linear viscoelastic composites," *Comptes Rendus Mécanique*, vol. 340, n°. 4-5, p. 387–399, 4 2012.

[154] F. Fritzen, S. Forest, T. Böhlke, D. Kondo et T. Kanit, "Computational homogenization of elasto-plastic porous metals," *International Journal of Plasticity*, vol. 29, p. 102–119, 2 2012.

[155] A. Benaarbia, A. Chrysochoos et G. Robert, "Fiber orientation effects on heat source distribution in reinforced polyamide 6.6 subjected to low cycle fatigue," *Journal of Engineering Mathematics*, vol. 90, n°. 1, p. 13–36, 2015.

[156] G. Chatzigeorgiou, N. Charalambakis, Y. Chemisky et F. Meraghni, "Periodic homogenization for fully coupled thermomechanical modeling of dissipative generalized standard materials," *International Journal of Plasticity*, vol. 81, p. 18–39, 6 2016.

[157] F. Praud, G. Chatzigeorgiou, Y. Chemisky et F. Meraghni, "Hybrid micromechanical-phenomenological modelling of anisotropic damage and anelasticity induced by micro-cracks in unidirectional composites," *Composite Structures*, vol. 182, p. 223–236, 12 2017.

[158] S. Kotha, D. Ozturk et S. Ghosh, "Parametrically homogenized constitutive models (phcms) from micromechanical crystal plasticity fe simulations, part i: sensitivity analysis and parameter identification for titanium alloys," *International Journal of Plasticity*, vol. 120, p. 296–319, 9 2019.

[159] G. Chatzigeorgiou, A. Benaarbia et F. Meraghni, "Piezoelectric-piezomagnetic behaviour of coated long fiber composites accounting for eigenfields," *Mechanics of Materials*, vol. 138, p. 103157, 2019.

[160] G. Chatzigeorgiou, F. Meraghni, N. Charalambakis et A. Benaarbia, "Multiscale modeling accounting for inelastic mechanisms of fuzzy fiber composites with straight or wavy carbon nanotubes," *International Journal of Solids and Structures*, vol. 202, p. 39–57, 2020.

[161] F. Praud, G. Chatzigeorgiou et F. Meraghni, "Fully integrated multi-scale modelling of damage and time-dependency in thermoplastic-based woven composites," *International Journal of Damage Mechanics*, vol. 30, p. 163–195, 2021.

[162] E. Tikarrouchine, A. Benaarbia, G. Chatzigeorgiou et F. Meraghni, "Non-linear fe2 multiscale simulation of damage, micro and macroscopic strains in polyamide 66-woven composite structures: analysis and experimental validation," *Composite Structures*, vol. 255, p. 112926, 2021.

[163] T. Mori et K. Tanaka, "Average stress in matrix and average elastic energy of materials with misfitting inclusions," *Acta metallurgica*, vol. 21, n°. 5, p. 571–574, 1973.

[164] Y. Remond, "Constitutive modelling of viscoelastic unloading of short glass fibre-reinforced polyethylene," *Composites Science and Technology*, vol. 65, n°. 3-4, p. 421–428, 3 2005.

[165] J. Aboudi, "Micromechanically established constitutive equations for multiphase materials with viscoelastic–viscoplastic phases," *Mechanics of Time-Dependent Materials*, vol. 9, n°. 2-3, p. 121–145, 9 2005.

[166] R. Mahnken, A. Schneidt et T. Antretter, "Macro modelling and homogenization for transformation induced plasticity of a low-alloy steel," *International Journal of Plasticity*, vol. 25, n°. 2, p. 183–204, 2 2009.

[167] D. Paquet, P. Dondeti et S. Ghosh, "Dual-stage nested homogenization for rate-dependent anisotropic elasto-plasticity model of dendritic cast aluminum alloys," *International Journal of Plasticity*, vol. 27, n°. 10, p. 1677–1701, 10 2011.

[168] Y. Benveniste, "A new approach to the application of mori-tanaka's theory in composite materials," *Mechanics of materials*, vol. 6, n°. 2, p. 147–157, 1987.

[169] D. C. Lagoudas, A. C. Gavazzi et H. Nigam, "Elastoplastic behavior of metal matrix composites based on incremental plasticity and the mori-tanaka averaging scheme," *Computational Mechanics*, vol. 8, n°. 3, p. 193–203, 1991.

[170] F. Desrumaux, F. Meraghni et M. L. Benzeggagh, "Generalised mori-tanaka scheme to model anisotropic damage using numerical eshelby tensor," *Journal of Composite Materials*, vol. 35, n°. 7, p. 603–624, 2001.

[171] N. Lahellec et P. Suquet, "On the effective behavior of nonlinear inelastic composites: I. incremental variational principles," *Journal of the Mechanics and Physics of Solids*, vol. 55, n°. 9, p. 1932–1963, 2007.

[172] G. Chatzigeorgiou et F. Meraghni, "Elastic and inelastic local strain fields in composites with coated fibers or particles: Theory and validation," *Mathematics and Mechanics of Solids*, vol. 24, n°. 9, p. 2858–2894, 2019.

[173] G. Chatzigeorgiou, "Study of multilayered composites through periodic homogenization and mori–tanaka methods," *Mechanics of Materials*, p. 104110, 2021.

[174] F. Zaïri, M. Naït-Abdelaziz, K. Woznica et J.-M. Gloaguen, "Elasto-viscoplastic constitutive equations for the description of glassy polymers behavior at constant strain rate," *Journal of Engineering Materials and Technology*, vol. 129, n°. 1, p. 29–35, 2007.

[175] J. Lemaitre et J. Chaboche, *Mechanics of solid materials*. Cambridge university press, 1994.

[176] C. Iacono, L. Sluys et J. G. van Mier, "Estimation of model parameters in nonlocal damage theories by inverse analysis techniques," *Computer methods in applied mechanics and engineering*, vol. 195, n°. 52, p. 7211–7222, 2006.

[177] M. F. Arif, F. Meraghni, Y. Chemisky, N. Despringre et G. Robert, "In situ damage mechanisms investigation of pa66/gf30 composite: effect of relative humidity," *Composites Part B: Engineering*, vol. 58, p. 487–495, 2014.

[178] I. Pires, "Vieillissement dans l'antigel de matériaux composites polyamide-6, 6 renforcé par des fibres de verre courtes," Thèse de doctorat, Montpellier 2, 2000.

[179] B. Ledieu, "Vieillissement en milieu eau/glycol du polyamide 66 renforce fibres de verre courtes pour l'application boite a eau de radiateur de refroidissement moteur," Thèse de doctorat, Arts et Métiers ParisTech, 2010.

[180] F. Masi et I. Stefanou, "Multiscale modeling of inelastic materials with thermodynamics-based artificial neural networks (tann)," *Computer Methods in Applied Mechanics and Engineering*, vol. 398, p. 115190, 2022.

[181] L. Wu, N. G. Kilingar, L. Noels *et al.*, "A recurrent neural network-accelerated multi-scale model for elasto-plastic heterogeneous materials subjected to random cyclic and non-proportional loading paths," *Computer Methods in Applied Mechanics and Engineering*, vol. 369, p. 113234, 2020.

[182] F. Chinesta, E. Cueto, E. Abisset-Chavanne, J. L. Duval et F. E. Khaldi, "Virtual, digital and hybrid twins: a new paradigm in data-based engineering and engineered data," *Archives of computational methods in engineering*, vol. 27, n°. 1, p. 105–134, 2020.

[183] M. Ortiz et J. Simo, "An analysis of a new class of integration algorithms for elastoplastic constitutive relations," *International journal for numerical methods in engineering*, vol. 23, n°. 3, p. 353–366, 1986.

[184] G. Allaire, "Homogenization and two-scale convergence," *SIAM Journal on Mathematical Analysis*, vol. 23, n°. 6, p. 1482–1518, 11 1992.

[185] A. Bensoussan, J. L. Lions, G. Papanicolaou et T. Caughey, "Asymptotic analysis of periodic structures," *Journal of Applied Mechanics*, vol. 46, n°. 2, p. 477–477, 2011.

Appendix A

VEVPD mechanical model numerical implementation

Technically speaking, the implementation of the model on the commercial finite element software (ABAQUS) requires developing a User-defined Material (UMAT) subroutine. At each time step, the strain, $\boldsymbol{\epsilon}$, and the strain increment, $\Delta\boldsymbol{\epsilon}$, are passed into the UMAT, and the stress and tangent operator must be calculated. To this end, the model needs to be discretized in time, and at each time step, the corresponding increments of the internal state variable have to be derived using an iterative algorithm, from which the stress and tangent modulus are obtained. To implement this process, a return mapping algorithm is required. With this in mind, the model presented in chapter 2 is first discretized in time using an implicit backward Euler time algorithm, and then linearized using " convex cutting plane" as the return mapping algorithm.

A.1 Time discretization

An implicit backward Euler scheme is imposed on the governing equations, particularly on the nullity conditions φ^{vp} and φ^{vi}, so as to discretize them into n time steps, Δt:

$$\varphi^{vi}_{n+1} = \frac{1}{1-D_{n+1}}\left(\mathbb{V}^{vi}\right)^{-1} : \boldsymbol{\sigma}^{vi}_{n+1} - \frac{\Delta\boldsymbol{\epsilon}^{vi}}{\Delta t}, \quad \text{with}\Delta\boldsymbol{\epsilon}^{vi} = \boldsymbol{\epsilon}^{vi}_{n+1} - \boldsymbol{\epsilon}^{vi}_{n} \tag{A.1}$$

$$\varphi^{vp}_{n+1} = \langle\frac{f_{n+1}}{R_{vp}}\rangle_{+}^{P_{vp}^{-1}} - \frac{\Delta r}{\Delta t}, \quad \text{with} \quad \delta r = r_{n+1} - r_n, \tag{A.2}$$

$$f_{n+1} = \frac{\boldsymbol{\sigma}^{eq}_{n+1}}{1-D_{n+1}} - R_{n+1} - R_0 \tag{A.3}$$

$$\boldsymbol{\sigma}_{n+1} = (1-D_{n+1})\mathbb{C}^e : \left(\boldsymbol{\epsilon}_{n+1} - \boldsymbol{\epsilon}^{vp} - \sum_{i=1}^{N_v}\boldsymbol{\epsilon}^{vi}_{n+1}\right) \tag{A.4}$$

$$\boldsymbol{\sigma}^{vi}_{n+1} = \boldsymbol{\sigma}_{n+1} - (1-D_{n+1})\mathbb{C}^{vi} : \boldsymbol{\epsilon}^{vi}_{n+1} \tag{A.5}$$

A.2 Linearization according to the convex cutting plane approach

In this section, in order to solve the time discretized relations, the return mapping algorithm is implemented on the constitutive equations, in which the gradients of the flow are ignored for more

simplicity [183]. The flow equations can be linearized based on the given evolution laws:

$$\delta\boldsymbol{\epsilon} = \boldsymbol{\Lambda}_{vp}\delta r, \quad \delta D = \Lambda_D \delta r, \tag{A.6}$$

where, from now on, the indices n and k are ignored. The linearization of the stress, the viscoelastic conjugate state variable, the yield function, and the viscoelastic and viscoplastic criteria are derived as:

- stress tensor linearization:

$$\begin{aligned}
\delta\boldsymbol{\sigma} &= \frac{\partial\boldsymbol{\sigma}}{\partial D}\delta D + \frac{\partial\boldsymbol{\sigma}}{\partial\boldsymbol{\epsilon}} : \delta\boldsymbol{\epsilon} + \frac{\partial\boldsymbol{\sigma}}{\partial\boldsymbol{\epsilon}^{vp}} : \delta\boldsymbol{\epsilon}^{vp} + \frac{\partial\boldsymbol{\sigma}}{\partial\boldsymbol{\epsilon}^{vi}} : \delta\boldsymbol{\epsilon}^{vi} \\
&= \boldsymbol{B}^e\delta D + \mathbb{B}^d : \delta\boldsymbol{\epsilon}^{vp} - \mathbb{B}^d : \sum_{j=1}^{N_v}\delta\boldsymbol{\epsilon}^{vj} \\
&= \boldsymbol{B}^e\Lambda_D\delta r + \mathbb{B}^d : \boldsymbol{\Lambda}_{vp}\delta r - \mathbb{B}^d : \sum_{j=1}^{N_v}\delta\boldsymbol{\epsilon}^{vj} \\
&= \boldsymbol{B}_p\delta r + \mathbb{B}^d : \delta\boldsymbol{\epsilon} - \mathbb{B}_d : \sum_{j=1}^{N_V}\boldsymbol{\epsilon}^{vj}
\end{aligned} \tag{A.7}$$

with

$$\boldsymbol{B}^e = -\mathbb{C}^e : \left(\boldsymbol{\epsilon} - \boldsymbol{\epsilon}^{vp} - \sum_{j=1}^{N_v}\boldsymbol{\epsilon}^{vj}\right) \tag{A.8}$$

$$\mathbb{B}^d = (1-D)\mathbb{C}^e \tag{A.9}$$

$$\boldsymbol{B}^p = \boldsymbol{B}^e\Lambda_D - \mathbb{B}^d : \boldsymbol{\Lambda}_{vp} \tag{A.10}$$

- viscoelastic conjugate state variable linearization:

$$\begin{aligned}
\delta\boldsymbol{\sigma}^{vi} &= \frac{\partial\boldsymbol{\sigma}^{vi}}{\partial\boldsymbol{\sigma}} : \delta\boldsymbol{\sigma} + \frac{\partial\boldsymbol{\sigma}^{vi}}{\partial\boldsymbol{\epsilon}^{vi}} : \boldsymbol{\epsilon}^{vi} + \frac{\partial\boldsymbol{\sigma}^{vi}}{\partial D}\delta D \\
&= \delta\boldsymbol{\sigma} - (1-D)\mathbb{C}^{vi} : \delta\boldsymbol{\epsilon}^{vi} + \mathbb{C}^{vi} : \boldsymbol{\epsilon}^{vi}\delta D \\
&= \mathbb{B}^p\delta r + \mathbb{B}^d : \delta\boldsymbol{\epsilon} - \mathbb{B}^d : \sum_{j=1}^{N_v}\delta\boldsymbol{\epsilon}^{vj} - (1-D)\mathbb{C}^{vi} : \delta\boldsymbol{\epsilon}^{vi} + \mathbb{C}^{vi} : \boldsymbol{\epsilon}^{vi}\Lambda_D\delta r \\
&= \mathbb{B}^d\delta\boldsymbol{\epsilon} + \boldsymbol{B}^{wi} - \mathbb{B}^h : \delta\boldsymbol{\epsilon}^{vi} - \mathbb{B}^d : \sum_{j=1(j\neq i)}^{N_v}\delta\boldsymbol{\epsilon}^{vj}
\end{aligned} \tag{A.11}$$

with

$$\boldsymbol{B}^{wi} = \boldsymbol{B}^p + \mathbb{C}^{vi} + \boldsymbol{\epsilon}^{vi}\Lambda_D \tag{A.12}$$

$$\mathbb{B}^h = \mathbb{B}^d + (1-D)\mathbb{C}^{vi} \tag{A.13}$$

- yield function linearization:

$$\begin{aligned}\delta f &= \frac{\partial f}{\partial \boldsymbol{\sigma}} : \delta\boldsymbol{\sigma} + \frac{\partial f}{\partial r}\delta r + \frac{\partial f}{\partial D}\delta D \\ &= f_{\boldsymbol{\sigma}} : \delta\boldsymbol{\sigma} + f_r \delta r + f_D \delta D\end{aligned} \tag{A.14}$$

with

$$f_{\boldsymbol{\sigma}} = \boldsymbol{\Lambda}_{vp} = \frac{\partial f}{\partial \boldsymbol{\sigma}} = \frac{\sqrt{3}\boldsymbol{\sigma}'}{2(1-D)\sqrt{J_2}} \tag{A.15}$$

$$f_r = \frac{\partial f}{\partial r} = H_p\, H_m\, r^{H_p - 1} \tag{A.16}$$

$$f_D = \frac{\partial f}{\partial D} = \frac{\sigma^{eq}}{(1-D)^2} \tag{A.17}$$

Substituting (A.7) into (A.14) yields:

$$\begin{aligned}\delta f &= \boldsymbol{\Lambda}_{vp} : \left(\boldsymbol{B}^p \delta r + \mathbb{B}^d : \delta\boldsymbol{\epsilon} - \mathbb{B}^d : \sum_{j=1}^{N_v} \boldsymbol{\epsilon}^{vj} \right) + f_r \delta r + f_D \Lambda_D \delta r \\ &= \boldsymbol{\Lambda}_{vp} : \left(\mathbb{B}^d : \delta\boldsymbol{\epsilon} - \mathbb{B}^d : \sum_{j=1}^{N_v} \delta\boldsymbol{\epsilon}^{vj} \right) + B^m \delta r\end{aligned} \tag{A.18}$$

with

$$B^m = \boldsymbol{\Lambda}_{vp} : \boldsymbol{B}^p + f_D \Lambda_D + f_r \tag{A.19}$$

- viscoelastic criterion linearization:

$$\begin{aligned}\delta\boldsymbol{\phi}^{vi} &= \frac{\partial \phi^{vi}}{\partial \boldsymbol{\sigma}^{vi}} : \delta\boldsymbol{\sigma}^{vi} + \frac{\partial \phi^{vi}}{\partial \boldsymbol{\epsilon}^{vi}} : \delta\boldsymbol{\epsilon}^{vi} + \frac{\partial \boldsymbol{\phi}^{vi}}{\partial D}\delta D \\ &= \frac{1}{1-D}\mathbb{V}^{vi\,-1} : \delta\boldsymbol{\sigma}^{vi} - \frac{1}{\Delta t}\delta\boldsymbol{\epsilon}^{vi} + \frac{1}{(1-D)^2}\mathbb{V}^{vi\,-1} : \boldsymbol{\sigma}^{vi}\delta D\end{aligned} \tag{A.20}$$

Substituting (A.11) into the above equation yields:

$$\begin{aligned}\delta\boldsymbol{\phi}^{vi} &= \frac{1}{1-D}\mathbb{V}^{vi\,-1} : \left(\mathbb{B}^d : \delta\boldsymbol{\epsilon} + \boldsymbol{B}^{wi}\delta r - \mathbb{B}^h : \delta\boldsymbol{\epsilon}^{vi} - \mathbb{B}^d : \sum_{j=1(j\neq i)}^{N_v} \delta\boldsymbol{\epsilon}^{vi} \right) \\ &\quad - \frac{1}{\Delta t}\delta\boldsymbol{\epsilon}^{vi} + \frac{1}{(1-D)^2}\mathbb{V}^{vi\,-1} : \boldsymbol{\sigma}^{vi}\Lambda_D\delta r \\ &= \frac{1}{1-D}\mathbb{V}^{vi\,-1} : \left(\mathbb{B}^d : \delta\boldsymbol{\epsilon} - \mathbb{B}^d : \sum_{j=1(j\neq i)}^{N_v} \delta\boldsymbol{\epsilon}^{vj} \right) - \mathbb{B}^{vi} : \delta\boldsymbol{\epsilon}^{vi} - \boldsymbol{B}^{gi}\end{aligned} \tag{A.21}$$

with

$$\mathbb{B}^{vi} = \frac{1}{1-D}\mathbb{V}^{vi-1} : \mathbb{B}^{h} + \frac{1}{\Delta t}\mathbb{I} \tag{A.22}$$

$$\boldsymbol{B}^{gi} = \frac{-1}{1-D}\mathbb{V}^{vi-1} : \boldsymbol{B}^{wi} - \frac{1}{(1-D)^2}\mathbb{V}^{vi-1} : \boldsymbol{\sigma}^{vi}\Lambda_D \tag{A.23}$$

- viscoplastic criterion linearization:

$$\begin{aligned}\delta\phi^{vp} &= \frac{\partial\phi^{vp}}{\partial f}\delta f + \frac{\partial\phi^{vp}}{\delta r}\delta r \\ &= \Omega^{*}\delta f - \frac{\delta r}{\Delta t}\end{aligned} \tag{A.24}$$

with

$$\Omega^{*} = \frac{1}{P_{vp}}\left(\frac{f+|f|}{2R_{vp}}\right)^{P_{vp}^{-1}-1}\frac{1+sgn(f)}{2R_{vp}} \tag{A.25}$$

Substituting (A.18) into (A.24) yields:

$$\delta\phi^{vp} = \Omega^{*}\left[\boldsymbol{\Lambda}_{vp} : \left(\mathbb{B}^{d} : \delta\boldsymbol{\epsilon} - \mathbb{B}^{d} : \sum_{j=1}^{N_v}\delta\boldsymbol{\epsilon}^{vj}\right) + B^{m}\delta r\right] - \frac{\delta r}{\Delta t} \tag{A.26}$$

A.3 Viscoelastic prediction-correction

In this algorithm, the total strain is considered constant ($\delta\boldsymbol{\epsilon} = \mathbf{0}$). Only the viscoelastic strains increments, $\delta\boldsymbol{\epsilon}^{vi}$, are activated and the remaining internal variables are assumed to be constant:

$$\delta r = \delta D, \quad \delta\boldsymbol{\epsilon}^{vp} = \mathbf{0} \tag{A.27}$$

According to (2.22), the iterative viscoelastic equation is expressed as:

$$-\delta\phi^{vi} = \phi^{vi} \tag{A.28}$$

Considering (A.21) and (A.27), the above equation is obtained as:

$$\mathbb{A}^{vi} : \sum_{j=1(j\neq i)}^{N_v}\delta\boldsymbol{\epsilon}^{vj} + \mathbb{B}^{vi} : \delta\boldsymbol{\epsilon}^{vi} = \varphi^{vi} \tag{A.29}$$

with

$$\mathbb{A}^{vi} = \frac{1}{1-D}\mathbb{V}^{vi-1} : \mathbb{B}^{d} \tag{A.30}$$

where can be shown more clearly as:

$$\begin{bmatrix} \mathbb{B}^{v1} & \mathbb{A}^{v1} & \mathbb{A}^{v1} & . & . & . & \mathbb{A}^{v1} \\ \mathbb{A}^{v2} & \mathbb{B}^{v2} & \mathbb{A}^{v2} & . & . & . & \mathbb{A}^{v2} \\ \mathbb{A}^{v3} & \mathbb{A}^{v3} & \mathbb{B}^{v3} & . & . & . & \mathbb{A}^{v3} \\ . & . & . & . & . & . & . \\ . & . & . & . & . & . & . \\ . & . & . & . & . & . & . \\ \mathbb{A}^{v\,N_v} & \mathbb{A}^{v\,N_v} & \mathbb{A}^{v\,N_v} & . & . & . & \mathbb{B}^{v\,N_v} \end{bmatrix} \begin{bmatrix} \delta\boldsymbol{\epsilon}^{v1} \\ \delta\boldsymbol{\epsilon}^{v2} \\ \delta\boldsymbol{\epsilon}^{v3} \\ . \\ . \\ . \\ \delta\boldsymbol{\epsilon}^{v\,N_v} \end{bmatrix} = \begin{bmatrix} \boldsymbol{\phi}^{v1} \\ \boldsymbol{\phi}^{v2} \\ \boldsymbol{\phi}^{v3} \\ . \\ . \\ . \\ \boldsymbol{\phi}^{v\,N_V} \end{bmatrix} \tag{A.31}$$

A.4 Full correction

Once $f \geq 0$, the viscoplastic deformation coupled with damage is activated. In order to implement the return mapping, full correction algorithm proposes an iterative algorithm where the damage and hardening state variable increments are also taken into account. However, the total strain is constant at each time step, and its increment $\delta\boldsymbol{\epsilon}$ is set to zero. The iterative equations are derived as:

$$\begin{cases} -\delta\phi^{vi} = \phi^{vi} \\ -\delta\phi^{vp} = \phi^{vp} \end{cases} \tag{A.32}$$

where, using (A.21) and (A.26), it is expanded to:

$$\begin{cases} \mathbb{A}^{vi} : \sum_{j=1(j\neq i)}^{N_v} \delta\boldsymbol{\epsilon}^{vj} + \mathbb{B}^{vi} : \delta\boldsymbol{\epsilon}^{vi} + \boldsymbol{B}^{gi}\delta r = \boldsymbol{\phi}^{vi} \\ \boldsymbol{A}^{vp} : \sum_{j=1}^{N_v} \delta\boldsymbol{\epsilon}^{vj} + B^s\delta r = \phi^{vp} \end{cases} \tag{A.33}$$

with

$$A^{vp} = \Omega^* \boldsymbol{\Lambda}_{vp} : \mathbb{B}^d \tag{A.34}$$

$$B^s = -\left(\Omega^* B^m - \frac{1}{\Delta t}\right) \tag{A.35}$$

(A.33) is expanded to its tensorial form as:

$$\begin{bmatrix} \mathbb{B}^{v1} & \mathbb{A}^{v1} & \mathbb{A}^{v1} & . & . & . & \mathbb{A}^{v1} & \boldsymbol{B}^{g1} \\ \mathbb{A}^{v2} & \mathbb{B}^{v2} & \mathbb{A}^{v2} & . & . & . & \mathbb{A}^{v2} & \boldsymbol{B}^{g2} \\ \mathbb{A}^{v3} & \mathbb{A}^{v3} & \mathbb{B}^{v3} & . & . & . & \mathbb{A}^{v3} & \boldsymbol{B}^{g3} \\ . & . & . & . & . & . & . & \\ . & . & . & . & . & . & . & \\ . & . & . & . & . & . & . & \\ \mathbb{A}^{v\,N_v} & \mathbb{A}^{v\,N_v} & \mathbb{A}^{v\,N_v} & . & . & . & \mathbb{B}^{v\,N_v} & \\ \boldsymbol{A}^{vp} & \boldsymbol{A}^{vp} & \boldsymbol{A}^{vp} & . & . & . & B^s & \end{bmatrix} \begin{bmatrix} \delta\boldsymbol{\epsilon}^{v1} \\ \delta\boldsymbol{\epsilon}^{v2} \\ \delta\boldsymbol{\epsilon}^{v3} \\ . \\ . \\ . \\ \delta\boldsymbol{\epsilon}^{v\,N_v} \\ \delta r \end{bmatrix} = \begin{bmatrix} \phi^{vp} \\ \phi^{vp} \\ \phi^{vp} \\ . \\ . \\ . \\ \phi^{vp} \end{bmatrix} \tag{A.36}$$

A.5 Tangent operators

Before plastic flow activation, the tangent stiffness tensor, $\mathbb{T}_{\boldsymbol{\epsilon}}^{\boldsymbol{\sigma}}$, is defined as the viscoelastic tangent operator by ignoring Δr, and after exceeding the yield surface, the full tangent operator is requested, in which Δr is taken into account. In this sense, it is assumed that the nullity of the criteria is satisfied, then the criteria increments are derived as:

$$\Delta\boldsymbol{\phi}^{vi} = \frac{1}{1-D}\mathbb{V}^{vi-1} : \Delta\boldsymbol{\sigma}^{vi} - \frac{1}{\Delta t}\Delta\boldsymbol{\epsilon}^{vi}\frac{1}{\Delta t}\Delta\boldsymbol{\epsilon}^{vi} + \frac{1}{(1-D)^2}\mathbb{V}^{vi-1} : \boldsymbol{\sigma}^{vi}\Delta D = \mathbf{0} \tag{A.37}$$

$$\Delta\phi^{vp} = \Omega^*\Delta f - \frac{\Delta r}{\Delta t} = \Omega^*\left(\boldsymbol{\Lambda}_{vp} : \Delta\boldsymbol{\sigma} + f_r\Delta r + f_D\Delta D\Delta D\right) - \frac{\Delta r}{\Delta t} = 0 \tag{A.38}$$

Substituting (A.11) and (A.7) into (A.37) and (A.38) respectively yields:

$$\Delta\boldsymbol{\phi}^{vi} = \mathbb{K}_{6(i)} : \Delta\boldsymbol{\epsilon} + \sum_{j=1}^{N_v}\mathbb{K}_{8(ij)} : \Delta\boldsymbol{\epsilon}^{vj} + \boldsymbol{K}_{7(i)}\Delta r = \mathbf{0} \tag{A.39}$$

$$\Delta\phi^{vp} = \boldsymbol{K}_9 : \Delta\boldsymbol{\epsilon} + \sum_{j=1}^{N_v}\boldsymbol{K}_{10} : \Delta\boldsymbol{\epsilon}^{vj} + K_{11}\Delta r = 0 \tag{A.40}$$

with

$$\mathbb{K}_{1(i)} = \frac{1}{1-D}\mathbb{V}^{vi-1} \tag{A.41}$$

$$\mathbb{K}_{2(i)} = \mathbb{V}^{vi-1} : \mathbb{C}^{vi} - \frac{\mathbb{I}}{\Delta t} \tag{A.42}$$

$$\boldsymbol{K}_{3(i)} = \frac{1}{1-D}\mathbb{V}^{vi-1} : \mathbb{C}^{vi} : \boldsymbol{\epsilon}^{vi}\Lambda_D + \frac{1}{(1-D)^2}\mathbb{V}^{vi-1} : \boldsymbol{\sigma}^{vi}\Lambda_D \tag{A.43}$$

$$\boldsymbol{K}_4 = \Omega^*\boldsymbol{\Lambda}^{vp} \tag{A.44}$$

$$K_5 = \Omega^*\, f_r + \Omega^*\, f_D\Lambda_D - \frac{1}{\Delta t} \tag{A.45}$$

$$\mathbb{K}_{6(i)} = \mathbb{K}_{1(i)} : \mathbb{B}^d \tag{A.46}$$

$$\boldsymbol{K}_{7(i)} = \mathbb{K}^p_{1(i):\boldsymbol{B}} + \boldsymbol{K}_{3(i)} \tag{A.47}$$

$$\sum_{j=1}^{N_v} \mathbb{K}8(ij) : \Delta\boldsymbol{\epsilon}^{vj} = \mathbb{K}_{2(i)} : \Delta\boldsymbol{\epsilon}^{vi} - \mathbb{K}_{1(i)} : \mathbb{B}^d : \sum_{j=1}^{N_v} \Delta\boldsymbol{\epsilon}^{vj} \tag{A.48}$$

$$\boldsymbol{K}_9 = \boldsymbol{K}_4 : \mathbb{B}^d \tag{A.49}$$

$$\boldsymbol{K}_{10} = -\boldsymbol{K}_9 \tag{A.50}$$

$$K_{11} = \boldsymbol{K}_4 : \boldsymbol{B}^p + K_5 \tag{A.51}$$

A.6 Viscoelastic tangent operator

In order to derive the viscoelastic tangent modulus, $\Delta\, r$ is ignored in (A.39), then $\Delta\,\boldsymbol{\epsilon}^{vi}$ with respect to $\Delta\boldsymbol{\epsilon}$ is given as:

$$\Delta\boldsymbol{\epsilon}^{vi} = \mathbb{K}_T^v : \Delta\boldsymbol{\epsilon} \tag{A.52}$$

with

$$\mathbb{K}_T^v = \begin{bmatrix} \mathbb{K}_{8(11)} & \mathbb{K}_{8(12)} & \mathbb{K}_{8(13)} & . & . & . & \mathbb{K}_{8(1\,N_v)} \\ \mathbb{K}_{8(21)} & \mathbb{K}_{8(22)} & \mathbb{K}_{8(23)} & . & . & . & \mathbb{K}_{8(2\,N_v)} \\ \mathbb{K}_{8(31)} & \mathbb{K}_{8(32)} & \mathbb{K}_{8(33)} & . & . & . & \mathbb{K}_{8(3\,N_v)} \\ . & . & . & . & . & . & . \\ . & . & . & . & . & . & . \\ . & . & . & . & . & . & . \\ \mathbb{K}_{8(N_v\,N_v)} & \mathbb{K}_{8(N_v\,N_v)} & \mathbb{K}_{8(N_v\,N_v)} & . & . & . & \mathbb{K}_{8(3\,N_v)} \end{bmatrix}^{-1} \begin{bmatrix} \mathbb{K}_{6(1)} \\ \mathbb{K}_{6(2)} \\ \mathbb{K}_{6(3)} \\ . \\ . \\ . \\ \mathbb{K}_{6(1N_v)} \end{bmatrix} \tag{A.53}$$

The stress increment, $\Delta\boldsymbol{\sigma}$, without plastic deformation is given as:

$$\Delta\boldsymbol{\sigma} = (1-D)\mathbb{C}^e : \left(\Delta\boldsymbol{\epsilon} - \sum_{i=1}^{N_v} \Delta\boldsymbol{\epsilon}^{vi}\right) \tag{A.54}$$

Substituting (A.52) into (A.54) results in:

$$\Delta\boldsymbol{\sigma} = (1-D)\left(\mathbb{C}^e - \sum_{i=1}^{N_v} \mathbb{K}_T^v\right) : \Delta\boldsymbol{\epsilon} \tag{A.55}$$

A.7 Full tangent operator

$\Delta\, r$ and $\Delta\boldsymbol{\epsilon}^{vi}$ with respect to $\Delta\boldsymbol{\epsilon}$ can be extracted from (A.39) and (A.40) as:

$$\begin{bmatrix} \Delta\boldsymbol{\epsilon}^{vi} \\ \Delta\, r \end{bmatrix} = \begin{bmatrix} \boldsymbol{X}^{vi} \\ \boldsymbol{X}^{r} \end{bmatrix} \Delta\boldsymbol{\epsilon} \tag{A.56}$$

where

$$\begin{bmatrix} \boldsymbol{X}^{v1} \\ \boldsymbol{X}^{v2} \\ \boldsymbol{X}^{v3} \\ . \\ . \\ . \\ \boldsymbol{X}^{v\,N_v} \\ \boldsymbol{X}^{r} \end{bmatrix} = \begin{bmatrix} \mathbb{K}_{8(11)} & \mathbb{K}_{8(12)} & \mathbb{K}_{8(13)} & . & . & . & \mathbb{K}_{8(1\,N_v)} & \boldsymbol{K}_{7(1)} \\ \mathbb{K}_{8(21)} & \mathbb{K}_{8(22)} & \mathbb{K}_{8(23)} & . & . & . & \mathbb{K}_{8(2\,N_v)} & \boldsymbol{K}_{7(2)} \\ \mathbb{K}_{8(31)} & \mathbb{K}_{8(32)} & \mathbb{K}_{8(33)} & . & . & . & \mathbb{K}_{8(3\,N_v)} & \boldsymbol{K}_{7(3)} \\ . & . & . & . & . & . & . & \\ . & . & . & . & . & . & . & \\ . & . & . & . & . & . & . & \\ \mathbb{K}_{8(N_v\,N_v)} & \mathbb{K}_{8(N_v\,N_v)} & \mathbb{K}_{8(N_v\,N_v)} & . & . & . & \mathbb{K}_{8(3\,N_v)} & \boldsymbol{K}_{7(N_v)} \\ \boldsymbol{K}_{10} & \boldsymbol{K}_{10} & \boldsymbol{K}_{10} & . & . & . & \boldsymbol{K}_{10} & K_{11} \end{bmatrix}^{-1} \begin{bmatrix} \mathbb{K}_{6(1)} \\ \mathbb{K}_{6(2)} \\ \mathbb{K}_{6(3)} \\ . \\ . \\ . \\ \mathbb{K}_{6(1N_v)} \\ \boldsymbol{K}_{9} \end{bmatrix} \tag{A.57}$$

Substituting (**??**) into (A.7) yields:

$$\Delta\boldsymbol{\sigma} = \left(\boldsymbol{B}^{p} \otimes \boldsymbol{X}^{r} + \mathbb{B}^{d} : \sum_{j=1}^{N_v} \boldsymbol{X}^{vj} \right) : \Delta\boldsymbol{\epsilon} \tag{A.58}$$

Appendix B

Nonlocal multi-scale framework asymptotic expansion

B.1 Asymptotic expansion of the local and nonlocal variables

To investigate composites, material behaviors are expressed at two scales: micro and macro. The microscopic scale allows understanding the mechanisms considering the different material constituents and their geometrical characteristics in the microstructure. However, the macroscopic scale specifies the global response of the body as a homogeneous medium. The global volume of the body is considered as $\bar{V}$ on the spatial domain $\bar{\mathcal{B}}$ bounded by the surface $\partial\bar{\mathcal{B}}$ with unit vector $\bar{n}_i$. The microscale is defined through the unit cell volume,V within the spatial domain $\mathcal{B}$ bounded by the surface $\partial\mathcal{B}$ identified by the normal vector n_i. The micro and macro coordinate systems are respectively identified by x_i and $\bar{x}_i$ and related through the characteristic length, ε:

$$x_i = \bar{x}_i/\varepsilon. \tag{B.1}$$

The global composite coordinate system is expressed as x_i^ε, and the related derivatives are derived based on the chain rule:

$$\frac{\partial}{\partial x_i^\varepsilon} = \frac{\partial}{\partial \bar{x}_i} + \frac{1}{\varepsilon}\frac{\partial}{\partial x_i}. \tag{B.2}$$

Asymptotic expansion of the displacement vector, u_i^ε is defined as [156, 184, 185]:

$$u_i^\epsilon = u_i^{(0)}(\bar{x}_k, x_k) + \varepsilon u^{(1)}(\bar{x}_k, x_k) + \dots \tag{B.3}$$

Based on the small deformation theory, the strain and stress tensors are considered as:

$$\epsilon_{ij}^\varepsilon = \frac{1}{2}\left(\frac{\partial u_i^\varepsilon}{\partial x_j^\varepsilon} + \frac{\partial u_j^\varepsilon}{\partial x_i^\varepsilon}\right), \quad \sigma_{ij}^\varepsilon = C_{ijkl}^{sc}\epsilon_{kl}^\varepsilon. \tag{B.4}$$

Substituting (B.3) into (B.4) yields:

$$\begin{aligned}\epsilon_{ij}^\varepsilon =& \frac{1}{2}\left(\frac{\partial u_i^{(0)}}{\partial \bar{x}_j} + \varepsilon^{-1}\frac{\partial u_i^{(0)}}{\partial x_j} + \frac{\partial u_j^{(0)}}{\partial \bar{x}_i} + \varepsilon^{-1}\frac{\partial u_j^{(0)}}{\partial x_i}\right) \\ &+ \frac{1}{2}\varepsilon\left(\frac{\partial u_i^{(1)}}{\partial \bar{x}_j} + \varepsilon^{-1}\frac{\partial u_i^{(1)}}{\partial x_j} + \frac{\partial u_j^{(1)}}{\partial \bar{x}_i} + \varepsilon^{-1}\frac{\partial u_j^{(1)}}{\partial x_i}\right) + \dots,\end{aligned} \tag{B.5}$$

where can be reduced as:

$$\epsilon_{ij}^{\varepsilon} = \varepsilon^{-1}\epsilon_{ij}^{(-1)}(\bar{x}_k, x_k) + \epsilon_{ij}^{(0)}(\bar{x}_k, x_k) + \varepsilon\epsilon_{ij}^{(1)}(\bar{x}_k, x_k) + \dots, \tag{B.6}$$

with

$$\epsilon_{ij}^{(-1)} = \frac{1}{2}\left(\frac{\partial u_i^{(0)}}{\partial x_j} + \frac{\partial u_j^{(0)}}{\partial x_i}\right), \tag{B.7a}$$

$$\epsilon_{ij}^{(k)} = \frac{1}{2}\left(\frac{\partial u_i^{(k)}}{\partial \bar{x}_j} + \frac{\partial u_j^{(k)}}{\partial \bar{x}_i} + \frac{\partial u_i^{(k+1)}}{\partial x_j} + \frac{\partial u_j^{(k+1)}}{\partial x_i}\right), \quad k = 0, 1, 2, \dots \tag{B.7b}$$

Using (B.4) and (B.6), the global stress tensor, $\boldsymbol{\sigma}^{\varepsilon}$, can be derived as:

$$\sigma_{ij}^{\varepsilon} = \varepsilon^{-1}C_{ijkl}^{sc}\epsilon_{kl}^{(-1)} + C_{ijkl}^{sc}\epsilon_{kl}^{(0)} + \varepsilon C_{ijkl}^{sc}\epsilon_{kl}^{(1)} + \dots, \tag{B.8}$$

where can be reduced as:

$$\sigma_{ij}^{\varepsilon}(x_k^{\varepsilon}) = \varepsilon^{-1}\sigma_{ij}^{(-1)}(\bar{x}_k, x_k) + \sigma_{ij}^{(0)}(\bar{x}_k, x_k) + \varepsilon\sigma_{ij}^{(1)}(\bar{x}_k, x_k) + \dots, \tag{B.9}$$

with

$$\sigma_{ij}^{(m)}(\bar{x}_k, x_k) = C_{ijkl}^{sc}\epsilon_{kl}^{(m)}, \quad m = -1, 0, 1, \dots \tag{B.10}$$

The stress equilibrium in absence of the body forces in the global composite coordinate is given as:

$$\frac{\partial \sigma_{ij}^{\varepsilon}}{\partial x_j^{\varepsilon}} = 0. \tag{B.11}$$

Considering (B.2), it yields:

$$\frac{\partial \sigma_{ij}^{\varepsilon}}{\partial x_j^{\varepsilon}} = \frac{\partial \sigma_{ij}^{\varepsilon}}{\partial \bar{x}_j} + \frac{1}{\varepsilon}\frac{\partial \sigma_{ij}^{\varepsilon}}{\partial x_j}. \tag{B.12}$$

Substituting (B.10) into (B.12) results in:

$$\varepsilon^{-2}\frac{\partial \sigma_{ij}^{(-1)}}{\partial x_j} + \varepsilon^{-1}\frac{\partial \sigma_{ij}^{(-1)}}{\partial \bar{x}_j} + \varepsilon^{-1}\frac{\partial \sigma_{ij}^{(0)}}{\partial x_j} + \frac{\partial \sigma_{ij}^{(0)}}{\partial \bar{x}_j} + ... = 0. \tag{B.13}$$

The sum of the terms with the same power of ε can be taken as zero. For ε^{-2}, the following can be deduced:

$$\frac{\partial \sigma_{ij}^{(-1)}}{\partial x_j} = 0. \tag{B.14}$$

Multiplying (B.14) in $u_i^{(0)}(x, \bar{x}_j)$ and integrating over the RVE yields:

$$\int_\Omega u_i^{(0)}(x_j, \bar{x}_j) \frac{\partial \sigma_{ij}^{(-1)}}{\partial x_j} dV = 0. \tag{B.15}$$

Using the divergence theorem:

$$\int_{\partial\Omega} u_i^{(0)}(x_j, \bar{x}_j) \sigma_{ij}^{(-1)} n_j dS - \int_\Omega \frac{\partial u_i^{(0)}(x_j, \bar{x}_j)}{\partial x_j} \sigma_{ij}^{(-1)} dV = 0. \tag{B.16}$$

Considering the anti-periodic term $\sigma_{ij}^{(-1)} n_j$ in (B.16), the surface integral is automatically zero, and the volume integral results in:

$$\frac{\partial u_i^{(0)}(x_j, \bar{x}_j)}{\partial x_j} = 0. \tag{B.17}$$

It means that $u_i^{(0)}$ does not depend on the microscopic position vector, x_i. Accordingly asymptotic expansion of the displacement can be written as:

$$u_i^\epsilon(\bar{x}_k, x_k) = u_i^{(0)}(\bar{x}_k) + \epsilon u^{(1)}(\bar{x}_k, x_k) + \dots \tag{B.18}$$

In a similar way and using the nonlocal equation, (4.15), for the nonlocal variable, r^{nl}, the following asymptotic expansion can be derived:

$$r^{nl\varepsilon}(\bar{x}_k, x_k) = r^{nl(0)}(\bar{x}_k) + \varepsilon r^{nl(1)}(\bar{x}_k, x_k) + \varepsilon^2 r^{nl(2)}(\bar{x}_k, x_k) + \dots \tag{B.19}$$

Accordingly, the asymptotic expansions can be written in summary as:

$$u_i^\epsilon(\bar{x}_k, x_k) = u_i^{(0)}(\bar{x}_k) + \varepsilon u^{(1)}(\bar{x}_k, x_k) + \dots, \tag{B.20a}$$

$$\epsilon_{ij}^\varepsilon(\bar{x}_k, x_k) = \epsilon_{ij}^{(0)}(\bar{x}_k, x_k) + \varepsilon \epsilon_{ij}^{(1)}(\bar{x}_k, x_k) + \dots, \tag{B.20b}$$

$$\sigma_{ij}^\epsilon(\bar{x}_k, x_k) = \sigma_{ij}^{(0)}(\bar{x}_k, x_k) + \varepsilon \sigma_{ij}^{(1)}(\bar{x}_k, x_k) + \dots, \tag{B.20c}$$

$$r^\varepsilon(\bar{x}_k, x_k) = r^{(0)}(\bar{x}_k, x_k) + \varepsilon r^{(1)}(\bar{x}_k, x_k) + \varepsilon^2 r^{(2)}(\bar{x}_k, x_k) + \dots, \tag{B.20d}$$

B.2 Stress equilibrium multi-scale model

B.2.1 Stress equilibrium in the microscale

By substituting (B.20c) into the stress equilibrium in absence of the body forces, one obtains:

$$\frac{\partial \sigma_{ij}^{\varepsilon}}{\partial x_j^{\varepsilon}} = 0, \tag{B.21}$$

where is expanded as:

$$\frac{\partial}{\partial x_j^{\varepsilon}} \left(\sigma_{ij}^{(0)} + \varepsilon \sigma_{ij}^{(1)} + \dots \right) = 0. \tag{B.22}$$

Considering the chain rule, the above equation gives:

$$\frac{\partial \sigma_{ij}^{(0)}}{\partial \bar{x}_i} + \varepsilon^{-1} \frac{\sigma^{(0)}}{\partial x_i} + \varepsilon \left(\frac{\partial \sigma_{ij}^{(1)}}{\partial \bar{x}_i} + \varepsilon^{-1} \frac{\sigma_{ij}^{(1)}}{\partial x_i} \right) + \dots = 0. \tag{B.23}$$

Taking the terms with the same power of ε, it is rewritten as:

$$\varepsilon^{-1} \frac{\sigma_{ij}^{(0)}}{\partial x_i} + \left(\frac{\partial \sigma_{ij}^{(0)}}{\partial \bar{x}_i} + \frac{\sigma_{ij}^{(1)}}{\partial x_i} \right) + \varepsilon \left(\frac{\partial \sigma_{ij}^{(1)}}{\partial \bar{x}_i} + \frac{\sigma_{ij}^{(2)}}{\partial x_i} \right) + \dots = 0. \tag{B.24}$$

Considering the term multiplied by ε^{-1}, one obtains the following equation:

$$\frac{\sigma_{ij}^{(0)}}{\partial x_i} = 0. \tag{B.25}$$

B.2.2 Stress equilibrium in the macro scale

Averaging the term multiplied by ε^0 in (B.24) gives:

$$\langle \frac{\partial \sigma_{ij}^{(0)}}{\partial \bar{x}_i} \rangle + \langle \frac{\partial \sigma_{ij}^{(1)}}{\partial x_i} \rangle = 0, \tag{B.26}$$

where "$\langle . \rangle$" denotes the average operator defined as an integral over V:

$$\langle . \rangle = \frac{1}{V} \int_V . \, dV \tag{B.27}$$

Accordingly,(B.26) can be expanded as:

$$\frac{\partial \langle \sigma_{ij}^{(0)} \rangle}{\partial \bar{x}_i} + \frac{1}{V} \int_V \frac{\partial \sigma_{ij}^{(1)}}{\partial x_i} dV = 0. \tag{B.28}$$

Using the divergence theorem, the above equation can be rewritten as following:

$$\frac{\partial \langle \sigma_{ij}^{(0)} \rangle}{\partial \bar{x}_i} + \frac{1}{V} \int_{\partial V} \sigma_{ij}^{(1)} n_j dS = 0. \tag{B.29}$$

Due to the anti-periodicity of $\sigma_{ij}^{(1)}$, the second term in the (B.29) vanishes:

$$\frac{\partial \langle \sigma_{ij}^{(0)} \rangle}{\partial \bar{x}_i} = 0, \tag{B.30}$$

or:

$$\frac{\partial \bar{\sigma}_{ij}}{\partial \bar{x}_i} = 0 \quad with \quad \langle \sigma_{ij}^{(0)} \rangle = \bar{\sigma}_{ij}. \tag{B.31}$$

B.3 Nonlocal equation multi-scale model

B.3.1 Nonlocal equation in the microscale

Nonlocal equation in the global composite coordinate system is expressed as:

$$\xi^{nl} \frac{\partial}{\partial x_i^{\varepsilon}} \left(\frac{\partial r^{nl\varepsilon}}{\partial x_i^{\varepsilon}} \right) + \gamma^{nl} \left(r^{\varepsilon} - r^{nl\varepsilon} \right) = 0 \tag{B.32}$$

The first derivative of the $r^{nl\varepsilon}$ can be defined as:

$$w_i^{nl\varepsilon} = \frac{\partial r^{nl\varepsilon}}{\partial x_i^{\varepsilon}} = \frac{\partial r^{nl\varepsilon}}{\partial \bar{x}_i} + \frac{1}{\varepsilon} \frac{\partial r^{nl\varepsilon}}{\partial x_i} \tag{B.33}$$

Substituting asymptotic expansion of $r^{nl\varepsilon}$ into (B.33) yields:

$$\begin{aligned} w_i^{nl\varepsilon}(\bar{x}_k, x_k) =& \frac{\partial}{\partial \bar{x}_i} \left(r^{nl(0)}(\bar{x}_k, x_k) + \varepsilon r^{nl(1)}(\bar{x}_k, x_k) + ... \right) \\ &+ \frac{1}{\varepsilon} \frac{\partial}{\partial x_i} \left(r^{nl(0)}(\bar{x}_k, x_k) + \varepsilon r^{nl(1)}(\bar{x}_k, x_k) + ... \right). \end{aligned} \tag{B.34}$$

where it is expanded to:

$$w_i^{nl\varepsilon} = \frac{\partial r^{nl(0)}}{\partial \bar{x}_i} + \varepsilon \frac{\partial r^{nl(1)}}{\partial \bar{x}_i} + ... + \varepsilon^{-1} \frac{\partial r^{nl(0)}}{\partial x_i} + \frac{\partial r^{nl(1)}}{\partial x_i} + ..., \tag{B.35}$$

where it can be rewritten as:

$$w_i^{nl\varepsilon} = \varepsilon^{-1} \frac{\partial r^{nl(0)}}{\partial x_i} + \left(\frac{\partial r^{nl(0)}}{\partial \bar{x}_i} + \frac{\partial r^{nl(1)}}{\partial x_i} \right) + \varepsilon \left(\frac{\partial r^{nl(1)}}{\partial \bar{x}_i} + \frac{\partial r^{nl(2)}}{\partial x_i} \right) + ... \tag{B.36}$$

Accordingly, (B.33) can be reduced to its asymptotic expansion form as:

$$w_i^{nl\varepsilon} = \varepsilon^{-1} w_i^{nl(-1)} + w_i^{nl(0)} + \varepsilon w_i^{nl(1)} + ..., \tag{B.37}$$

with

$$w_i^{nl(-1)} = \frac{\partial r^{nl(0)}}{\partial x_i} = 0, \tag{B.38a}$$

$$w_i^{nl(0)} = \frac{\partial r^{nl(0)}}{\partial \bar{x}_i} + \frac{\partial r^{nl(1)}}{\partial x_i}, \tag{B.38b}$$

$$w_i^{nl(1)} = \frac{\partial r^{nl(1)}}{\partial \bar{x}_i} + \frac{\partial r^{nl(2)}}{\partial x_i}. \tag{B.38c}$$

Inserting (B.36) into (B.32) yields:

$$\xi^{nl} \frac{\partial w_i^{nl\varepsilon}}{\partial x_i^{\varepsilon}} + \gamma^{nl}(r^{(0)} - r^{nl(0)}) + \varepsilon\gamma^{nl}(r^{(1)} - r^{nl(1)}) + ... = 0, \tag{B.39}$$

where it is expanded as:

$$\xi^{nl}\left(\frac{\partial w_i^{nl\varepsilon}}{\partial \bar{x}_i} + \frac{1}{\varepsilon}\frac{\partial w_i^{nl\varepsilon}}{\partial x_i}\right) + \gamma^{nl}(r^{(0)} - r^{nl(0)}) + \varepsilon\gamma^{nl}(r^{(1)} - r^{nl(1)}) + ... = 0. \tag{B.40}$$

Substituting (B.37) into (B.40) yields:

$$\begin{aligned}&\xi^{nl}\left(\frac{\partial w_i^{nl(0)}}{\partial \bar{x}_i} + \varepsilon\frac{\partial w_i^{nl(1)}}{\partial \bar{x}_i} + ... + \varepsilon^{-2}\frac{\partial w_i^{nl(-1)}}{\partial x_i} + \varepsilon^{-1}\frac{\partial w_i^{nl(0)}}{\partial x_i} + \frac{\partial w_i^{nl(1)}}{\partial x_i} + ...\right) \\ &+ \gamma^{nl}(r^{(0)} - r^{nl(0)}) + \varepsilon\gamma^{nl}(r^{(1)} - r^{nl(1)}) + ... = 0.\end{aligned} \tag{B.41}$$

where it is reduced to:

$$\varepsilon^{-1}\xi^{nl}\frac{\partial w_i^{nl(0)}}{\partial x_i} + \left[\xi^{nl}\frac{\partial w_i^{nl(0)}}{\partial \bar{x}_i} + \xi^{nl}\frac{\partial w_i^{nl(1)}}{\partial x_i} + \gamma^{nl}\left(r^{(0)} - r^{nl(0)}\right)\right] + ... = 0. \tag{B.42}$$

The next sections discuss two probable cases concerning the relationship between the RVE size, l^{ε}, and the nonlocal length scale, l^{nl}: first, $l^{nl} \leq l^{\varepsilon}$ or l^{nl} comparable to l^{ε} , and second, $l^{nl} \gg l^{\varepsilon}$.

B.3.1.1 Nonlocal equation in the microscale in case 1: $l^{nl} \leq l^{\varepsilon}$ or l^{nl} comparable to l^{ε}

In this case, the length scale is less than or comparable to the RVE size. In other words, if $l^{\varepsilon} \to 0$ then $l^{nl} \to 0$, and the second term of (B.42) tends to become trivial when $l^{\varepsilon} \to 0$. Thus,

the whole nonlocal equation (B.32) is present exclusively on the microscale and disappears from the macroscale. It has been shown in the literature that such case may cause issues on the homogenization framework [95].

B.3.1.2 Nonlocal equation in the microscale in case 2: $l^{nl} \gg l^{\varepsilon}$

In this case, it is assumed that $l^{nl} \gg l^{\varepsilon}$. With this in mind, the nonlocal variable, r^{nl}, stays uniform inside the RVE. Therefore,(B.42) is written as:

$$\frac{\partial w_i^{nl(0)}}{\partial x_i} = \frac{\partial}{\partial x_i}\left(\frac{\partial r^{nl(0)}}{\partial \bar{x}_i} + \frac{\partial r^{nl(1)}}{\partial x_i}\right) = 0. \tag{B.43}$$

(B.43) is the nonlocal equation in the microscale when $l^{nl} \gg l^{\varepsilon}$.

The first derivative of $r^{nl(1)}$ in the microscopic level can be assumed as:

$$\frac{\partial r^{nl(1)}}{\partial x_i} = \frac{\partial \mathcal{N}_j}{\partial x_i}\frac{\partial r^{nl(0)}}{\partial \bar{x}_j}. \tag{B.44}$$

Substituting (B.44) into (B.43) yields:

$$\frac{\partial}{\partial x_i}\left(\frac{\partial r^{nl(0)}}{\partial \bar{x}_j}\delta_{ij} + \frac{\partial \mathcal{N}_j}{\partial x_i}\frac{\partial r^{nl(0)}}{\partial \bar{x}_j}\right) = 0, \tag{B.45}$$

where it is reduced to:

$$\frac{\partial}{\partial x_i}\left(\delta_{ij} + \frac{\partial \mathcal{N}_j}{\partial x_i}\right) = 0. \tag{B.46}$$

where it means that $\partial N_j/\partial x_i$ is an arbitrary unknown constant, which can be taken zero. Hence, $w_i^{nl(0)}$ can be derived as:

$$w_i^{nl(0)} = \left(\delta_{ij} + \frac{\partial \mathcal{N}_j}{\partial x_i}\right)\frac{\partial r^{nl(0)}}{\partial \bar{x}_j} = \frac{\partial r^{nl(0)}}{\partial \bar{x}_i}, \tag{B.47}$$

where its average is obtained as:

$$\langle w_i^{nl(0)} \rangle = \frac{\partial r^{nl(0)}}{\partial \bar{x}_j}. \tag{B.48}$$

B.3.2 Nonlocal equation in the macroscale in case 2: $l^{nl} \gg l^{\varepsilon}$

Averaging the second term of (B.42) and considering $l^{\varepsilon} \to 0$, the macroscale equation is obtained as:

$$\langle \xi^{nl} \frac{\partial w_i^{nl(0)}}{\partial \bar{x}_i} + \xi^{nl} \frac{\partial w_i^{nl(1)}}{\partial x_i} + \gamma^{nl}(r^{(0)} - r^{nl(0)}) \rangle = 0. \tag{B.49}$$

Considering the periodicity of $w_i^{nl(1)}$ in x_i, the second term vanishes:

$$\xi^{nl} \frac{\partial \langle w_i^{nl(0)} \rangle}{\partial \bar{x}_i} + \langle \gamma^{nl} r^{(0)} \rangle - \langle \gamma^{nl} \rangle r^{nl(0)} = 0. \tag{B.50}$$

Substituting (B.48) into (B.50) yields:

$$\xi^{nl} \frac{\partial}{\partial \bar{x}_i} \left(\frac{\partial r^{nl(0)}}{\partial \bar{x}_i} \right) + \langle \gamma^{nl} r^{(0)} \rangle - \langle \gamma^{nl} \rangle r^{nl(0)} = 0. \tag{B.51}$$

Résumé étendu

1 Préface

Les polymères peuvent être renforcés à l'aide de différents types d'inclusions pour former des composites polymères aux performances thermomécaniques et chimiques supérieures. Les composites à base de polyamide sont parmi les matériaux les plus utilisés dans de nombreuses industries d'ingénierie telles que l'aérospatiale, l'automobile et l'énergie en raison de leur durabilité, de leur multifonctionnalité et de leur résistance. Les polyamides sont considérés comme des polymères semi-cristallins avec une structure moléculaire ordonnée. Une caractéristique importante des polyamides est leur sensibilité aux conditions environnementales. Ils ont un fort taux d'absorption d'humidité et leur comportement peut passer de vitreux à caoutchouteux en raison du changement de la température de transition vitreuse. Par conséquent, plusieurs mécanismes de déformation inélastique peuvent se produire en fonction des conditions environnementales et de chargement. Le modèle numérique doit tenir compte de ces aspects pour obtenir une prédiction plus précise. À cette fin, une rhéologie non linéaire doit être conçue en tenant compte des mécanismes dominants, puis le modèle phénoménologique et les lois constitutives correspondantes sont dérivés. Cependant, à des niveaux élevés d'endommagement, les polymères présentent un adoucissement du matériau, ce qui conduit à des problèmes mal posés et, par conséquent, à des réponses non uniques. Afin de résoudre ce problème, il est nécessaire d'appliquer une approche non locale et de définir un modèle d'homogénéisation multi-échelle approprié pour modéliser le comportement des composites polymères. Dans les sections suivantes, une vue d'ensemble des réponses mécaniques des polymères, les modèles et les approches actuels, la méthodologie proposée et une partie des résultats et des conclusions de cette étude sont brièvement présentés.

2 Comportement des thermoplastiques avec sensibilité à la pression et asymétrie tension-compression

Pour étudier les réponses mécaniques des thermoplastiques renforcés de verre, il est d'abord nécessaire de modéliser correctement le comportement inélastique non linéaire de la phase matrice. De nombreux rapports dans la littérature ont étudié les mécanismes actifs à travers des tests mécaniques macroscopiques [1–4]. De nombreuses lois constitutives ont été proposées pour le comportement non linéaire des thermoplastiques en utilisant des approches basées sur les réseaux macromoléculaires [5, 6] et des approches phénoménologiques [1, 7–9].

La plupart de ces modèles ont été formulés dans le cadre de la thermodynamique des processus irréversibles [10, 11]. Dans la présente étude, un modèle rhéologique viscoélastique viscoplastique

(VEVP) est adopté pour décrire les mécanismes dissipatifs impliqués pendant le processus de déformation du matériau. L'endommagement est défini comme une variable d'état interne scalaire, et introduit dans le modèle par le concept de contrainte effective [12–14]. La mise en œuvre du présent modèle rhéologique nécessite la définition d'une fonction d'élasticité appropriée. Dans ce qui suit, la sensibilité à la pression et l'asymétrie en tension-compression sont discutées, et une fonction de limite d'élasticité appropriée est introduite.

Les thermoplastiques sont des matériaux sensibles à la pression qui présentent un comportement d'élasticité asymétrique, dans lequel la limite d'élasticité est légèrement supérieure en compression. Cependant, les modèles phénoménologiques classiques pour les thermoplastiques sont généralement basés sur la fonction de von Mises, basée sur J_2 (invariant de contrainte), [1, 15, 16], dans laquelle les polymères sont considérés comme des matériaux insensibles à la pression avec un comportement symétrique. Ainsi, elle n'est pas assez précise pour capturer la plasticité des thermoplastiques. À ce propos, Ghorbel a développé une fonction d'élasticité générale qui prend en compte l'asymétrie traction-compression et l'effet de la pression hydrostatique pour un matériau viscoplastique [17]. Cependant, ce modèle ne capture pas la viscoélasticité et l'endommagement. Dans cette recherche, une fonction d'élasticité I_1-J_2, inspirée de [17], est intégrée dans le modèle VEVPD. Le modèle thermodynamique, développé dans [1], est modifié par la nouvelle fonction d'élasticité. Ensuite, les lois constitutives correspondantes sont dérivées et implémentées sur le modèle de calcul.

2.1 Étude paramétrique du modèle I_1-J_2

Le modèle de I_1-J_2 est implémenté sur un modèle numérique en utilisant l'algorithme du "convex cutting plane", pour lequel un subroutine UMAT est développé. Le polyamide 66 conditionné à 50% d'humidité relative (HR50) est considéré, et une étude paramétrique est réalisée à travers des exemples numériques pour étudier l'effet du paramètre d'asymétrie (le ratio entre les limites d'élasticité en compression et en traction) sur les réponses mécaniques du modèle. À cette fin, un outil 0D est utilisé, et les réponses mécaniques sont obtenues comme des courbes de contrainte-déformation sous charge de traction et de compression dans la figure 1. Comme observé, une augmentation du paramètre d'asymétrie augmente le niveau de contrainte. Ce phénomène est plus marqué en compression, comme prévu.

3 Identification des paramètres et validation du modèle

Deux modèles VEVPD ont été présentés : avec la fonction de von Mises supposant un comportement insensible à la pression et avec la fonction I_1-J_2 considérant l'effet de la pression hydrostatique

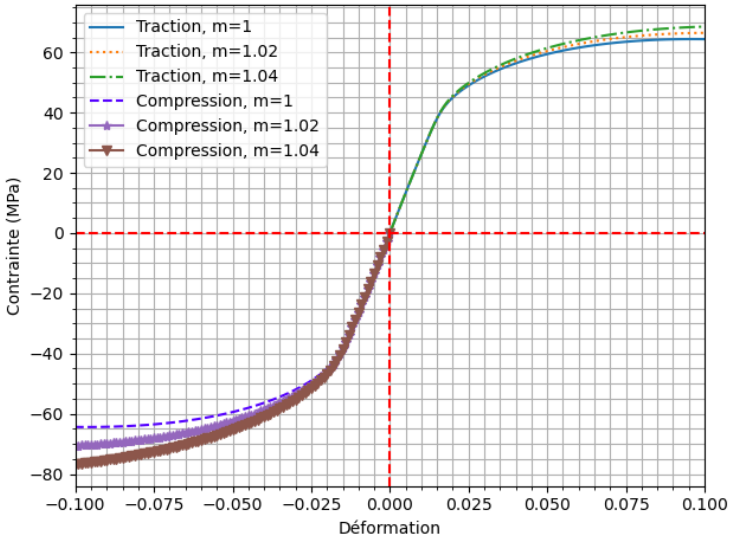

FIGURE 1 – Variation de m et son influence sur la réponse du matériau sous chargement monotone.

et de l'asymétrie traction-compression. Aucun de ces modèles n'a été calibré expérimentalement pour différentes HR dans la littérature. La procédure de calibration, les types de chargement et la forme des éprouvettes dépendent des mécanismes à identifier. Ainsi, la première étape consiste à soumettre les éprouvettes de dog bone à différents types de chargement à plusieurs vitesses et les résultats sont utilisés pour calibrer et valider le modèle classique basé sur la fonction de von Mises, dans lequel l'asymétrie traction-compression est ignorée. Pour le modèle de I_1-J_2, les éprouvettes spécialement conçus (diabolo) sont soumis à des essais de traction-torsion monotones à différentes vitesses et l'asymétrie de la limite d'élasticité du PA 66 est capturée. Les courbes force-déplacement et moment-angle globales ainsi que les données obtenues avec les éprouvettes de dog bone sont utilisées pour calibrer le modèle de I_1-J_2, dans lequel le paramètre d'asymétrie est identifié comme un nouveau paramètre.

3.1 Calibration et validation du modèle von Mises

Comme indiqué précédemment, une campagne expérimentale appropriée est conçue pour capturer tous les mécanismes et identifier les paramètres associés à différentes HR (HR0%, HR25%, HR50%, HR65% et HR80%). Afin de contrôler le taux d'absorption d'eau, les éprouvettes sont placées dans une chambre de conditionnement dans un environnement sec pour extraire toute humidité résiduelle du processus d'usinage. Pour reconditionner à différentes HR, ils sont placés dans la chambre hygrométrique à la température et à l'humidité correspondantes.

Pour calibrer et valider le modèle VEVPD basé sur la fonction de von Mises, plusieurs tests

mécaniques sont effectués pour capturer les mécanismes dominants. À cette fin, les mécanismes dépendants du temps sont capturés par des tests de traction monotones avec différents taux de déplacement. L'évolution de l'endommagement ductile est identifiée en utilisant le test de charge-décharge et les mécanismes viscoélastiques et viscoplastiques sont capturés par des tests de fluage-récupération. Les données expérimentales et un solveur 0D sont utilisés pour identifier les paramètres du modèle par un algorithme d'optimisation (Nelder-Mead). Les paramètres identifiés sont représentés en fonction de l'humidité relative et sont illustrés sur la figure 2. Les modules viscoélastiques ont une tendance décroissante avec l'augmentation de l'humidité relative sauf un d'entre eux qui augmente. Certains des paramètres viscoplastiques et d'endommagement peuvent être adaptés avec des lignes de tendance croissantes ou décroissantes. La validation du modèle de von Mises est réalisée par des essais de fluage-récupération, des essais cycliques et des essais de charge-décharge. Une partie des résultats des essais de charge-décharge est présentée sur la figure 3. Comme observé, les résultats sont mieux validés lorsque l'humidité relative est supérieure à 50%. Cependant, les résultats numériques sont plus proches des données expérimentales pour HR50 et HR65.

3.2 Calibration et validation du modèle I_1-J_2

Le modèle de I_1-J_2 est calibré par des essais multiaxiaux de traction-compression, mais imposer une charge de compression aux éprouvettes thermoplastiques est très compliqué en raison du risque de flambement. Les éprouvettes diabolo sont donc conçues pour effectuer des essais de traction-torsion en tant que chargement multiaxial au lieu de la traction-compression. À cette fin, comme les éprouvettes de dog bone, les éprouvettes de diabolo sont également reconditionnées à HR0, HR25, HR50, HR65 et HR80 et les essais de traction-torsion monotones sont effectués à différents taux de chargement. Comme discuté précédemment, la quantité d'eau affecte la réponse mécanique du matériau, du caoutchouteux au vitreux. La figure 4 confirme ce fait. Comme dans la section précédente, l'algorithme d'optimisation de Nelder-Mead est utilisé pour identifier les paramètres du modèle, mais ici le paramètre d'asymétrie est également calibré. Pour inclure les nouveaux tests de traction-torsion sur les diabolos dans la procédure de calibration, il est nécessaire d'utiliser le solveur ABAQUS (avec l'UMAT implémenté). Selon les résultats de calibration et de validation du modèle de von Mises, le modèle rhéologique est plus compatible avec le matériau à un niveau élevé de HR. Donc, pour le modèle de I_1-J_2, l'identification des paramètres est effectuée uniquement à HR égal ou supérieur à 50%. Les résultats de la calibration révèlent que le matériau a un comportement asymétrique à HR50 mais présente un comportement symétrique à HR65. Cela peut être dû à la diffusion non uniforme de l'eau dans l'échantillon en raison de la géométrie complexe du diabolo. Le modèle de I_1-J_2 est validé en utilisant les données expérimentales des essais de traction-torsion

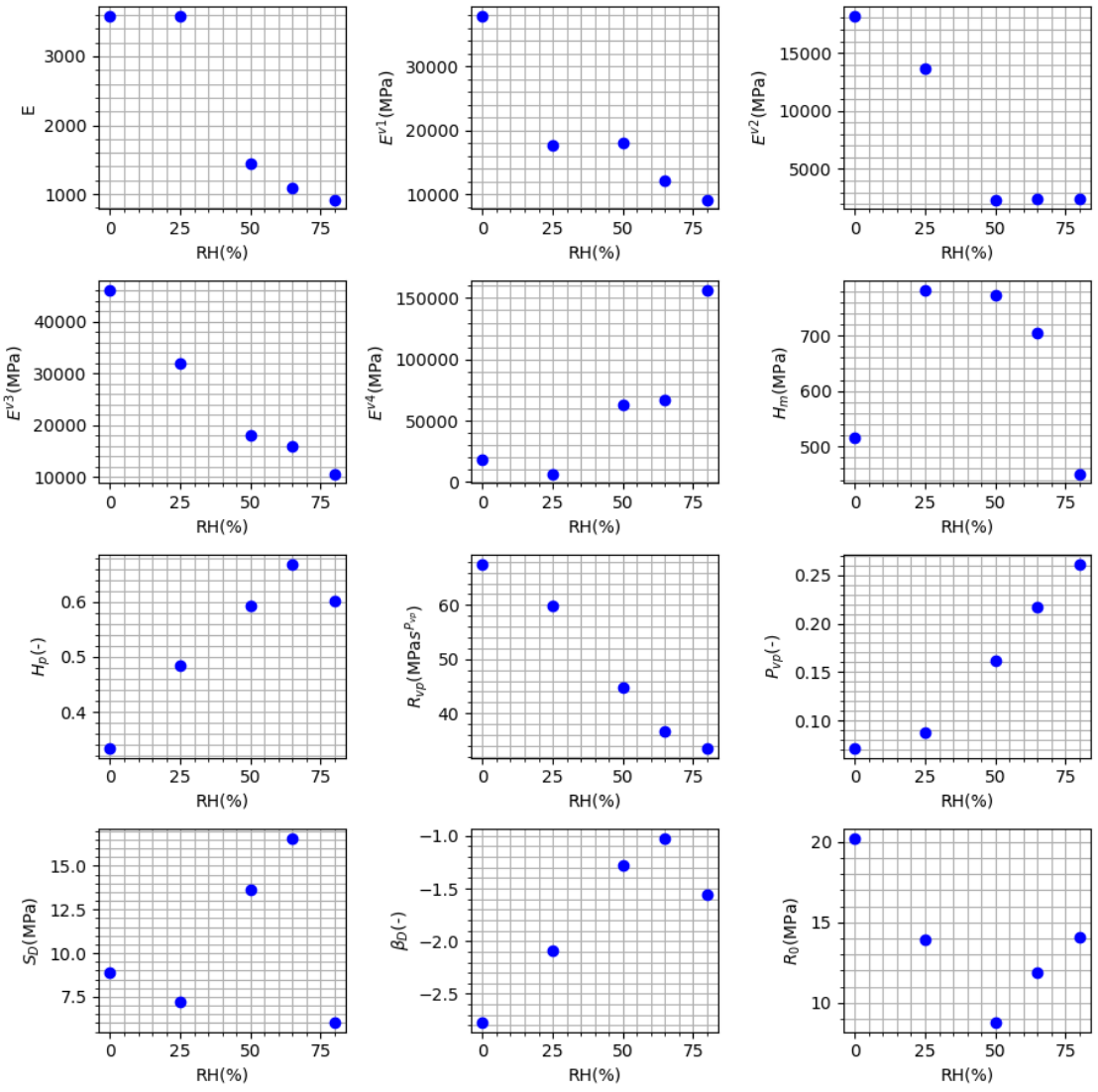

FIGURE 2 – Variation des paramètres du modèle en fonction de l'humidité relative.

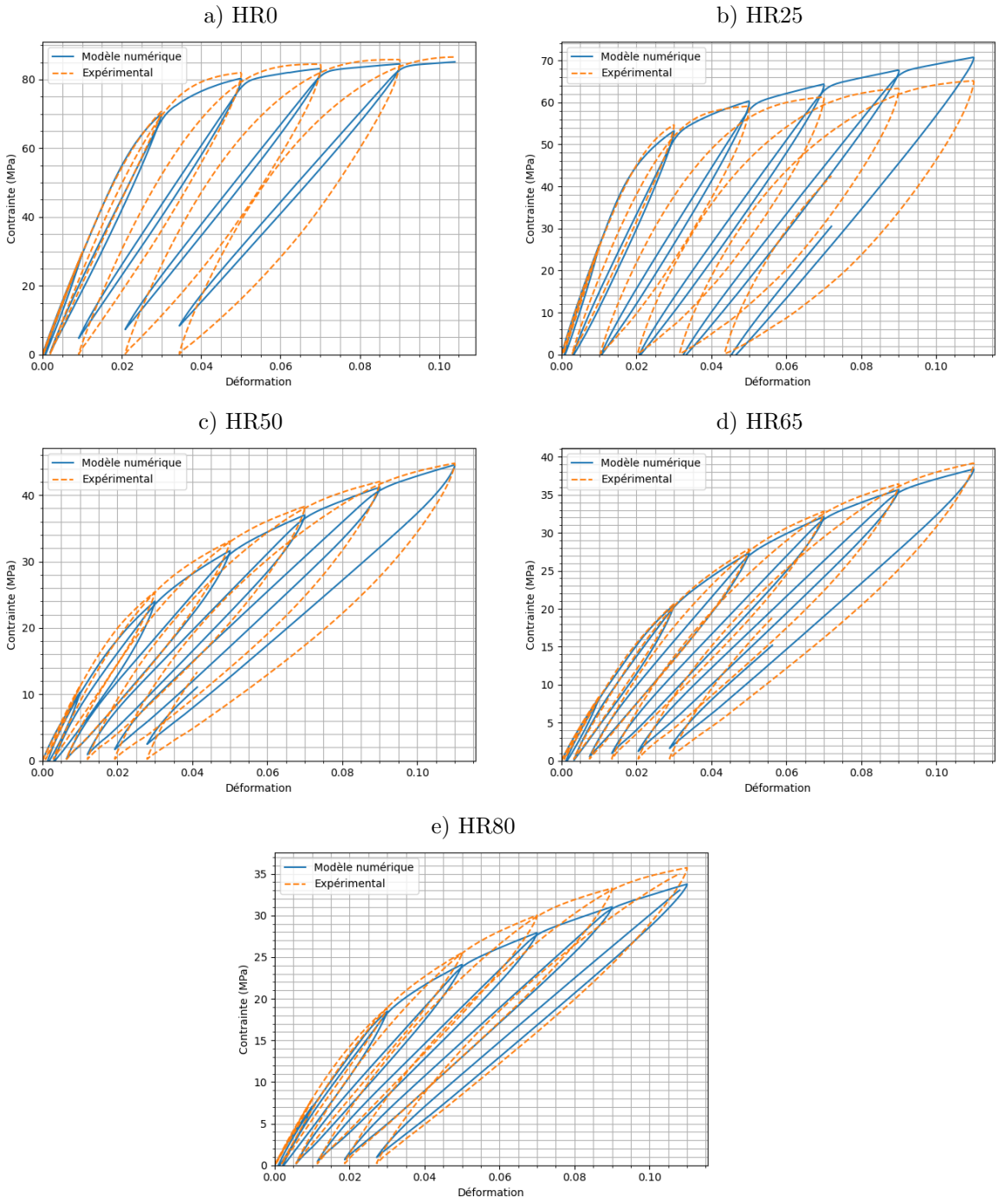

FIGURE 3 – Résultats de validation en utilisant des tests de charge-décharge à : a) HR0, b) HR25, c) HR50, d) HR65, e) HR80.

et les données des essais de fluage-récupération, cycliques et de charge-décharge utilisés dans la phase de validation du modèle de von Mises. Une partie des résultats est présentée pour HR50 sur la figure 5. Comme observé, le modèle de I_1-J_2 fournit des réponses qui sont mieux adaptées aux données expérimentales que celles du modèle de von Mises.

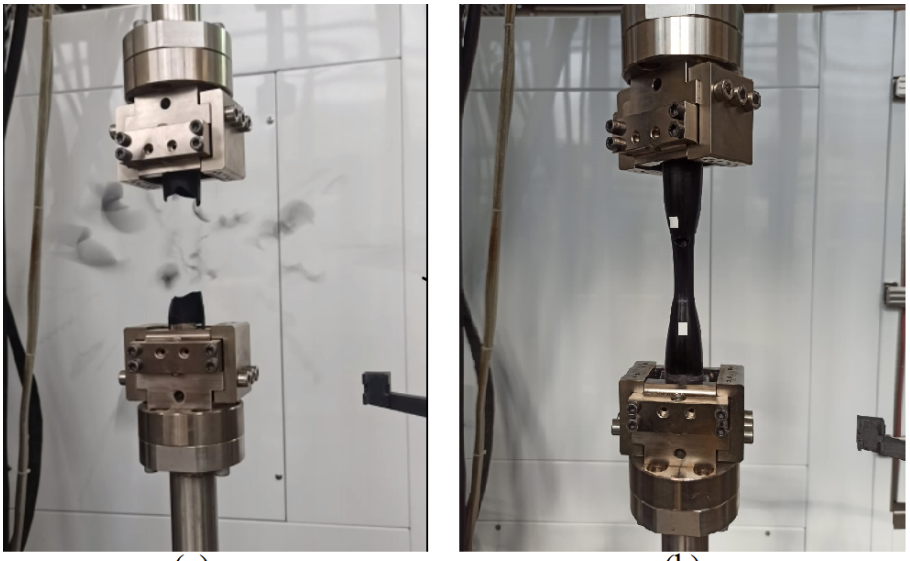

FIGURE 4 – a) Essai de traction-torsion pour le diabolo à HR0 ; b) Essai de traction-torsion pour le diabolo à HR50.

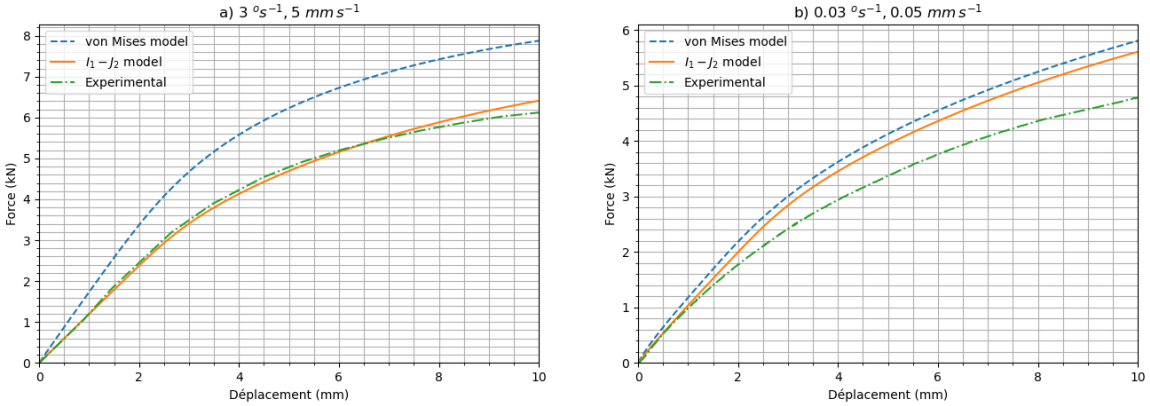

FIGURE 5 – Validation des résultats force-déplacement pour le modèle de I_1-J_2 à HR50 sous des tests de traction-torsion avec différents taux de chargement : a) $3\,^{\circ}\,\mathrm{s}^{-1}$ and $5\,\mathrm{mm\,s}^{-1}$, b) $0.03\,^{\circ}\,\mathrm{s}^{-1}$ et $0.05\,\mathrm{mm\,s}^{-1}$.

4 Modèle non local

Comme discuté dans les sections précédentes, la prédiction du comportement des thermoplastiques renforcés de verre nécessite le développement d'un modèle multi-échelle approprié. Ce modèle doit capturer les comportements inélastiques non linéaires de la matrice et traiter les limitations des modèles classiques, comme la sensibilité à la pression, le comportement asymétrique et les résultats non uniques à des niveaux d'endommagement élevés. En considérant la fonction de I_1-J_2, l'effet de la pression hydrostatique et l'asymétrie compression-traction sont capturés. De plus, l'identification du modèle à différentes HR permet d'étudier l'effet de l'humidité sur les paramètres du modèle et de prédire les réponses mécaniques des thermoplastiques à différents niveaux d'humidité relative. Cependant, la formulation locale n'est pas capable de produire des réponses physiques et uniques dans les modèles de calcul dans les zones très endommagées en raison du adoucissement du matériau.

En général, l'adoucissement signifie la dégradation du matériau par l'augmentation de la déformation, ce qui se produit souvent pour les polymères par rapport à l'humidité et la température. Ce phénomène physique conduit à un problème mal posé et par conséquent à l'instabilité du modèle numérique. La limitation du modèle à des niveaux élevés d'endommagement est traitée en utilisant un modèle non local. À cette fin, le modèle constitutif est formulé en considérant un potentiel thermodynamique renforcé par un gradient, qui est la fonction de variables d'état locales et non locales.

Différentes approches non locales sont rapportées dans la littérature. Certains auteurs appliquent la forme intégrale dans laquelle la variable locale est remplacée par sa variante non locale dérivée d'une moyenne pondérée sur le voisinage correspondant [18–22]. Selon cette méthode, les variables non locales dépendent non seulement de leurs positions locales mais aussi de leur moyenne pondérée dans le corps entier (figure 6). L'expansion de Taylor de la formulation non locale intégrale conduit à des formes à gradient qui sont plus simples à implémenter dans les logiciels d'éléments finis que la formulation intégrale [22–26]. De plus, d'autres méthodes basées sur des approches de champ de phase, micromorphiques et péridynamiques sont également employées largement dans la littérature, pour lesquelles des informations plus détaillées sont disponibles dans [27–32]. Ce travail propose une approche thermodynamique non locale pour les polyamides semi-cristallins formulée sous l'hypothèse de petites déformations et rotations.

Le modèle thermodynamique étendu est proposé en présentant la variable non locale et la longueur interne non locale ($l^{nl} = \sqrt{\xi^{nl}/\gamma^{nl}}$) et les lois constitutives sont exprimées avec les nouveaux termes nonlocaux supplémentaires. Le paramètre non local, ξ^{nl}, détermine le degré de régularisation

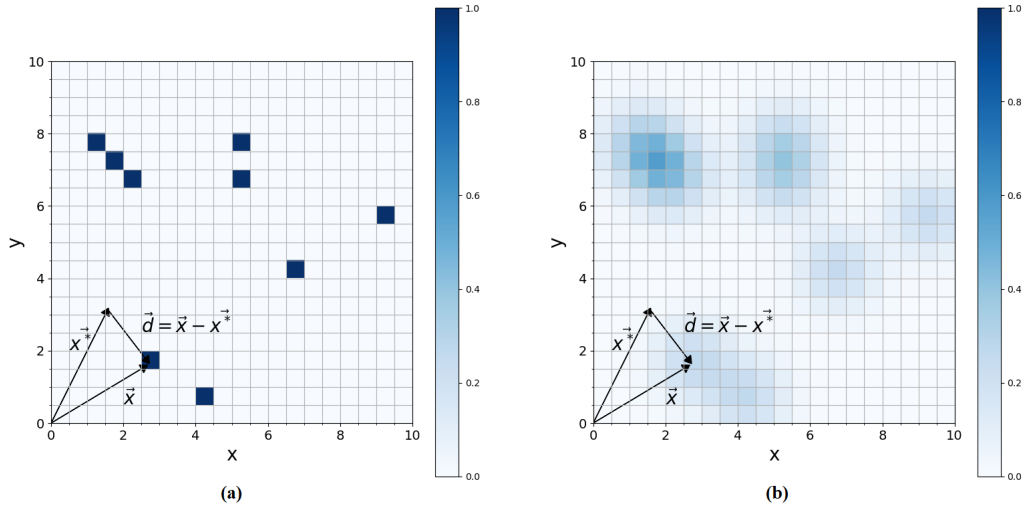

FIGURE 6 – a) Schéma du modèle local dans un champ spatial 2D ; b) Schéma du modèle non local dans un champ spatial 2D.

non locale et γ^{nl} ajuste l'interaction entre la variable locale et la variable non locale. La variable non locale est choisie en considérant les mécanismes dominants. Pour capturer la localisation de l'endommagement et traiter la sensibilité du maillage dans les calculs par éléments finis, le modèle non local est formulé dans deux cas différents : le premier considère l'endommagement non local et le deuxième considère la variable d'état de durcissement non locale.

4.1 Implémentation numérique

Les lois constitutives non locales sont implémentées numériquement à travers le "convex cutting plane". Cependant, le développement d'un modèle non local dans le code EF de ABAQUS nécessite une équation non locale ainsi que l'équation d'équilibre des contraintes. Afin d'imposer l'équation non locale dans un code EF commercial comme ABAQUS, trois méthodes différentes sont disponibles : premièrement, le développement d'un élément défini par l'utilisateur (UEL) [26, 33] et deuxièmement, en utilisant l'analogie entre l'équation non locale et l'équation de la chaleur quand la variable non locale est un scalaire [34, 35]. Dans cette étude, grâce à l'endommagement scalaire, l'analogie entre l'équation non locale et l'équation de la chaleur est utilisée pour l'étude paramétrique. À cette fin, le subroutine HETVAL est employé pour résoudre l'équation non locale.

4.2 Étude paramétrique du modèle non local

Comme déjà indiqué, la variable non locale peut être dérivée de la variable d'endommagement ou de la variable d'état de durcissement. Dans la première étape, l'efficacité du modèle d'endomma-

gement non local pour contrôler la localisation de l'endommagement est étudiée puis comparée au modèle dérivé de la variable d'état de durcissement non local. La plaque pré-entaillée est considérée sous une charge de traction et l'analyse de l'endommagement est effectuée dans différentes tailles de maillage. Les courbes force-déplacement globales pour les modèles local et non local avec différents paramètres non locaux sont tracées dans la figure 7. Comme observé, l'introduction des paramètres non locaux dans ce cas conduit à des défaillances plus rapides par rapport au modèle local. De plus, le profil de l'endommagement montre toujours la localisation dans différentes tailles de maillage et le problème des réponses non uniques n'est pas traité (figure 8). Le même comportement est également observé dans les profils de la variable d'état de durcissement, qui se localise dans une zone plus étroite à chaque raffinement du maillage (figure 9). Puisque dans le présent modèle, la viscoplasticité conduit à l'endommagement, une variable non locale basée sur la variable d'état de durcissement peut contrôler la localisation de l'endommagement.

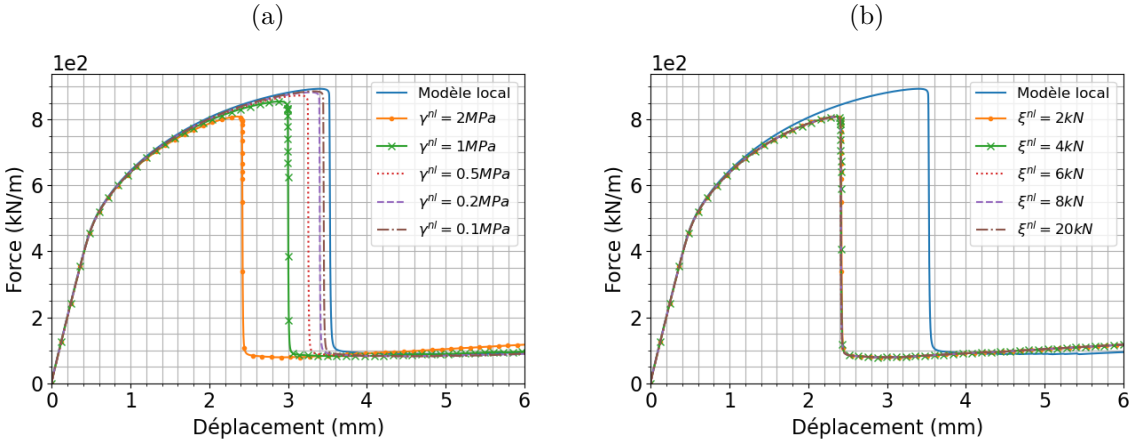

FIGURE 7 – Courbes force-déplacement pour la plaque pré-entaillée sous une charge de traction monotone uniaxiale quand le modèle non local est basé sur un l'endommagement non local : a) différentes valeurs de γ^{nl}, b) différentes valeurs de ξ^{nl}.

Dans la deuxième option, la variable non locale est dérivée de la variable d'état de durcissement. Le modèle est implémenté sur le même exemple. Les réponses sont présentées sous forme de courbes force-déplacement dans la figure 10. Comme observé, la zone d'adoucissement dans les réponses non locales est plus étendue par rapport à celles du modèle local et elles diminuent plus doucement (figure 10-a). De plus, les réponses montrent que la dépendance au maillage diminue en augmentant les paramètres non locaux (figure 10-b) et la figure 11 le confirme clairement à travers les profils d'endommagement uniques dans différentes tailles de maillage. Comme observé, les endommagements sont plus diffus par rapport au modèle local et les réponses mécaniques sont

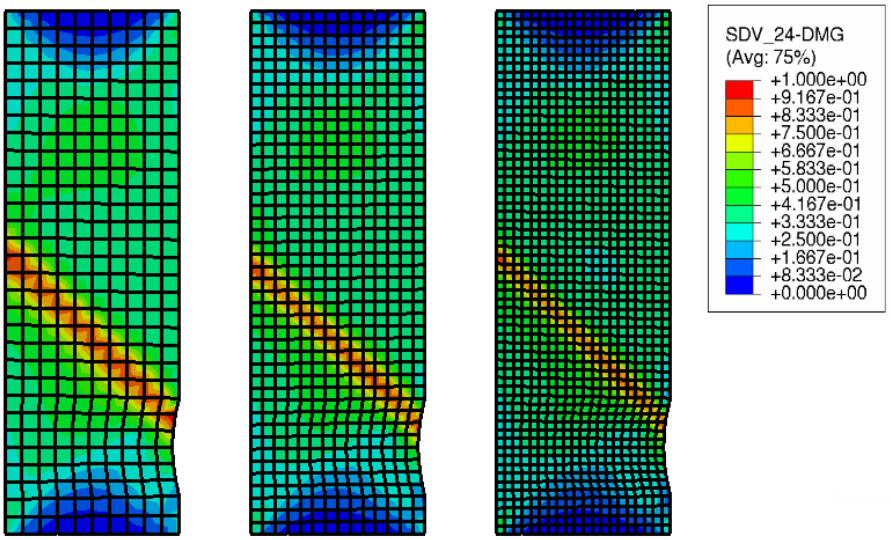

FIGURE 8 – Distribution de l'endommagement de la plaque pré-entaillée en utilisant le modèle d'endommagement non local sous une charge de traction monotone uniaxiale.

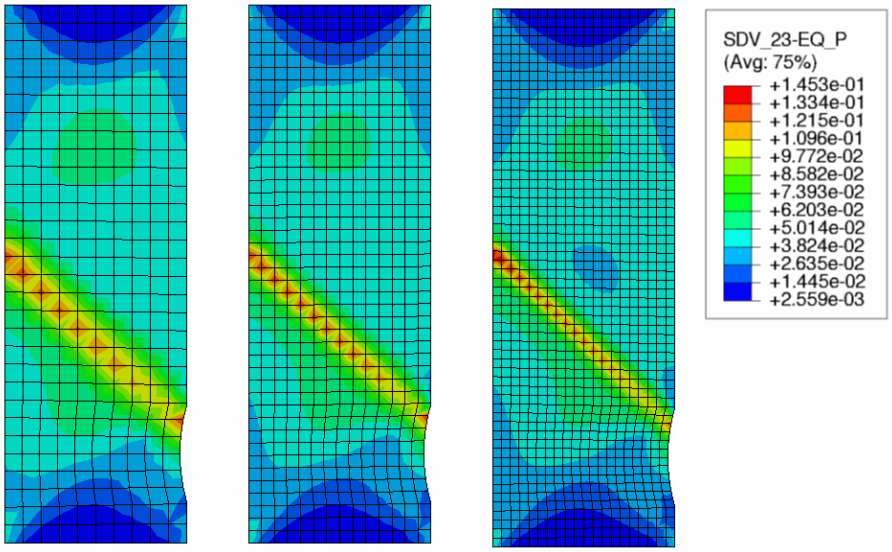

FIGURE 9 – Distribution de la variable d'état de durcissement dans la plaque pré-entaillée en utilisant le modèle d'endommagement non local sous une charge de traction monotone uniaxiale.

uniques.

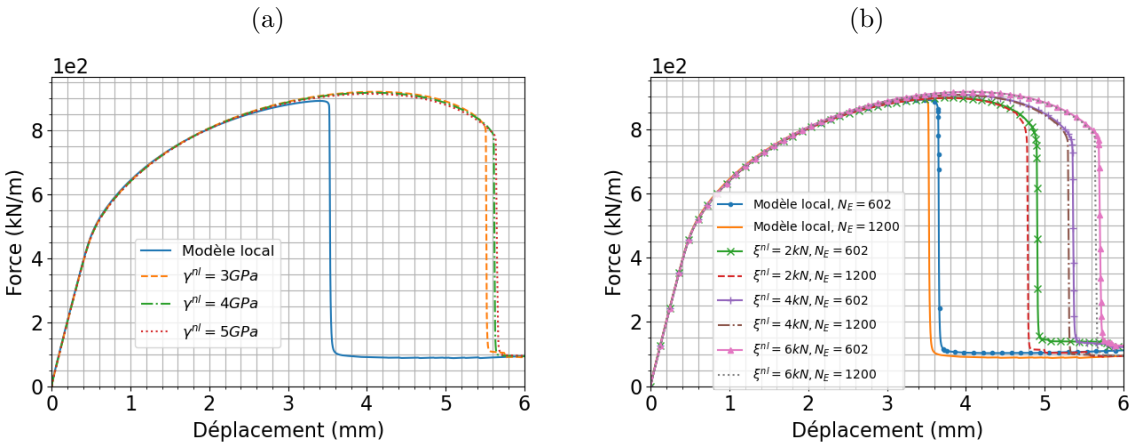

FIGURE 10 – Courbes force-déplacement pour la plaque pré-entaillée sous une charge de traction monotone uniaxiale lorsque le modèle non local est basé sur la variable d'état de durcissement non local : a) différentes valeurs de γ^{nl}, b) différentes valeurs de ξ^{nl}.

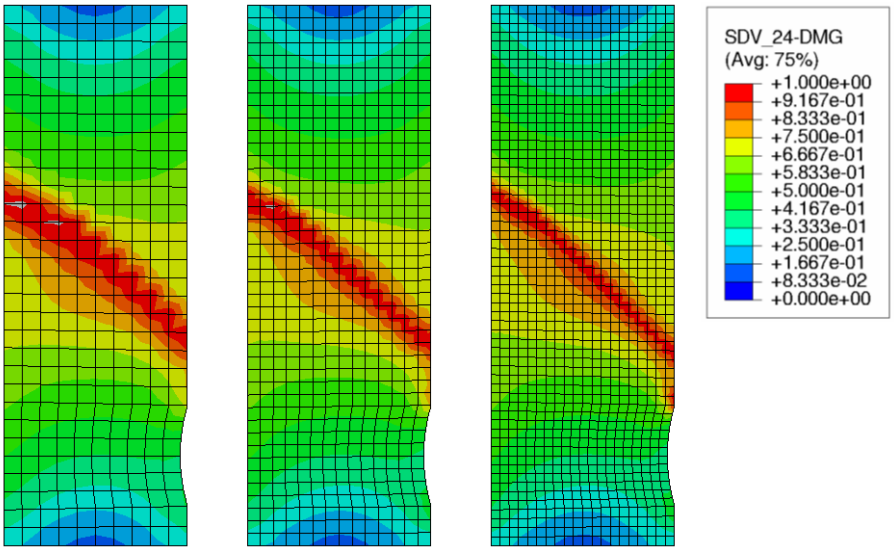

FIGURE 11 – Distribution de l'endommagement dans la plaque pré-entaillée en utilisant la variable d'état de durcissement non local sous une charge de traction monotone uniaxiale.

5 Modèle multi-échelle non local pour les thermoplastiques renforcés de verre

Le modèle non local, présenté dans la section précédente, est utilisé dans le modèle multi-échelle visant à prédire la réponse mécanique du polyamide renforcé de verre. À cette fin, le modèle phénoménologique viscoélastique viscoplastique est adopté pour capturer la réponse non linéaire de la phase de matrice. Ensuite, une approche d'homogénéisation appropriée en combinaison avec le modèle non local est considérée pour obtenir la réponse globale du composite. Le modèle d'homogénéisation multi-échelle traite du comportement des composites à la fois à l'échelle macro et micro. Il considère les mécanismes des constituants du composite ainsi que leurs caractéristiques géométriques et leurs configurations dans la microstructure. A ce sujet, de nombreuses approches d'homogénéisation par éléments finis et par champ moyen sont proposées dans la littérature [36–52].

5.1 Modélisation multi-échelle

Dans le présent modèle composite, trois tailles sont très importantes : la taille globale de la structure, L, la taille du VER, l^{ε}, et la longueur interne non locale, l^{nl}, de la phase matricielle. En supposant que la taille de VER est toujours beaucoup plus petite que la taille réelle de la structure ($L \gg l^{\varepsilon}$), deux cas différents sont examinés :

- premièrement, lorsque la taille du VER est suffisamment grande ou comparable à la longueur interne ($l^{nl} \leq l^{\varepsilon}$ or l^{nl} dans le même ordre que l^{ε}),
- deuxièmement, lorsque la longueur interne est beaucoup plus grande que la taille VER ($l^{nl} \gg l^{\varepsilon}$), mais l^{nl} est toujours inférieure à L.

Pour illustrer les différences entre les deux cas, l'expansion asymptotique de l'équilibre des contraintes et de l'équation non locale est étudiée. Pour le premier cas (longueur interne inférieure ou du même ordre que la taille du VER), l'équation non locale n'apparaît qu'à l'échelle microscopique, et il provoque des difficultés d'homogénéisation et de séparation d'échelle, comme indiqué dans la littérature [53]. Pour le second cas (longueur interne beaucoup plus grande que la taille du VER), l'équation non locale apparaît à l'échelle macroscopique, et la séparation d'échelle a un formalisme plus "classique".

Pour étudier le comportement du modèle à l'échelle microscopique, plusieurs exemples sont examinés : une cellule unitaire périodique et un groupe de cellules unitaires périodiques constituées de fibres longues unidirectionnelles et d'une matrice PA 66. Pour chaque cas, l'analyse est réalisée en utilisant ABAQUS et l'endommagement est étudié. Pour le premier cas, les profils d'endommagement sont illustrés sur la figure 12. Les profils d'endommagement ne sont pas identiques et

uniformes dans l'ensemble des VERs et il n'est pas clair lequel illustre le véritable endommagement, donc le VER n'est pas représentatif. Pour le second cas, un exemple similaire est étudié. La figure13 montre que les profils d'endommagement des VER sont identiques, donc le VER est représentatif. Selon les résultats ci-dessus, on conclut que le deuxième cas (longueur interne beaucoup plus grande que la taille du VER) est plus compatible avec le modèle multi-échelle que le premier parce que le VER est représentatif et il satisfait l'hypothèse de périodicité et le formalisme classique de séparation d'échelle. Considérant cette hypothèse, une approche Mori-Tanaka/TFA [54–56] est utilisée comme approche d'homogénéisation du champ moyen.

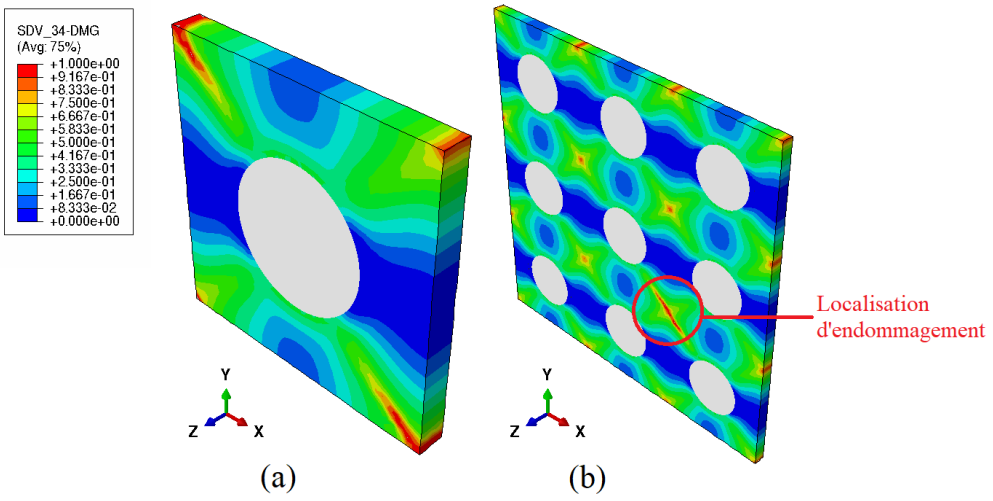

FIGURE 12 – Profil d'endommagement sous chargement monotone quand $l^{nl} = 0.01\, l^{\varepsilon}$ $(l^{nl} < l^{\varepsilon})$: a) un seul VER renforcé par des fibres longues, b) un groupe des VERs.

5.2 Implémentation numérique du modèle multi-échelle non local

Selon la discussion précédente, la longueur interne est considérée être beaucoup plus grande que la taille du VER et l'équation non locale est résolue à l'échelle macroscopique. L'implémentation numérique se compose de trois étapes différentes : premièrement, les mécanismes inélastiques à l'échelle microscopique dans la matrice sont calculés en utilisant le subroutine VEVPD, deuxièmement, le subroutine du modèle micromécanique fournit le tenseur de contrainte global et le module sécant, et troisièmement, l'équation non locale est résolue à l'échelle macroscopique en utilisant l'analogie entre l'équation de chaleur et l'équation non locale. L'interaction entre ces étapes et les entrées et sorties associées sont brièvement présentées dans la figure 14.

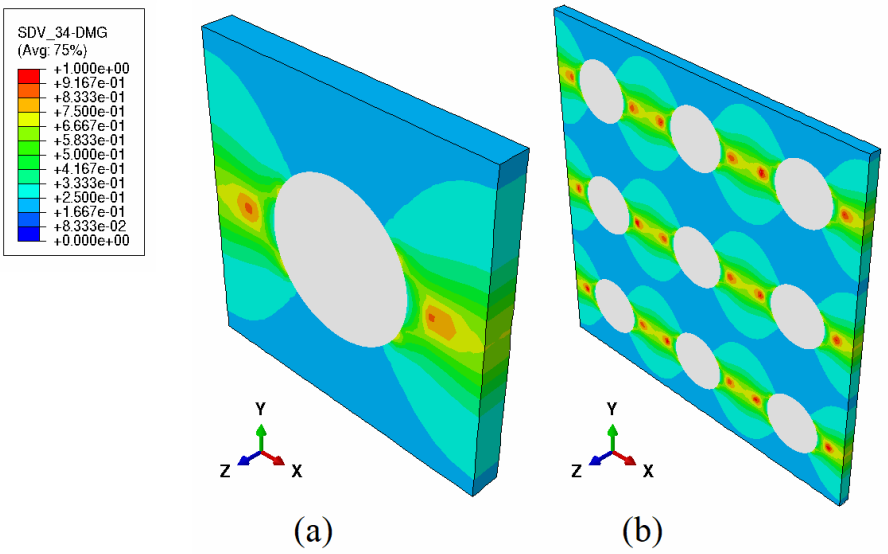

FIGURE 13 – Profil d'endommagement sous chargement monotone quand $l^{nl} = 100\, l^{\varepsilon}$ ($l^{nl} \gg l^{\varepsilon}$) : a) un seul VER renforcé par des fibres longues, b) un groupe des VERs.

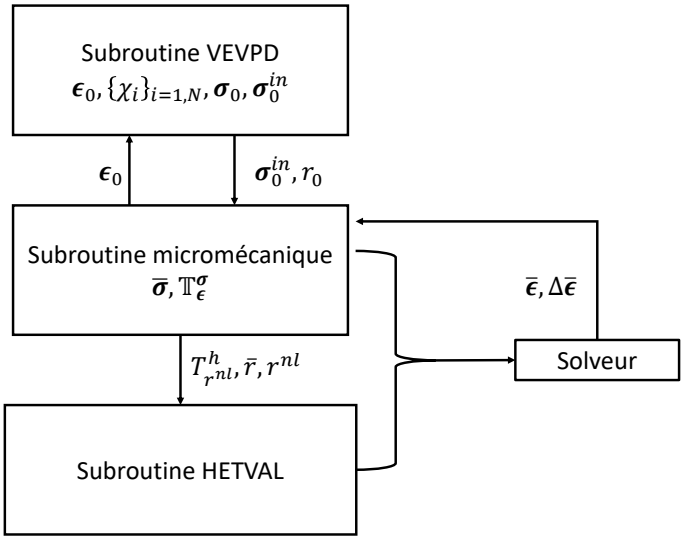

FIGURE 14 – Schéma de l'implémentation numérique du modèle multi-échelle non local dans le logiciel EF.

5.3 Validation du modèle multi-échelle et étude paramétrique

La validité du modèle Mori-Tanaka/TFA proposé peut être étudiée en utilisant un modèle composite multicouche [57]. L'homogénéisation proposée est réalisée sur la structure soumise à une charge monotone, puis les résultats obtenus sont comparés à un modèle structurel complet sans homogénéisation. Les réponses des deux modèles sous les mêmes conditions limites sont tracées comme des courbes force-déplacement dans la figure 15. Comme observé, il y a un bon accord entre les deux analyses.

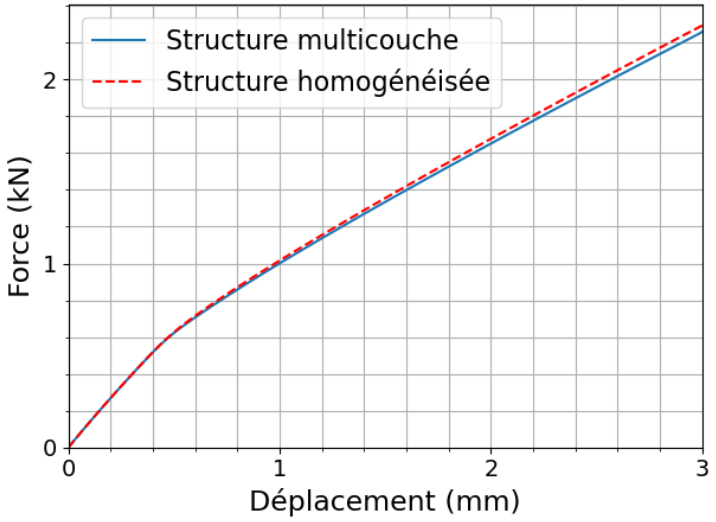

FIGURE 15 – Courbe force-déplacement sous une charge de traction monotone et comparaison entre le modèle de structure complète et le modèle d'homogénéisation Mori-Tanaka/TFA.

Pour comparer les modèles local et non local, une plaque composite pré-entaillée (avec une longue entaille) est soumise à une charge de traction monotone et étudiée par les modèles local et non local. La figure 16 compare les courbes force-déplacement. Comme observé, la force ultime est plus faible dans le modèle local et le modèle non local est relativement plus stable. La figure 17 montre la distribution 3D de l'endommagement de la matrice pour les modèles local et non local. Dans le modèle local, l'endommagement est localisé dans la zone de fissure traversant la structure. Cependant, dans le modèle non local, l'endommagement reste autour de la région de l'entaille. En d'autres termes, le modèle non local fournit des réponses plus stables dans la zone de petite déformation par rapport au modèle local.

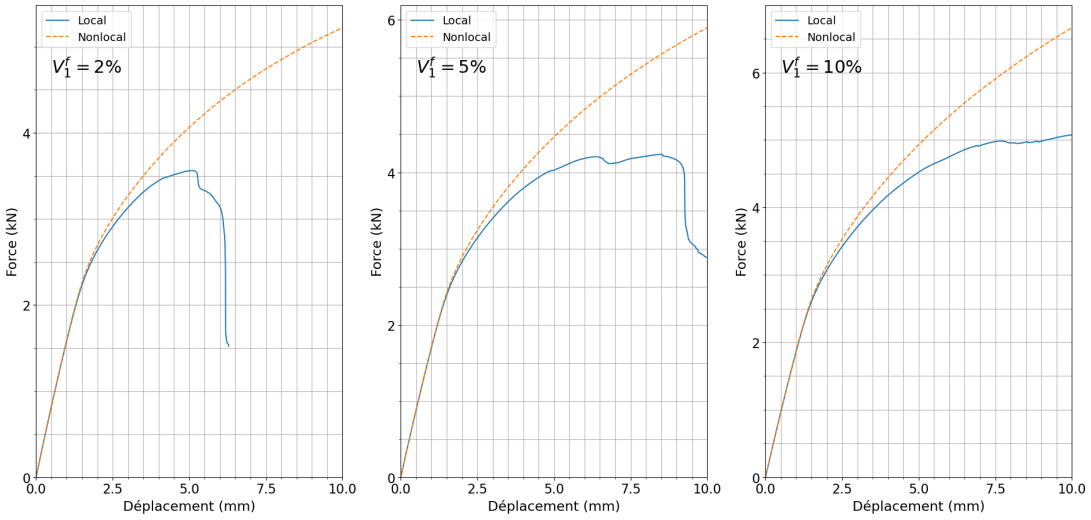

FIGURE 16 – Courbes force-déplacement pour la plaque composite pré-entaillée sous une charge de traction monotone en utilisant les modèles local et non local.

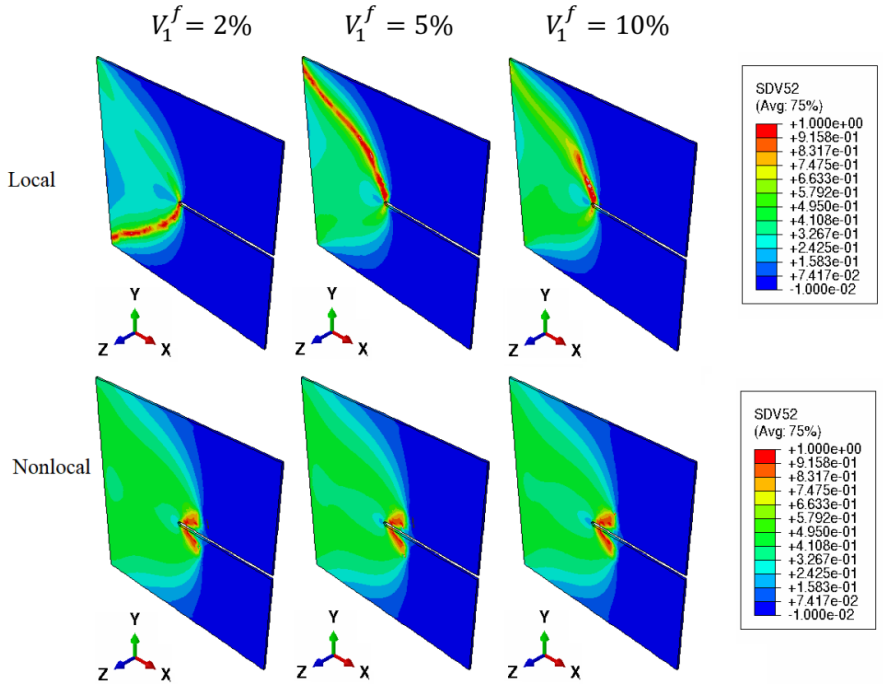

FIGURE 17 – Distribution de l'endommagement de la matrice dans la plaque pré-entaillée sous une charge de traction monotone en utilisant les modèles local et non local.

6 Conclusions

Le but de cette recherche est d'étudier le comportement non linéaire du polyamide 66 et du polyamide 66 renforcé de verre en considérant les conditions environnementales (humidité relative), la sensibilité à la pression et l'asymétrie traction-compression. Ces matériaux présentent une asymétrie traction-compression lorsqu'ils subissent une charge non proportionnelle et une grande sensibilité aux conditions environnementales, notamment à l'humidité. De plus, un niveau élevé d'endommagement en eux est accompagné d'un adoucissement qui conduit à des problèmes mal posés et à des résultats non uniques dans les modèles de calcul. Dans le présent travail, un modèle viscoélastique viscoplastique avec l'endommagement ductile (VEVPD) a été présenté, dans lequel l'effet de pression hydrostatique et l'asymétrie traction-compression sont inclus. Une campagne expérimentale a été conçue pour étudier les mécanismes dominants et identifier les paramètres du modèle proposé. Ensuite, le modèle a été amélioré en utilisant l'approche non locale à gradient pour obtenir des réponses physiques et uniques pour le matériau fortement endommagé. Cette approche a été étendue à un modèle multi-échelle afin de modéliser le comportement des composites. Dans la suite, les conclusions sont brièvement présentés.

- Le modèle VEVPD développé par Praud et al. [1] a été étendu à un modèle plus avancé tenant compte de l'asymétrie traction-compression et de l'effet de la pression hydrostatique. L'étude paramétrique a révélé que l'effet du paramètre d'asymétrie est plus important quand le matériau subit un chargement multi-axial ou cyclique en traction-compression.

- Une campagne expérimentale a été conçue et réalisée. Elle a permis d'étudier la variation de la réponse mécanique de caoutchouteuse à vitreuse en reconditionnant le matériau polyamide 66 à différentes conditions d'Humidité Relative (HR). Avant cette étude, le modèle VEVPD basé sur von Mises n'avait été calibré et validé que pour le PA66 à HR50 [1]. Pour la première fois, le modèle VEVPD basé sur la fonction de von Mises a été calibré et validé pour le PA66 avec HR0, HR25, HR65, et HR80. Afin de capturer l'asymétrie traction-compression, des tests de traction-torsion ont été réalisés sur des éprouvettes de diabolo. Les courbes force-déplacement et moment-angle globales obtenues ont été utilisées pour calibrer le modèle basé sur I_1-J_2. Le paramètre d'asymétrie identifié dans HR50 ($m = 1.05$) indique que la limite d'élasticité en compression est légèrement supérieure à la limite d'élasticité en traction.

- Pour traiter les réponses non physiques à des niveaux élevés d'endommagement, une approche de gradient non local a été présentée. Pour la variable non-locale, deux options ont

été étudiées : l'endommagement non local et la variable d'état de durcissement non local. Les études paramétriques montrent que le modèle d'endommagement non local ne fournit pas les résultats souhaités, parce que la localisation de la viscoplasticité n'est pas prise en compte. Cependant, le modèle non local à gradient basé sur la variable d'état de durcissement non local est plus efficace et conduit à des réponses uniques.

- Le modèle non local a été étendu à un modèle multi-échelle. En considérant la longueur interne non locale beaucoup plus grande que la taille du VER, un modèle non local Mori-Tanaka/TFA approprié a été formulé pour la première fois. Le modèle multi-échelle a été validé avec un modèle d'éléments finis composite multicouche à structure complète et une étude paramétrique a été réalisée pour examiner son efficacité. Les résultats de l'étude paramétrique montrent que les réponses du modèle non local sont plus stables à un haut niveau d'endommagement que celles du modèle local.

Références

[1] F. Praud, G. Chatzigeorgiou, J. Bikard, and F. Meraghni, "Phenomenological multi-mechanisms constitutive modelling for thermoplastic polymers, implicit implementation and experimental validation," *Mechanics of Materials*, vol. 114, pp. 9–29, 11 2017.

[2] A. Benaarbia, A. Chrysochoos, and G. Robert, "Kinetics of stored and dissipated energies associated with cyclic loadings of dry polyamide 6.6 specimens," *Polymer Testing*, vol. 34, pp. 155–167, 4 2014.

[3] A. Benaarbia, A. Chrysochoos, and G. Robert, "Influence of relative humidity and loading frequency on the pa6.6 cyclic thermomechanical behavior : part i. mechanical and thermal aspects," *Polymer Testing*, vol. 40, pp. 290–298, 12 2014.

[4] A. Benaarbia, A. Chrysochoos, and G. Robert, "Thermomechanical analysis of the onset of strain concentration zones in wet polyamide 6.6 subjected to cyclic loading," *Mechanics of Materials*, vol. 99, pp. 9–25, 8 2016.

[5] E. Arruda and M. Boyce, "A three-dimensional constitutive model for the large stretch behavior of rubber elastic materials," *Journal of The Mechanics and Physics of Solids*, vol. 41, no. 2, pp. 389–412, 1993.

[6] N. Billon, "New constitutive modeling for time-dependent mechanical behavior of polymers close to glass transition : Fundamentals and experimental validation," *Journal of Applied Polymer Science*, vol. 125, pp. 4390–4401, 3 2012.

[7] A. Launay, M. Maitournam, Y. Marco, I. Raoult, and F. Szmytka, "Cyclic behaviour of short glass fibre reinforced polyamide : Experimental study and constitutive equations," *International Journal of Plasticity*, vol. 27, pp. 1267–1293, 8 2011.

[8] A. Krairi and I. Doghri, "A thermodynamically-based constitutive model for thermoplastic polymers coupling viscoelasticity, viscoplasticity and ductile damage," *International Journal of Plasticity*, vol. 60, pp. 163–181, 2014.

[9] A. Benaarbia, Y. Rae, and W. Sun, "Unified viscoplasticity modelling and its application to fatigue-creep behaviour of gas turbine rotor," *International Journal of Mechanical Sciences*, vol. 136, pp. 36–49, 2 2018.

[10] B. Halphen and Q. Nguyen, "On the generalized standards materials (in french)," *Journal de Mécanique*, vol. 14, pp. 39–63, 1975.

[11] P. Germain, P. Suquet, and Q. Nguyen, "Continuum thermomechanics," *ASME Transactions Series E Journal of Applied Mechanics*, vol. 50, pp. 1010–1020, 1983.

[12] L. Kachanov, "Time of the rupture process under creep conditions. izvestiia akademii nauk sssr, otdelenie teckhnicheskikh nauk," vol. 8, pp. 26–31, 1958.

[13] Y. Rabotnov, *Creep rupture*, pp. 342–349. Springer Berlin Heidelberg, 1968.

[14] J. L. Chaboche, "Thermodynamic formulation of constitutive equations and application to the viscoplasticity and viscoelasticity of metals and polymers," *International Journal of Solids and Structures*, vol. 34, pp. 2239–2254, 6 1997.

[15] I. Doghri and A. Ouaar, "Homogenization of two-phase elasto-plastic composite materials and structures : Study of tangent operators, cyclic plasticity and numerical algorithms," *International Journal of Solids and structures*, vol. 40, no. 7, pp. 1681–1712, 2003.

[16] M. Haddad, I. Doghri, and O. Pierard, "Viscoelastic-viscoplastic polymer composites : Development and evaluation of two very dissimilar mean-field homogenization models," *International Journal of Solids and Structures*, vol. 236, p. 111354, 2022.

[17] E. Ghorbel, "A viscoplastic constitutive model for polymeric materials," *International Journal of Plasticity*, vol. 24, pp. 2032–2058, 11 2008.

[18] G. Pijaudier-cabot and Z. Bažant, "Nonlocal damage theory," *Journal of Engineering Mechanics*, vol. 113, pp. 1512–1533, 10 1987.

[19] M. Jirásek, Jirásek, M, Jirásek, M, S. Rolshoven, and P. Grassl, "Nonlocal models for damage and fracture : Comparison of approaches," *International Journal for Numerical and Analytical Methods in Geomechanics*, vol. 35, no. 6, pp. 653–670, 1998.

[20] M. Jirásek, "Objective modeling of strain localization," *Revue Française de Génie Civil*, vol. 6, pp. 1119–1132, 1 2002.

[21] M. Jirásek, S. Rolshoven, and P. Grassl, "Size effect on fracture energy induced by non-locality," *International Journal for Numerical and Analytical Methods in Geomechanics*, vol. 28, pp. 653–670, 6 2004.

[22] M. Jirásek, "Nonlocal damage mechanics," *Revue européenne de génie civil*, vol. 11, pp. 993–1021, 10 2007.

[23] Z. Bažant, T. Belytschko, and T. Chang, "Continuum theory for strain-softening," *Journal of Engineering Mechanics*, vol. 110, pp. 1666–1692, 12 1984.

[24] R. Peerlings, M. Geers, D. Borst, and W. Brekelmans, "A critical comparison of nonlocal and gradient-enhanced softening continua," *International Journal of Solids and Structures*, vol. 38, no. 44, pp. 7723–7746, 2001.

[25] S. Forest, "Micromorphic approach for gradient elasticity, viscoplasticity, and damage," *Journal of Engineering Mechanics*, vol. 135, pp. 117–131, 3 2009.

[26] B. Dimitrijevic and K. Hackl, "A regularization framework for damage-plasticity models via gradient enhancement of the free energy," *International Journal for Numerical Methods in Biomedical Engineering*, vol. 27, no. 8, pp. 1199–1210, 2011.

[27] S. Silling, "Reformulation of elasticity theory for discontinuities and long-range forces," *Journal of The Mechanics and Physics of Solids*, vol. 48, no. 1, pp. 175–209, 2000.

[28] S. Silling and R. Lehoucq, *Peridynamic theory of solid mechanics*, vol. 44, pp. 73–168. Elsevier, 2010.

[29] K. Saanouni and M. Hamed, "Micromorphic approach for finite gradient-elastoplasticity fully coupled with ductile damage : Formulation and computational aspects," *International Journal of Solids and Structures*, vol. 50, pp. 2289–2309, 7 2013.

[30] C. Miehe, M. Hofacker, and F. Welschinger, "A phase field model for rate-independent crack propagation : Robust algorithmic implementation based on operator splits," *Computer Methods in Applied Mechanics and Engineering*, vol. 199, no. 45, pp. 2765–2778, 2010.

[31] C. Miehe, F. Aldakheel, and A. Raina, "Phase field modeling of ductile fracture at finite strains : A variational gradient-extended plasticity-damage theory," *International Journal of Plasticity*, vol. 84, pp. 1–32, 2016.

[32] R. De Borst and C. Verhoosel, "Gradient damage vs phase-field approaches for fracture : Similarities and differences," *Computer Methods in Applied Mechanics and Engineering*, vol. 312, pp. 78–94, 12 2016.

[33] B. Kiefer, T. Waffenschmidt, L. Sprave, and A. Menzel, "A gradient-enhanced damage model coupled to plasticity—multi-surface formulation and algorithmic concepts," *International Journal of Damage Mechanics*, vol. 27, no. 2, pp. 253–295, 2018.

[34] C. Hortig, *Local and non-local thermomechanical modeling and finite-element simulation of high-speed cutting.* PhD thesis, Dortmund, Techn. Univ., Diss., 2010, 2010.

[35] R. Ostwald, E. Kuhl, and A. Menzel, "On the implementation of finite deformation gradient-enhanced damage models," *Computational Mechanics*, vol. 64, pp. 847–877, 2 2019.

[36] L. Wu, L. Noels, L. Adam, and I. Doghri, *Non-local damage-enhanced mfh for multiscale simulations of composites*, pp. 115–121. Springer New York, 2013.

[37] E. Tikarrouchine, G. Chatzigeorgiou, F. Praud, B. Piotrowski, Y. Chemisky, and F. Meraghni, "Three-dimensional fe2 method for the simulation of non-linear, rate-dependent response of composite structures," *Composite Structures*, vol. 193, pp. 165–179, 6 2018.

[38] C. Mareau, V. Favier, B. Weber, A. Galtier, and M. Berveiller, "Micromechanical modeling of the interactions between the microstructure and the dissipative deformation mechanisms

in steels under cyclic loading," *International Journal of Plasticity*, vol. 32-33, pp. 106–120, 5 2012.

[39] P. Ponte-Castaneda, "The effective mechanical properties of nonlinear isotropic composites," *J. Mech. Phys. Solids*, vol. 39, pp. 45–e71, 1991.

[40] K. Terada and N. Kikuchi, "A class of general algorithms for multi-scale analyses of heterogeneous media," *Computer Methods in Applied Mechanics and Engineering*, vol. 190, pp. 5427–5464, 7 2001.

[41] F. Meraghni, F. Desrumaux, and M. Benzeggagh, "Implementation of a constitutive micromechanical model for damage analysis in glass mat reinforced composite structures," *Composites Science and Technology*, vol. 62, pp. 2087–2097, 12 2002.

[42] B. Love and R. Batra, "Determination of effective thermomechanical parameters of a mixture of two elastothermoviscoplastic constituents," *International Journal of Plasticity*, vol. 22, pp. 1026–1061, 6 2006.

[43] P. Suquet, "Four exact relations for the effective relaxation function of linear viscoelastic composites," *Comptes Rendus Mécanique*, vol. 340, pp. 387–399, 4 2012.

[44] F. Fritzen, S. Forest, T. Böhlke, D. Kondo, and T. Kanit, "Computational homogenization of elasto-plastic porous metals," *International Journal of Plasticity*, vol. 29, pp. 102–119, 2 2012.

[45] A. Benaarbia, A. Chrysochoos, and G. Robert, "Fiber orientation effects on heat source distribution in reinforced polyamide 6.6 subjected to low cycle fatigue," *Journal of Engineering Mathematics*, vol. 90, no. 1, pp. 13–36, 2015.

[46] G. Chatzigeorgiou, N. Charalambakis, Y. Chemisky, and F. Meraghni, "Periodic homogenization for fully coupled thermomechanical modeling of dissipative generalized standard materials," *International Journal of Plasticity*, vol. 81, pp. 18–39, 6 2016.

[47] F. Praud, G. Chatzigeorgiou, Y. Chemisky, and F. Meraghni, "Hybrid micromechanical-phenomenological modelling of anisotropic damage and anelasticity induced by micro-cracks in unidirectional composites," *Composite Structures*, vol. 182, pp. 223–236, 12 2017.

[48] S. Kotha, D. Ozturk, and S. Ghosh, "Parametrically homogenized constitutive models (phcms) from micromechanical crystal plasticity fe simulations, part i : sensitivity analysis and parameter identification for titanium alloys," *International Journal of Plasticity*, vol. 120, pp. 296–319, 9 2019.

[49] G. Chatzigeorgiou, A. Benaarbia, and F. Meraghni, "Piezoelectric-piezomagnetic behaviour of coated long fiber composites accounting for eigenfields," *Mechanics of Materials*, vol. 138, p. 103157, 2019.

[50] G. Chatzigeorgiou, F. Meraghni, N. Charalambakis, and A. Benaarbia, "Multiscale modeling accounting for inelastic mechanisms of fuzzy fiber composites with straight or wavy carbon nanotubes," *International Journal of Solids and Structures*, vol. 202, pp. 39–57, 2020.

[51] F. Praud, G. Chatzigeorgiou, and F. Meraghni, "Fully integrated multi-scale modelling of damage and time-dependency in thermoplastic-based woven composites," *International Journal of Damage Mechanics*, vol. 30, pp. 163–195, 2021.

[52] E. Tikarrouchine, A. Benaarbia, G. Chatzigeorgiou, and F. Meraghni, "Non-linear fe2 multiscale simulation of damage, micro and macroscopic strains in polyamide 66-woven composite structures : analysis and experimental validation," *Composite Structures*, vol. 255, p. 112926, 2021.

[53] F. Fantoni, A. Bacigalupo, M. Paggi, and J. Reinoso, "A phase field approach for damage propagation in periodic microstructured materials," *International Journal of Fracture*, vol. 223, no. 1, pp. 53–76, 2020.

[54] G. J. Dvorak and Y. Benveniste, "On transformation strains and uniform fields in multiphase elastic media," *Proceedings of the Royal Society of London. Series A : Mathematical and Physical Sciences*, vol. 437, no. 1900, pp. 291–310, 1992.

[55] M. Barral, G. Chatzigeorgiou, F. Meraghni, and R. Léon, "Homogenization using modified mori-tanaka and tfa framework for elastoplastic-viscoelastic-viscoplastic composites : theory and numerical validation," *International Journal of Plasticity*, vol. 127, p. 102632, 2020.

[56] Q. Chen, G. Chatzigeorgiou, and F. Meraghni, "Extended mean-field homogenization of viscoelastic-viscoplastic polymer composites undergoing hybrid progressive degradation induced by interface debonding and matrix ductile damage," *International Journal of Solids and Structures*, vol. 210, pp. 1–17, 2021.

[57] G. Chatzigeorgiou, "Study of multilayered composites through periodic homogenization and mori–tanaka methods," *Mechanics of Materials*, p. 104110, 2021.

Soheil SATOURI

Modélisation hygro-mécanique non locale de l'endommagement dans les structures thermoplastiques renforcées en relation avec la microstructure.

Résumé : Les thermoplastiques présentent souvent des mécanismes inélastiques non linéaires. Pour prédire leurs réponses mécaniques, la viscoélasticité, la viscoplasticité et l'endommagement ductile sont pris en compte. Un critère plastique I1-J2 est présenté pour capturer l'effet de la pression hydrostatique et le comportement asymétrique tension-compression, sur la base duquel une étude paramétrique est réalisée, prenant en compte des chargements cycliques et multiaxiaux. L'influence de l'absorption d'eau sur le comportement des thermoplastiques est étudiée à travers une campagne expérimentale permettant de calibrer, à différents niveaux d'humidité relative, les modèles basés sur les critères plastiques de von Mises et I_1-J_2. Les thermoplastiques présentent un adoucissement à des niveaux d'endommagement élevés, ce qui conduit à un problème mal posé dans le cadre du continuum local et à une non-objectivité dans les modèles éléments finis. Pour résoudre ce problème, une approche non locale est utilisée, avec deux options différentes introduites comme variables non locales. Une étude paramétrique est mise en œuvre pour évaluer l'efficacité des deux options. Pour utiliser un modèle de type non local pour les composites à base de polymères, la séparation d'échelle et l'application du champ non local aux échelles macro et micro sont étudiées, en définissant un modèle d'homogénéisation Mori-Tanaka/TFA approprié. Les études paramétriques révèlent que lorsque longueur interne non locale est définie à l'échelle microscopique, les hypothèses théoriques de base de l'homogénéisation ne sont pas respectées et la localisation non-objective des variables d'état à l'échelle macroscopique n'est pas traitée. Comme conclusions clés de la présente étude, l'application de la variable d'état d'écrouissage non locale se révèle pertinent pour la prise en compte de la localisation des variables d'état internes, tandis que le cadre multi-échelles non local conduit à des réponses plus stables par rapport au modèle local lorsque le matériau est fortement endommagé.

Mots clés : thermoplastiques renforcés de verre, approche non locale, humidité relative, analyse multi-échelles, asymétrie tension-compression.

Abstract: Thermoplastics often exhibit nonlinear inelastic mechanisms. To predict their mechanical responses, viscoelasticity, viscoplasticity, and ductile damage are taken into account, and a I_1-J_2 yield function is presented to capture hydrostatic pressure effect and asymmetric yield behavior, based on which a parametric study considering cyclic and multi-axial loading is performed. The influences of water uptake on the behavior of thermoplastics is studied through an experimental campaign, and the models based on von Mises and I_1-J_2 yield functions are calibrated at different Relative Humidity (RH) levels. Thermoplastics exhibit softening at high levels of damage leading to an ill-posed problem in the local continuum framework and non-objectivity in the finite element models. To address this, a gradient enhanced nonlocal approach is used, and two different options are introduced as nonlocal variables. A parametric study is implemented to evaluate the effectiveness of both options. To adopt a nonlocal-type model for polymer-based composites, the scale separation and application of the nonlocal field at macro and micro scales are investigated, upon which an appropriate Mori-Tanaka/TFA homogenization framework is defined. Parametric studies reveal that when the nonlocal length scale is set at the microscale, the basic theoretical assumptions of homogenization are not satisfied, and the non-objective localization of state variables at the macroscale is not addressed. As a key conclusion from the present study, the application of the nonlocal hardening state variable shows good efficiency in addressing the localization of internal state variables, and the presented nonlocal multi-scale framework leads to more stable responses compared to the conventional model when the material is heavily damaged.

Keywords: glass reinforced thermoplastics, nonlocal approach, relative humidity, multi-scale analysis, tension-compression asymmetry.